Prenylation dynamics of RAS oncogenes: a chemical biology investigation into alternative prenylation phenomena

A thesis presented for the degree of
Doctor of Philosophy
of Imperial College London

Sarah M. Hassan

Department of Chemistry
Imperial College London
82 Wood Lane
London W12 0BZ

November 2023

Copyright

The copyright of this thesis rests with the author. Unless otherwise indicated, its contents are licensed under a Creative Commons Attribution-Non Commercial 4.0 International Licence (CC BY-NC). Under this licence, you may copy and redistribute the material in any medium or format. You may also create and distribute modified versions of the work. This is on the condition that: you credit the author and do not use it, or any derivative works, for a commercial purpose. When reusing or sharing this work, ensure you make the licence terms clear to others by naming the licence and linking to the licence text. Where a work has been adapted, you should indicate that the work has been changed and describe those changes. Please seek permission from the copyright holder for uses of this work that are not included in this licence or permitted under UK Copyright Law.

Statement of originality

I, Sarah M. Hassan, certify that this thesis and the research to which it refers are the product of my own work, and that any ideas or quotations from the work of other people, published or otherwise, are fully acknowledged and highlighted throughout this work, in accordance with the standard referencing practices of the discipline.

Prenylation dynamics of RAS oncogenes: a chemical biology investigation into alternative prenylation phenomena

Abstract

Protein prenylation comprises a class of post-translational modifications that regulates the localization and function of over 100 proteins, including RAS oncogenes. Farnesyl transferase (FTase) and geranylgeranyl transferase type 1 (GGTase-1) catalyze the attachment of a farnesyl or geranylgeranyl isoprenoid to a canonical C-terminal motif. Efforts to disrupt this process, such as the development FTase and GGTase inhibitors (FTIs, GGTIs), have largely been futile due to complex compensatory prenylation mechanisms. KRAS, a well-characterized oncogene, is geranylgeranylated in the presence of FTIs, allowing it to undergo membrane localization and exert downstream function, effectively subverting therapeutic efficacy. In contrast, HRAS remains unprenylated upon FTI treatment, making it uniquely susceptible to FT inhibition. However, it remains unknown as to what drives alternative prenylation dynamics upon inhibition of prenyltransferases, and platforms traditionally used in the study of protein lipidation are not currently fit to robustly interrogate this system. Deconvoluting prenyl substrate criteria and potential interaction partners that mediate or inhibit this switch could reveal novel drug targets in RAS-driven cancers. Moreover, alternatively prenylated RAS species may be exposed to new vulnerabilities that can be leveraged for combinatorial drug therapy. This project outlines an investigation into alternative prenylation mechanisms and potential regulators of these processes, particularly in response to farnesylation inhibition, and how this might be exploited in a therapeutic context. Utilizing a dual chemical probe system, prenylation profile changes can be evaluated on a global scale to deconvolute the activity of RAS binding partners and their responses to an FTI.
I then introduce the use of a novel CRISPR screening platform to conduct mutagenesis scanning of known RAS regulatory domains to explore their roles in alternative prenylation. Finally, RAS isoforms are funneled into proximity-based interactome mapping to identify putative drug targets that can potentiate FTI activity. Together, these techniques enable the deconvolution of complex prenylation dynamics and may contribute to the revelation of novel lipidation-dependent vulnerabilities in cancer.

Acknowledgements

Evidently, this was the most enjoyable, but most difficult, section of my thesis to write. It's only just settled how many people have contributed to my personal and scientific development during these last four years. Many of those contributions have been the most significant of my life so far. I am, if anything, a very lucky scientist.

Firstly, I would like to thank Ed, my endlessly brilliant supervisor, who has given me every opportunity to succeed. Thank you for your generosity, for instilling a confidence in me I didn't know I had, and for letting me truly become an independent scientist throughout the years you supervised me, starting all the way back in 2018 when I joined your lab as a timid MRes student. I am grateful for all the trust you placed in me to carry this project, and all the little side ones. I'd also like to thank you for putting together the most impossibly friendly and talented group of people I have had the pleasure of working with – the Tate Group is incredibly special, and not just by my own account. I also to need to thank Dr. Tom Lanyon-Hogg, who is now all the way in Oxford running his own group. Thank you for teaching me that science is magic, but real. I don't think I'd be here, wrapping up this thesis, without your unmatched mentorship.

To Rita and Seb, who have been my "parents" in London since nearly the beginning of this PhD. Thank you for all the love and life you have given to me, in good times and bad. I can't wait for our next Sunday night dinner in Utrecht. To Gui and Mattia, who have now taken on the role of my "London parents", thank you for always keeping me in mind, for introducing me to the fish market, for our adventures in Bilbao, and for making sure I kept sane throughout the writing of this thesis. To Roxani, the impossibly cool Greek sister I didn't know I had before joining Imperial; there is too much to say that I can fit on this sheet of paper – I love you. To Eddie B, who continues to insist I go climbing with him. I'll join you at RavensWall sometime soon, I swear. Thank you for being our boulder. To Tom J, who I once had pizza with the year before COVID, when we toasted to the great PhD years we had ahead of us. There was so much we didn't know then, but I'm glad we kept eating pizza together - thank you for your unwavering friendship. To Ana L, thank you for your patience and kindness, for moussaka, for sunny days in Santander, and for lively nights of salsa dancing. To Sachi and Delia, for our time in Italy (twice over!), for Vesuvius, and for our shared love of oversharing. To Archie, who has been the glue that keeps us together in our corner of the third floor, thank you for being my confidant, my fruit dealer, and dare I say, my good friend. To Ammar, who always had my back (literally, I'll miss the days you sat right behind me), thank you for keeping my spirits up, for complimenting my jumpers, and for letting me practice my Arabic. I promise I'll make you *molokheiya* one day. To Jack and Giulia, who have been among the brightest people I have met through this group, both in talent and demeanor. A little extra thank you to Jack, for proteomics parties, and of course, for introducing me to Sculpture. To Amina, I still lament that I lost you to Dan as an MRes student, but I am so glad you stayed in the group. Thank you for being among the kindest I have met at Imperial, for easy conversation (even if you struggle to hear me sometimes), and for the flowers. To Coach Dan, for being my partner in crime during COVID, for b-ball, and for the sick beats. To Matt, for the snacks (Hanutas in particular), Venn diagrams, and endless memes. FrankenRas lives on. To Thomas M, who has made me laugh (almost) every day since joining the Tate group – thank you for all your questions,

and for showing me how to use the probe sonicator. To Lame, for your passion, energy, and moral compass – thank you for always being so happy to see me, I'm always just as happy to see you. To Shradda, for your ability to listen and advise – thank you for always showing that you care. To Vincent, for being French, and for making Roche Continents that much more fun. To Lior, for your ability to calm me down, for our ~~strange~~ great time at FASEB, and for making prenylation great again. To Elena, for being a pillar in the Tate group, for karaoke, and for our brief (but great) collaborations. To Anne, for your brilliance, your kindness, and for being the best desk neighbor I have ever had -- only matched by Leran and Tom. Thank you for keeping my PC awake while I was away. To Leran, thank you for your support throughout the years you were in the Tate Group, for the surprise origami, and the delicious teas. To Tom B, thanks for keeping the sass alive in our bay, and for the nuggets of wisdom throughout the writing process. To Aidan, for jumping into the Tate Group headfirst, thank you for your intensity, espresso, and for always finding ways for us to have a good time. To Efthymios, for the music recommendations, constant encouragement, and for being the only person who appreciated my messages in the WhatsApp group. To Zhangping, who maintains a level of zen that I can only dream of achieving – thank you for always being patient, helpful and brilliant. To Manuel, for reviewing Chapter 3 in record time, thank you for your generosity and your wisdom.

To Jim, Simeon, Fangyuan, Cyrille, Qisi, Mira, Masha, Wouter, Dasha, Jana, Janine, Patry, Zuzanna, Josephine, Ryan H, Andrea, Feny, Kwang, Remi, Charlotte, Kai, Nicole, Caitlin, Henry, Ceire, and anyone else I may be forgetting, Tate Group past and present. Thank you for helping make these years among the most memorable of my life.

To Kacper, the friendliest ghost. You held my heart throughout all of this. Thank you for patience and support, and for all the ziti you made me these last few years. I cherish all of it.

To Dahlia/Dhalia, my sister who I have endless love for, thank you for being my forever best friend. You are the single most amazing person I have ever had the pleasure of meeting, and I am lucky enough to have grown up with you. I have too much to thank you for. To Ismail, my big little brother, your wisdom is far beyond your age. Thank you for keeping me grounded. To Mama, who is the funniest and kindest person in existence, according to me at least. Thank you for your unconditional love, green bananas, and regular calls. Oh, and I'd vote for you, every term. To Baba, for being there, even in the worst of times – thank you for your steadfastness and your patience. To Teeta Tuska and Heba, my grandmother and aunt, respectively, who have shown me that a PhD can be worth it (most of the time). Thank you for being such inspirational women in my life. And to the rest of my big, beautiful family in New Jersey, France, Saudi Arabia, and Egypt, mother of the world. I am always so pleasantly surprised at all the love we have for each other, even if we have lived thousands of miles apart for most of our lives. Thank you.

I would like to explicitly *not* thank my lower left wisdom tooth, which almost killed me (literally) in January 2022. The memory of hamster jaw haunts me. I would also *not* like to thank my right eye, which has given me a fair bit of trouble this last year or so. I'm glad I got to keep you, in the end. I would also like to say, space permitting, that if nothing else, history has shown us that violence begets violence. I hope this simple adage is someday internalized and enacted by those in power.

I hope I live to see the day where every human life is valued. And I hope I live to see the day some semblance of peace is restored to the Middle East, where my heart and my home remain.

لأحبائي

Statement of collaboration

The results presented in this thesis has been supported by collaborations with members at the Tate Group (Imperial College London) and the Francis Crick Institute.

Key contributions are noted here.

General:

- Dr. Jack Houghton aided in final proteomic sample MS submission. Dr. Houghton also conducted EvoSep desalting, Orbitrap DIA searches and TIMS-TOF DIA/DDA searches.
- Dr. Helen Flynn (Francis Crick Institute) conducted MS samples runs on the Eclipse Orbitrap mass spectrometer.

Chapter 2:

- H23 SmgGDS-607 KO cell line was generated by Dr. Kaja Kostyrko (UCSF).
- Sample pulldown using YnMyr (KingFisher optimization) was performed alongside Dr. Lior Soday.
- Proteomic sample submission from the precipitation optimization experiment was performed alongside Dr. Lior Soday.

Chapter 4:

- Dr. Andreas Damianou (University of Oxford) designed and generated all APEX2-RAS cell lines.
- Dr. Lior Soday aided in the validation of the APEX2 workflow and proteomic sample generation.
- Erika Bernardini aided in the generation and maintenance of MiniTurboID-RAS cell lines.

Publications and presentations

Publications:

- Yahyia S, Saunders CN*, **Hassan S*,** Straschil U, Fischer OJ, Rueda-Zubiaurre A, Haase S, Vizcay Barrena G, Famodimu MT, Jordan S, Delves MJ, Tate EW, Barnard A, Fuchter MJ, Baum J. **A novel class of sulphonamides potently block malaria transmission by targeting a Plasmodium vacuole membrane protein.** *Disease Models and Mechanisms 2023, 16 (2), dmm049950.*

- Jamshidiha M, Lanyon Hogg T , Sutherell C, Penacoba M, De Vita E, Brustur D, **Hassan S,** Petracca R, Craven G, Morgan R, Mann D, Cota E, and Tate EW. **Identification of the first structurally-validated covalent ligands of the small GTPase Rab27a.** *RSC Med. Chem. 2022, 13 (2), 150-155.*

- Losada A*, **Hassan S***, Tate EW. **Deconvoluting the biology and druggability of protein lipidation using chemical proteomics.** *Curr. Opin. Chem. Biol. 2021, 60, 97-112.*

(*) Denotes equal contribution

Presentations:

- Poster Presentation *at EMBL Chemical Biology* (Heidelberg, DE) - Sept 2022

- Invited Graduate Speaker at *FASEB Protein Lipidation Conference* (Vermont, USA) - Aug 2022

- Oral Presentation Prize *at Imperial College London Postgraduate Symposium* (London, UK) - July 2022 **

- Poster Prize *at RSC Chemical Biology Postgraduate Symposium* (York, UK) - April 2022 *

- Poster Prize *at Imperial College London Chemistry Postgraduate Symposium* (London, UK) - July 2021 *

Prize awarded for best (*) or runner-up (**) presentation/poster

Abbreviations

Alk	Alkyne
APE	Acyl PEG Exchange
Az	Azide
AzB	Azide-PEG3-Biotin capture reagent
AzRB	Azide-Biotin capture reagent with arginine cleavage site
AzT	Azide-TAMRA capture reagent
AzTB	Azide-TAMRA-Biotin capture reagent
B-GPP	Biotin-geranyl pyrophosphate
bp	Base pair
BSA	Bovine serum albumin
CAA	Chloroacetamide
cDNA	Copy DNA
CRC	Colorectal carcinoma
CuAAC	Copper(I)-catalyzed azide-alkyne cycloaddition
Cys	Cysteine
DMSO	Dimethyl sulfoxide
DPBS	Dulbecco's Phosphate buffer saline
EDTA	Ethylenediaminetetraacetic acid
ER	Endoplasmic reticulum
EtOH	Ethanol
FBS	Fetal bovine serum
FLAG	DYKDDDDK peptide sequence
FOH	Farnesol
FPP	Farnesyl pyrophosphate

FRET	Fluorescence resonance energy transfer
FTase	Farnesyltransferase
FTI	Farnesyltransferase inhibitor
gDNA	Genomic DNA
GDP	Guanosine diphosphate
GGOH	Geranylgeraniol
GGPP	Geranylgeranyl pyrophosphate
GGTase	Geranylgeranyltransferase
GGTI	Geranylgeranyl transferase-1 inhibitor
GO	Gene ontology
GTP	Guanosine-5'-triphosphate
HDV	Hepatitis delta virus
HGPS	Hutchinson-Gilford progeria syndrome
HMG-CoA	3-Hydroxy-3-methyl-glutaryl-coenzyme A
HNSCC	Head and neck squamous cell carcinoma
iMet	Initiator methionine
KD	Knock down
KDa	Kilodalton
KO	Knock out
LC	Liquid chromatography
LFQ	Label free quantification
LUAD	Lung adenocarcinoma
LVX	Lentiviral construct
m/z	Mass-to-charge ratio
Mal-PEG	Maleimide-PEG
MeCN/ACN	Acetonitrile

MeOH	Methanol
MetAP	Methionine aminopeptidase
NADH	Nicotinamide adenine dinucleotide
NGS	Next-generation sequencing
NMT	*N*-myristoyltransferase
PAT	Protein acyl transferase
PCR	Polymerase chain reaction
PDAC	Pancreatic ductal adenocarcinoma
PEG	Polyethylene glycol
Pi	Inorganic phosphate
PP	Pyrophosphate
PTI	Prenyltransferase inhibitor
PTM	Post-translational modification
PTXQC	Proteomics quality control
PVDF	Polyvinylidene difluoride
RABGGTase	RAB geranylgeranyl transferase
RT	Room temperature
SDS	Sodium dodecyl sulfate
SDS-PAGE	Sodium dodecyl sulfate polyacrylamide gel electrophoresis
sgRNA	Single guide RNA
STRING	Search Tool for the Retrieval of Interacting Genes/Proteins
T2A	T2A self-cleaving peptides
TAE	Tris-acetate-EDTA
TAMRA	5-Carboxytetramethylrhodamine
TBTA	Tris[(1-benzyl-1H-1,2,3-triazol-4-yl)methyl]amine
TIMS-TOF	Trapped ion mobility spectrometry - Time of flight
TMT	Tandem-mass tag

WB	Western blot
WT	Wildtype
Yn	Alkyne
YnF	Alkynyl-farnesol
YnGG	Alkynyl-geranylgeraniol
YnMyr	Alkyne myristate
YnP/YnPal	Alkyne palmitate
ZDHHC	Zinc-finger Asp-His-His-Cys motif

Table of contents

Copyright **2**

Statement of originality **2**

Abstract **3**

Acknowledgements **4**

Statement of collaboration **8**

Publications and presentations **9**

Abbreviations **10**

Table of contents 14

List of tables **18**

List of figures **19**

Chapter 1: Introduction 25

1.1. The biochemical expansion of proteome function 26

1.2. The study of protein lipidation 27

1.2.1 Major classes of protein lipidation 28

1.2.2. Protein *S*-prenylation 31

1.2.3. Isoprenoids 33

1.2.4. Substrate specificity 34

1.2.5. Post-prenylation processing 37

1.2.6. RAB proteins 38

1.2.7. Chaperone proteins 39

1.3. Protein prenylation in disease 41

1.3.1. Cardiovascular and metabolic diseases 42

1.3.2. Choroideremia 43

1.3.3. Hutchinson-Gilford Progeria Syndrome (HGPS) 43

1.4. Prenyltransferase inhibitors 46

1.5. RAS proteins 49

1.5.1. Lipidation of RAS proteins 50

1.5.2. Therapeutic targeting of RAS in cancer 53

1.6. Chemical tools in the study of protein *S*-prenylation....55
1.7.Project Aims....61

Chapter 2: Optimization of global prenylation profiling in the study of RAP1GDS1-regulated prenylation dynamics....64

2.1. Introduction....65
2.2. Results and discussion....72
2.2.1. Development of an SmgGDS variant-specific global prenylation profiling strategy....72
2.2.1.1. SmgGDS (RAP1GDS1) and prenylated interactors....72
2.2.2. Isolating SmgGDS splice variant-specific effects and cell model selection....74
2.2.3. Proof of concept: benchmarking automated sample preparation for membrane-associated proteins....83
2.2.3. Proof of concept: optimization of protein sample purification for membrane-associated proteins....86
2.2.3. Optimization of protein sample purification for membrane-associated proteins....91
2.2.4. Comparison of differentially enriched *S*-prenylated substrates in WT and SmgGDS-607 KO profiling experiments....99
2.2.5. SmgGDS-607 and its effect on tipifarnib sensitivity in H23 cells....101
2.2.6. Deep proteome analysis of H23 WT and SmgGDS-KO cell lines....107
2.2.7. Cell fractionation (membrane-enrichment) to study the influence of tipifarnib and SmgGDS-607 KO on protein localization.....111
2.3. Chapter summary and future work....127

Chapter 3: Development of a CRISPR-enhanced drug resistance mutagenesis approach to deconvolute alternative *S*-prenylation dynamics....132

3.1 Introduction....133
3.2. Results and discussion....138
3.2.1. Conceptualization of a CRISPR-enhanced drug-resistance mutagenesis approach....138
3.2.2 Designing a control assay for CRISPR-enhanced drug-resistance mutagenesis....140
3.2.3 Optimizing KRAS amplicon sequencing for NGS analysis....144
3.2.3 Evaluating mutagenesis efficiency using designed KRAS sgRNAs....146
3.2.4. Optimizing drug selection conditions for CRISPR-enhanced drug-resistance mutagenesis.....147
3.2.5. CRISPR-enhanced drug-resistance mutagenesis for HRAS alternative prenylation....152

3.2.6. Transitioning to an HRAS-dependent system for CRISPR-enhanced drug-resistance mutagenesis. 157
3.2.7. Adapting CRISPR-enhanced drug-resistance mutagenesis screening to 3D cell culture models 162
3.2.8. Investigating *S*-prenylation-dependent *S*-palmitoylation in the context of tipifarnib treatment. 166
3.2.9. Revisiting RAS chimera proteins to investigate *S*-prenylation and *S*-palmitoylation interplay. 178
3.3. Chapter summary and future directions 182

Chapter 4: RAS interactome studies to identify novel tipifarnib-associated vulnerabilities 188

4.1 Introduction 189

4.2. Results and discussion 193
4.1. Validation and optimization of APEX2 proximity labelling strategy 193
4.2. Validation of APEX2-RAS fusion *S*-prenylation status and response to tipifarnib. 199
4.3. APEX2-KRAS^{G12D} interactome benchmarking study 204
4.4. APEX2-RAS interactome study in the presence and absence of tipifarnib 209
4.5. Transitioning to a MiniTurboID interactome profiling strategy 217
4.3. Chapter summary and future directions 228

Chapter 5: Conclusions and future perspectives 231

Chapter 6: Materials and methods 235

Bibliography **..... 261**

Chapter 7: Appendix **..... 300**

List of tables

Chapter 1:

- Table 1.1. Isoprenoid probes reported in literature

Chapter 2:

- Table 2.1. PBR-containing RAP1GDS1 interactors.
- Table 2.2. Novel or recently annotated prenylated substrates enriched in H23 dataset.

Chapter 3:

- Table 3.1: Enriched CXXX proteins in YnP dataset

Chapter 4:

- Table 4.1. Comparison of commonly used proximity labelling techniques

Appendix:

- Table 4.1. Comparison of commonly used proximity labelling techniques
- Table 7.1. List of cell lines used throughout the study
- Table 7.2. List of antibodies used throughout the study
- Table 7.3. List of plasmids generated or used throughout the study
- Table 7.4. List of siRNAs used throughout the study
- Table 7.5. List of KRAS oligonucleotides used for sgRNA vector design
- Table 7.6. List of genomic amplicon PCR primers used throughout the study
- Table 7.7. List of HRAS oligonucleotides used for sgRNA vector design
- Table 7.8a. List of primers used for SDM generation of FLAG-RAS mutants
- Table 7.8b. High-throughput PCR set up for SDM of FLAG-RAS mutants
- Table 7.9. STRING KEGG of RAP1GDS1 interactors without prenylated proteins

List of figures

Chapter 1:

- Figure 1.1. Overview of protein *N*-myristoylation and *S*-palmitoylation
- Figure 1.2. Overview of protein *S*-prenylation
- Figure 1.3. The mevalonate pathway and isoprenoid biosynthesis
- Figure 1.4. Prenyltransferases structures (alpha and beta subunits).
- Figure 1.5. CXXX-protein sequence alignments and putative criteria for *S*-farnesylation or *S*-geranylgeranylation.
- Figure 1.6. A selection of prenyltransferases inhibitor (PTI) clinical candidates. PTIs grouped by target (FTase or GGTase) and stage of clinical investigation
- Figure 1.7. RAS homology and hypervariable domain PTMs
- Figure 1.8. RAS isoform specific lipidation dynamics
- Figure 1.9. RAS molecular switch activity and downstream effector pathways.
- Figure 1.10. Metabolic incorporation of dual isoprenoid probes (YnF and YnGG)

Chapter 2:

- Figure 2.1.1. Structures of SmgGDS (RAP1GDS1) splice variants
- Figure 2.1.2. Schematic depiction of SmgGDS variant-specific effects on small GTPase
- Figure 2.1.3. Putative roles of SmgGDS in alternative prenylation.
- Figure 2.2.1. Meta-analysis of SmgGDS (RAP1GDS1) interactors.
- Figure 2.2.2. Establishing an SmgGDS splice variant-specific cell system.
- Figure 2.2.3. YnF and YnGG incorporation profiles for H23 WT and SmgGD-607 KO cell lines
- Figure 2.2.4. H23 WT and SmgGD-607 KO cell line responses to tipifarnib.
- Figure 2.2.5 Initial chemical proteomic investigation of prenylation dynamics upon SmgGDS-607 KO.
- Figure 2.2.6. Benchmarking of an automated workflow for membrane-associated protein enrichment.
- Figure 2.2.7. Comparison of protein isolation and purification workflows for membrane-associated protein enrichment
- Figure 2.2.8. Devised sample preparation strategy for global prenylation profiling upon KO of SmgGDS-607.
- Figure 2.2.9. Summary data of H23 parent and SmgGDS-607 KO cell lines global prenylation profiling.

- Figure 2.2.10. Highlighted categories of YnF and YnGG enriched substrates in WT and SmgGDS-607 KO cell lines.
- Figure 2.2.11. WT and SmgGDS-KO YnF and YnGG enrichment plots
- Figure 2.2.12. Direct comparison of differentially enriched substrates in WT and SmgGDS-KO cell profiling experiments.
- Figure 2.2.13. Effect of tipifarnib on YnF and YnGG incorporation in WT and SmgGDS-607 KO cell profiling experiments
- Figure 2.2.14. Global profiling of PBR-containing GTPases and RHO GTPases.
- Figure 2.2.15. Global profiling of RAS alternative prenylation
- Figure 2.2.16. Evaluation of tipifarnib sensitivity across WT and SmgGDS-607 KO cell lines.
- Figure 2.2.17. Workflow for deep proteome profiling of tipifarnib-treated WT and SmgGDS-607 KO cell lines.
- Figure 2.2.18. Whole proteome DDA analysis of H23 WT and SmgGDS-607 KO cell lines in the presence and absence of tipifarnib.
- Figure 2.2.19. Whole proteome DIA analysis of H23 WT and SmgGDS-607 KO cell lines in the presence and absence of tipifarnib.
- Figure 2.2.20. Cell fractionation as a probe-free alternative to profiling *S*-prenylation dynamics.

Chapter 3:

- Figure 3.1.1 RAS homology
- Figure 3.2.1. CRISPR repair pathways
- Figure 3.2.2. Protein-centric CRISPR-enhanced drug-resistance mutagenesis concept.
- Figure 3.2.3. Strategy for KRASG12C CRISPR-enhanced drug-resistance mutagenesis
- Figure 3.2.4 sgRNA design for KRASG12C CRISPR-enhanced drug-resistance saturation mutagenesis.
- Figure 3.2.5 Optimizing parameters for sgRNA transfection efficiency.
- Figure 3.2.6. Optimizing amplicon PCRs for KRAS sequencing.
- Figure 3.2.7 T7 mutagenesis surveyor assay to validate on-target activity of designed sgRNAs.
- Figure 3.2.8. Workflow and optimization of CRISPR-enhanced drug-resistance mutagenesis in H23 cells.
- Figure 3.2.9. Sanger sequencing discordance analysis following drug-resistance saturation mutagenesis of KRASG12C
- Figure 3.2.10. Strategy for HRAS CRISPR-enhanced drug resistance mutagenesis.

- Figure 3.2.11. PCR optimization and validation of sgRNAs for HRAS drug-resistance saturation mutagenesis.
- Figure 3.2.12. First phase of resistance mutagenesis screening in H23 cells shows enrichment of *S*-palmitoylation-deficient HRAS mutants
- Figure 3.2.13. Second phase of resistance mutagenesis screening in H23 cells shows enrichment of loss-of-function HRAS mutants
- Figure 3.2.15. Evaluating transfection efficiency in MelJuSo and RL952 cell lines.
- Figure 3.2.16. Generation and validation of HRAS-driven Cas9 cell lines
- Figure 3.2.17. CRISPR-enhanced drug-resistance mutagenesis of HRAS-driven cell lines.
- Figure 3.2.18. Establishing tipifarnib toxicity in spheroid models of HRAS-driven cell lines.
- Figure 3.2.19. CRISPR-enhanced drug-resistance mutagenesis as applied to 3D spheroid model.
- Figure 3.2.20. *S*-palmitoylation dynamics in the presence of tipifarnib.
- Figure 3.2.21. Meta-analysis of dual *S*-prenylation and *S*-palmitoylation substrates.
- Figure 3.2.22 Global profiling of *S*-palmitoylation in H23 cells using YnPalm-based enrichment.
- Figure 3.2.23. Tipifarnib-sensitive *S*-palmitoylated substrates in H23 cells
- Figure 3.2.24. Global profiling of *S*-palmitoylation in H23 cells reveals FTI-induced changes in *S*-palmitoylation dynamics.
- Figure 3.2.25 Hierarchical clustering analysis of YnPalm dataset reveals *S*-palmitoylated substrates sensitive to tipifarnib treatment.
- Figure 3.2.26. Designing RAS lipidation mutants to validate role of *S*-palmitoylation in alternative prenylation
- Figure 3.2.27. Development of a membrane localization readout for drug-resistance saturation mutagenesis

Chapter 4:

- Figure 4.1.1. Distribution of RAS isoform drivers in human cancers
- Figure 4.1.2. Deconvoluting alternative RAS prenylation through interactome studies.
- Figure 4.2.1. APEX2 proximity labelling offers high temporal control for RAS interactome capture.
- Figure 4.2.2. Optimizing APEX2-RAS induction conditions for proximity labelling experiments.
- Figure 4.2.3. Validation of APEX2-RAS biotinylation and optimization of interactor enrichment.
- Figure 4.2.4. Validation of *S*-prenylation status of APEX2 constructs

- Figure 4.2.5. Validation of alternative prenylation status for APEX2-RAS constructs.
- Figure 4.2.6. Proteomic strategy for profiling APEX2-KRAS^{G12D} isoform interactors.
- Figure 4.2.7. Preliminary proteomic analysis of APEX2-KRAS^{G12D} interactome.
- Figure 4.2.8. Proteomic analysis of APEX2-KRAS^{G12D} interactome in the presence of tipifarnib.
- Figure 4.2.9. Proteomic strategy for profiling APEX2-RAS isoform interactors
- Figure 4.2.10. Data analysis workflow of APEX2-RAS interactome study using multi-batch TMT labelling
- Figure 4.2.11. Proteomic analysis of APEX2-RAS interactomes in the presence and absence of tipifarnib
- Figure 4.2.12. Comparison between alternatively and non-alternatively prenylated interactomes
- Figure 4.2.13. Comparisons between APEX2-RAS isoform datasets
- Figure 4.2.14. MiniTurboID proximity labelling strategy for RAS interactome mapping.
- Figure 4.2.15. Testing MiniTurboID-RAS constructs for proximity labelling experiments
- Figure 4.2.16. Proteomic strategy for profiling MiniTurboID-RAS isoform interactors
- Figure 4.2.17. Proteomic analysis of MiniTurboID-KRAS4A and 4B interactomes
- Figure 4.2.18. Comparison of MiniTurboID-KRAS4A and 4B interactomes
- Figure 4.2.19. Proteomic analysis of MiniTurboID-KRAS4A interactome in the presence of tipifarnib

Appendix:

- Figure 7.1. Validation of endogenous model system for KRAS prenylation switching
- Figure 7.2. Validation of endogenous model system for HRAS pull-down
- Figure 7.3. Skyline analysis of PEG contamination across purified protein samples
- Figure 7.4. Unit vector scaling of H23 *S*-prenylation profiling experiment
- Figure 7.5. STRING analysis of substrates in DDA and DIA whole proteome studies of H23 tipifarnib treatment
- Figure 7.6. Correlation analysis of DIA and DDA whole proteome data of H23 cells

- Figure 7.7. Sanger sequencing of KRAS exon in H23 cells reveals heterozygous G12C mutation
- Figure 7.8. Confocal imaging (top) and flow cytometry analysis of mCherry transfected T24 cells to evaluate transfection efficiency. Bottom panel showing maximal transfection efficiency achieved by flow cytometry.
- Figure 7.9. IncuCyte images of H23 spheroid formation using increasing seeding densities (top). Spheroids form within 4 days (bottom)
- Figure 7.10. Example vector map of plasmid used to generate APEX2-RAS cell lines (shown here for $KRAS^{G12D}$)

Chapter 1
Introduction

1.1. The biochemical expansion of proteome function

The diversity of the human proteome is not directly ascribed to protein genomic composition[1]. Although alternative splicing, mRNA processing, and epigenetic regulation expand genome complexity by some measure, organism complexity is not proportional to genome size[2]. Moreover, while gene sequences can change throughout evolutionary timescales, organisms require highly dynamic and transient adaptations that underlie the vast majority of cellular functions. To fulfill these requirements, organisms have evolved protein post-translation modifications (PTMs).

PTMs provide the largest source of proteome diversity in organisms, imparting additional functionalities to proteins that surpass their primary sequence-driven capabilities[3]. These mainly consist of covalent modifications of protein polypeptide chains that confer new chemical properties, enabling temporal and spatial control of proteins and the phenomena they engender[4]. PTM groups comprise a wide range of sizes and properties, from small chemical groups to larger polypeptides and carbohydrates. To date, there have been over 600 chemically distinct PTM classes described[5]. These are appended or processed by enzymes that encompass up to a significant 5% of the eukaryotic proteome, underscoring their importance in cellular regulation[6].

Almost every eukaryotic protein is subject to post-translation modification, allowing cells to control their fate and function in a rapid and dynamic manner, without relying on protein turnover to alter or adjust their functions. This can be compounded by attachment of multiple PTMs to a single protein, which may consist of sequential or conditional chemical transformations[6,7]. Additionally, PTMs can differ in their permanence, and include both reversible and irreversible modifications. Reversible PTMs often form the basis of modular signaling networks that adapt to different stimuli or cellular requirements, and are controlled enzymatically by “writers” and “erasers”. On the other hand, irreversible PTMs impart properties that persist throughout the lifetime of the modified protein and are ultimately related to native protein function, including stable localization or proteolytic processing events[4]. As PTMs play essential roles in regulating cellular processes,

dysregulation of PTMs can have profound consequences, frequently manifesting as disease. Equally however, PTMs offer a multitude of opportunities to pharmacologically control protein function and have consequently been the subject of many drug discovery efforts. Inhibiting or modifying PTMs offers the benefit of acting upstream of a target protein to modulate its function, which is convenient in targeting proteins that lack druggable motifs, including but not limited to RAS proteins, discussed in depth later in this chapter[8].

1.2. The study of protein lipidation

Protein lipidation is a diverse and widespread class of PTMs that play key roles in cell signaling, the regulation of protein-protein interactions, protein localization, and secretion, to name a few. Enzyme-mediated lipid transfer to encoded substate protein sites increases protein hydrophobicity, promoting membrane association[9]. Unlike other PTM classes, lipidation uniquely establishes protein interactions with cellular membranes, leading to membrane partitioning events that can have drastic consequences on protein function[10]. These consequences are often driven by changes to subcellular localization that in turn modulate the microenvironment and interactome of the lipidated protein. The importance of protein lipidation is recapitulated in its involvement with pathological states; dysregulation or loss of protein lipidation events are associated with various diseases, including cancer, inflammation, neurological disorders and infection[10]. As such, proteins that regulate lipidation, mainly lipid transferases, have been targeted in numerous drug discovery contexts, indeed with some notable successes[7]. Still, the substrate scope and dynamic interplay of these modifications have long evaded comprehensive analysis, severely limiting our understanding of the roles lipidation plays in various contexts and how they may be leveraged for therapeutic benefit. The study of protein lipidation bears complex analytical challenges brought about by the very nature of the modification itself, including hydrophobicity and the lack of exploitable functional groups[11].

Traditional techniques to study protein lipidation include the use of radiolabeled (i.e. titrated) and synthetic lipid analogs, which are incorporated by substrate proteins in

enzymatic assays[12]. Other similar *in vitro* applications historically provided valuable insight into lipidation substrate requirements and the kinetics of incorporation[13]. However, due to the inherent complexities regarding crosstalk and signaling events that modulate lipidation on a global scale, our understanding of how certain modifications contribute to phenotypes of interest remained limited. The study of protein lipidation and their dysregulation requires interdisciplinary approaches that evade standard, low-throughput analytical methods, which are often divorced from the global cellular environment.

Over the last 20 years, chemical biology and mass spectrometry-based proteomics have afforded technologies that enable the global profiling of PTMs and their functional consequences. Notably, the use of chemical probes has contributed significantly to this, which are molecules that mimic their endogenous PTM counterparts, or molecules that modulate protein function (i.e. inhibitors)[14]. These molecules can be functionalized with bioorthogonal handles used to analyze or isolate the proteins they modify[13]. Thus, the field has largely progressed towards endogenous, global profiling strategies afforded by chemical proteomics. In particular, the advent and application of click chemistry to proteomic techniques was a revolutionary development in the study of PTMs as whole, which has enabled researchers to contextualize PTM events, including lipidation, within the complex cellular environment[15]. The installation of alkyne or azide tags in endogenous lipid analogs has thus yielded various orthogonal readouts alongside global chemical proteomic profiling, including the use of flow cytometry, gel analysis, imaging and protein-interaction studies, greatly contributing to our understand of lipidation dynamics in the cellular milieu[7].

1.2.1. Major classes of protein lipidation

Protein lipidation can be generally classified into irreversible and reversible modifications, each of which engender distinct functional outcomes. Irreversible protein lipidation can be attached both co- and post-translationally, and constitutes a native, integral component of the substrate that remains on the protein until it is eventually degraded

through protein turnover.[10] Major classes of irreversible lipidation include *N*-myristoylation[16] and *S*-prenylation, the latter of which is further categorized into *S*-farnesylation and *S*-geranylgeranylation[17].

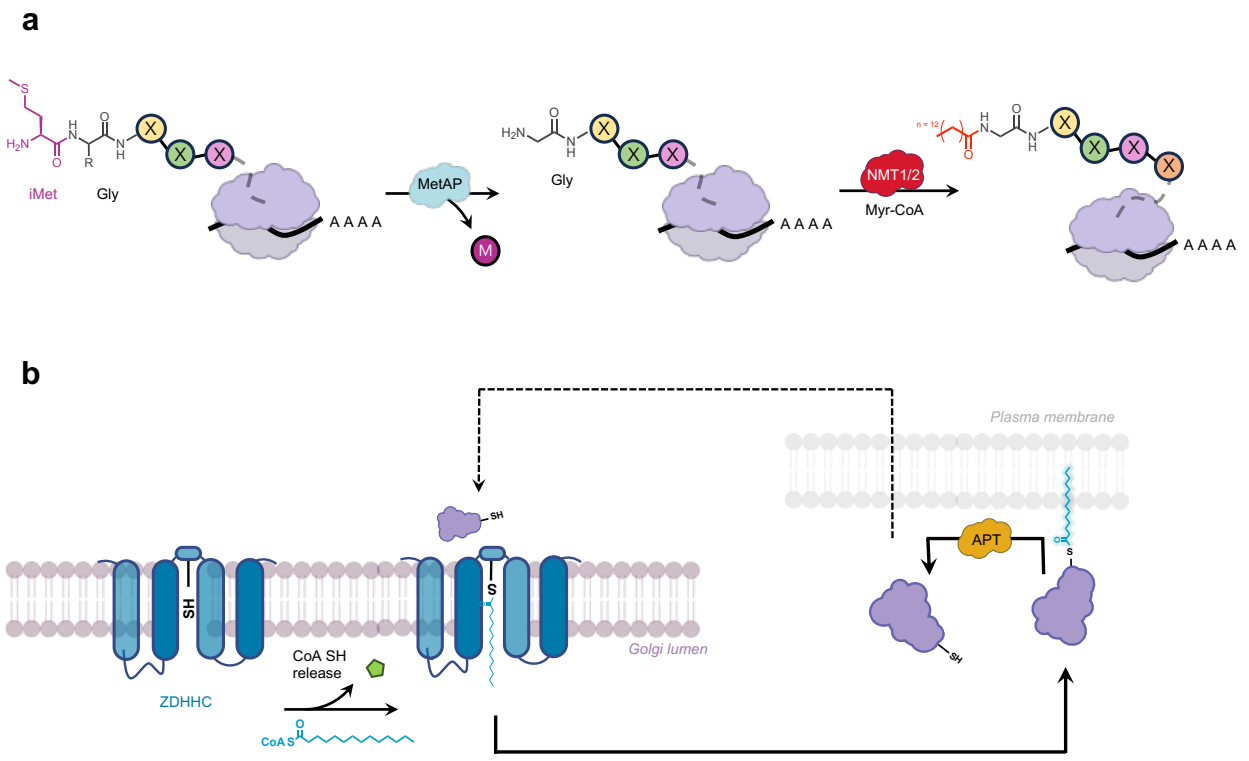

Figure 1.1. Overview of protein *N*-myristoylation and *S*-palmitoylation. (a) Overview of co-translation *N*-myristoylation. Here, *N*-myristoylation occurs at the ribosome following MetAP-mediated cleavage of the substrate initiator methionine (iMet). NMT1 or 2 then appends a myristate group to the newly revealed N-terminal glycine. **(b)** *S*-palmitoylation is catalyzed by PATs, which are largely of the zDHHC family of transmembrane enzymes, concentrated at the Golgi apparatus. Fatty acid CoA is loaded onto the zDHHC enzyme and is then transferred to a substrate protein that then translocates to its target membrane. Acylprotein thioesterases (APTs) hydrolyze the modification, restarting the dynamic cycle.

N-terminal myristoylation describes the condensation of a 14-carbon saturated fatty acid, myristate (C14; tetradecanoic acid), from myristoyl-coenzyme A to the N-terminal glycine of substrate proteins, a process catalyzed by two isozymes – *N*-myristoyl transferase 1 and 2 (NMT1 and 2), which harbor some level of functional redundancy[18]. *N*-myristoylation usually occurs co-translationally at the ribosome following cleavage of the initiator methionine by methionine aminopeptidases (MetAPs)[19] (Fig. **1.1a**) However, *N*-

myristoylation has also been demonstrated to occur post-translationally following the revelation of a cryptic glycine by proteolytic digestion, such as through caspase-related cleavage events during apoptosis[20]. *N*-myristoylation occurs for some 400 substrates across the human proteome and has been globally profiled in both human cell lines and parasites (e.g. *Plasmodium falciparum*[21], *Trypanosoma brucei*[22], *and Leishmania*[23] species) using click functionalized probes azido-Myr (AzMyr) and alkyne-Myr (YnMyr)[20,24].

S-prenylation is a central focus of this thesis and will be discussed extensively throughout. It refers to the attachment of farnesyl (C15) or geranylgeranyl (C20) isoprenoids via a thioether linkage at a cysteine within a canonical C-terminal motif, known as a "CAAX" box[17]. Farnesyltransferase (FTase) and geranylgeranyltransferases (GGTases) respectively append these isoprenoids to substrates in a cognate manner[25]. Because the modification is irreversible and occurs shortly after translation, *S*-prenylation has been described to assign a level primary or dominant control of native protein localization.

Reversible lipidation, by contrast, can be appended and cleaved in a dynamic fashion and is more closely associated with events like signal transduction. *S*-palmitoylation (or *S*-acylation) is the only known class of reversible protein lipidation and refers to the post-translational covalent attachment of a long-chain fatty acid, ranging from 16 – 22 carbons in length, onto surface exposed cysteines through a labile thioester linkage[26] (Fig. **1.1b**). Palmitoyl acyltransfersases (PATs) of the ZDHHC family catalyze this transfer. Because the attachment of C16 has been found to be among the most common for *S*-acylation, the modification has been generally referred to as *S*-palmitoylation, and will referred to as such throughout this thesis[27]. *S*-palmitoylation is additionally subject to controlled removal via acyl-protein thioesterases (APTs) which, together with PATs, shape membrane localization cycles that form the basis of signal compartmentalization across several protein networks[28].

RAS proteins are a significant class of lipidated proteins that are highly regulated by their localization status, which in turn can be a function of their lipidation state[29]. RAS proteins

sit atop many signaling cascades involved in cell differentiation, proliferation, metabolism, and apoptosis[30]. RAS proteins are also of particular interest due to their notorious involvement in cancer, as RAS isoform mutations rates are the highest across most cancers[31]. Moreover, RAS mutations are commonly associated with cancers that have some of the lowest five-year survival rates, including pancreatic, lung, and colorectal cancer, which can be as low as 5%[31].

RAS proteins are also particularly well-studied in the context of *S*-prenylation and *S*-palmitoylation[30]. The lipidation dynamics of RAS proteins provide a model case for how a class of highly homologous proteins remain non-redundant in the face of evolutionary pressure, and instead collectively generate key diverse signaling outputs in the cell.

1.2.2. Protein *S*-prenylation

As previously mentioned, protein *S*-prenylation refers to the irreversible attachment of farnesyl (C15) and geranylgeranyl (C20) isoprenoids via a thioether linkage at C-terminal cysteines through the action of FTases and GGTases (Fig. **1.2)**. This is known to occur at a C-terminal motif called a "CAAX" box, where "A" represents an aliphatic residue while "X" is any residue[32]. However, as our knowledge of prenylation scope deepens through global profiling studies, the use of "CAAX" may no longer be comprehensive enough[33,34]. As a result, it is instead referred to as a "CXXX"-box throughout this work. In humans, four prenyltransferases (PTases) catalyze protein prenylation. FTase and GGTase-I serve as the canonical PTases for typical CXXX substrates[35,36]. GGTase-II, or RABGGTase, singly or doubly attaches geranylgeranyl isoprenoids to a lesser conserved C-terminal motif of RAB proteins and that can contain up to two cysteines (CC, CXC, or CXXX, CXXC)[37]. GGTase-III is a recently identified prenyltransferase that consists of the RABGGTase β-subunit in a heterodimer complex with orphan protein PTAR1, which forms its α-subunit[38]. SNARE protein YKT6 and E3 ligase subunit FBXL2 are currently the only known substrates of GGTase-III, and the *S*-geranylgeranylation of these substrates remain unique within the canon of *S*-prenylation[38,39]. YKT6 is geranylgeranylated at a cysteine upstream of its CXXX-box, and prior *S*-farnesylation of

the CXXX-motif itself is required for this geranylgeranylation to proceed, giving rise to a previously unknown sequential heterogenous double prenylation modification[39]. FBXL2 is geranylgeranylated at a typical CXXX motif, however it was demonstrated to also make extended contacts with PTAR1, the GGTase-III α-subunit, which is not a characteristic of substrate recognition for all other recognized types of *S*-prenylation[38,39].

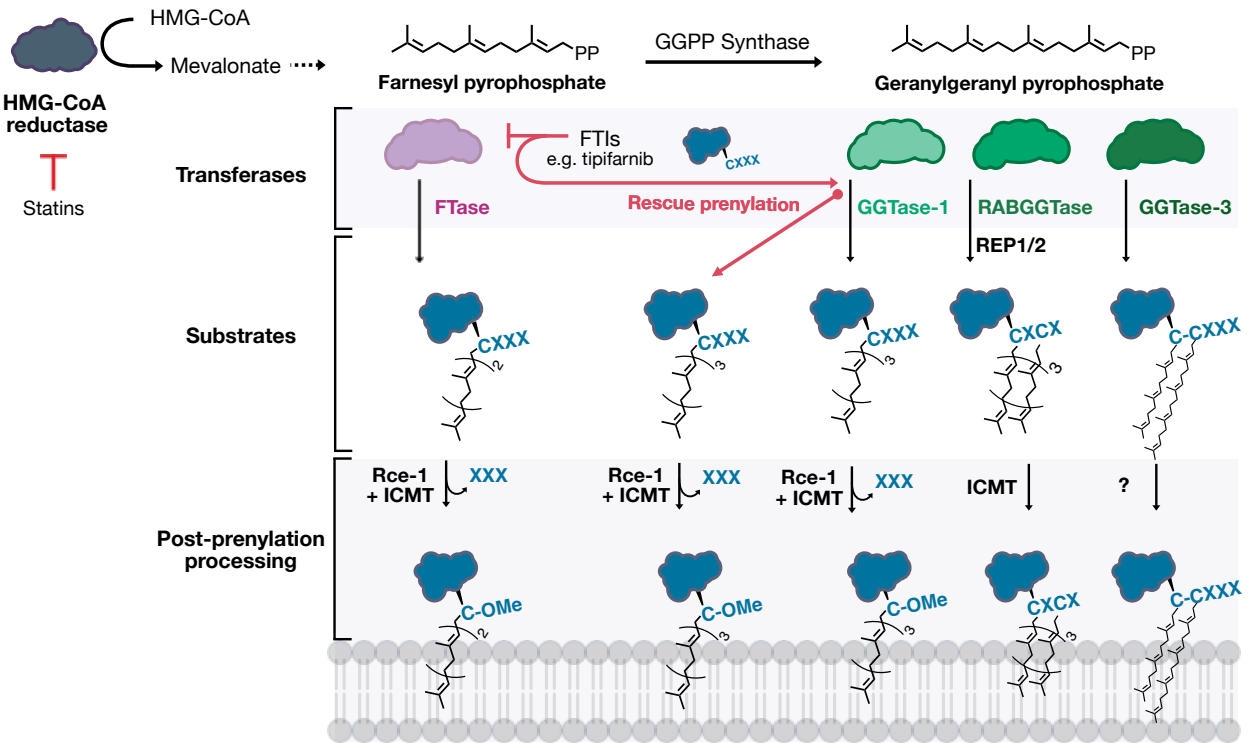

Figure 1.2. Overview of protein *S*-prenylation. Isoprenoid biosynthesis is initiated by 3-hydroxy-3-methylglutaryl-coenzyme A (HMG-CoA) reductase, which is inhibited by statins. Farnesyltransferase (FTase) and geranylgeranyltransferase-1 (GGTase-1) append a single farnesyl or geranylgeranyl, respectively, to the Cys of the CXXX motif of substrate proteins, which may undergo further processing by RCE-1 (endoproteolysis) and ICMT (carboxyl methylation). Farnesyltransferase inhibitors (FTIs) cause delocalization of substrates. A small subset of proteins can undergo alternative prenylation by GGTase-1 in the presence of an FTI (e.g. KRAS, NRAS). RabGGTase (GGTase-2) appends one or two geranylgeranyl groups to the RAB C-terminus and requires REP1/2 chaperone proteins. GGTase-3 performs atypical prenylation, including dual, heterogenous prenylation (shown here; YKT6 is the known substrate that undergoes this type of atypical prenylation). Processed prenylated proteins are then trafficked to their target membranes.

1.2.3. Isoprenoids

Mammalian cells produce two isoprenoids that are transferred to substrate proteins by their cognate prenyltransferases: farnesyl (C15) and geranylgeranyl (C20)[40]. Chemically, they consist of repeating five-carbon isoprene units, where geranylgeranyl consists of one additional unit to farnesyl. These lipids are synthesized as intermediates of a larger biosynthesis pathway, called the mevalonate pathway, that is also responsible for the biosynthesis of cholesterol (Fig. **1.3**) [40]. The process is initiated by HMG-CoA reductase (β-Hydroxy β-methylglutaryl-CoA reductase), an ER-resident enzyme[41,42]. Production of HMG-CoA by HMG-CoA reductase is the first and rate-limiting step of the mevalonate pathway. Consequently, HMG-CoA reductase is extremely well-characterized in the context of cardiovascular disease (CVD), stemming from its involvement in the biosynthesis of cholesterol. HMG-CoA reductase inhibitors were thus developed, commonly known as statins, in an attempt to mitigate CVD and other inflammatory disorders[43]. However, statins simultaneously inhibit the production of isoprenoids, depleting them from cellular lipid pools and consequently limiting protein prenylation in the cell[44]. Although the FDA has approved the use of statins for cholesterol-associated CVDs long ago, it is now evident that some of the anti-inflammatory and CVD ameliorating effects associated with statins can be attributed to attenuation of protein *S*-prenylation[45]. Statins are generally well-tolerated drugs, however they are also associated with various pleiotropic effects, some of which may be explained by their indirect effect of *S*-prenylation; still, many of these effects remain poorly characterized[45,46].

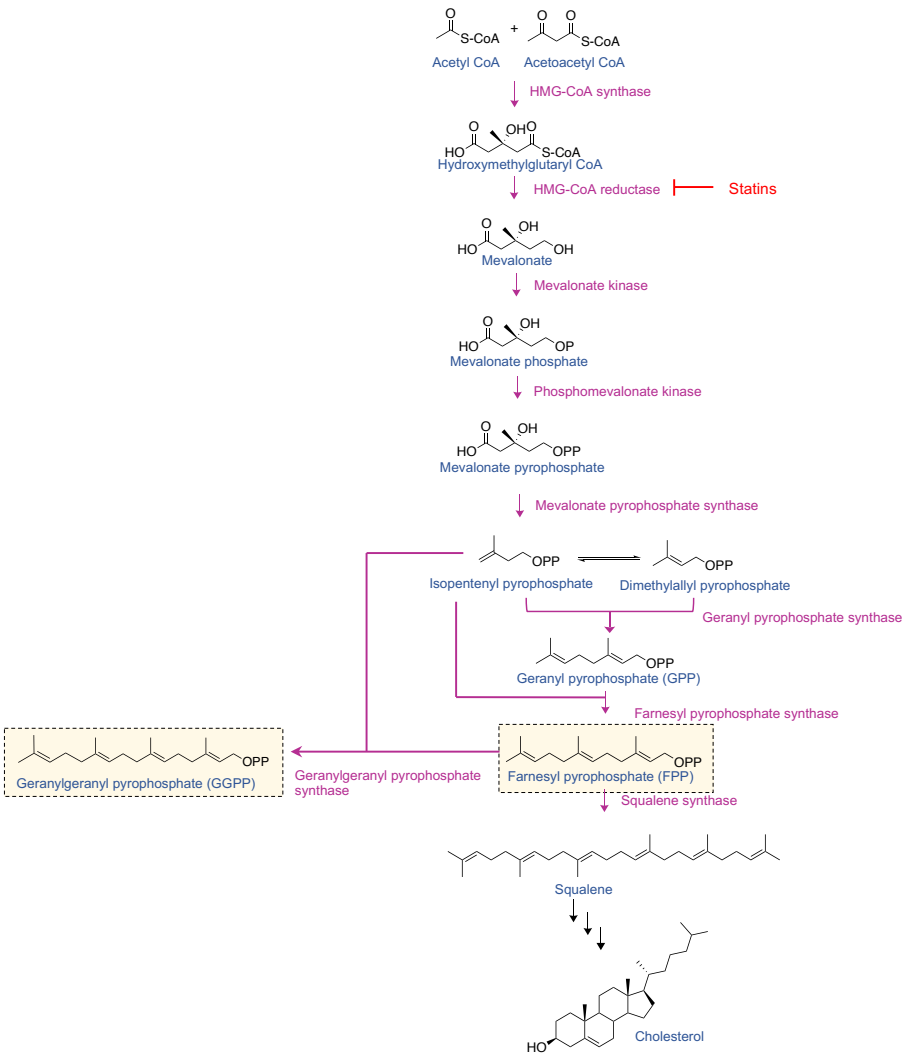

Figure 1.3. The mevalonate pathway and isoprenoid biosynthesis. Biosynthesis of isoprenoids is governed by the mevalonate pathway, which is also inhibited by statins. The pathway is also responsible for the biosynthesis of cholesterol. Substrates are shown in blue, enzymes are shown in magenta. GGPP and FPP, the substrates for *S*-prenylation, are highlighted.

1.2.4. Substrate specificity

All prenyltransferases consist of an alpha and beta subunit, with the catalytic active site formed at the interface (Fig. **1.4**)[47–49]. It has been demonstrated that some level of prenyltransferase selectivity originates from variation of the X_4 amino acid, which can putatively determine whether a substate undergoes *S*-farnesylation or *S*-geranylgeranylation. This was initially established by *in vitro* studies that have shown that

methionine (Met), glutamine (Glu), and serine (Ser) amino acids at the X_4 position are favored by FTases, whereas alanine (Ala), threonine (Thr), and cysteine (Cys) can be tolerated. On the other hand, leucine (Leu) at X_4 is favored by GGTases, while valine (Val) and phenylalanine (Phe) are considered to be tolerated residues[25,32,48]. These "CXXX" requisites have been bolstered by structural and modelling studies of prenyltransferases, revealing that the X_4 residue undergoes extensive van der Waals interactions within the active site cavity, which binds the C-terminal peptide and structurally differs, if only slightly, between the prenyltransferases[47,50].

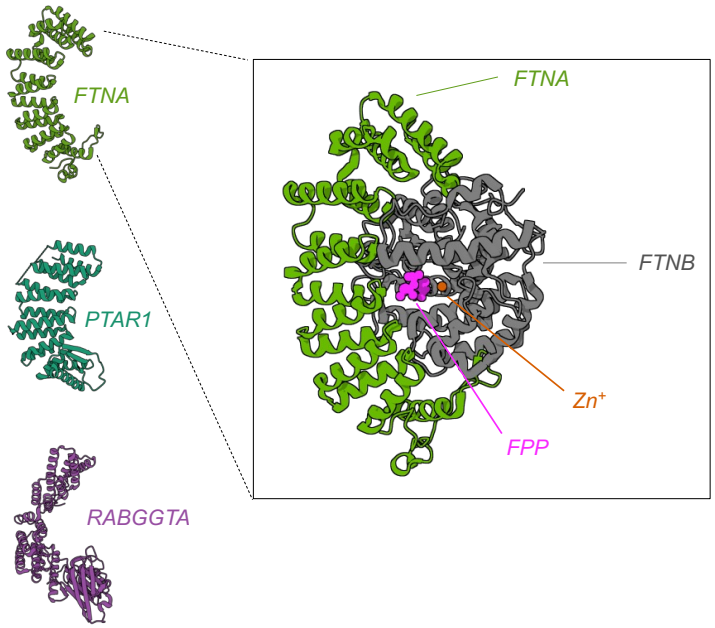

Figure 1.4. Prenyltransferases structures (alpha and beta subunits). Crystal structures of prenyltransferases alpha-subunits. FTNA (FTase; GGTases-1); PTAR1 (GGTase-3) and RABGGTA (RABGGTase). Beta-subunits (such as FNTB for FTase, shown in gray) determine specificity for the isoprenoid (FPP, shown in magenta). The subunits together, along with a zinc ion (shown in orange) make up the holoenzyme. **PDBs**: FNTA (2F0Y); PTAR1(6O60); RABGGTA (3E30).

Importantly however, these trends have not fully held throughout the profiling and deconvoluting of global protein *S*-prenylation, and do not translate to exclusive substrate specificity for prenyltransferases. For example, the modelling and *in vitro* studies that have assigned the aforementioned X_4 residue specificities have also shown that the

leucine (Leu) is not tolerated for FTase. However, more recent studies have shown that RHOF (CXXX = CLLL) can be a substrate for FTase, while RAC1, which harbors an identical CXXX motif, is exclusively a substrate for GGTase[51]. Other studies have also attributed residues immediately upstream of the CXXX-box to the reactivity of prenyltransferase substrates and may contribute to the preferences that are observed *in vitro*. Nevertheless, sequence alignment of the last 25 amino acids of high-confidence prenyltransferases substrates shows a significant level of clustering between canonically farnesylated and geranylgeranylated proteins (Fig. **1.5**).

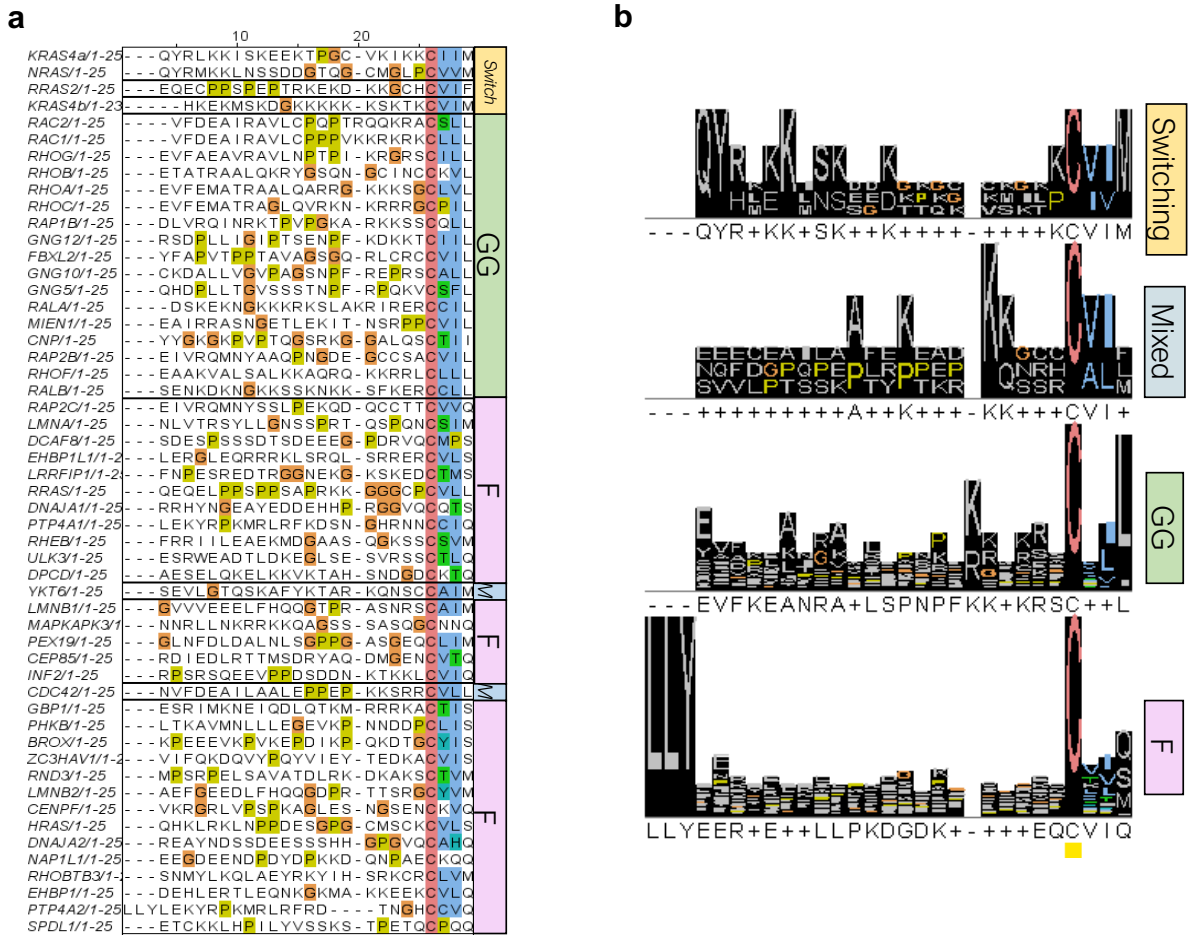

Figure 1.5. CXXX-protein sequence alignments and putative criteria for *S*-farnesylation or *S*-geranylgeranylation. Sequence alignments for final 25 amino acids of canonical *S*-prenylated substrates. Performed with AutoMAFFT. Alignment recapitulates most observed *S*-prenylation patterns in the cell. However, proteomic profiling experiments have revealed some differences in *S*-prenylation status that aren't explained by sequence alone. Mixed prenylation (accepts both F and GG), switching (undergoes alternative prenylation in the presence of a farnesyltransferase inhibitor (FTI)).

Notably, the more subtle discrepancies that are observed in global profiling studies, such as the given RHOF and RAC1 example, are not integrated into this analysis. Moreover, the phenomenon of alternative prenylation, which describes a resistance mechanism that a small subset of *S*-farnesylated proteins undergo in the presence of a farnesyltransferase inhibitor (FTI), does not conform to these prenyltransferases preferences[52]. During alternative prenylation, a canonically *S*-farnesylated protein instead undergoes *S*-geranylgeranylation when FTI activity is lost, allowing the substrate to properly localize and effectively thwarting the intended action of the inhibitor[53,54]. High profile substrates like KRAS and NRAS are known to undergo alternative prenylation, and it is not yet clear exactly why certain proteins harbor this compensatory ability, while others, like HRAS, remain susceptible to FTI action. These discrepancies, taken with the fact that *in vitro* studies have not fully recapitulated what is observed in global profiling studies, suggest that prenyltransferases substrate specificity is dictated by a complicated amalgam of features within the primary sequence of the C-termini of substrate proteins, or that substrate specificity can arise from external factors, such as other concurrent PTMs or protein-protein interactions. This is especially important to consider in the development of *S*-prenylation targeted drugs, including farnesyltransferase inhibitors.

1.2.5. Post-prenylation processing

Prenylated proteins often undergo further processing at their C-termini following attachment of either farnesyl or geranylgeranyl – a series of steps collectively referred to as prenylated protein “maturation”[55]. This begins with proteolysis of the last three amino acids of the CXXX-box (X_{1-3}) by RCE1 (RAS-converting CAAX endopeptidase 1). Proteolysis leads to increased hydrophobicity of the C-terminus and consequently facilitates the eventual membrane partitioning of the target substrate[56]. This is followed by carboxyl methylation, or “capping” of the now free, prenylated cysteine by ICMT (Protein-*S*-isoprenylcysteine O-methyltransferase) and further contributes to increasing the hydrophobicity of the substrate C-terminus. This effect is generally more profound for *S*-farnesylated proteins when compared to *S*-geranylgeranylated proteins, as the *S*-farnesyl modification is less hydrophobic on its own[57]. These events occur sequentially at

the cytoplasmic face of the Endoplasmic reticulum (ER) lumen and rapidly capture substrate proteins soon after they are prenylated in the cytoplasm.

Not all *S*-prenylated substrates undergo complete post-prenylation processing. A small subset of CXXX proteins bypass this process and localize to their target membrane immediately following *S*-prenylation in what is known as the shunted post-prenylation pathway[58]. It remains possible that chaperone proteins play a role in this process, whereby newly *S*-prenylated proteins are sequestered by chaperone binding and are trafficked to the plasma membrane, while other proteins are left to diffuse to the ER where they undergo post-prenylation processing[34]. Moreover, disruption of ICMT activity appears to affect the half-life of some substrate proteins that require post-prenylation processing for efficient localization, such as RHOA, which exhibits a markedly shorter half-life in cells when ICMT activity is lost. On the other hand, ICMT disruption results in an increased half-life for some RAS proteins, which may have unpredictable connotations for therapeutic intervention[59].

1.2.6. RAB proteins

RAB proteins are small GTPases that form the largest class of RAS superfamily proteins, holding vital roles in directing vesicle trafficking and secretory pathways in the cell. In contrast to other *S*-prenylated proteins, RAB proteins are prenylated by a single enzyme, RABGGTase (also known as GGTase-II), which singly or doubly attaches geranylgeranyl isoprenoids to a variety of C-terminal cysteine motifs that can contain up to two cysteines, mainly CC, CXC, CXXC and CXXX sequences[60]. RAB proteins also uniquely require accessory proteins REP1/REP2 to undergo *S*-geranylgeranylation, as they are unable to bind RABGGTase independently of them[61,62]. Following prenylation, REP proteins then act as chaperones for newly *S*-geranylgeranylated RAB species, and aid in their translocation to target membranes. Furthermore, while most RAB proteins undergo *S*-geranylgeranylation, a very small subset has been found to undergo *S*-farnesylation instead, such as RAB28, which harbors the CXXX sequence CAVQ[63].

1.2.7. Chaperone proteins

Substrate proteins achieve a hydrophobic character upon *S*-prenylation, which largely takes place in the cytosol where prenyltransferases are located. Therefore, the trafficking of these proteins throughout the cell is an integral part of their controlled translocation and eventual membrane partitioning. Chaperone proteins bind proximal to the prenylated motif on their client substate proteins, shielding the hydrophobic lipid from the aqueous environment[34]. This maintains the protein in the cytosol by forming a transient soluble complex as they are shuttled to their target membranes. For example, RHOGDIs (RHO guanosine nucleotide dissociation inhibitors) bind *S*-geranylgeranylated RHO GTPases, another class of RAS superfamily GTPases, at their prenylated C-terminus directly following *S*-prenylation processing[64,65]. They also possess the ability to extract RHO proteins from membranes by solubilizing them in a similar fashion. RHOGDIs then direct and redistribute RHO proteins to membrane compartments across the cell, depending on the nature of upstream signaling, thus preserving compartmentalized signal transduction. RHOGDIs also inhibit nucleotide exchange and GTP cycling activities that are native to their target GTPase function, thereby inhibiting substrate-mediated downstream signal transduction for as long as they are bound[66]. This is accomplished by obstructing the GTPase switch region, where the GTP nucleotide is bound and undergoes hydrolysis, as well as by restricting access to other RHO GTPases accessory proteins that facilitate GTP cycling, which include GEFs (guanidine nucleotide exchange factors) and GAPs (guanidine nucleotide activating proteins). The inhibitory actions of RHOGDIs likely serve to inhibit premature or uncompartmentalized RHO signaling whilst they are trafficked through the cell. Only when RHO GTPases, like other small GTPases, are localized to their target membranes are they then able to initiate signaling[67,68]. RABGDIs hold analogous roles in the trafficking of RAB proteins[69]. GDI release factors (GRFs) that are localized to membrane compartments facilitate the release of GDI from their client GTPases, however to date, few of these proteins have been characterized. In some cases, RAS superfamily effector proteins have been shown to possess GRF capabilities instead, which contributes to the extreme fine-tuning of signal transduction that occurs at membrane compartments[70,71].

Phosphodiesterase delta (PDE) proteins serve a GDI-like function for RAS proteins, with interactions with KRAS being the best studied[72,73]. The δ subunit of phosphodiesterase type 6 (PDE6D) binds RAS, as well as a broad range of other farnesylated proteins, at its prenyl motif and shuttles the protein to a target membrane, which is, more often than not, the plasma membrane. PDE6D plays an essential role in maintaining RAS signaling at the plasma membrane, mainly by trapping RAS into the recycling endosome system, and subsequently redelivering it to the membrane by unidirectional vesicular transport[72,73]. This forces the equilibrium of RAS localization to shift drastically to the plasma membrane through cellular direction, often in response to growth factors or other upstream proliferative signaling pathways. Without this mechanism, RAS distribution veers towards a more equal dispersion across endomembranes[30,74]. GRF proteins for RAS have not been extensively studied, however ARL2/3, which is part of another class of small GTPases, has been shown to act as a GRF for KRAS when it is delivered to membranes by PDE6D. ARL2/3 localization thus marks where RAS can be accepted across cellular membranes, which serves as an additional regulatory mechanism for compartmentalized RAS signaling[70].

Other RAS prenyl-binding proteins have been identified. Prenyl-binding protein (PrBP/δ) holds a similar role to PDE6D and appear to possess overlapping cargoes, including RHEB, part of another class of small GTPases[75]. RND proteins, which are a subclass of RHO GTPases, have been shown to bind 14-3-3 scaffold proteins, which harbor a prenyl-binding pocket[76]. 14-3-3 scaffold proteins have a unique binding mechanism whereby they exclusively bind prenylated GTPases with a phosphorylated serine (Ser) directly upstream of the CXXX-motif.

SmgGDS is another class of prenyl-binding proteins, which putatively execute multiple functions in their regulation of GTPase activity[77]. In some cases, SmgGDS have been shown to act as a guanidine nucleotide exchange factor (GEF) for small GTPases, facilitating their activation cycling when membrane bound[78]. SmgGDS has also been implicated in increasing prenylation turnover rates for some small GTPases, including RHO and RAS proteins, which is proposed to be accomplished by prompting the release of these GTPases from prenylation machinery (i.e. FTase or GGTase-I)[79–81]. The best

characterized role for its regulation of GTPases is through the binding and trafficking of clients to cellular compartments, in the same manner as other prenyl-binding proteins[81,82]. SmgGDS (gene name: *RAP1GDS1*) is expressed as two splice variants, SmgGDS-607 and SmgGDS-558, which are named based on their respective sizes; the short form variant, SmgGDS-558, lacks a single repeating motif that is present in the long form variant. Consequently, this changes their binding dynamics to client GTPases, where SmgGDS-607 putatively prefers binding to GTPases with a polybasic region (PBR) and shuttles them to their cognate prenyltransferases[83,84]. The short-form, with its lack of an additional repeat domain, is able to bind the client GTPase after it has been prenylated and shuttles them to their target membrane. Notably, the equilibrium between SmgGDS-607 and 558 expression is not always in present, and in some cancers, the equilibrium is shifted towards the long-form variant, putatively suggesting that SmgGDS-607 is more oncogenic[80,85]. However, the literature on SmgGDS has not established a consensus on the mechanisms of trafficking, which substrates are clients, and the resulting phenotypic consequences, as its prenyl-binding roles appear to be highly client and context specific. It remains unclear how SmgGDS contributes to prenylation overall. Regardless, its characterization has opened an interesting line of inquiry into novel prenylation modulators, and how they may be targeted for therapeutic benefit.

1.3. Protein prenylation in disease

S-prenylation is predicted to occur for more than 200 proteins across the proteome[63]. Consequently, *S*-prenylation plays an integral role in directing the localization of many proteins, and thus has profound implications on their downstream function. Dysregulation of *S*-prenylation is implicated in many diseases, including cardiometabolic diseases[86,87], retinal disease[88], developmental disorders[89], infection[90–93] and cancer[94]. Some of these diseases are discussed below.

1.3.1. Cardiovascular and metabolic diseases

Metabolic diseases, including diabetes, have increased in incidence in developed countries greatly over the last half century[95]. This has been mainly driven by the rise in type 2 diabetes (T2D) diagnoses, a complex metabolic disorder characterized by insulin resistance. This is engendered by an initial level of insulin resistance driven by extended inflammation, for reasons that remain poorly understood. This initial resistance causes pancreatic β-cells to produce more insulin as a compensatory mechanism, however their increased metabolic activity drives more inflammation through the production of reactive oxygen species (ROS) and other inflammatory biomarkers that eventually prompts immune cell response and subsequent β-cell loss[96,97]. This exacerbates general inflammation and leads to chronic insulin resistance that presents as a myriad of complications. RAC1, a prenylated member of the RHO GTPase family, has been implicated in the pathogenesis of diabetes[98]. RAC1 regulates reactive oxidative species generation; through modulation of NOX2 (NADPH oxidase) activity at the plasma membrane, RAC1 is able to control ROS production in a localization dependent manner[99,100]. RAC1 hyperactivation is associated with ROS production in pancreatic β-cell. In the same way, RAC1 is also active in the retina and regulates ROS production via NOX2 and appears to contribute to the development of diabetic retinopathy[101]. Some reports have suggested that inhibition of RAC1 prenylation, or the reduction of isoprenoid biosynthesis through the use of statins, may have therapeutic benefit in diabetes[100]. However, a recent study demonstrated that lack of RAC1 prenylation instead increases inflammatory markers in some cell types, complicating its potential for therapeutic targeting in this context[100].

RHO family proteins are also key regulators of vascular structure and have been heavily implicated in the pathogenesis of atherosclerosis, mainly driven by RHOGEFs and activation of pro-inflammatory pathways via the RHO/ROCK (RHO-associated protein kinase) signaling pathways[102,103]. Statins are widely prescribed for cardiovascular disease (CVD) and associated atherosclerosis, not only due to cholesterol lowering effects through suppression of the mevalonate pathway, but also due to putative loss of

RHO/ROCK signaling through attenuated prenylation[104,105]. The involvement of RHO GTPases in CVD is extensive and wide-ranging, and remain highly active fields of study[86].

1.3.2. Choroideremia

Choroideremia is an X-linked genetic retinal degeneration disorder that is characterized by loss-of-function of the gene that encodes REP1 (*CHM*).[106] The disease is known to affect approximately 1 in 50,000 people and leads to the degeneration of integral retinal components, including the retinal epithelium, photoreceptors and the choroid, where its name is derived from. This results in gradual loss of vision in patients, and eventually complete blindness by middle age. Interestingly, the REP2 isoform is unable to compensate for loss of REP1, suggesting a lack of redundancy in the eye[107,108]. Loss of REP1 results in the accumulation of unprenylated RAB proteins, including RAB27A, which has long been considered to be a driver of disease pathogenesis[109]. This has been bolstered by *in vitro* analysis of the RAB27A:REP1 complex, which was found to be a better substrate for RABGGTase, and potentially more dependent on REP1[110]. A recent prenylation profiling study demonstrated that REP1 knockout (KO) cells in a mouse model choroideremia results in the specific loss of prenylation for a subset of RAB proteins, including RAB12, RAB7 and RAB27B. Gene therapy trials that attempt to restore REP1 in afflicted patients are ongoing and have shown great promise, with some trials now in stage 3[111].

1.3.3. Hutchinson-Gilford Progeria Syndrome (HGPS)

Hutchinson-Gilford Progeria Syndrome (HGPS) is a rare genetic disorder characterized mainly by a premature, rapidly accelerated aging phenotype[112]. The disease is uniformly fatal, with death usually occurring in adolescence. The genetic origin of HGPS is well-defined and stems from a *de novo* point mutation in the LMNA gene, which encodes lamin A/C, a nuclear *S*-farnesylated protein that plays many roles related to cell structure, motility and chromosome organization[113,114]. LMNA undergoes normal prenylation processing by RCE1 and ICMT, as discussed previously, resulting in its eventual targeting to the nuclear endomembrane where ZMPSTE4 resides. ZMPSTE4 is involved in the

maturation of LMNA by proteolytically cleaving the farnesylated C-terminus, which allows it to translocate to the nuclear lamina and engage as a key structural component there[115]. The HGPS mutation results in a truncation that drives the synthesis of a protein known as progerin. Progerin lacks the sequence that is recognized and cleaved by ZMPSTE4, which results in the aberrant accumulation of *S*-farnesylated progerin within nuclear endomembranes[116,117]. This causes various nuclear defects that underlie the canonical disease pathology, resulting in the rapid emergence of the clinical features of aging, including genome instability, cellular senescence, and mitochondrial dysfunction. Ultimately, most patients with HGPS succumb to cardiovascular disorders that are engendered by the aging phenotype[112]. Inhibiting *S*-farnesylation of progerin using farnesyltransferase inhibitors (FTIs) is now an established therapeutic strategy for HGPS patients[118]. Lonafarnib (Zokinvy) is the only FDA approved FTI currently on the market, with HGPS being a key indication. Lonafarnib was demonstrated to improve clinical markers in HGPS patients, including cardiovascular parameters, however it is not curative and therapeutic intervention generally manifests as a relatively moderate effect on disease progression in patients[119]. Critically, non-farnesylated progerin still accumulates in the nucleoplasm, as opposed to the nuclear envelope, which ameliorates but does not eliminate the associated nuclear defects[120]. Moreover, mouse studies have demonstrated that FTIs also seem to decrease total progerin in the cell, and the production of progerin without the CXXX-box still contributed to the disease phenotype, implying that *S*-farnesylation may have a more minor role than initially suspected[121]. Nevertheless, lonafarnib has been shown to increase patient lifespan by approximately 3 months for each of the first 3 years of treatment, with an overall average increased lifespan of 2.5 years[122,123]. While this is still significant given that patients succumb to the disease very early in life, other therapies are still being investigated as better alternatives to FTIs in this context.

1.3.4. Cancer

Significant interest associated with *S*-prenylation, including its therapeutic targeting, partially stems from the fact RAS proteins rely heavily on prenylation to exert their

downstream function[124]. RAS proteins are among the best studied oncogenes, and collectively are the most commonly mutated cancer drivers, holding key roles in tumor initiation, growth, and metastasis[31]. Characteristic point mutations result in defects in RAS GTPase cycling, leading to hyperactivation of RAS and, consequently, a highly proliferative phenotype. RAS, namely KRAS, NRAS and HRAS, are notoriously difficult to target directly, with only one class of KRAS-targeted drug ($KRAS^{G12C}$) validated to date[125–127]. Thus, targeting RAS function through *S*-prenylation was initially an extremely attractive therapeutic strategy, as prenyltransferases are much more tractable drug targets, and prenylation is critical for RAS function; delocalization of RAS from the plasma membrane results in attenuated signaling and reduced proliferation[128,129]. Unfortunately, FTIs were met with great disappointment in initial clinical trials, as it was later found that KRAS and NRAS undergo a resistance mechanism whereby they are alternatively prenylated by GGTase-I in the absence of an active FTase, resulting in persistent membrane localization and associated signaling[54]. HRAS, however, uniquely does not undergo alternative prenylation and remains unprenylated in the presence of FTIs. This phenomenon is a key question in this PhD project will be discussed in the next sections and throughout this thesis.

Other studies have implicated elevated FTase activity in itself as being associated with cancer, however it is unclear exactly how this results in a proliferative phenotype, beyond the calculable downstream *S*-farnesylation of other cancer-associated GTPases[130]. Other prenylated proteins that are implicated in the development and progression of cancer include RHO family GTPases, which are largely *S*-geranylgeranylated[131–133]. This, coupled with the now known phenomenon of alternative prenylation, encouraged the development of GGTase inhibitors (GGTis) in an attempt to attenuate hyperactivated GTPase signaling using some combination with FTIs[134,135]. The development of PTIs, particularly in the context of RA*S*-driven cancers, is discussed in more detail in the next sections.

1.4. Prenyltransferase inhibitors

Prenyltransferases are among the most highly targeted PTM-related enzymes in the context of drug discovery, largely due to the notoriety of their known substrates. As discussed in the previous sections, *S*-prenylated substrates include RAS, RHO and RHEB GTPases, which are highly implicated in cancer, as well as nuclear lamins, RABs, and variety of kinases and phosphatases that are other prominent disease targets, ranging from infection to developmental disorders[136].

Most inhibitors of prenyltransferases act as peptide-substrate competitors[137]. Early farnesylation inhibitors (FTIs) were peptidomimetics derived from the KRAS CXXX-motif "CVIM", with the X_2 position mutated to a phenylalanine, which is bulky enough to displace the substrate peptide thereby inhibits farnesylation[138]. Later generations of FTIs preserved the overarching strategy of displacing the substrate peptide at the X_2 position, but instead opted for scaffolds with less amide bonds, imparting greater compound stability. Tipifarnib and its close relative, BMS-214663, coordinate a zinc ion required for enzyme activity proximal to the active site[139,140]. An imidazole moiety coordinates the ion, while an aromatic ring obscures the X_2 peptide binding site[139]. Lonafarnib (SCH66336) possesses a slightly different mode of action, which involves the obstruction of the X_2 peptide binding site, but no coordination of the zinc ion[141]. Both inhibitor classes are highly potent and specific for FTase over GGTases (Fig. **1.6**).

GGTase inhibitors were initially designed based on FTI peptide-substrate competitor analogues, which were modified to contain bulkier, more hydrophobic groups to fit into the larger GGTase active site[142]. The introduction of a zinc coordinating motif, analogous to newer generation FTIs, resulted in potent and highly selective GGTase-I inhibitors (approximately 250-fold selectivity over FTase)[142]. By contrast, the development of inhibitors against RABGGTase was significantly more challenging due to structural homology with other prenyltransferases[143,144]. Moreover, broad inhibition of RABGGTase was expected to be more toxic than FTase or GGTase-I inhibition alone, due to the vast

substrate scope of RABGGTase and the essentiality of RAB proteins in maintaining vesicular trafficking in the cell[145,146].

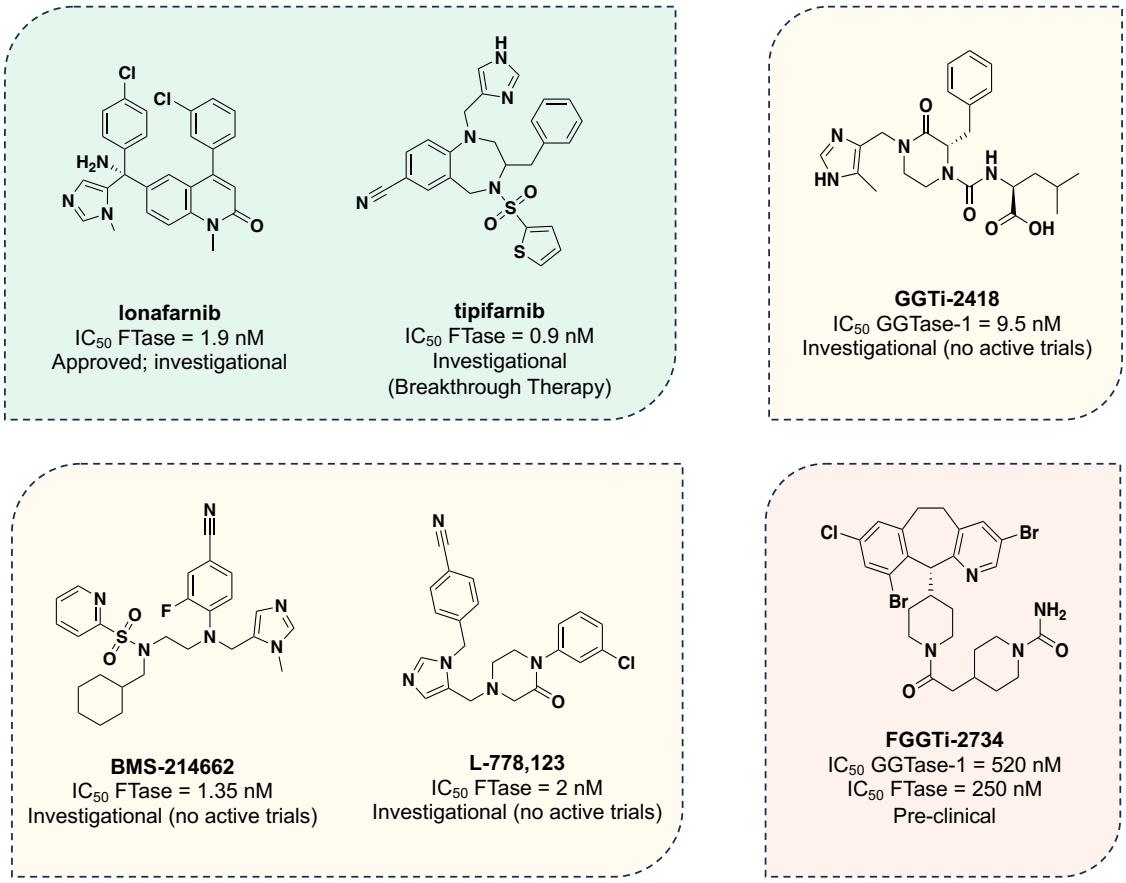

Figure 1.6. A selection of prenyltransferases inhibitor (PTI) clinical candidates. PTIs grouped by target (FTase or GGTase) and stage of clinical investigation.[135,137,139,141,147,148]

Over 40 years of research has yielded hundreds of prenyltransferases inhibitors (PTIs) that have been studied extensively *in vitro* and *in vivo*, with many reaching clinical trials[137]. Few, however, have made it past clinical trials, with only one FTI achieving FDA approval (lonafarnib) for the treatment of hepatitis D (HDV) and HGPS, and another achieving breakthrough therapy status for the treatment of some HRAS-driven cancers (tipifarnib), with both designations given in just the last three years[122,149–151]. While FTIs in particular have been found to be surprisingly well-tolerated in clinical trials, treatment outcomes have been disappointing, partly owing to the phenomenon of alternative prenylation.

Moreover, hematological dose-limiting toxicities have been observed with long-term treatment regimens that are required to sustain their benefit in responsive cancers[152]. This has complicated their administration as a single-agent treatment, and an emphasis is now being placed on identifying combinatorial therapies that synergize with tipifarnib to attenuate these toxicities.

GGTase inhibitors, on the other hand, were found to have very narrow therapeutic indices and exhibited high gastrointestinal toxicity[135,145]. Consequently, these inhibitors were largely abandoned from a therapeutic standpoint, although some work has been done to develop dual FTase and GGTase inhibitors as a way to tackle alternative prenylation[148]. These were successful in preventing alternative prenylation in pre-clinical models, however doses that were required to achieve this endpoint were found to be highly toxic[148]. Recent studies also have also shown that *S*-geranylgeranylation can mediate inhibition of RHO GTPase-effector interactions that left unrestrained lead to hyperactivation of inflammatory pathways, suggesting that a specific balance of prenylated and non-prenylated RAC1 regulates the inflammasome[153]. This may also partially explain the observed GGTi toxicities.

Other attempts at drugging post-prenylation processing pathways have been undertaken with limited success. RCE1 genetic disruption only yielded modest effects on cell proliferation and other phenotypes of interest, which in turn did not encourage drug development programs[154]. ICMT genetic disruption, by contrast, exhibited profound antiproliferative effects[155]. ICMT inhibitors later demonstrated some efficacy in xenograft models, especially when combined with other therapeutics, such as tyrosine-kinase inhibitors (TKIs)[156–159]. However, as there currently are limited methodologies to study post-prenylation processing on a global scale, it is difficult to ascertain these effects to a set of substrates. Along with the fact that ICMT inhibition seems to have differential effects on RAS isoform half-lives and signaling, as discussed in a previous section, ICMT inhibitors still require substantial development to unpick these differentials and identify suitable patient populations.

1.5. RAS proteins

RAS superfamily GTPases are a large family of molecular switches that integrate a wide range of cellular signals, many of which converge around cell proliferation, as well as cytoskeletal organization, trafficking, migration and cell differentiation[160,161]. RAS regulation occurs at multiple levels, which include PTMs, GTP-activity accessory proteins, chaperones and effector proteins.

Molecular switch activity, which is at the heart of RAS GTPase function, occurs through a well-characterized activation and deactivation cycle[162]. This is defined as the hydrolysis of GTP to GDP, the subsequent release of GDP and inorganic phosphate, and the eventual re-uptake of GTP to re-initiate the cycle. GTPases are “active” when GTP-bound, and “inactive” when GDP-bound. This cycling action is assisted by a set of accessory proteins, which have been described earlier in this chapter. GEFs promote the binding of GTP, GAPs stimulate GTP hydrolysis to GDP, and GDIs inhibit the release of GDP from the GTPase, maintaining it in an active state[136,163]. Cycling dynamics almost exclusively occur at endomembranes and the plasma membrane, as RAS GTPases often remain GDI or chaperone bound, thus inactive, when traversing the cytosol.[73] This is considered to be a mechanism that ensures compartmentalized and controlled RAS signaling, which is diverse but tightly regulated under normal physiological conditions.

From a structural perspective, RAS GTPases contain a G-domain, which consists of the N-terminal catalytic domain that harbors the nucleotide-binding site[164]. This domain is made of a P-loop, along with switch regions I and II that undergo conformational changes during GTP hydrolysis. G-domains are principally homologous across the major RAS isoforms, which are defined here to be KRAS4A, KRAS4B, NRAS and HRAS (Fig. **1.7**). RAS GTPases also share a homologous effector binding domain, which is located near the G-domain. However, sequence homology decreases significantly towards the C-terminus, down from 100% at the N-terminus to approximately 15% at the C-terminus[165]. Importantly, this is where membrane targeting motifs are located, meaning the major differences between RAS isoforms arise at the level of cell localization and

compartmentalization. This is also a putative explanation for why these closely related RAS isoforms persisted in the face of over 400 million years of evolution[160].

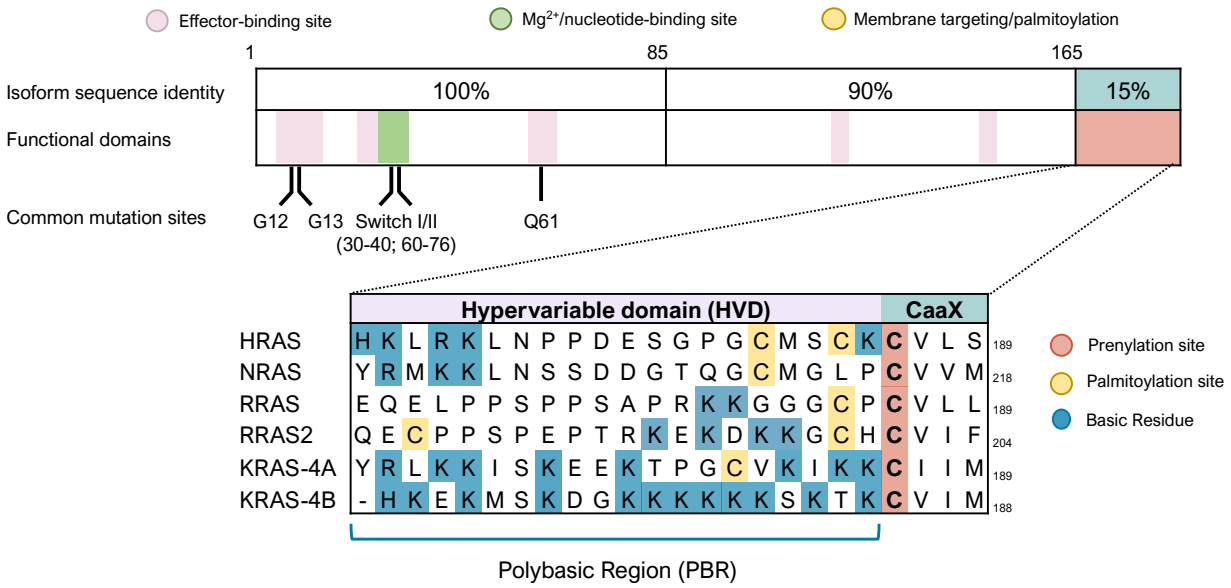

Figure 1.7. RAS homology and hypervariable domain PTMs. Alignment and functional annotation of RAS isoform sequences, highlighting sequence homology and divergence at the hypervariable domain (HVD) and CXXX-box, where homology level drops to ~15%. Shared functional domains are shown, including effector binding domains and the G-domain switch region. Common mutations site (G12, G13 and Q61) are also shown.

1.5.1. Lipidation of RAS proteins

RAS signaling compartmentalization is essential to produce distinct signaling outputs in the cell, which in turn contribute to a large variety of essential cellular functions[29,30]. The RAS protein C-terminal domain is sub-divided into two regions, the hypervariable domain (HVD) and CXXX-box. As mentioned, RAS protein homology decreases significantly in this region. All RAS proteins harbor an *S*-prenylated CXXX-box, which is *S*-farnesylated under normal conditions[129,166–168]. Cardinal differences arise at the level *S*-palmitoylation within the HVD[169]. *S*-palmitoylation (also known as *S*-acylation) is another class of post-translational lipidation, referring to addition of thioester-linked long chain fatty acid, of a length between C16 and C20, to a surface exposed cysteine residue[26]. As described previously, *S*-palmitoylation is unique among the known classes of post-translational

lipidation in that it is reversible and dynamic. *S*-palmitoylation thus serves an important role in the directing target substrates to different endomembranes in a signal and context-specific manner. While *S*-prenylation is wholly necessary for plasma membrane localization for RAS proteins, a secondary membrane-targeting signal is also essential for stable and targeted RAS plasma membrane localization, particularly for RAS proteins[170]. For HRAS, NRAS and KRAS4A, this secondary signal is *S*-palmitoylation, as it imparts an estimated 100-fold greater affinity for membranes than the prenylated species alone[171,172]. HRAS is doubly *S*-palmitoylated, while NRAS and KRAS4A are singly *S*-palmitoylated. This allows efficient capture of HRAS and NRAS at the Golgi, where they eventually translocate to the plasma membrane via vesicular transport[173].

In contrast, KRAS4B does not contain an *S*-palmitoylated cysteine. Instead, it harbors a polybasic region (PBR), which is a short stretch of basic residues (hexalysine) within its hypervariable domain[168,174]. This imparts a positive charge along its C-terminus that facilitates electrostatic interactions with the negatively charged inner leaflet of the plasma membrane, allowing for efficient membrane targeting and partitioning. As a result, KRAS4B largely bypasses vesicular trafficking to the membrane via the Golgi[175,176]. This feature is significant as this makes it so that KRAS4B targeting cannot be dynamically controlled through a secondary lipidation-mediated signal. However, there is evidence to suggest that phosphorylation Ser181 in the HVD prevents the PBR from interacting with the plasma membrane, giving some level of dynamic control over plasma membrane targeting outside of the primary *S*-prenylation step[177].

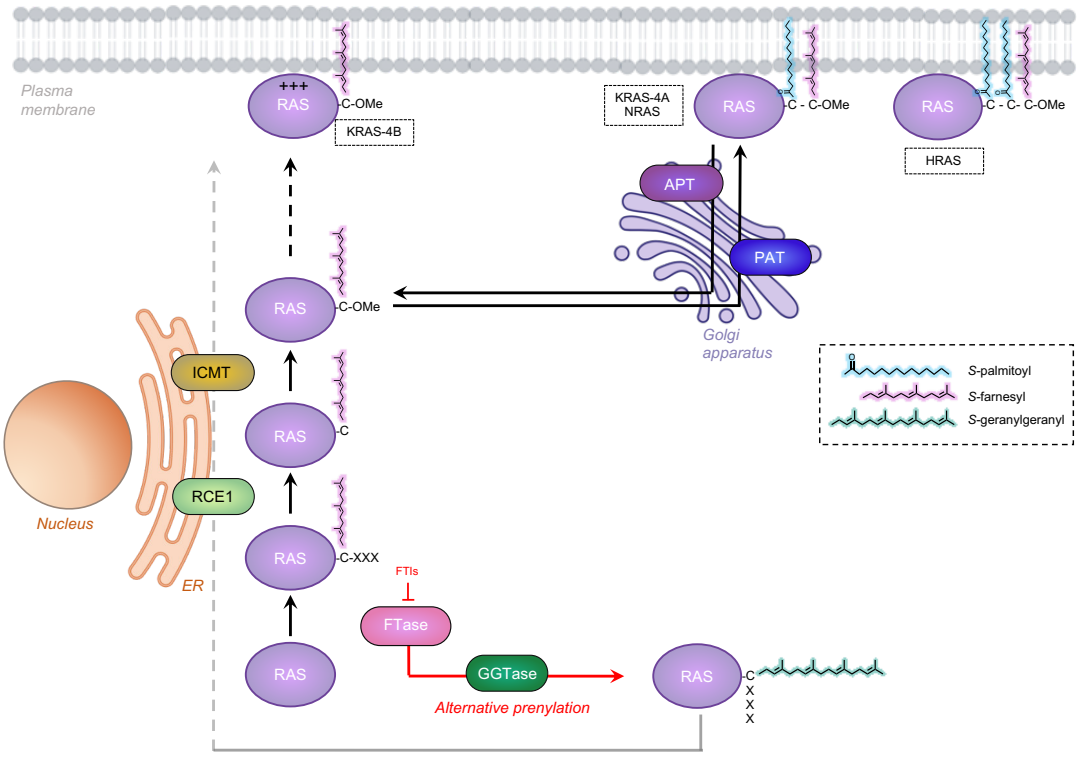

Figure 1.8. RAS isoform specific lipidation dynamics. A summary of lipidation dynamics that form the basis of RAS isoform signaling compartmentalization.

These differential targeting motifs and lipidation dynamics engender different functional outcomes for each isoform (Fig. **1.8**). For example, transcriptomic studies have demonstrated that NRAS and HRAS activate different signaling pathways in an *S*-palmitoylation-dependent manner[178]. NRAS-driven hematological cancers have also been shown to be *S*-palmitoylation dependent, with a recent study implicating RAB27B in the regulation of this process in acute myeloid leukemia (AML) models[179,180]. KRAS4A also interacts with hexokinase-1 (HK1) at the mitochondria endomembrane when de-palmitoylated, whereas KRAS4B does not[181]. Other studies have attributed broader cellular consequences to RAS isoform signaling from different cell compartments. HRAS signaling from the plasma membrane appeared to enhance apoptosis via TP53, a well-established tumor suppressor, whilst HRAS signaling at the Golgi reversed this effect and instead potentiated cell survival via TP53[182].

1.5.2. Therapeutic targeting of RAS in cancer

RAS proteins are major oncogenic drivers, and activating point mutations are present in over 30% of all cancers. These characteristic mutations occur within the RAS G-domain, and stabilizes an active GTP-bound state. This conformation is able to interact with various effectors at the plasma membrane that activate cell proliferation pathways, most notably through MAPK (RAF/MEK/ERK) and PI3K (PI3K/AKT/mTOR) pathways[127,183] (Fig. **1.9**).

Inhibiting RAS localization at the plasma membrane was once considered an attractive therapeutic strategy for RAS-driven cancers. However, as discussed earlier in this chapter, results from clinical trials were initially disappointing due to dose-limiting toxicities and a lack of efficacy for KRAS and NRAS-driven cancers. FTIs and GGTIs have been largely been abandoned in RAS therapeutic development, apart from select applications in HRAS-driven cancers[151,184,185]. It is thus somewhat surprising that there have been limited efforts to uncover the mechanisms and consequences of alternative prenylation, which may lead to the discovery of novel drug targets in RAS-driven cancers.

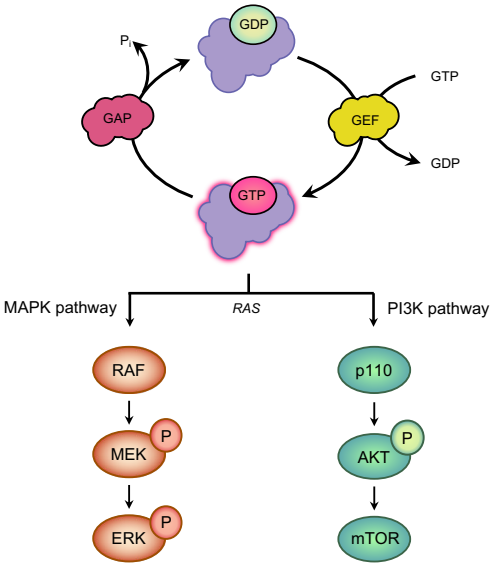

Figure 1.9. RAS molecular switch activity and downstream effector pathways. RAS molecular switch activity, which mediates cycling between active (GTP-bound) and inactive (GDP-

bound) states. Active RAS then binds effector proteins, such as RAF and p110, to activate the MAPK and PI3K signaling cascades, respectively.

Other lipidation targeted strategies include targeting *S*-palmitoylation of NRAS. A recent study reported the molecule ABD957, an ABHD17 inhibitor, the acyl-protein thioesterase responsible for de-palmitoylating NRAS[186,187]. Somewhat counterintuitively, inhibiting this enzyme stabilizes NRAS at the plasma membrane, leading to disrupted signaling patterns, ultimately resulting in an antiproliferative phenotype. Other APT inhibitors have been reported, but few have been investigated in a clinical context[188,189].

Other strategies have targeted downstream RAS pathways, including the MAPK and mTOR signaling axes. These have yielded a series of therapeutics for cancers harboring BRAF-mutations, with several MEK inhibitors (MAPK pathway) now available in the clinic[127]. Unfortunately, these have largely been ineffective for RAS-mutant cancers. Targeting other pathway components, including ERK and BRAF, has also resulted in clinically available inhibitors, however these have all failed as monotherapies in the context of RAS-mutant cancers[127,190]. This has been hypothesized to be related to loss of pathway feedback loops that regulate the activity of the pathway, resulting in the activation of adjacent proliferative pathways. For example, direct inhibition of the MAPK pathway can result in undesirable activation of the PI3K pathway in RAS-mutant backgrounds[191]. Current strategies utilize combinations of MEK, PI3K and other RAS signaling component inhibitors, as targeting one pathway is likely to incite resistance from another[127,192]. These inhibitors are also being explored as combinatorial therapeutics with tipifarnib in clinical trials[185].

Inhibiting RAS effector interactions is also an emerging therapeutic strategy. In particular, PDEδ (or PDE6D) inhibitors have been explored in this context. PDEδ inhibitors, which target the prenyl-binding pocket that binds *S*-prenylated KRAS, prevent KRAS from translocating to the plasma membrane, where the majority of its proliferative signaling takes place[193–195]. Deltarasin and deltazinone are two reported PDEδ inhibitors that have demonstrated limited success in KRAS-driven cancers, suggesting that residual signaling

from endomembranes may be attenuating the antiproliferative effect of the drugs, and may potentially require combination therapies to fully realize their utility[196,197].

The most successful attempts at inhibiting RAS have come from mutant allele targeted therapeutics. Just ten years ago, RAS was almost unilaterally considered to be undruggable by direct targeting[198,199]. In 2013 however, structural studies eventually uncovered a cryptic pocket in $KRAS^{G12C}$, which was advantageously located proximal to the nucleotide-binding pocket and switch regions[200]. Covalent ligands were thus developed to directly target the G12C mutation in an effort to specifically occupy this pocket, which eventually yielded sotorsarib and adagrasib in the 2020s – the only KRAS inhibitors currently available in the clinic [201–203]. These inhibitors lock $KRAS^{G12C}$ in an inactive state, resulting in potent antiproliferative effects. However, recent clinical studies have reported the emergence of resistance phenotypes in several patient populations[204,205]. Moreover, this strategy can only be directed to a single RAS-isoform mutation, making it highly specific, and consequently non-versatile in the realm of RAS-targeted therapeutics. Nevertheless, the discovery of these inhibitors has been transformative in the field of cancer therapeutics and has resulted in a resurgence in allele-targeted therapeutic discovery for RAS[126].

1.6. Chemical tools in the study of protein *S*-prenylation

The importance of *S*-prenylation in various pathologies, as well as the challenges associated with therapeutic intervention at this level, highlights the importance of deconvoluting the prenylated proteome. Historically, enzymatic assays and *in vitro* labelling approaches using titrated lipid analogs, or environmentally sensitive fluorescent substrate peptides, were often coupled with genetic manipulation of putative enzymes and substates[206–209]. Though these studies have formed the backbone of prenylation kinetic studies and have greatly contributed to our understanding of how prenyltransferases function, the techniques employed were restricted to the study of isolated systems, divorced from the complex cellular environment. Moreover, they cannot be readily applied to monitor lipidation dynamics across the whole proteome.

Upon the establishment of click chemistry and click-functionalized probes in chemical biology, lipid probes were developed to achieve the goal of profiling lipid PTMs within the cellular environment[210]. Early attempts at this began with the development azide-tagged farnesyl probes (AzC15, AzC15PP), which enabled metabolic labelling of *S*-farnesylated proteins the cell that could be then analyzed by gel or mass spectrometry[211], or through enzymatic assays[212–214]. FTase can utilize these probe derivatives similarly to the endogenous isoprenoid, however appreciable levels of incorporation were only achieved by the use of statins, which deplete the endogenous isoprenoid pool and encourage probe uptake[215,216]. Click functionalized probes can be bioorthogonally ligated to various capture/reporter reagents for downstream analysis, including those that incorporate combinations of affinity handles (biotin), fluorescent molecules (TAMRA) and cleavable motifs (proteolytic sites)[217]. Various derivatives of these probes were developed in following years and have been used to profile various *S*-prenylated proteomes, including cancer[7,52,85,218,219], Alzheimer's disease (AD)[220], and parasitic infection *(Plasmodium falciparum*[221,222]) and bacterial infection (*Legionella pneumophila*[223]) models (Table **1.1**). This range of probes include alkynyl derivatives (Alk-C10PP and Alk-C15PP), as well as a farnesol probe (Alk-C15OH) that more readily diffuses across the cell membrane compared to analogous pyrophosphate derivatives[7].

Another profiling technique captures proteins that have disrupted *S*-prenylation dynamics. The application of an PTI or statin, for example, results in some substrates lacking a modified CXXX-box. Lysates from disrupted conditions are harvested along with their corresponding controls, and subject to *in vitro* labelling using a biotinylated isoprenoid probe and a recombinant RABGGTase enzyme[37,224–226]. The allows the re-prenylation of substrates that would otherwise be prenylated in control conditions, and standard biotin enrichment protocols, such as the use of 'avidin-functionalized beads, enable a limited deconvolution of the prenylated proteome. This re-prenylation approach is particularly useful to the study of metabolically inactive samples, including tissues and patient-derived cells. Importantly however the native cellular environment is not interrogated here, as cellular localization and temporal-related controls are not recapitulated in lysates.

Moreover, as this technique only allows insight into disrupted or lost prenylation upon a perturbation of interest, native prenylation dynamics can only be inferred during analysis.

Isoprenoid probes have been extended to a range of orthogonal analytical techniques, including confocal imaging[227], 2D-gel analysis[228], and flow cytometry[228], particularly when coupled with fluorescent reporters. These technologies have extensively been covered by other reviews. Importantly however, none of these probes or techniques differentiate between *S*-farnesylation and *S*-geranylgeranylation and can be incorporated by all known prenyltransferases. Moreover, the required statin treatment for probe uptake can result in alterations of endogenous lipid pools that in turn give rise to pleotropic effects, diverging further from a physiologically relevant system[45]

Table 1.1. Isoprenoid probes reported in literature

Structure	Variations	Selected applications
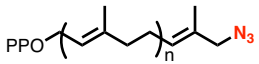	AzC10OPP (n=1) AzC15OPP (n=2) AzC20OPP (n=3)	• Re-prenylation assay[217] (HEK293T) • Kinetic enzyme assay (*S. cerevisiae*[208], *E. coli*[209] FTase)
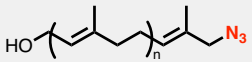	AzC15 (n=1) AzC20 (n=2)	• Metabolic labelling of immortalized cell lines[221] • Yeast screening assay[210] (*S. cerevisiae)*
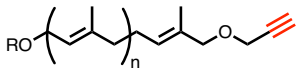	Alk-C15 (n=2, R=H) Alk-C15 (n=2, R=PP)	• Metabolic labelling of brain of transgenic mouse model[215]; *P. falciparum*[216,217]*; L. pneumophila* [218]*;* primary cells[215] • Metabolic labelling of immortalized cell lines[85,221] • Yeast screening assay[210] (*S. cerevisiae* FTase*)*
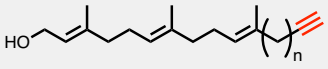	Alk-C15-2 (n=1) Alk-C15-3 (n=2)	• Metabolic labelling of immortalized cell lines[221]
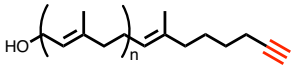	YnF (n=1) YnGG (n=2)	• Metabolic labelling of immortalized cell lines[52] • Metabolic labelling of choroideremia cell model[52] (mouse embryonic fibroblasts [MEFs])
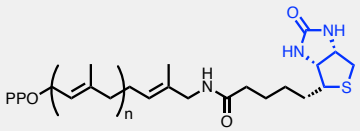	B-FPP (n=1) B-GPP (n=2)	• Re-prenylation assay[211] (various immortalized cell lines, choroideremia patient samples[222])

To address these shortcomings, a new generation of alkyne *S*-prenylation probes were developed by the Tate group[52]. These dual probes, YnF and YnGG, mimic endogenous farnesol (FOH) and geranylgeraniol (GGOH) and crucially retain the native chain length and hydrophobicity of each respective isoprenoid (Fig. **1.10**) The use of an alcohol derivative also contributed to making statins superfluous for efficient metabolic incorporation, which constituted a major development in the field. Proteomic analysis of YnF and YnGG incorporation revealed that each probe is selectively processed by the cognate transferase, enabling distinct profiling of *S*-farnesylated and *S*-geranylgeranylated substrates for the first time. Profiling experiments captured a total of 80 prenylated proteins, 64 of which were quantified for the first time at the endogenous level. A disadvantage of these probes lies in the use of the alcohol derivative, which offers better cellular uptake, but requires intracellular conversion to the pyrophosphate precursor through a very poorly characterized mechanism, called the salvage pathway[229]. This pathway is a rescue mechanism that cells employ to utilize farnesol and geranylgeraniol, and is not equally utilized in all cell types, making incorporation dynamics difficult to ascertain or predict when investigating other cellular systems.

YnF and YnGG incorporation studies also revealed substrates that have mixed prenylation, such as RRAS2, CDC42 and YKT6, meaning each of these proteins can undergo both *S*-farnesylation and *S*-geranylgeranylation. This analysis also revealed that *S*-geranylgeranylation of YKT6 was uniquely sensitive to FTI treatment, which was later explained by a study that demonstrated *S*-geranylgeranylation of YKT6 was mediated by the newly discovered prenyltransferase GGTase-III[39]. *S*-geranylgeranylation of YKT6 could not proceed without initial *S*-farnesylation of an adjacent CXXX cysteine, giving rise to a novel dual prenylation modification.

These probes can also capture alternative prenylation dynamics, which is quantified by by YnF:YnGG incorporation ratios across FTI-treated samples. It was found that, interestingly, only KRAS, NRAS, and RRAS2 were shown to undergo alternative prenylation upon tipifarnib treatment. This may imply that there are additional factors that

confer the propensity to be alternatively *S*-prenylated, however these dynamics have yet to be investigated in greater detail.

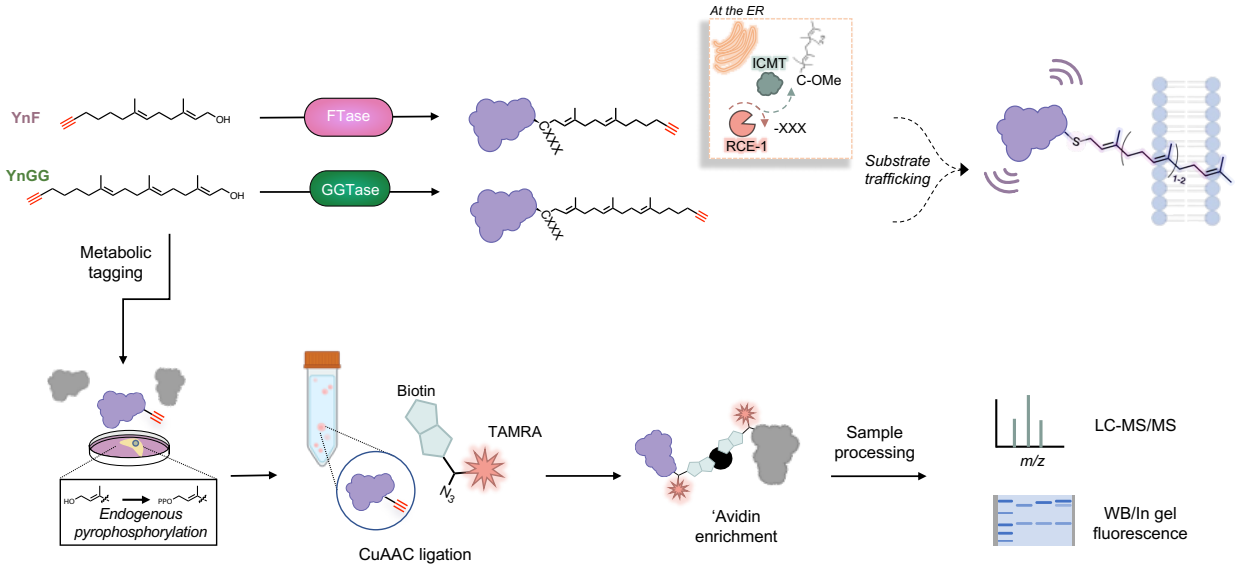

Figure 1.10. Metabolic incorporation of dual isoprenoid probes (YnF and YnGG). General workflow for YnF and YnGG probe incorporation experiments. Probes are processed by their cognate prenyltransferases and mimic the endogenous modification, undergoing normal post-prenylation processing and membrane partitioning. Cells treated with the dual probes are harvested, and resultant proteins are click ligated to capture reagents (shown here AzTB) and optionally 'avidin enriched on beads. Samples are then analyzed by mass spectrometry or SDS-PAGE/Western blot.

1.7. Project Aims

1.7.1. Current status

RAS isoforms remain attractive drug targets despite decades of drug discovery yielding a comparatively small handful of effective therapies. The markedly high prevalence of RAS-driven cancers, coupled with the fact that current therapeutic modalities can only target a limited selection of isoform-specific mutations, have significantly contributed to the on-going interest in RAS therapies.

All RAS isoforms harbor the propensity to acquire constitutively activating point mutations. Moreover, while RAS proteins share remarkably high sequence homology, they can differ greatly in their compartmentalized signaling dynamics. These divergences are attributed to the presence of different membrane targeting motifs in each RAS isoform C-terminus. These differences also present themselves as divergent responses to FT inhibition, where KRAS and NRAS are alternative prenylated, while HRAS remains susceptible. It can be hypothesized that this phenomenon may hold unique promise in the identification of isoform-specific vulnerabilities potentiated by FTI treatment. For example, the identification of novel *S*-geranylgeranylated KRAS-specific interactors, or deconvoluting the criteria that engenders the ability to undergo alternative prenylation, may in turn reveal new therapeutic modalities for RAS-driven cancers.

1.7.2. Thesis aims

Deciphering prenylation dynamics and alternative prenylation events in living systems has been made possible by the aforementioned dual chemical probe system, which allows distinct interrogation of *S*-farnesylation and *S*-geranylgeranylation profiles within the cellular milieu. Uncovering the mechanisms that underlie alternative prenylation may result in the revelation of novel drug targets in RAS-driven cancers, which remains an active area of therapeutic development. At the same time, understanding the consequences of alternative prenylation, or FTI treatment in isolation, may also reveal

novel druggable vulnerabilities that can be potentiated by generally well-tolerated drugs, such as tipifarnib.

However, systems-wide approaches are required to understand the processes that enable substrates to undergo alternative prenylation, as well as to identify vulnerabilities brought about by FTI treatment. Therefore, this thesis aims to establish new techniques that enable the deconvolution of complex lipidation dynamics in living systems.

A three-pronged approach was thus employed:

a) **Chapter 2**: I investigate a poorly characterized chaperone protein (SmgGDS) to define its role in regulating *S*-prenylation dynamics in the presence and absence of tipifarnib, a well-characterized and potent FTI. Various optimizations of the dual chemical isoprenoid probe system are explored to enable this interrogation, as well as the use of a proteomics-based cell fractionation technique.

b) **Chapter 3**: I conceptualize and implement a novel CRISPR-enhanced drug-resistance mutagenesis approach to investigate potential sequence-specific criteria for alternative prenylation.

c) **Chapter 4**: I apply proximity labelling (PL) approaches to profile the interactomes of RAS isoforms and their responses to tipifarnib treatment, in an attempt to deconvolute potential modulators of alternative prenylation, and/or identify novel drug targets that can be potentiated by tipifarnib treatment.

Chapter 2
Optimization of global prenylation profiling in the study of RAP1GDS1-regulated prenylation dynamics

2.1. Introduction

RAS superfamily GTPases are known to associate with chaperone proteins that facilitate their trafficking throughout the cell[230]. The specificity and binding capacity of these chaperones is thought to both depend on and influence the prenylation state of small GTPases, which may harbor implications for divergent prenylation dynamics across RAS proteins. This may be particularly critical in the context of prenyltransferases inhibitor (PTI) treatment, where resistance mechanisms such as alternative prenylation are observed[54].

To accommodate a substrate's newly hydrophobic character, chaperones bind proximal to its prenylated motif, shielding the lipid to maintain protein solubility as it diffuses across the aqueous cytosol. Given that prenylation occurs shortly after protein translation, these newly prenylated substrates must be efficiently released from the modifying prenyltransferase and transferred to the ER, where downstream CXXX-processing enzymes RCE1 and ICMT reside[231]. This initial product release is thought to be the rate-limiting step in the prenylation cascade, meaning that the dissociation and subsequent withdrawal of prenylated substrates from the site of lipidation are important in the accumulation of prenylated products[36,232]. These roles are often fulfilled by chaperone proteins, highlighting their significance in sustaining RAS functionality, and therefore their potential for drug targeting[230].

Prenylated proteins ultimately translocate to their target membranes for anchorage, which in the case of RAS proteins is often the Golgi apparatus and/or plasma membrane, sometimes sequentially to accommodate multiple processing steps[233]. Chaperones are thought to aid in each of these steps for small GTPases, as well as for other *S*-prenylated substrates. RAB proteins, for example, rely on REP1 and REP2 to associate and dissociate from RABGGTase, as well as to eventually reach their destination membranes[234]. While the role of REP1 and 2 have been well-characterized in this context, chaperones for other prenylated substrates appear to be more diverse, and their effect on prenylation dynamics is not as well understood.

An example is PDE6D (or PDE6δ), an established prenyl-binding chaperone that allows RAS proteins, in a palmitoylation or charge dependent manner, to translocate between different membranes in the cell[235]. This enables RAS proteins to bypass the need for vesicular transport to some degree. PDE6δ also re-solubilizes RAS from recycling endosomes that work to maintain a functional distribution of RAS proteins at the plasma membrane[236]. Re-solubilization actively counteracts this equilibrium-establishing process, promoting RAS entrapment at the plasma membrane and increased RAS signaling as a result. This is often observed in oncogenic contexts where RAS is mutationally hyperactivated, leading to high PDE6δ expression[237]. Indeed, PDE6D has been the subject of drug discovery efforts against RAS hyperactivation and has led to the development of a suite of protein interaction inhibitors (PPIs) with picomolar affinity[238,239]. However, limited on-target toxicity has been observed in mutant RAS models despite some efficacy in causing RAS delocalization, which is hypothesized to arise from inhibitor "ejection" from the KRAS-binding pocket of PDE6D[239,240]. Additionally, off-target cytotoxicity is an active challenge in the field, perhaps owing to structural homology with GPCRs and RHOGDIs, which have broader functions in RAS activation[241]. Newer generations of these compounds aim to circumvent these issues and aim to leverage the use of combinatorial therapies to target RAS activation on multiple fronts[193]. Nevertheless, targeting RAS chaperones remains an attractive strategy for modulating RAS membrane localization. Moreover, chaperone proteins may also hold other important roles for the regulation of RAS lipidation that are difficult to explain by amino acid sequence alone, including the propensity for alternative and/or dual prenylation events. Therefore, understudied chaperones may underlie novel vulnerabilities in RAS lipidation and downstream signaling, meriting further investigation in the context of therapeutic intervention.

SmgGDS (gene name: RAP1GDS1) is one such chaperone protein. It is mainly implicated in the promotion of RAS and RHO GTPase prenylation by way of shuttling substrates to their cognate prenyltransferase, or conversely by destabilizing the formation of prenyltransferase:GTPase complexes[81,242,243]. Both processes impact prenylation

turnover in the cell. SmgGDS is structurally unique compared to other known RAS chaperones, which are typically homologous to RHOGDIs – an important consideration in drug development[84]. Recent work outlining genetic interaction studies and dual-CRISPR knockout screens has also revealed SmgGDS-related KRAS-dependent susceptibilities; dual knockout (KO) of SmgGDS and RHOA, another RAS family GTPase, was shown to be synthetically lethal only in KRAS-dependent cancers, while KRAS-independent cancers were largely unsusceptible[244]. The mechanism and protein interaction network that engenders this phenomenon is still under investigation, however it is possible that SmgGDS modulates KRAS activity by promoting prenylation of RHO proteins that are essential for intact KRAS signaling and consequent oncogenic transformation. This relationship may also be explained by a direct effect of SmgGDS on KRAS prenylation states, meaning that an SmgGDS-depleted system may inhibit KRAS activity by modulating its prenylation state. However, the relationship between SmgGDS and RAS prenylation dynamics remains unclear.

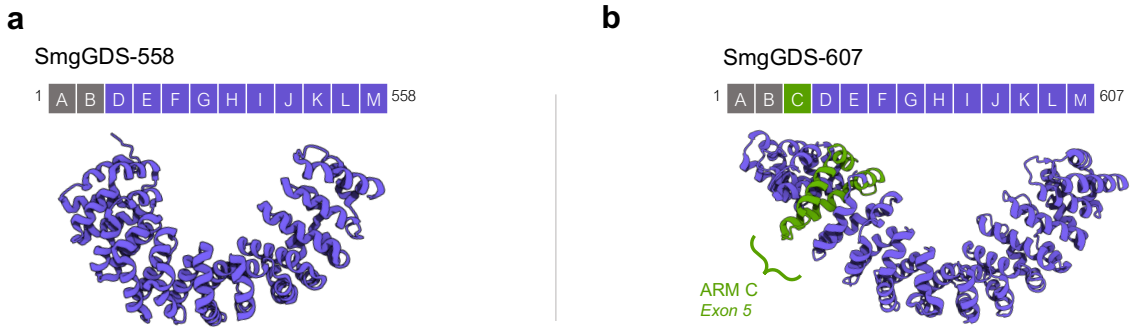

Figure 2.1.1. Structures of SmgGDS (RAP1GDS1) splice variants. Due to exon 5 skipping during translation, **(a)** SmgGDS-558 lacks ARM domain C, creating a hydrophobic pocket between domains A and B. **(b)** SmgGDS-607 possesses all 13 ARM domains (A–M); the presence of ARM C precludes binding of prenylated substrates due to the occlusion of the hydrophobic pocket found in 558. PDB **5XGC**.

Importantly, RAP1GDS1 is produced as two splice variants, SmgGDS-558 and SmgGDS-607, with the former resulting in the lack of an armadillo repeat motif (ARM C) in the protein via skipping exon 5 during transcription[245] (**Fig. 2.1.1**). This absence of this ARM gives rise to a hydrophobic pocket that can accommodate the prenyl group on modified substrates. In contrast, SmgGDS-607 exclusively binds pre-prenylated substrates (**Fig.**

2.1.2). As a result, these splice variants appear to differentially regulate prenylation events in a context and protein-specific matter. SmgGDS-607 has been shown to promote prenylation in various studies, perhaps by modulating substrate delivery to prenyltransferases, and was demonstrated to be more oncogenic than the short-form variant SmgGDS-558, particularly in breast[246] and lung[243] cancer. However, SmgGDS-607 also appears to have a broader role in regulating entry into the prenylation pathway, as in some contexts it can prevent prenylation of RHOA and DIRAS1[80,81,246]. SmgGDS-558, in contrast, binds prenylated substrates after lipid modification and shuttles them across the cell[242]. It may have roles in both the delivery of prenylated proteins to the ER for processing, and their subsequent anchorage to the plasma membrane or Golgi apparatus, as it was shown to interact with both pre- and post-processed (i.e. proteolyzed and methylated) *S*-prenylated substrates[82]. Notably, studies investigating these proposed dynamics have varied greatly, with trends and mechanisms difficult to establish owing to general difficulties in the study of global protein *S*-prenylation, and protein lipidation as a whole.

SmgGDS-607 oncogenicity suggests that it could be a novel drug target in the realm of prenylation, where elevated 607:558 ratios serve as potential therapeutic biomarkers.

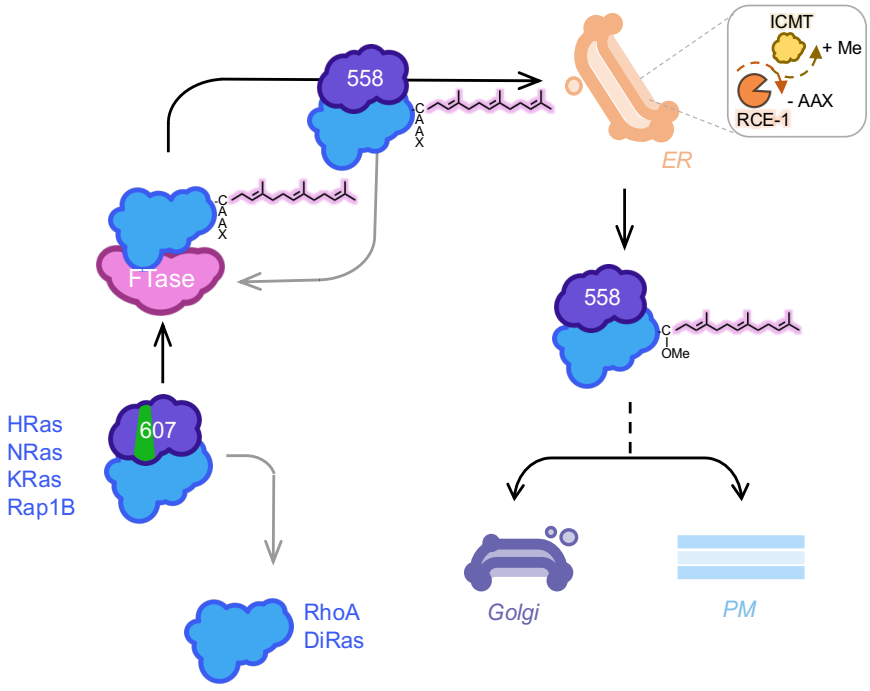

Figure 2.1.2. Schematic depiction of SmgGDS variant-specific effects on small GTPase protein prenylation. (a) SmgGDS-607 has been shown to selectively shuttle RAS GTPases to farnesyltransferase (FTase), whilst preventing farnesylation for other GTPases, including RhoA and DiRas. SmgGDS-558 harbors a prenyl-binding pocket and shuttles the newly prenylated protein to the ER, where RCE1 (Ras Converting CAAX Endopeptidase 1) and ICMT (Protein-*S*-isoprenylcysteine O-methyltransferase) further process the prenyl modification. SmgGDS-558 may also play a role in shuttling the prenylated substrate to other endomembranes, such as the Golgi apparatus or the plasma membrane.

Targeting a single splice variant may offer significant benefits over pharmacological inhibition of PTases as a way of modulating small GTPase lipidation, as it may be less susceptible to dose-limiting toxicities seen so often with PTI treatment[150,247,248]. A splice variant switching strategy using an engineered oligonucleotide was thus developed to target Exon 5 of SmgGDS-607 (SSO Ex5), which specifically inhibits expression of the long-form oncogenic variant[85]. Initial proteomic studies have shown diminished oncogenicity by supressing global prenylation, although it remains to be seen how inhibition or knockdown of SmgGDS-607 affects *S*-farnesylation or *S*-geranylgeranylation specifically.

FTI treatment can further complicate SmgGDS binding dynamics; FTI-277, a peptidomimetic inhibitor of FTase, appeared to enhance KRAS binding to SmgGDS-607, perhaps pointing towards a possible mechanism by which some RAS substrates are shunted towards GGTase-1 during prenyl switching[79] (**Fig. 2.1.3**). In contrast, HRAS was shown to favor SmgGDS-558 binding, which enhanced FTase-binding turnover and consequently an increased rate of farnesylation, however the relationship between HRAS prenylation dynamics and SmgGDS binding in the presence of FTIs has not yet been well-characterized.

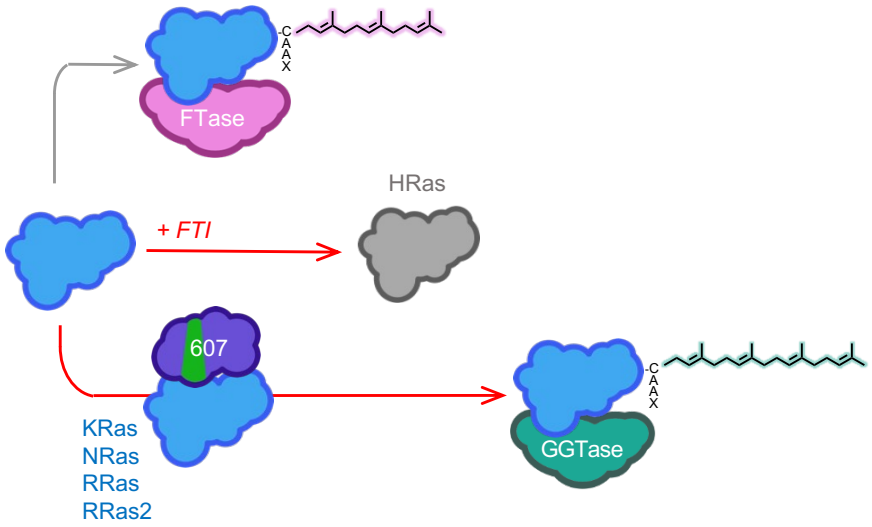

Figure 2.1.3. Putative roles of SmgGDS in alternative prenylation. SmgGDS-558 may increase prenyl turnover of HRas by FTase, enhancing rate of farnesylation of HRas. HRas remains unprenylated in the presence of an FTI. In contrast, SmgGDS-607 may play a role in facilitating alternative prenylation of KRAS and other prenyl-switching substrates, such as NRAS, in the presence of an FTI.

Several unknowns prevent a more complete understanding of SmgGDS splice variants in prenylation dynamics, and consequently their potential as prenylation-related drug targets. Key limitations of previous studies on SmgGDS include the lack of differentiation between *S*-farnesylation and *S*-geranylgeranylation after knockdown or pharmacological inhibition of SmgGDS-607 (e.g. via SSO Ex5) in a physiologically relevant context, thereby obscuring any specific effect on substrates or prenyltransferases. This is also crucial in deconvoluting any role SmgGDS may have on alternative prenylation, which remains a key obstacle in treating KRAS-driven cancers by pharmacological delocalization (i.e., FTIs). Furthermore, differentiating prenylation dynamics upon potentially subtle perturbations, such as knockdown or knockout of a splice variant, may prove challenging, and may require significant optimizations in global prenylation profiling and chemical proteomic techniques.

This chapter outlines a chemical proteomic investigation into SmgGDS splice variants, specifically the oncogenic SmgGDS-607 variant, and their roles in modulating prenylation dynamics. The chapter also seeks to investigate the potential role of SmgGDS in

alternative prenylation, and whether the variant-specific interactions outlined in previous studies also translate to divergent responses to FTI treatment in the case of prenyl-switching and non-switching substrates.

2.2. Results and discussion

2.2.1. SmgGDS (RAP1GDS1) and prenylated interactors

SmgGDS has been primarily studied in the context of small GTPases, owing to its initial discovery as an interactor of RAP1A and RAP1B. Unsurprisingly, gene ontology analysis of high-confidence physical interactors (extracted from BIOGRID) shows significant enrichment for small GTPase biological function, with the top ten enriched pathways relating to small GTPases and their signaling pathways[249] (**Fig. 2.2.1a**). Moreover, around 25% of known interactors are CXXX-containing proteins, the majority of which (79.5%) are *S*-geranylgeranylated (**Fig. 2.2.1b**).

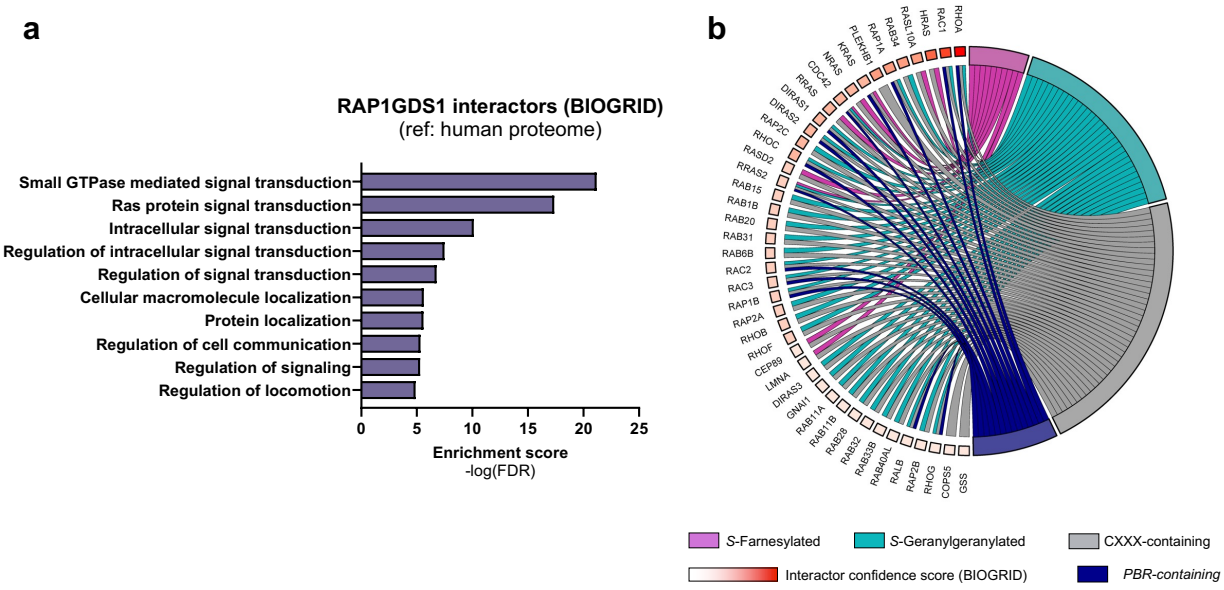

Figure 2.2.1. Meta-analysis of SmgGDS (RAP1GDS1) interactors. (a) STRING analysis of SmgGDS (RAP1GDS) interactors extracted from BIOGRID public database. **(b)** Chord diagram of RAP1GDS1 interactors and their prenylation states (Magenta: *S*-farnesylation; cyan: *S*-geranylgeranylation; gray: CXXX-containing; navy: Polybasic region (PBR)-containing proteins). Protein entries are annotated to contain the confidence score of each interactor (extracted from BIOGRID).

This is in congruence with previous studies highlighting various interactions with RHO/RAP proteins, which are largely *S*-geranylgeranylated[250]. When excluding

prenylated substrates from gene ontology analysis of SmgGDS interactors, most other interactors are present in the ER or cytosol and have roles in regulating ER trafficking and cytoskeletal movement, pointing to its primary role as a protein chaperone, perhaps most consistently to and from the ER where post-prenylation processing occurs (Appendix Table **7.9**). However, data available for meta-analysis is currently limited due to the lack of differentiation between splice variants, with few insights into *S*-farnesylation and *S*-geranylgeranylation specific modalities.

Table 2.1. PBR-containing RAP1GDS1 interactors.

Protein	ID[1]	PBR	CXXX-box
RHOA	P61586	E M A T **R** A A L Q A **R R** G **K K K** S G	CLVL
RHOB	P62745	T **R** A A L Q **K R** Y G S Q N G **C** I N **C**	CKVL
RHOC	P08134	E M A T **R** A G L Q V **R K** N **K R R R** G	CPIL
RHOD	O00212	V A L S S **R** G **R** N F W **R R** I T Q G F	CVVT
RHOG	P84095	A E A V **R** A V L N P T P I **K R** G **R** S	CILL
RHOH	Q15669	A V N Q A **R R R** N **R R R** L F S I N E	CKIF
RAC1	P63000	E A I **R** A V L **C** P P P V **K K R K R K**	CLLL
RAC2	P15153	E A I **R** A V L **C** P Q P T **R** Q Q **K R** A	CSLL
RAC3	Q9Y6Q9	E A I **R** A V L **C** P Q P T **R** Q Q **K R** A	CSLL
CDC42	P60953-1	D E A I L A A L E P P E T Q P **K R K**	CCIF
CDC42_2	P60953-2	D E A I L A A L E P P E P **K K** S **R R**	CVLL
RND1	Q92730	P S **R** S E L I S S T F **K K** E **K** A **K** S	CSIM
RND2	P52198	Q L S G **R** P D **R** G N E G E I **H K** D **R**	CNLM
RND3	P61587	L **K K** I S **K** E E **K** T P G **C** V **K** I **K K**	CTVM
KRAS-4A	P01116-1	**K** E **K** M S **K** D G **K K K K K K** S **K** T **K**	CIIM
KRAS-4B	P01116-2	**R** Q I N **R K** T P V P G **K** A **R K K** S S	CVIM
RRAS2	P62070	**C** P P S P E P T **R K** E **K** D **K K** G **C H**	CVIF
RAP1A	P62834	V **R** Q I **R K** T P V E **K K K** P **K K K** S	CLLL
RAP1B	P61224	**R** Q I N **R K** T P V P G **K** A **R K K** S S	CQLL
RHEB	Q15382	I I L E A E **K** M D G A A S Q G **K** S S	CSVM
DIRAS1	O95057	I D G **K R** S G **K** Q **K R** T D **R** V **K** G **K**	CTLM
DIRAS2	Q96HU8	I D G **K K** S **K** Q Q **K R K** E **K** L **K** G **K**	CVIM
DIRAS3	O95661	E P E **K K** S Q M P N T T E **K** L L D **K**	CIIM

Basic residues | ***Cysteine***

[1]Uniprot accession ID

Many of the *S*-prenylated proteins that interact with SmgGDS also harbor a polybasic region (PBR)[251] (see **Table 2.1**). This patch of positively charged residues enables electrostatic interactions with a corresponding electronegative patch near the GTPase-binding site of SmgGDS. Notably, the PBR of a selection of these proteins also contains Cys residues that may also be *S*-palmitoylated in the cell. *S*-palmitoylation of these proteins may thus prevent SmgGDS-binding in a dynamic manner, as it is the only known reversible class of protein lipidation[78,82,251]. This potentially offers an additional level of regulation in the shuttling of *S*-prenylated substrates between endomembranes and the plasma membrane, and may be a reason for differential binding dynamics to SmgGDS observed in the literature. It is also worth noting that many of these previous studies were performed *in vitro* and would not have included the *S*-palmitoyl group on any of these Cys residues[82]. Thus, understanding isoform-specific SmgGDS effects on protein *S*-prenylation in an endogenous, global manner is necessary to establish its role and potential for druggability in RAS-driven cancers.

2.2.2. Isolating SmgGDS splice variant-specific effects and cell model selection

Although the current body of literature related to this phenomenon is not cohesive, there is some agreement that the long-form splice variant SmgGDS-607 is more oncogenic, with higher 607:558 ratios found in some types of cancer[85]. This is putatively due to SmgGDS-607 promoting prenylation turnover, with some studies suggesting that higher expression is correlated with an increased demand for *S*-prenylation of oncogenic substrates, such as RAS and RHO GTPases[85]. In the context of FTI treatment, increased 607:558 ratios could be hypothesized to mediate pharmacologically induced shunting of KRAS to GGTase-I, where it can be alternatively prenylated and subvert inhibition of malignant transformation. However, studies that have attempted to elucidate these trends were unable to selectively probe *S*-farnesylation and *S*-geranylgeranylation events in cells due to the use of a non-specific isoprenoid probe. Thus, studying this system using the dual chemical probes YnF and YnGG would allow deconvolution of prenyl-switch dynamics in response to selective SmgGDS splice variant depletion.

a **b**

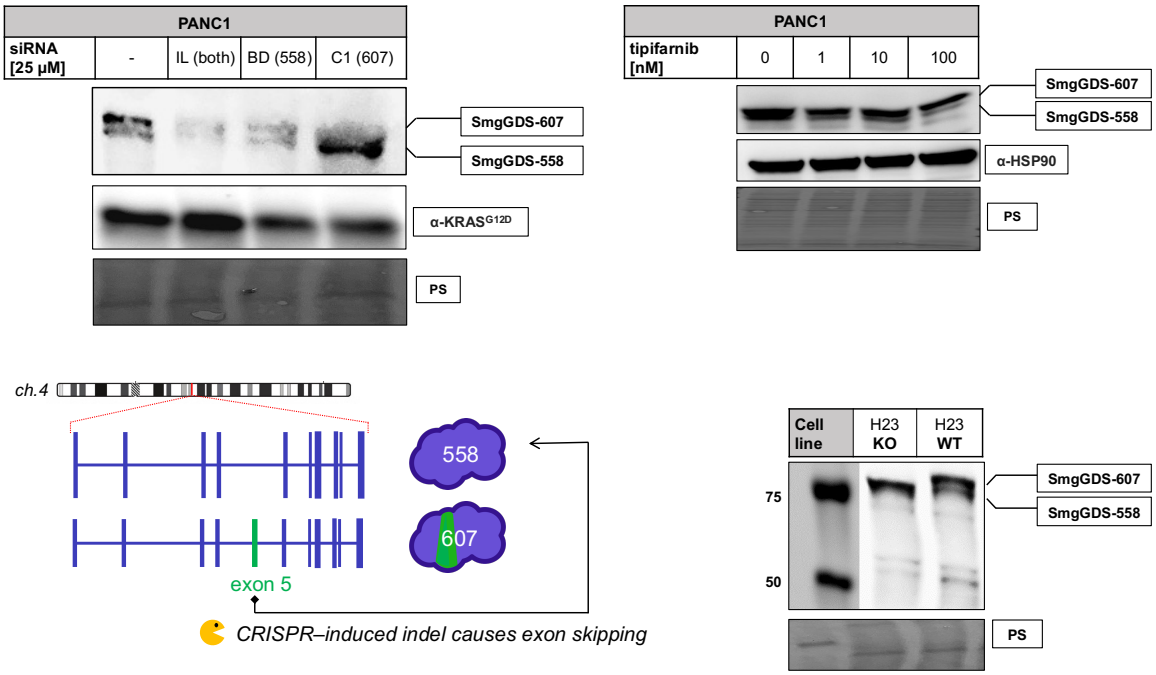

Figure 2.2.2. Establishing an SmgGDS splice variant-specific cell system. (a) siRNA-mediated knockdown (KD) of SmgGDS revealed generally nonspecific depletion SmgGDS-588 (BD) depletion, however was successful in KD of SmgGDS-607 (C1) and both splice variants simultaneously (IL). $KRAS^{G12D}$ expression was not affect by any KD. **(b)** SmgGDS splice variant ratio shifts to the oncogenic variant (607) in response to tipifarnib and is dose-dependent**. (c)** Schematic presenting CRISPR strategy employed for KO of SmgGDS-607. **(d)** Western blot demonstrating successful and selective KO of SmgGDS-607.

In order to investigate variant-specific effects on protein prenylation, a suitable cell model must be established. The ideal cell model should consist of a stable KD or KO of one or both variants, in a cell line that sufficiently incorporates YnF and YnGG probes. Initially, a small interfering RNA (siRNA) based approach was explored for this purpose. Previous studies have identified siRNAs that selectively knockdown (KD) SmgGDS-607 (C1), or both isoforms (IL)[83]. These published siRNAs, as well as a less robust siRNA designed to KD SmgGDS-588 (BD), were tested in cells to achieve selective depletion of either or both isoforms (see SI Table for sequences). PANC-1 cells were selected for this purpose, as previous attempts at YnF and YnGG labelling were successful (Appendix **Fig. 7.1 and 7.2**). Moreover, PANC-1 cells harbor $KRAS^{G12D}$, the only reliable form of endogenous KRAS detectable by Western blot, providing a potentially useful metric for understanding KRAS-specific prenylation, including alternative prenylation, in the context of SmgGDS variant ratio manipulation[252]. Successful knockdown of SmgGDS-607 (C1) and both

isoforms (IL) was achieved, while depletion of the short-form variant SmgGDS-588 (BD) was unclear (**Fig. 2.2.2a**). This, however, was consistent with literature reports. Additionally, some degree of upregulation of the short-form isoform (SmgGDS-558) was observed upon KD of SmgGDS-607 (siRNA C1). While this effect was not investigated further, it remains possible that expression of the alternative isoform occurs as a compensatory response to KD of a single splice variant, perhaps in a context dependent manner. $KRAS^{G12D}$ expression did not seem to significantly change upon either KD.

Next, potential changes to SmgGDS splice variant ratios were investigated in the context of farnesyltransferase inhibition. Previous studies have suggested that FTIs, including tipifarnib, may alter the dynamics of SmgGDS prenylation modulation, which may result from a shift in the endogenous 607:558 expression ratio[81]. Changes in the 607:558 expression ratio were thus investigated in PANC-1 cells upon tipifarnib treatment by Western blot. Preliminary results demonstrated slightly heightened 607:558 ratio was observed with increasing concentrations of tipifarnib, which may putatively correspond an increased demand for FTI-induced $KRAS^{G12D}$ shunting to GGTase-I (**Fig. 2.2.2b**). This may also support the hypothesis that SmgGDS, particularly the long-form oncogenic variant, plays a role in FTI-related compensatory mechanisms. Attempts at investigating SmgGDS splice variant-specific effects on $KRAS^{G12D}$ prenylation state in the presence and absence of tipifarnib were carried out, however due to the unreliable and short-lived effects of the siRNA approach, results were largely inconclusive, and follow-up was interrupted by the COVID-19 pandemic (data not shown).

At this point, a collaboration with UCSF (Prof. Alejandro Sweet-Cordero) and Stanford University (Prof. Peter Jackson) was established to investigate the role of SmgGDS in prenylation. H23 cells with an SmgGDS-607 CRISPR knockout (KO) and the corresponding wild-type parental cell line were obtained from the Sweet-Cordero lab at UCSF to selectively profile the prenylated substrates modulated by the oncogenic isoform, with some interest in understanding SmgGDS (RAP1GDS1) and RHOA dual KO synthetic lethality that is observed exclusively in KRAS-dependent cancers, described in their previous study[244]. H23 cells (a model for lung adenocarcinoma, or LUAD) were

selected for isoform-specific KO as SmgGDS/RHOA synthetic lethality was reliably demonstrated in this context. Moreover, the cell line also provides a suitable background for investigating SmgGDS-607 oncogenicity as LUAD has been found to have increased 607:558 ratios (also observed in **Fig. 2.2.2c and d**), and the cell line is KRAS-driven, harboring the hyperactivated G12C mutation. Thus, SmgGDS-607 was chosen as the KO, due to our specific interest in its oncogenicity[243]. Moreover, producing an SmgGDS-558 KO was hypothesized to be more challenging, possibly requiring a full SmgGDS KO and subsequent transient transfection of the full gene.

The KO cell line was produced by Dr. Kaja Kostyrko (UCSF) using a CRISPR-Cas9 system, where lentiviral transduction and subsequent antibiotic (hygromycin) selection allowed stable expression of the Cas9 enzyme. This was followed by transfection of a single guide RNA (sgRNA) targeting exon 5. CRISPR-induced indels in this region cause skipping of exon 5, allowing for exclusive expression of the SmgGDS-558 (**Fig. 2.2.2c**). Clones were screened by Western blot and pooled, whilst the parent line was produced by pooling H23-Cas9 cells transfected with a non-targeting sgRNA.

H23-SmgGDS-607 KO (hereby referred to as H23 KO) and H23 parent (referred to as H23 WT) cells were then initially subjected to probe labelling efficiency experiments, where YnF and YnGG probes were titrated in cells to determine optimal incorporation conditions. Cells were lysed after a standard 12-16h labelling protocol, and subject to Cu^{II}-catalyzed click with Azide-TAMRA (AzT) for analysis by in-gel fluorescence. Both cell lines exhibited modest and comparable probe incorporation with optimal labelling occurring at around 10 μM for each probe (**Fig. 2.2.3**). A signal drop-off was observed at higher concentrations, consistent with previous in-gel fluorescence observations of YnF/GG labelling in other cell lines.

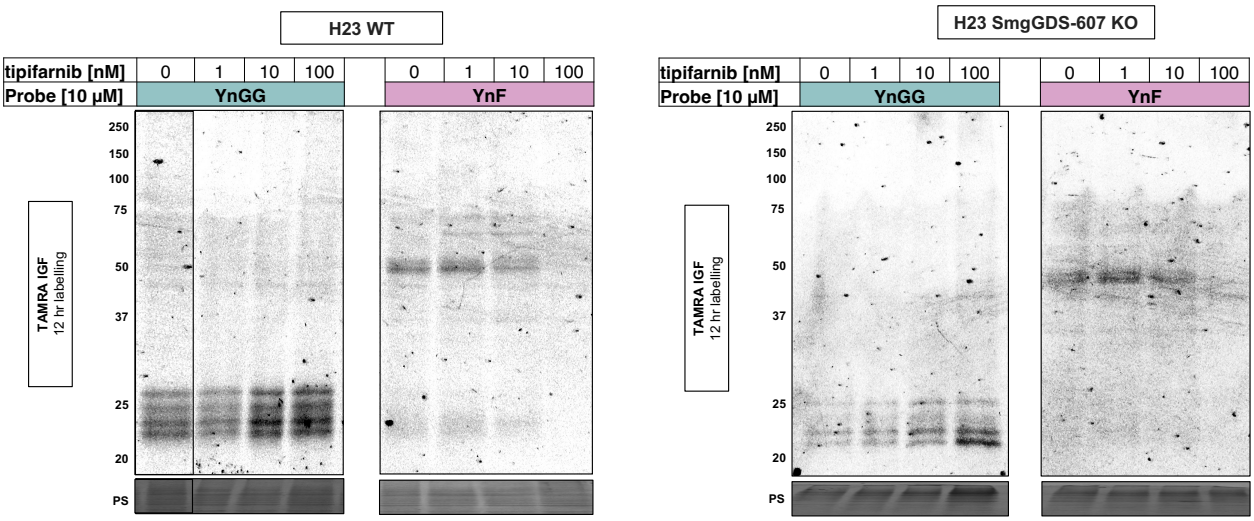

Figure 2.2.3. YnF and YnGG incorporation profiles for H23 WT and SmgGD-607 KO cell lines. H23-Cas9 parental line YnF and YnGG incorporation profile, showing successful labelling after overnight probe incubation, with labelling signalling peaking at around 10 µM. H23 SmgGDS-607 KO line displayed a similar profile.

Cells were then investigated for response to tipifarnib in an attempt to discern differences in incorporation profiles of YnF and YnGG upon KO of SmgGDS-607. A similar probe labelling experiment was performed at the determined optimal concentration for both probes (10 µM) with increasing concentrations of tipifarnib. However, no obvious discrepancies were observed (**Fig 2.2.4a)**. Cells were also profiled for proliferation in response to tipifarnib using live-cell imaging analysis (Incucyte, Sartorious), with KO cells demonstrating a greater sensitivity to tipifarnib. However as the cell lines were observed to have different growth patterns, potentially due to clonal effects, this was not the most reliable metric for sensitivity (**Fig. 2.2.4b**).

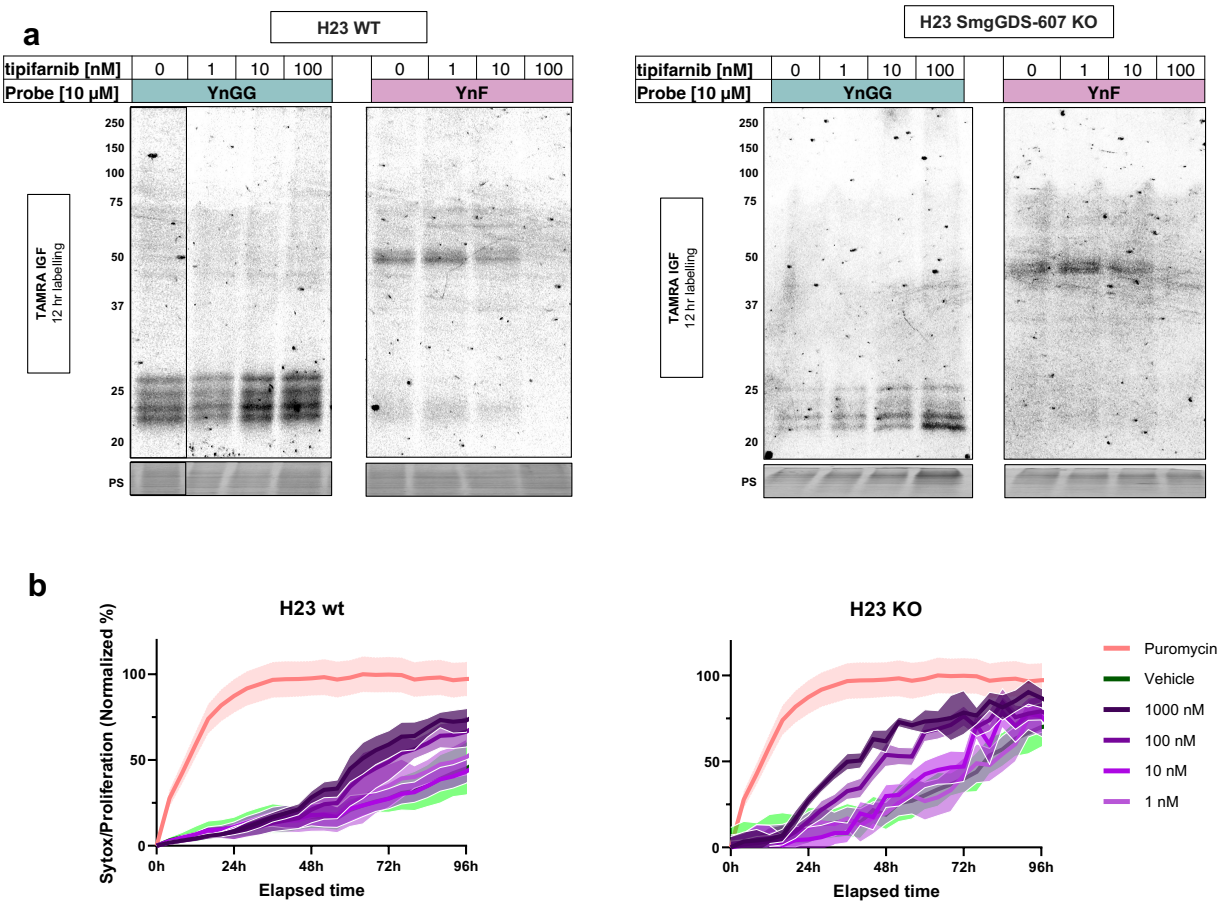

Figure 2.2.4. H23 WT and SmgGD-607 KO cell line responses to tipifarnib. (a) Tipifarnib dose-response experiment using 10 μM of YnF and YnGG. H23 WT cells showed that YnGG signal did not change with increasing concentrations of tipifarnib, whilst YnF signal decreased in a dose-dependent manner with no signal present at 100 nM tipifarnib. KO cells mirrored this response. Lane 1 was cropped from another location for clarity (shown by outline). (PS – ponceau S stain). (b) Tipifarnib toxicity experiments carried out in H23 WT and KO cells over 96h. Toxicity was defined as Sytox green labelling/confluency (represented on the y-axis). Shading represents error (standard deviation -SD).

These conditions were taken forward to design a proteomics profiling strategy for the H23 WT and KO cell lines. Here, a tandem-mass tag (TMT) labelling approach was chosen to compare the global prenylation profiles of H23 SmgGDS-607 KO and WT cells. TMT-based proteomics involves the use of isobaric tags to label N-terminal amines and lysine side-chains of peptides[253]. These tags have identical properties and masses at the MS1 level, however their fragmentation at the MS2 level generates reporter ions of different masses, enabling enhanced quantification (i.e. fewer missing values) of peptides labelled with a particular tag within a multiplexed TMT sample, compared to standard label-free

quantification approaches. Thus, experiments performed under a given set of conditions can be uniquely tagged and multiplexed into a single MS run, allowing head-to-head comparisons of peptide abundances across experimental conditions or replicates, whilst reducing MS running time.

Samples were treated according to the strategy outlined in **Fig 2.2.5a**. Both cell lines were subject to treatment with increasing concentrations of YnF or YnGG and pooled into TMT 9-plexes encompassing a DMSO (vehicle) control, YnF titration, and YnGG titration of each cell line. Concentration and substrate-dependent incorporation of YnF or YnGG would then then be plotted as function of fold change in protein abundance (normalized intensity). This can then be transformed to a linear scale, and following background correction, these parameters can be fit into Michaelis-Menten-like curves (**Fig. 2.2.5b**). In theory, *bona fide S*-prenylated substrates would give a good Michaelis-Menten curve fit[254]. Changes in curve fitting of a particular substrate in the SmgGDS-607 KO line may indicate that the oncogenic SmgGDS-607 specifically modulates its prenylation state under WT conditions, where a sigmodal curve indicates positive cooperativity, and a hyperbolic curve fit indicates negative cooperativity of SmgGDS-607. Substrates that exhibit such trends can then be investigated further for how these responses change in the presence of tipifarnib.

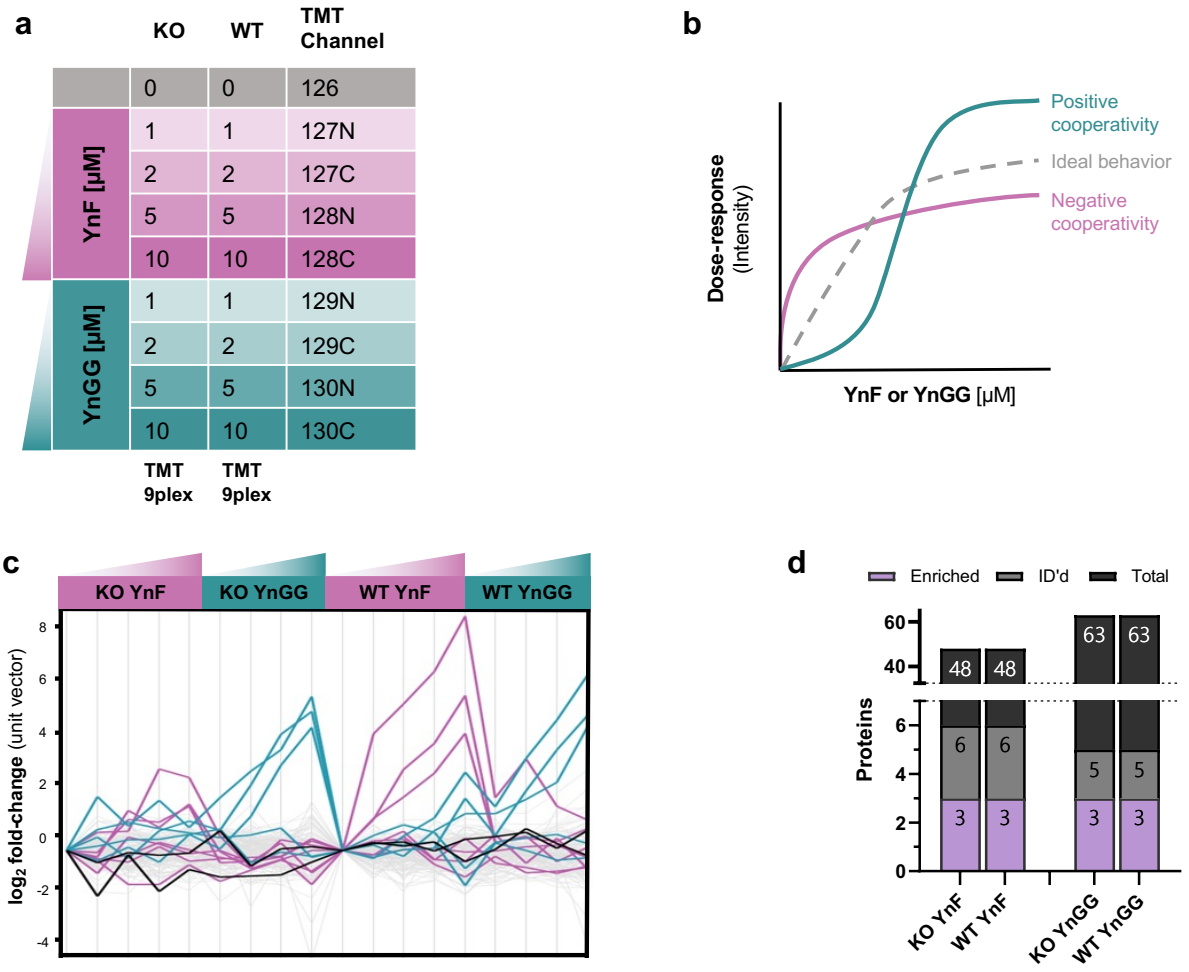

Figure 2.2.5 Initial chemical proteomic investigation of prenylation dynamics upon SmgGDS-607 KO. (a) H23 WT and SmgGDS-607 KO cells were treated with increasing concentrations of each probe and labelled according to the TMT strategy outlined. **(b)** Schematic representing Michaelis-Menten-like curve fitting of YnF and YnGG probe incorporation. **(c)** Profile plot of dose-dependent pull-down of known YnF or YnGG high-abundance targets. **(d)** Summary of enriched versus expected *S*-farnesylated and *S*-geranylgeranylated substrates in each cell line profiled.

Samples were processed using a biotin-neutravidin enrichment-based chemical proteomic strategy[216] (described in Methods). Briefly, samples were subject to a click reaction with capture reagent azide-arginine-biotin (AzRB) and enriched using Neutravidin-coated agarose beads. After reduction and alkylation of the enriched proteins, samples were enzymatically digested on-bead using sequence-grade trypsin, where the installed arginine group in AzRB also undergoes tryptic cleavage, removing the

biotin affinity handle from the ligated probe, thereby enhancing elution and increasing the ionization-capacity of peptides on the LC/MS. Digested peptides were collected, TMT labelled, and multiplexed into the specified sample pools. TMT pools then underwent 8-layer fractionation to decrease sample complexity, improving sequence coverage and dynamic range of peptide identification[255]. Fractions were run on a QExactive Orbitrap spectrometer, and MS2 reporter ions were used for quantification. MaxQuant was used to search MS spectra and Perseus was used for downstream data analysis[256] (acquisition parameters and data analysis detailed in Methods).

Results confirmed that high abundance substrates, including LMNB1 and DNA1JA, were enriched by YnF in a dose-dependent manner. RAB proteins, such as RAB6C, were similarly enriched by YnGG in a dose-dependent manner. Taken together, this indicated that probe incorporation was consistent and selective (**Fig. 2.2.5c**). Moreover, global *S*-farnesylation was observed to be reduced upon SmgGDS-607 KO, while *S*-geranylgeranylation appeared to be minimally affected. This is somewhat in agreement with a previous study, where an alkyne prenyl probe (C15AlkOPP) was used to profile the prenylation status of substrates affected by KD of SmgGDS-607 using SSO Ex5[85]. In this study, a decrease in overall prenylation was observed, including substrates known to be *S*-geranylgeranylated. However, this could potentially be partially attributed to previously reported pleiotropic changes in the abundance of select *S*-geranylgeranylated substrates upon statin treatment, which is required for metabolic incorporation of C15AlkOPP. Moreover, as C15AlkOPP is unable to differentiate between *S*-farnesylation and *S*-geranylgeranylation, this observed specific decrease in substrate *S*-farnesylation could not have been demonstrated by the previous study[257].

However, the relatively low number of identified proteins in the present study implied that the global level of YnF and YnGG probe incorporation (and/or enrichment) was less than sufficient to capture differential enrichment profiles for high priority substrates such as KRAS, with a maximum of 12.5% canonically prenylated substrates identified, and only up to 6.25% significantly enriched (**Fig. 2.2.5d**). Quality control analysis of raw MS files (processed by PTXQC, described in Methods) did not reveal any major contamination

issues that could have contributed to poor sample ionization or chromatography, such as the presence of detergents, plastics, or excess trypsin[258,259]. This suggested that complications were likely arising at the level of incorporation. After closer investigation, it was revealed that the batch of fetal bovine serum (FBS) used in cell culture at the time of the experiment was unfortunately changed without prior notice, which significantly affected H23 cell metabolism and viability, and therefore leading to poor incorporation of the probes. Indeed, switching back to the original batch of FBS restored cell viability and incorporation of probes. The experiment was thus planned to be repeated under more favorable conditions.

2.2.3. Proof of concept: benchmarking automated sample preparation for membrane-associated proteins

The failure of this initial profiling experiment prompted a re-evaluation of sample preparation methodologies to improve the consistency and reliability of proteomic-grade enrichment protocols, as well as to ensure enrichment of high priority substrates, some of which may be membrane-associated to some degree. Considering that the aforementioned experiment required 54 samples to be processed with minimal batch effects, a feat not easily accomplished by manual pipetting, an alternative enrichment protocol was adopted to automate the pull-down steps, reducing human error and potentially increasing reproducibility. A KingFisher™ device was thus trialed using a well-established lipid probe (alkyne myristate, YnMyr) in a model cell line (HEK293) to benchmark the system for the enrichment of membrane-associated proteins[24,260] (**Fig. 2.2.6a**).

The KingFisher™ device (ThermoFisher) utilizes a 96-well plate format, where probe-labelled samples clicked to a suitable capture reagent (e.g. AzRB) are pipetted into a deep-well plate. Pull-down is initiated by the addition of magnetic streptavidin beads (see Methods for more details), while a set of magnetic rods, corresponding to the given plate wells and dimensions, mixes the beads by magnetizing the rods in set intervals, as well as by simple agitation via rod oscillation. This ensures adequate and consistent mixing throughout the pull-down/enrichment stage. Beads are then washed by magnetically

transferring them to a series of 96-deep-well plates containing wash buffers, and after which they are transferred to a digest-compatible buffer, where the enriched bead-bound proteins are reduced, alkylated, and digested by the addition of sequence-grade trypsin. Samples are then left to shake at 37°C overnight. Finally, bead removal is carried out by the magnetic rods, and the resulting peptides are transferred to processing steps directly from the plate.

A simple benchmarking experiment was designed, where a triplicate set of HEK293 lysates, treated with either DMSO or 20 μM YnMyr (16h treatment), was clicked to AzB (Azide-PEG3-Biotin, Cayman Chemicals). These samples were then split into either the automated KingFisher™ workflow, or the corresponding manual workflow, using the same batch of magnetic beads. The manual workflow was carried out simultaneously to the automated version to ensure a close reproduction of conditions, so that differences in enrichment can be reliably attributed to the use of automation, rather than confounding batch effects. Dr. Lior Soday aided in the setup of pulldown experiments.

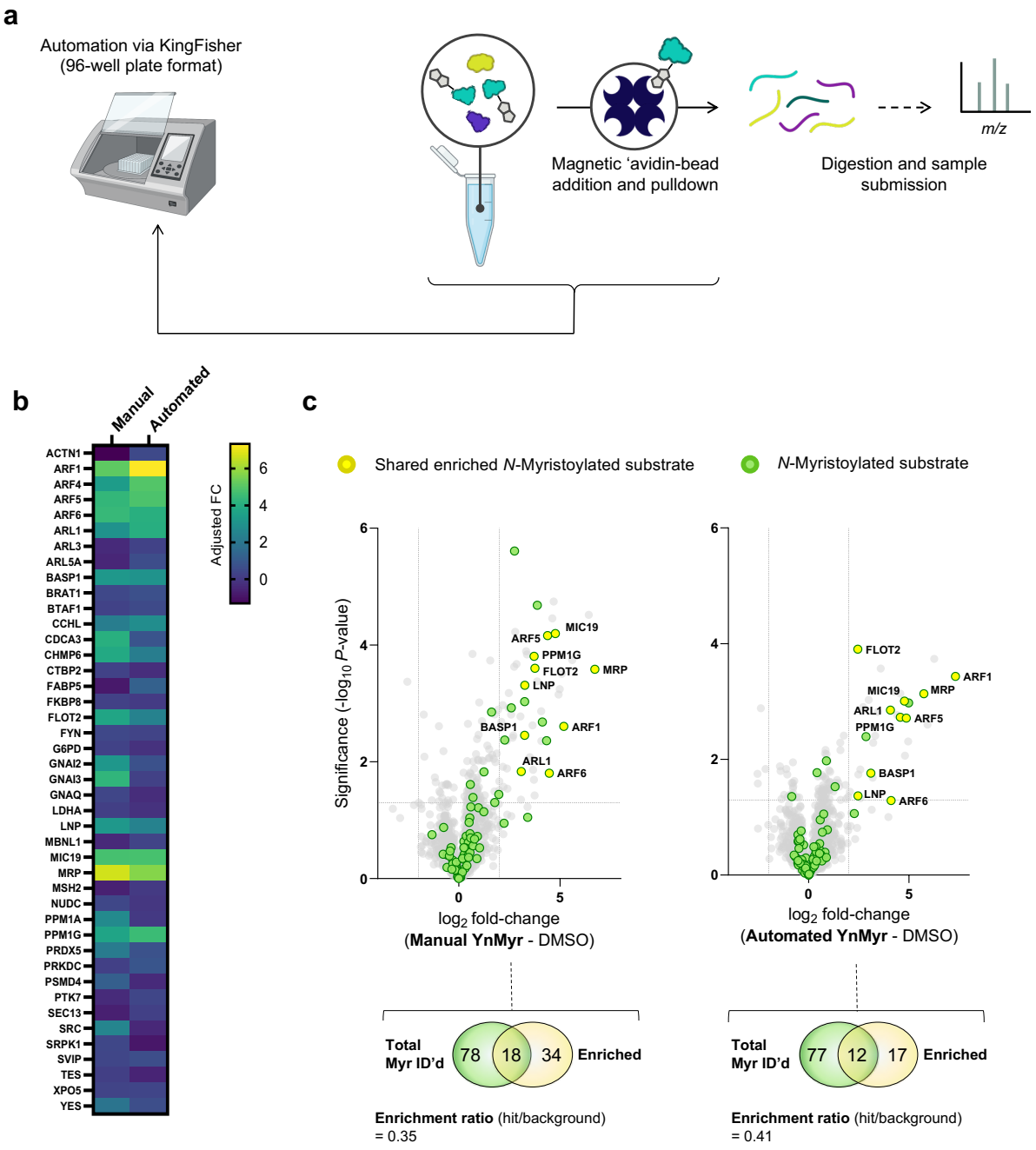

Figure 2.2.6. Benchmarking of an automated workflow for membrane-associated protein enrichment. (a) Schematic of workflow for adapting proteomic probe-based enrichment protocols for automation using a KingFisher device. Lysates metabolically labelled with a lipid probe (here, YnMyr) are subject to click ligation using a biotin-containing capture reagent (AzB). After clean-up of excess click reagents, samples are pipetted into a 96-deep well plate and placed in the KingFisher device. Magnetic 'avidin beads are added to each well, initiating pulldown. Samples are agitated by the device for 2 hours, after which the device then washes the beads and transfers them to a digest-compatible buffer. Proteins are digested off the beads overnight. The device removes the beads and the resulting peptides are taken forward to MS-based analysis. **(b)**

Heatmap representing fold-change (log_2FC) enrichment of YnMyr substrates over the corresponding DMSO controls in using manual and automated sample preparation workflows (n=3). **(c)** Volcano plots depicting YnMyr enriched substrates (two sample student's t-test; S0 = 0.1, FDR = 0.05, n=3). Canonical N-myristoylated substrates are highlighted in green. High confidence hits shared between the two datasets are highlighted in yellow. Venn-diagrams are used to demonstrate enrichment over background for significant hits ($p \leq 0.05$, $log_2FC \geq 1.2$).

Results demonstrated successful YnMyr-enrichment of canonical *N*-myristoylated substrates using both methods when compared to each dataset's respective DMSO control (**Fig. 2.2.6b**). Notably, subtle differences were observed between automated and manually enriched populations, with the manual approach offering slightly more significant canonical *N*-myristoylated hits: 18 proteins compared to the 12 enriched in the automated sample set (FDR = 0.05, S0 = 0.1). Of these enriched proteins, 10 were shared between the two datasets, including high-confidence hits ARL1, BASP1 and various ARF-family proteins[24]. Manual and automated enrichment ratios (defined as hit/background) were generally comparable (0.35 and 0.41 respectively), indicating that automation could serve as a suitable alternative to manual enrichment strategies for chemical proteomic workflows. While slightly fewer overall identifications in the automated sample set may hamper identification of novel substrates, this is compensated by the lower background observed. Unfortunately however, repeated submission of samples processed using magnetic beads (both automated and manual) resulted in the accumulation of MS contaminants, affecting column performance and thereby impairing chromatography and column lifetime. Moreover, bead transfer and washing were complicated during the final buffer wash, as beads became prone to aggregation after the depletion of detergent (SDS), an essential step before on-bead tryptic digest. Due to pandemic-related constraints in attempts to mitigate these issues, proteomic sample processing using magnetic-beads was temporarily halted. However, this did not preclude the use of automation for samples intended for gel-based analysis and provides a useful workflow for such purposes (as demonstrated in later chapters).

2.2.4. Proof of concept: optimization of protein sample purification for membrane-associated proteins

Other parameters important for the optimization of membrane-associated protein enrichment workflows include sample isolation and purification. This would most demonstrably require the optimization of lysis methods for H23 cells, as well as the subsequent removal of detergents and other contaminants (i.e. click reagents) for proteomic analysis. Lysis buffers can be formulated to enhance membrane-associated protein recovery, including low-solubility and transmembrane proteins, which may be of interest[261]. Typically, these proteins are difficult to isolate due to their hydrophobic nature and propensity for aggregation. The use of buffers that include non-ionic surfactants such as Non-idet 40 (NP-40), Triton X-100 (TX100) or n-Dodecyl-beta-Maltoside (DDM) can enhance the solubilization of such proteins, however they are generally poorly compatible with MS-related workflows, leading to signal suppression and diminished sensitivity, as well as contamination of the liquid chromatography column and mass spectrometer. Therefore, efficient removal of contaminants is crucial to enable the use of such detergents in proteomic sample preparation, as well as to increase overall sequence coverage and peptide identification. Nevertheless, it has been shown that 1% SDS can isolate most proteins, including those that are membrane-associated, although efficient removal of high concentrations of SDS is also necessary for clean and reliable sample preparation[261].

At this time, the Tate Group most frequently utilized a standard chloroform-methanol (TCM-MeOH) precipitation protocol[262]. However, sample variability was commonly high due to the protein pellet presenting at the solvent interface as a thin film, making pellet disruption during wash steps difficult to avoid. Thus, sample recovery was often compromised. Moreover, removal of detergents using TCM-MeOH was subpar, prohibiting the use of non-ionic surfactants or high concentrations of ionic detergents. This is recapitulated in a recent study comparing TCM-MeOH precipitation to other proteomic-compatible workflows[263]. Solid-phase enhanced sample preparation (SP3), for example, is another common protein purification strategy that involves the use of carboxylate-coated magnetic beads[263,264]. In the presence of organic solvent, protein aggregates are captured on the beads that remain bound during high-solvent (80% ethanol) washing steps. Captured proteins are then readily eluted when the beads are

submerged in aqueous buffer. The system is advantageous in that it is amenable to high-throughput automated workflows though the use of the aforementioned KingFisher™ device. In a previous study, SP3, as well as other common precipitation methods, outperformed TCM-MeOH in almost every parameter, including the isolation of endo- and plasma membrane associated proteins[263]. This strongly suggests that alternatives to TCM-MeOH precipitation should be explored, particularly in lipid-PTM chemical proteomic enrichment strategies.

Another recent study highlighted SP4 (solvent precipitation SP3) as an alternative and highly favorable protein purification method[264]. SP4 involves acetonitrile-induced protein precipitation and subsequent capture of aggregates by centrifugation, with the pellet conveniently forming at the bottom of the vessel rather than at a solvent interface, or alternatively onto inert (i.e. glass) beads for high-throughput applications. Compared to SP3, SP4 recovered proteins with improved reproducibility and yielded greater isolation of low solubility and membrane-associated proteins. Additionally, the more minimalistic SP4 strategy features lower costs per sample prepared and is highly translatable to our current workflow, making it another attractive alternative to TCM-MeOH.

Therefore, three methods for protein purification (TCM-MeOH, SP3 and SP4), were compared by whole proteome analysis to determine their suitability for membrane-associated protein identification, as well as for overall removal of contaminants to ensure high sample quality across future experiments (**Fig 2.2.7a**). HEK293 cells were selected as a cell model due to its common use across various experiments in the Tate group. Two lysis buffers were compared across the three precipitation workflows: Radioimmunoprecipitation assay buffer (RIPA), a common lysis buffer which contains non-ionic detergents such as Triton X-100, and 1% SDS. The RIPA condition was omitted for TCM-MeOH processed samples due to concerns of MS instrument contamination, as previous experiments have confirmed incomplete removal of detergents using this protocol.

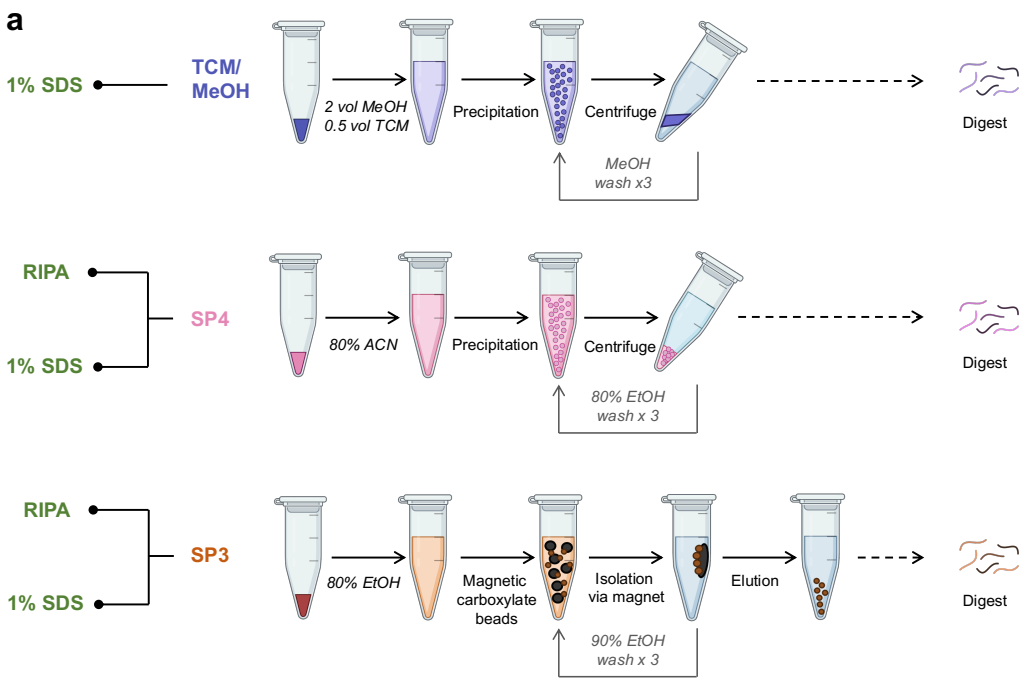
a
1% SDS
TCM/
MeOH
2 vol MeOH
0.5 vol TCM
Precipitation
Centrifuge
Digest
MeOH
wash x3
RIPA
1% SDS
SP4
80% ACN
Precipitation
Centrifuge
Digest
80% EtOH
wash x 3
RIPA
1% SDS
SP3
80% EtOH
Magnetic
carboxylate
beads
Isolation
via magnet
Elution
Digest
90% EtOH
wash x 3

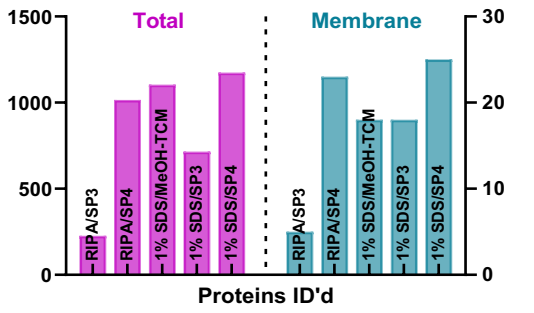
b
Total
Membrane
1500
1000
500
0
30
20
10
0
RIPA/SP3
RIPA/SP4
1% SDS/MeOH-TCM
1% SDS/SP3
1% SDS/SP4
Proteins ID'd

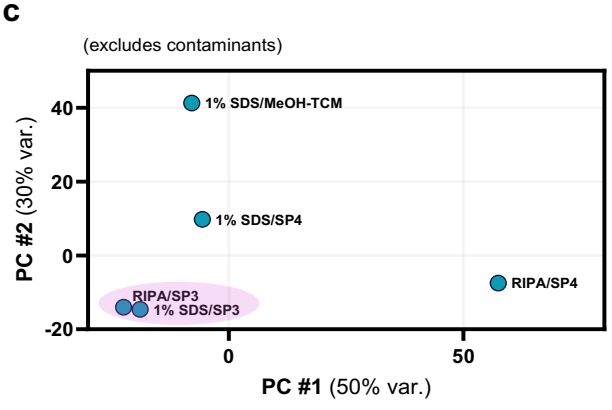
c
(excludes contaminants)
1% SDS/MeOH-TCM
1% SDS/SP4
RIPA/SP4
RIPA/SP3
1% SDS/SP3
PC #2 (30% var.)
40
20
0
-20
0
50
PC #1 (50% var.)

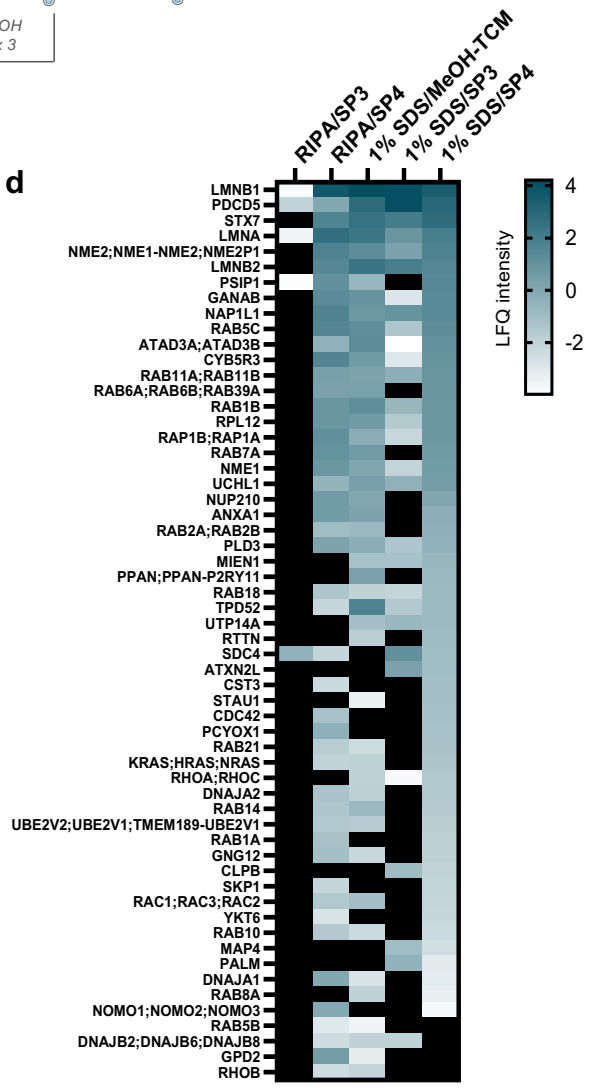
d
RIPA/SP3
RIPA/SP4
1% SDS/MeOH-TCM
1% SDS/SP3
1% SDS/SP4
LFQ intensity
4
2
0
-2
LMNB1
PDCD5
STX7
LMNA
NME2;NME1-NME2;NME2P1
LMNB2
PSIP1
GANAB
NAP1L1
RAB5C
ATAD3A;ATAD3B
CYB5R3
RAB11A;RAB11B
RAB6A;RAB6B;RAB39A
RAB1B
RPL12
RAP1B;RAP1A
RAB7A
NME1
UCHL1
NUP210
ANXA1
RAB2A;RAB2B
PLD3
MIEN1
PPAN;PPAN-P2RY11
RAB18
TPD52
UTP14A
RTTN
SDC4
ATXN2L
CST3
STAU1
CDC42
PCYOX1
RAB21
KRAS;HRAS;NRAS
RHOA;RHOC
DNAJA2
RAB14
UBE2V2;UBE2V1;TMEM189-UBE2V1
RAB1A
GNG12
CLPB
SKP1
RAC1;RAC3;RAC2
YKT6
RAB10
MAP4
PALM
DNAJA1
RAB8A
NOMO1;NOMO2;NOMO3
RAB5B
DNAJB2;DNAJB6;DNAJB8
GPD2
RHOB

Figure 2.2.7. Comparison of protein isolation and purification workflows for membrane-associated protein enrichment. (a) Schematic of workflow used to test alternative protein purification strategies following lysis and/or click reaction. SP4, TCM-MeOH and SP3 were tested using RIPA and 1% SDS lysis buffers to evaluate removal of detergents and isolation of membrane-associated (i.e. *S*-prenylated) proteins. Precipitation and proteomic sample preparation was performed alongside Dr. Lior Soday (**b**) Total protein and membrane-associate protein counts for each of the tested conditions (n=1). (**c**) PCA plot showing clustering of SP3-purified samples. (**d**) Heatmap depicting normalized LFQ intensities of *S*-prenylated proteins in each of the tested conditions (n=1).

Total protein recovery was found to be consistently higher (approximately over 85%) for SP4 processed samples when compared to either SP3 or TCM-MeOH, with the latter demonstrating the least reliable sample recovery of the trialed techniques (across multiple experiments, data not shown). Contaminant analysis of submitted samples showed significantly less MS contaminants in SP4 conditions, with up to two-fold less PEG contamination in SP4 processed samples (Appendix Fig. **7.3**). SP3 samples contained the most PEG, likely due introduced by the beads themselves. PCA analysis revealed that SP3-processed samples also strongly clustered together compared to other methods, which is consistent with literature findings[263] (**Fig 2.2.7b**). When analyzing the total number proteins identified, SP3 generally performed poorly compared to both SP4 and TCM-MeOH, irrespective of lysis buffer used. When taking lysis buffer into account, RIPA was least promising of the two, only outperforming 1% SDS/TCM-MeOH and both SP3 conditions in prenylated protein identification. Notably, SP4 consistently outperformed other precipitation methods in respect to total proteins identified, as well as prenylated proteins, with over 68% more identified compared to SP3 and TCM-MeOH, particularly when using 1% SDS lysis buffer (**Fig 2.2.7b and c**).

Though this experiment was only performed in a single replicate, other similar experiments performed in the Tate Group during this time reproduced these results, with similar conclusions drawn (data not shown). Thus, the 1% SDS/SP4 conditions were taken forward for future global prenylation profiling experiments and has generally become the standard in proteomic sample preparation within the Tate Group.

2.2.5. Optimization of protein sample purification for membrane-associated proteins

With optimized conditions for the enrichment of prenylated proteins in hand, a new workflow for investigating the involvement of SmgGDS-607 on protein *S*-prenylation was devised. A simplified sample setup was favored over the initially proposed YnF/GG probe dose-response response experiment, partially owing to obstacles using magnetic-bead enrichment protocols, which limited our use of automation for proteomic sample preparation. Instead, a single optimal probe labelling concentration (determined to be 10 μM for both YnF and YnGG labelling) was chosen and used to determine probe-dependent enrichment (when compared to a DMSO no probe control). Tipifarnib (100 nM) treated probe-labelled samples were also generated to determine the drug's effect on either YnF or YnGG enrichment. These experiments were performed for both SmgGDS-607 KO and WT H23 cell lines (**Fig. 2.2.8**). This would not only determine changes in prenylation dynamics upon KO of the SmgGDS oncogenic variant, but would also enable us to unpick FTI-specific responses in the KO context, revealing if SmgGDS indeed plays a role in alternative prenylation, or "prenyl-switching", of substrates such as KRAS.

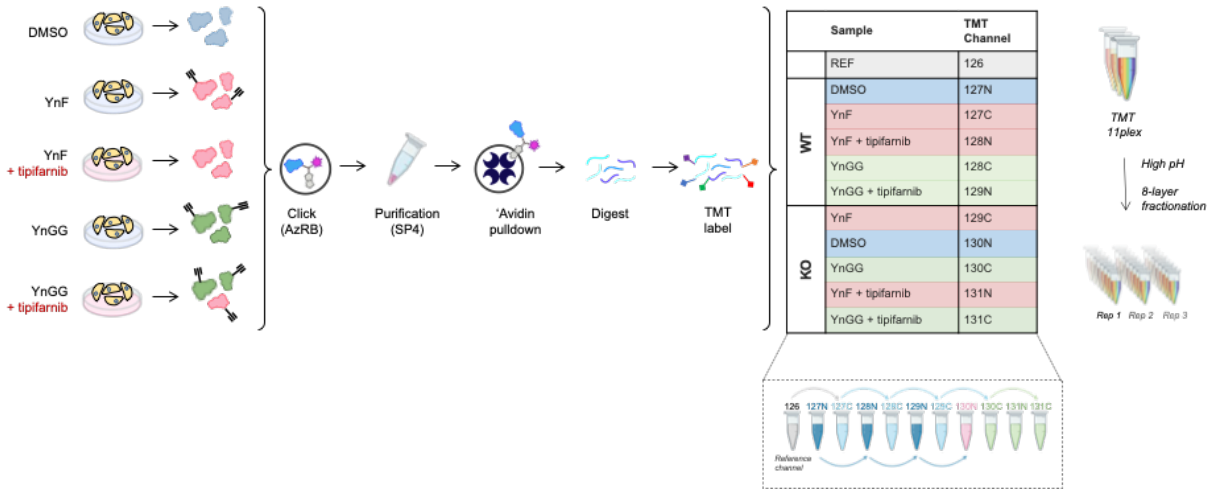

Figure 2.2.8. Devised sample preparation strategy for global prenylation profiling upon KO of SmgGDS-607. Optimized sample treatment strategy and probe-based enrichment workflow for SmgGDS-607 KO model cells. Notable optimizations included the use of SP4 are a purification strategy as well as TMT-label staggering to avoid channel crosstalk.

A similar enrichment strategy, using click ligation to AzRB and neutravidin-agarose beads, was employed. Here, 1% SDS was used as the lysis buffer and SP4 precipitation after click ligation. TMT labelling was also optimized to include a reference channel, which is a pooled channel containing an equimolar sample of all samples throughout the entire experiment[265]. This can be used to normalize all samples in a multi-batch TMT experiment and may additionally boost protein identifications across the TMTplexes. Moreover, samples were also arranged within the TMTplex to reduce crosstalk/bleeding of adjacent channels, thereby minimizing contamination of control (DMSO) samples, as well as YnF channels bleeding into YnGG channels (or vice-versa)[265].

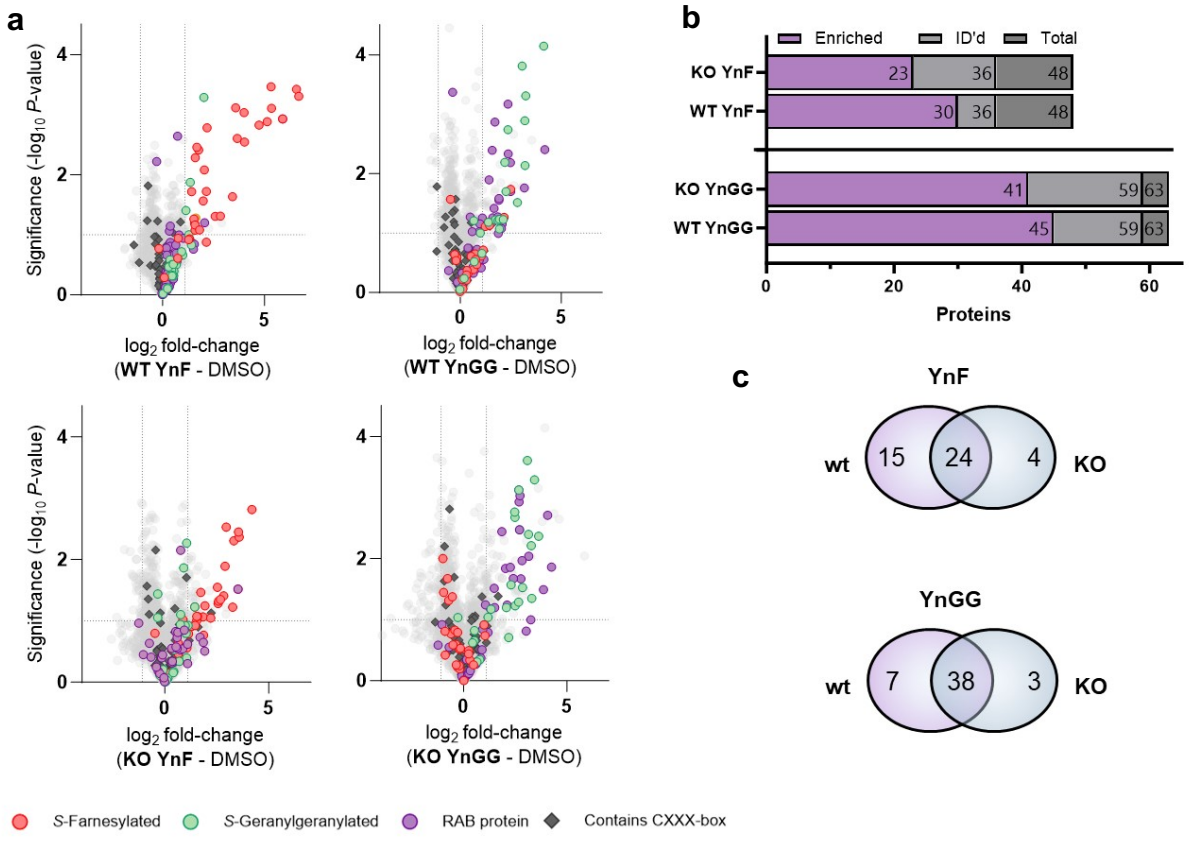

Figure 2.2.9. Summary data of H23 parent and SmgGDS-607 KO cell lines global prenylation profiling. (a) Profiling of YnF and YnGG-treated H23 WT and KO cells using the optimized protocol. Enrichment in upper right quadrant is defined as $p \leq 0.05$ and $\log_2FC \geq 1.2$,

determined by a 90% confidence interval (where over 90% of substrates in upper right quadrant are canonically prenylated). Canonically *S*-farnesylated proteins are highlighted in red, *S*-geranylgeranylated proteins highlighted in green, with RAB proteins shown in purple. Other CXXX proteins are shown as black diamonds (n=3). **(b)** Summary of enriched versus expected substrates in each cell line profiling experiment. **(c)** Venn diagrams representing enriched, overlapping substrates between WT and KO cell line profiling experiments.

A summary of the profiling experiment is shown in **Fig. 2.2.8**. Pleasingly, about 95 prenylated substrates were identified across WT and KO cell lines, not including non-canonical substrates that were enriched in either YnF or YnGG conditions (FDR = 0.05, S0 = 0.1). Improvements to *S*-prenylated protein profiling, as compared to both published studies and the previous attempt outlined earlier in this chapter, may be attributed to the optimizations in proteomic sample isolation and processing. However, samples were also run on a newer generation mass spectrometer (ThermoFisher Eclipse vs QExactive), which enabled the differentiation of reporter ions from co-isolated peptides at the MS^3 level, thereby improving quantification[266]. Nevertheless, improvements to our proteomic workflow have enabled more reliable sample production with fewer contaminants across probe-based experiments across the group.

Overall, the total number of assigned enriched proteins was greater in WT samples compared to the KO, and markedly so in the YnF condition. This was consistent with the findings from the previous attempt at *S*-prenylation profiling described earlier in this chapter, as well as the previously discussed literature studies that employed C15AlkOPP. Interestingly, this effect was not captured by the in-gel fluorescence (AzT) labelling experiments described earlier in the chapter, possibly indicating that this difference in enrichment required a more sensitive technique to establish. Overlap of significantly enriched substrates was also observed to be greater in YnGG samples compared to YnF, implying that SmgGDS-607 KO may have a stronger effect on the prenylation status of certain substrates over others.

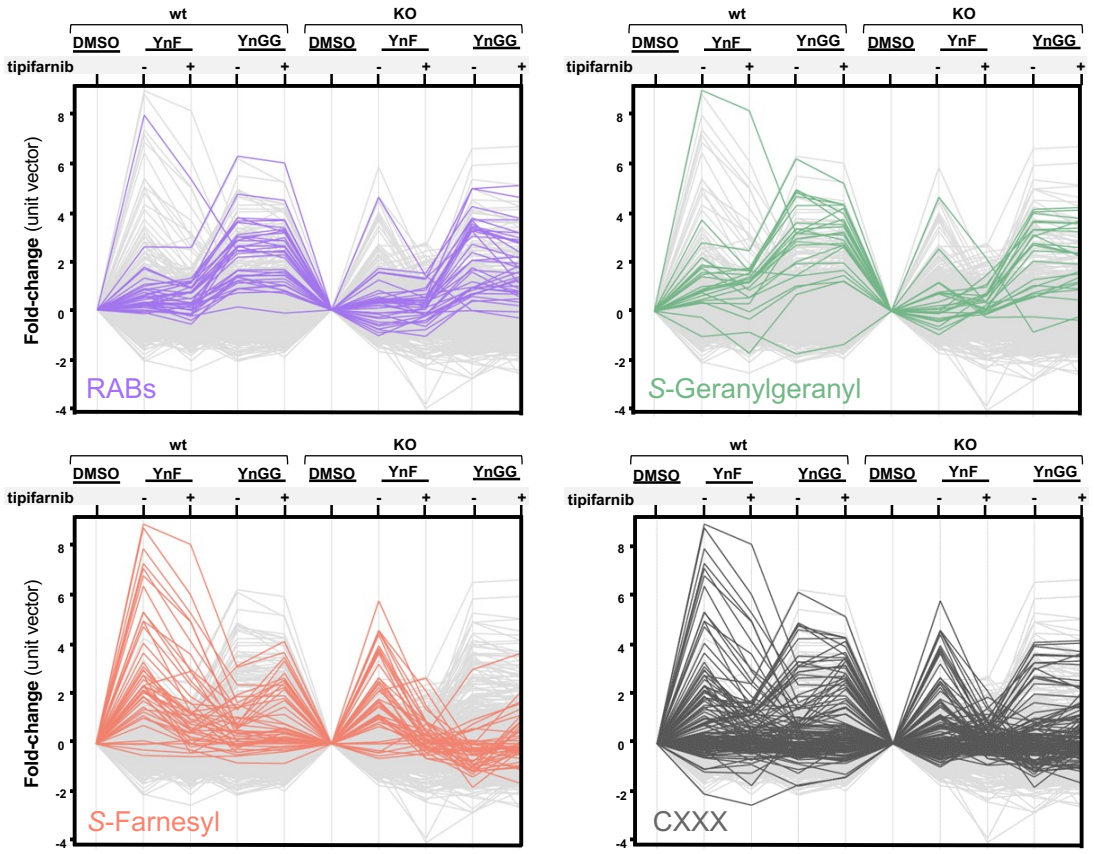

Figure 2.2.10. Highlighted categories of YnF and YnGG enriched substrates in WT and SmgGDS-607 KO cell lines. Profile plots showing YnF and YnGG enriched substrates in WT and SmgGDS-607 KO cell lines (fold-change (UV); n=3). Highlighted categories are RAB (purple) and *S*-geranylgeranylated (green) substrates which are enriched in YnGG-treated samples, and *S*-farnesylated substrates (red), which are enriched in YnF-treated samples.

When visualizing global prenylation as profile plots, where the mean fold-change of the abundance of each protein is shown in context of all other experimental conditions, there emerged a concern that clonal differences between the cell lines may also be contributing to the observed lower level of YnF incorporation in the KO cell line, as the abundances of unenriched substrates were not effectively normalized by background subtraction of the DMSO controls of each cell line (Appendix Fig. **7.4**). For example, differences in cell metabolism could affect the rate of uptake of each probe, resulting in differential labelling efficiencies between the cell lines that cannot be attributed to PTase activity. Using unit vector scaling, which refers to a technique used to normalize the values of different attributes (i.e. proteins) in a dataset, brought the fold-changes between the two cell lines to a comparable scale so that they do not dominate the analysis based on their original

magnitude[267]. This was demonstrated by a normalization of the background proteins between the two cell lines after unit vector scaling (Appendix Fig. **7.4**). This scaling revealed that the observed lower levels of *S*-farnesylation in the KO cell line persisted even after normalization, giving credence to the direct effect SmgGDS-607 has on global *S*-farnesylation[85]. Data shown in **Fig. 2.2.10** shows the result of unit vector scaling and the effect that SmgGDS-607 KO has on YnF and YnGG enrichment, in the presence and absence of tipifarnib. The influence of tipifarnib in this study is discussed in detail later in the chapter.

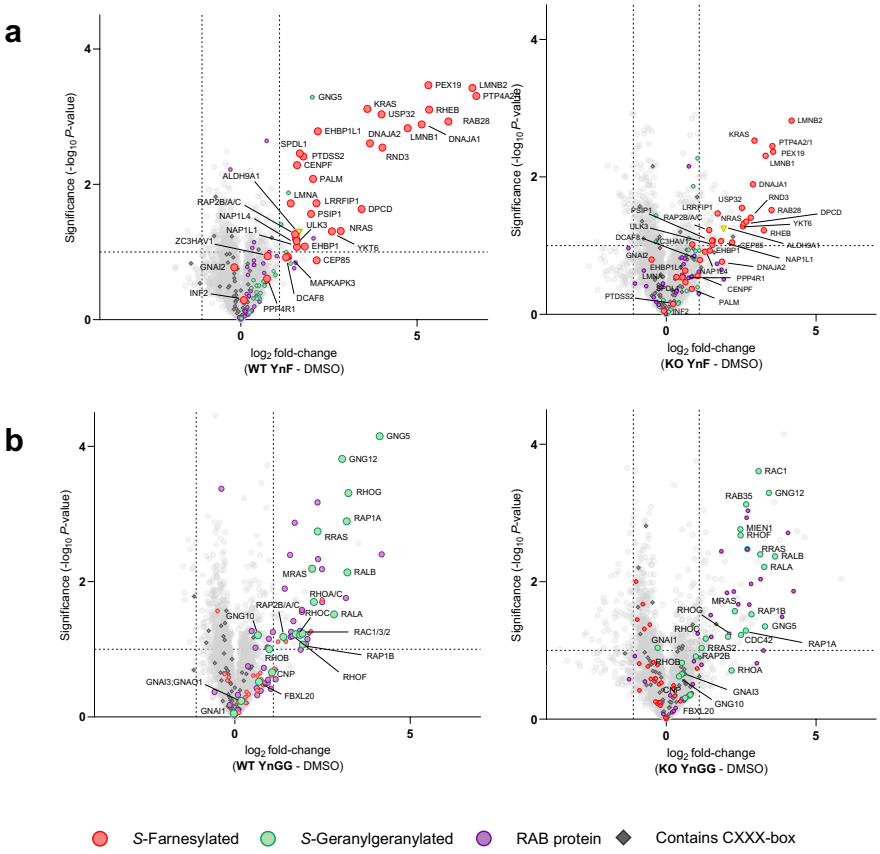

Figure 2.2.11. WT and SmgGDS-KO YnF and YnGG enrichment plots. Chemical proteomic analysis of **(a)** YnF and **(b)** YnGG enriched substrates in WT and SmgGDS-607 KO cell lines (two sample student's t-test; S0 = 0.1, FDR = 0.05, n=3). Substrates are highlighted according to the provided legend.

A closer look at identified substrates reveals enrichment of both well-established *S*-farnesylated and *S*-geranylgeranylated proteins, as well as more obscure substrates that remain poorly studied in the context of *S*-prenylation[52] (**Fig. 2.2.9**). ZC3HAV1, DCAF8,

LRRFIP1 and DPCD have only been recently described to be *S*-farnesylated, while PSIP1, PPP4R1 and ALDH9A1 are novel *S*-farnesylated substrates[268]. NRDG1, TMX3, MIGA1, TNFRSF10A and ANKRD26 were found to be *S*-geranylgeranylated; however, only minor isoform/splice variants of these proteins were enriched, and the biological significance of their potential prenylation is not known. Additional information on these substrates is summarized in **Table 2.2**.

Table 2.2. Novel or recently annotated prenylated substrates enriched in H23 dataset.

ID	Gene	Protein name	CXXX	F/GG	Log_2(Intensity) (Probe - DMSO)	
Q7Z2W4-1	ZC3HAV1	Zinc Finger CCCH-Type Containing, Antiviral 1	CVIS	F	WT	0.77
					KO	0.87
Q5TAQ9-1	DCAF8	DDB1 And CUL4 Associated Factor 8	CMPS	F	WT	1.28
					KO	1.29
Q32MZ4	LRRFIP1	Leucine-rich repeat flightless-interacting protein 1	CTMS	F	WT	2.45
					KO	1.72
Q9BVM2	DPCD	Deleted In Primary Ciliary Dyskinesia Homolog	CKTQ	F	WT	3.43
					KO	2.67
O75475-2	PSIP1	PC4 and SFRS1 interacting protein	CNLQ	F	WT	1.99
					KO	1.56
J3QRV2	PPP4R1	Protein phosphatase 4 regulatory subunit 1	CSIP	F	WT	0.75
					KO	1.05
A0A6Q8PGJ1	NDRG1	N-myc downstream regulated 1	CLVD	GG	WT	0.70
					KO	0.68
B4DIE3	TMX3	Protein disulfide-isomerase TMX3	CKTF	GG	WT	0.68
					KO	0.94
E5RFH1	TNFRSF10A	TNF receptor superfamily member 10a	CMDR	GG	WT	1.53
					KO	1.55
A0A6Q8PG48	ANKRD26	Ankyrin repeat domain-containing protein 26	CACN	GG	WT	2.37
					KO	2.89
P49189	ALDH9A1	4-trimethylaminobutyraldehyde dehydrogenase, 9A1	N/A	F	WT	1.63
					KO	1.91

Other non-CXXX substrates, such as cell surface antigens (CD9, CD44, CD63, CD81 and CD151), DNAJC5, NPC1, PODXL, PROCR, REEP5, TFRC, TSPAN6, TSPAN11, SLC44A1, SCARB2, SCAMP1 were found to be highly enriched in YnGG-labelled samples, whilst unenriched in YnF samples. YnGG-mediated selective enrichment of these proteins was noted in a previous study using YnF and YnGG probes (unpublished). This was hypothesized to be the result of co-enrichment by association with other prenylated substrates. Importantly, all of the aforementioned proteins are membrane resident, with many present in RAB-containing exosomes or lysosomes. Other proteins, such as NPC1, contain lipid-binding motifs, and may be partial to direct binding with YnGG[269]. However, it is somewhat unexpected that this enrichment is evidently YnGG-specific, perhaps meriting further study to understand this phenomenon. For example, it can be hypothesized that proteolytic processing of some proteins may reveal a cryptic prenylation motif that serves as a substrate for either of the prenyltransferases. However, this was beyond the scope of the present study as none of these proteins were significantly differentially enriched in the WT and KO cell lines.

A variety of these identified substrates possessed interesting characteristics that may present new paradigms in protein *S*-prenylation. Among these, PSIP1 and ALDH9A1 are briefly discussed as case studies in this regard.

PSIP1

PC4 And SRSF1 Interacting Protein 1 (PSIP1) is a relatively understudied protein, described as a transcriptional co-activator in neuroepithelial stem cell differentiation and stress response. Interestingly, isoform 2 (also known as LEDGF/p52) is the only prenylated form of PSIP1 (CXXX = CNLQ) and has been shown to be the dominant transcriptional co-activator[270,271]. Chromosomal aberrations relating to LEDGF/p52 isoform have been described in recurrent AML, where NUP98 (nucleoporin 98)-LEDGE/p52 fusions were identified, with various transcripts notably containing the CXXX motif. It would be interesting to determine the function of the prenylated isoform and whether inhibiting *S*-farnesylation of PSIP1 or other CXXX-fusions has any therapeutic

benefit. Importantly, this example highlights the potential existence of CXXX-containing fusion proteins resulting from molecular rearrangement. Gain of function prenylation has not yet been described in disease contexts and may represent an untapped application for FTIs such as tipifarnib. Gain of function prenylation as a result of acquired mutations, molecular rearrangement, or proteolysis is thus being investigated as a separate project (not covered in this thesis).

ALDH9A1

ALDH9A1 (Aldehyde Dehydrogenase 9 Family Member A1) is a part of a large family of aldehyde dehydrogenases that catalyze NAD^+-dependent oxidation of aldehydes to carboxylic acids or thioesters, and are widely implicated in the regulation of cellular oxidative and electrophilic stress[272,273]. Mechanistically, the active site catalytic cysteine acts as a reactive nucleophile and attacks the substrate carbonyl, resulting in reduction of the NAD+ cofactor and oxidation of the substrate.

ALDH9A1 was found to be selectively enriched in YnF-treated samples, equally in both WT and KO cell lines. However, the protein lacks a CXXX-box, which is canonically required for FTase-mediated *S*-farnesylation. Indeed, it was also found that this degree of YnF-enrichment persisted at the same intensity upon addition of an FTI (tipifarnib), which is described in more detail in a later section of this chapter. This implied that the farnesyl modification is not catalyzed by farnesyltransferase. A very recently published study using C15AlkOPP described the same phenomenon, however they were not able to differentiate between *S*-farnesylation and geranylgeranylation, as geranylgeranyl transferase inhibitors also has no effect on the labelling of ALDH9A1 by C15AlkOPP[274].

This study also conducted *in vitro* enzymatic studies to show that farnesal (FCHO) may be a substrate for ALDH9A1, where a unique labile thioester bond is putatively generated during oxidation of the isoprenoid aldehyde to the less reactive α,β-unsaturated acid[274]. Because the transient prenyl modification does not seem to change the localization of ALDH9A1, which remains in cytosolic puncta, a proposed biological consequence of this

modification lies in the metabolism of natural prenylated protein degradation products. In this context, PYCOX1 (prenylcysteine oxidase 1) is hypothesized to cleave the thioether bond of free prenyl-L-cysteines in the final step of prenylated protein degradation, producing the reactive aldehyde that acts as a substrate for ALDH9A1, allowing for sequestration of the reactive isoprenoid[275]. While this full mechanism was not shown directly, the ALDH9A1 active site cysteine (Cys288) was demonstrated to be labelled by C15lkOPP by MS analysis, indicating that covalent modification of the active site is possible, hence its capture in global prenylation profiling experiments. While perhaps more remains to be elucidated regarding this noncanonical modification, we can tentatively establish YnF as a *bona fide* substrate for ALDH9A1, and a non-substrate of FTase. Importantly, this can serve as a useful control for susceptibility to FTI-mediated loss of YnF labelling in global prenylation experiments, which is discussed later in this chapter.

2.2.6. Comparison of differentially enriched *S*-prenylated substrates in WT and SmgGDS-607 KO profiling experiments

A direct comparison of profiling experiments in WT and KO cells reveals subtle differences in the enrichment of specific substrates (**Fig. 2.2.12**). Notably, KRAS and NRAS enrichment by YnF does not significantly change upon SmgGDS-607 KO. HRAS was unfortunately not detected due to high homology with other RAS isoforms, making identification of unique peptides challenging. Surprisingly, RHOA does not seem to be differentially enriched between the WT and KO, which could imply that the regulation of its prenylation status isn't a determinant for synthetic lethal interactions KRAS and SmgGDS[276]. However, PBR-containing substrates RAP1A and RHOG were the most differentially enriched, with significantly greater enrichment in both WT YnF and YnGG-treated samples when compared to the SmgGDS-607 KO. This may indicate that they are the favored endogenous substrates of SmgGDS-607, represented by the abolishment of low-level *S*-farnesylation of these substrates in the KO cell line.

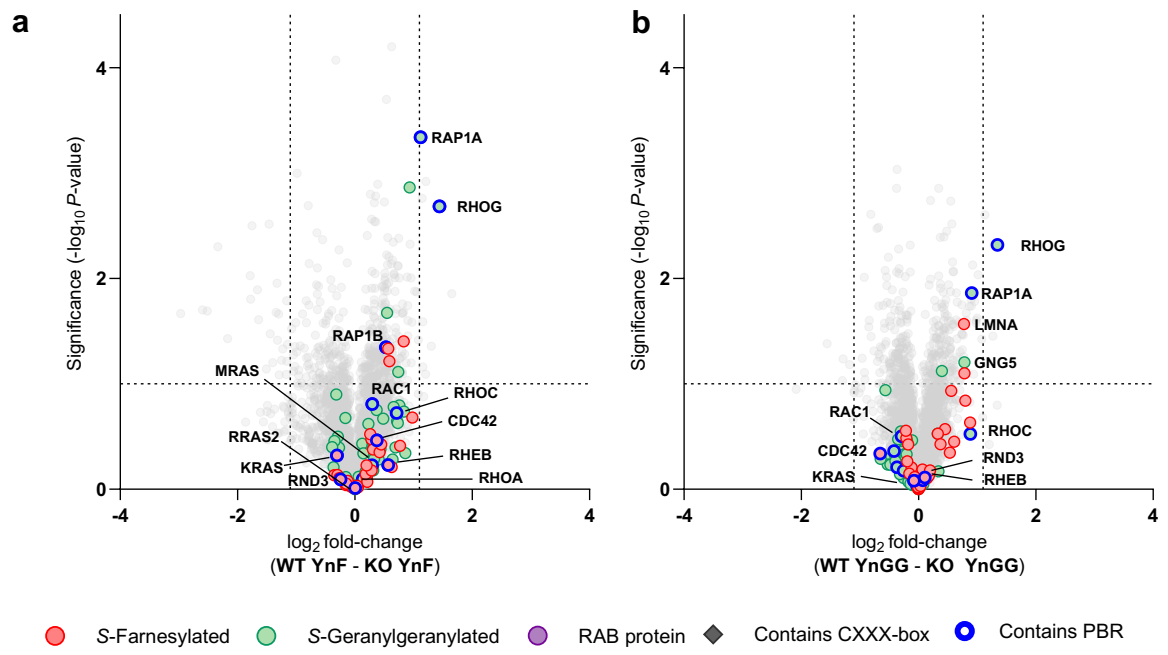

Figure 2.2.12. Direct comparison of differentially enriched substrates in WT and SmgGDS-KO cell profiling experiments. Chemical proteomic analysis of YnF and YnGG enriched substrates in **(a)** WT and **(b)** SmgGDS-607 KO cell lines (two sample student's t-test; S0 = 0.1, FDR = 0.05, n=3). Substrates are highlighted according to the provided legend.

Although both RAP1A and RHOG are canonically *S*-geranylgeranylated substrates, low levels of *S*-farnesylation may be present and only detected by sensitive enrichment experiments[250]. A previous study using YnF and YnGG probes also detected low levels of *S*-farnesylation of canonically *S*-geranylgeranylated substrates, including various RHO GTPases, although they are indeed predominantly labelled by YnGG (unpublished data). It is also worth noting that in the present study, RAP1A and RHOG are only significantly enriched in YnGG-treated samples, and the low-level enrichment of these proteins by YnF is not significantly disrupted by tipifarnib (shown later in this chapter), meaning that labelling at this level likely cannot be reliably quantified. Moreover, there is no recognized biological significance of this putative low-level *S*-farnesylation. The observed differential enrichment may perhaps be caused by an unexpected uptake of the YnF probe by GGTases, or some metabolic conversion between YnF and YnGG during the endogenous pyrophosphorylation of the probes. Although *in vitro* enzymatic studies counter this hypothesis, lipidomic and/or metabolomic analysis of YnF and YnGG probe treatment are likely necessary to rule this out at the cellular level[52]. Alternatively, this

differential may be explained by a downregulation of RAP or RHO GTPases upon KO of SmgGDS-607, which could be a direct effect of the KO itself or an artefact of cell clonality. This hypothesis is more readily tested by whole proteome analysis of these cell lines and is discussed further later in this chapter.

2.2.7. SmgGDS-607 and its effect on tipifarnib sensitivity in H23 cells

As previously discussed, the role of SmgGDS is not well characterized in the context of FTI treatment, although a few enzymatic and over-expression studies imply that KRAS favors SmgGDS-607 binding in the presence of FTI-277, perhaps pointing towards a possible mechanism by which some RAS substrates are shunted towards GGTase-1 during alternative prenylation. In contrast, HRAS was shown to putatively favor SmgGDS-558 binding, which prompts enhanced FTase turnover and consequently an increased rate of *S*-farnesylation[81].

Prenylation profiling of the WT and SmgGDS-607 KO lines was thus undertaken in the presence and absence of tipifarnib. Tipifarnib was chosen as an FTI due to its stability, potency and clinical significance[277]. Additionally, the FDA recently granted tipifarnib (Zarnestra) breakthrough therapy designation for the treatment of certain HRAS-driven cancers, such as head and neck squamous cell carcinoma (HNSCC), as HRAS is uniquely susceptible to FTIs compared to other RAS isoforms[278]. Characterizing tipifarnib activity in the context of other cancers, such as this LUAD (H23) example, may also be useful in furthering the applications of this inhibitor by identifying other sensitive substrates or related biomarkers.

A summary of the prenylation profiling workflow with tipifarnib is outlined in **Fig. 2.2.10,** with results shown in **Fig. 2.2.13.** Aligning *S*-prenylated substrates by CXXX-box sequence reveals a significant level of sequence-recognition by prenyltransferases. Canonically *S*-farnesylated substrates appear to cluster independently from *S*-geranylgeranylated substrates, with a few exceptions. In general, substrates with CXXX motifs ending in -Leu have a stronger preference for *S*-geranylgeranylation, whilst

substrates ending in -Ser or -Met favor *S*-farnesylation[279]. These trends are recapitulated in the literature, where *in vitro* enzymatic studies have largely determined these preferences, as opposed to global cellular studies. Exceptions found in this study include RALA (CIIL) and RALB (CCIL), where there remains some level of YnF-enrichment. Additionally, substrates ending in -Phe, such as RRAS2 (CVIF), seemed to exhibit no strong preference for either modification.

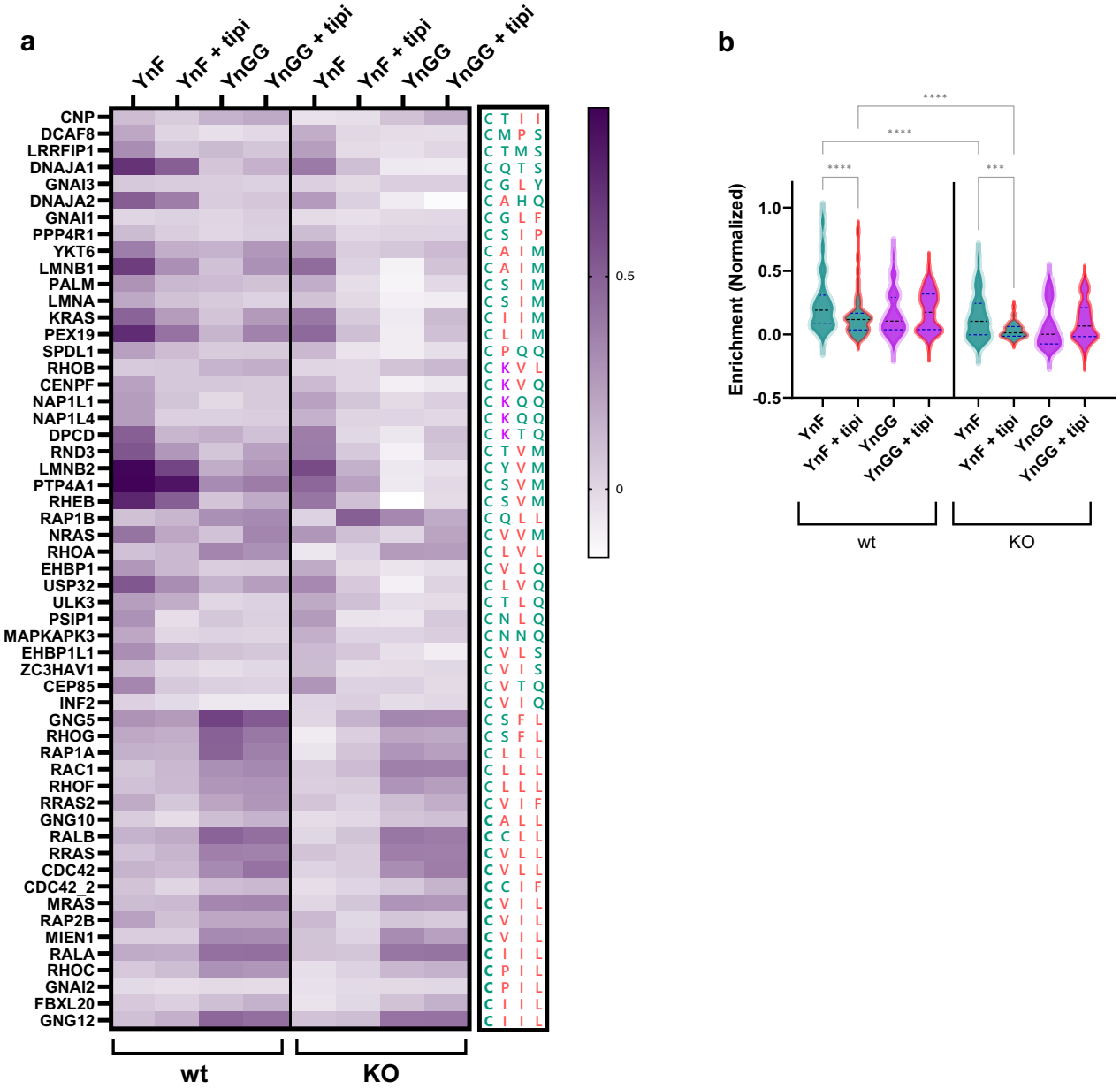

Figure 2.2.13. Effect of tipifarnib on YnF and YnGG incorporation in WT and SmgGDS-607 KO cell profiling experiments. (a) Heatmap depicting fold-change [log_2(fold-change)] in YnF and YnGG mediated enrichment in WT and KO cell lines. Only high-confidence *S*-prenylated substrates are shown here. Proteins were aligned by CXXX-box sequence using ClustalOmega alignment algorithm. Basic amino acids are shown in magenta, small hydrophobic residues in red, and hydroxyl, sulfhydryl, amine (incl. glycine) are shown in green. **(b)** Violin plot showing mean distributions (normalized enrichment values, unit vector) of main treatment categories. Significant difference in mean distribution were found between WT (YnF vs. YnF + tipifarnib), KO (YnF vs. YnF + tipifarnib), YnF (KO vs. WT) and YnF + tipifarnib (KO vs. WT). one-way ANOVA (**** $p \leq 0.01$, **** $p \leq 0.001$).

Traditionally, prenyltransferase substrate preference was mainly attributed to X_4, however in more recent years the field has shown that the entire CXXX-motif can be involved in dictating substrate selectivity[280]. Other studies have also attributed prenyltransfrase preference to stem from amino acids immediately upstream of the CXXX-box, such as the hypervariable region (HVR) of RAS proteins[29]. However, this and other similar global profiling studies have revealed discrepancies that are not easily explained by amino acid preference alone, particularly in the case of alternative prenylation. NRAS (CVVM) and KRAS (CIIM/CVIM) reliably switch to *S*-geranylgeranylation in the presence of an FTI (e.g. tipifarnib), as demonstrated here[52]. PEX19 (CLIM), LMNB1 (CAIM) and RND3 (CTVM) also exhibited some level of 'switching' ability. On the other hand, other substrates ending in -Met, such as PTP4A1 (CSVM), do not appear to switch. HRAS (CVLS) was unfortunately not quantified across the experiment, however it is known to have exclusivity for FTase and does not undergo alternative prenylation[184]. Similarly, other substrates ending in -Ser do not exhibit switching behavior. As demonstrated here and elsewhere, it remains likely that some factors for alternative prenylation lie in CXXX preference for specific prenyltransferases. However, the more subtle differences, as well as some discrepancies, observed in global profiling experiments indicate that other factors may be at play.

The role SmgGDS-607 plays in global *S*-farnesylation is also recapitulated by one-way ANOVA analysis (**Fig 2.2.13b**), where the mean fold-change distribution of high-confidence *S*-prenylated substrates was compared across conditions. The most significant changes were found to be between WT and KO YnF-labelled samples, and

between DMSO and YnF-treated samples within each cell line. Differences in YnGG distributions did not meet the significance cut-off ($p \leq 0.001$), which is in line with the other discussed interpretations of this dataset.

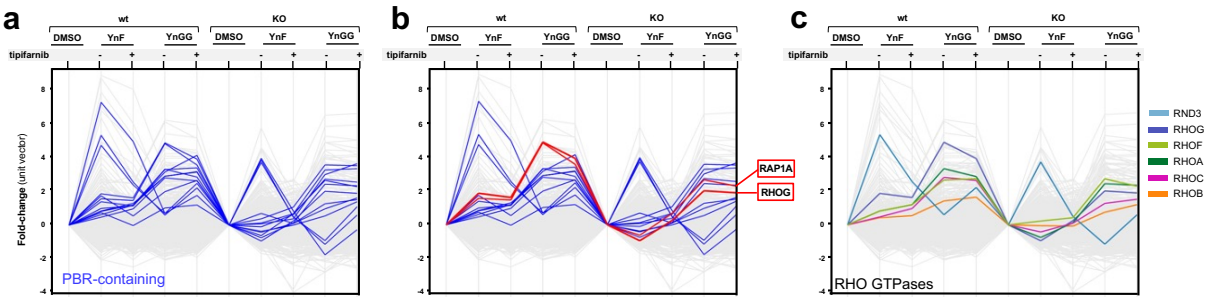

Figure 2.2.14. Global profiling of PBR-containing GTPases and RHO GTPases. Profile plots highlighting YnF and YnGG-enrichment of **(a)** PBR-containing proteins, **(b)** RAP1A and RHOG, which were found to be differentially enriched between WT and SmgGDS-607 KO cell lines and (c) all quantified RHO GTPases (n=3).

Other PBR-containing substrates were investigated for SmgGDS-607 KO induced changes in *S*-prenylation status. RAP1A and RHOG, which were found to be differentially enriched between WT and KO profiling experiments, showed lower levels of both *S*-farnesylation and *S*-geranylgeranylation (**Fig. 2.2.14a**). Other RHO GTPases exhibited a similar trend (**Fig. 2.2.14b**). In contrast, enrichment of other *S*-geranylgeranylated substrates using YnGG, such as RAB proteins, remained largely unchanged across all conditions. This may indicate that SmgGDS-607 facilitates *S*-geranylgeranylation of specific substrates, while it plays a more global role in *S*-farnesylation. SmgGDS-607 could thus harbor a target preference, determined by substrate sequence or localization, in chaperoning RAS and RHO small GTPases specifically. Alternatively, SmgGDS-607 may not shuttle proteins that are substrates of RABGGTase. Further studies, such as immunoprecipitation (IP) experiments using SmgGDS as a bait protein, would be required to establish such an effect. From a biological perspective, an increase in the 607:558 ratio would then specifically drive prenylation of RAS and RHO GTPases and enhance cell proliferation of RAS-addicted cancers, where higher ratios are typically found, whilst RAB proteins may hold a more minor role in this.

However, SmgGDS-607 does not appear to have a direct role in alternative prenylation; KRAS and NRAS remain able to switch prenylation status in the presence of tipifarnib upon KO of SmgGDS-607 (**Fig 2.2.13a** and **2.2.15**). Here, ALDH9A1 was used as a convenient internal control between the cell lines, as its modification by YnF is not mediated by prenyltransferases (**Fig. 2.2.15b**).

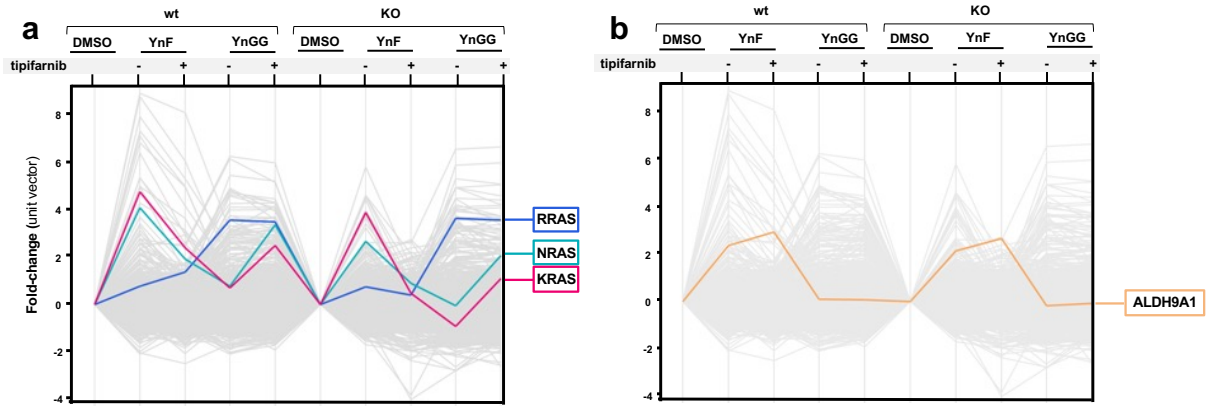

Figure 2.2.15. Global profiling of RAS alternative prenylation. Profile plots highlighting YnF and YnGG-enrichment of **(a)** KRAS, NRAS and RRAS2, which under alternative prenylation in the presence of tipifarnib (100 nM). **(b)** ALDH9A1 was selected as an internal control, since its modification by YnF is uniquely not FTase-dependent.

Tipifarnib sensitivity was thus evaluated at the global level to both rank *S*-prenylated substrate sensitivity and to discern whether SmgGDS-607 plays a role in determining this. Moreover, if a substrate of interest is made more sensitive to tipifarnib by SmgGDS-607 KO, this may point to a synergistic therapeutic strategy.

YnF-enrichment experiments were then compared to corresponding tipifarnib-treated samples (**Fig. 2.2.16a**). This revealed the most sensitive substrates in WT and KO samples. KRAS was shown to be the most sensitive substrate in WT and KO cell lines alike, and PEX19, LMNAB1, LMNAB2, DNAJA1 and USP32 exhibited comparable sensitivity. Overall, the level of observed sensitivity was obscured by the low-level of YnF incorporation in the KO cell line. This is also compounded by the lower significance values, as potential clonal effects, caused by the pooling of CRISPR KO cells, could have

hampered reproducibility. Thus, a regression analysis was performed with the normalized log_2FCs (YnF – YnF + tipifarnib) of each cell line, where ALDH9A1 intensity was used as the cut-off value for sensitivity (**Fig. 2.2.16b**). KRAS was found to be more sensitive to tipifarnib in the KO cell line, however this change in sensitivity may not be biologically significant. Other substrates shown to be more sensitive in the KO line are shown in the residual plot in **Fig. 2.2.16c**, where values outside the established cut-off values were deemed differentially sensitive across the two cell lines.

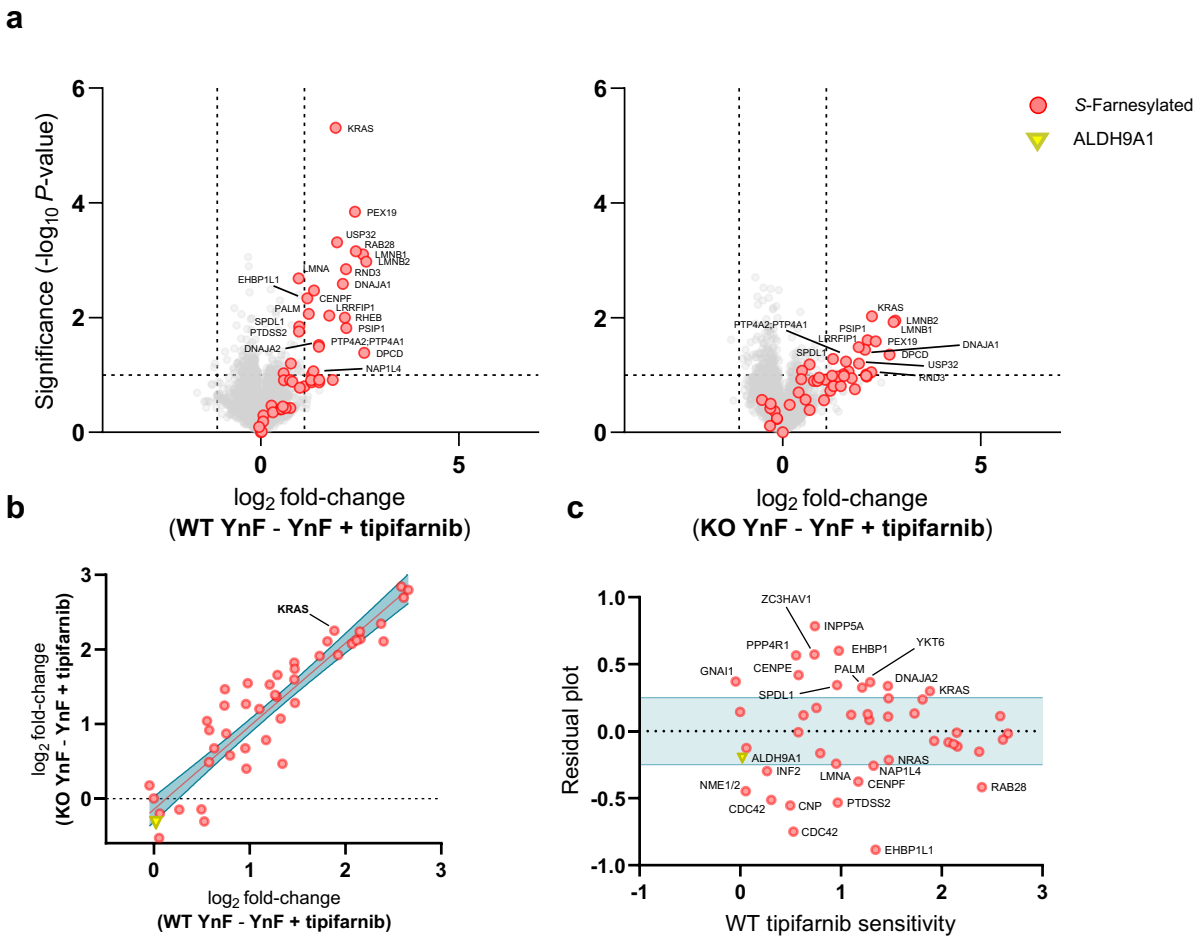

Figure 2.2.16. Evaluation of tipifarnib sensitivity across WT and SmgGDS-607 KO cell lines. **(a)** volcano plots depicting tipifarnib-sensitive substrates in WT and KO cell lines. *S*-farnyeslated substrates are highlighted in red. (student's t-test; FDR = 0.05, S0 = 0.1) **(b)** Regression analysis of tipifarnib sensitivity (defined here by log_2FC [YnF - YnF+tipifarnib]). Proteins falling outside the blue area are differentially sensitive. Residuals are plotted in **(c)** where ALDH9A1 was used to define threshold for differential sensitivity.

Proteins such as INPP5A, ZC3HAV1, PPP4R1 and EHBP1 were found to be more sensitive upon SmgGDS-607 KO. Though few conclusions can be drawn from this dataset in isolation, some of these hits may hold significance. For instance, ZC3HAV1, a PARP family protein, was recently found to be upregulated in KRAS-addicted cancers and can positively regulate its expression. Tipifarnib combined with an SmgGDS splice switching strategy could be hypothesized to synergize with other KRAS-directed treatments in this context[281]. However, orthogonal validation of any of these sensitivities is required to fully establish this effect. Significant differences in enrichment of these substrates between KO and WT lines should be determined by Western blot, for example, as well as potentially a tipifarnib dose-response proteomic study in KO and WT cell lines. A small set of substrates were initially chosen for Western blot validation. However, the antibodies selected necessitated substantial optimization, which has yet to be completed due to time constraints. As a result, the validation process for these substrates is still ongoing.

2.2.8. Deep proteome analysis of H23 WT and SmgGDS-KO cell lines

Whole proteome analysis was deemed necessary to establish clonal differences in the cell lines at hand, as well as to determine if any proteins of interest, namely *S*-prenylated substrates, change abundance upon SmgGDS-607 KO. This would, importantly, instill greater confidence in our established global prenylation profiling strategy, as the differences in enrichment observed in the aforementioned probe experiments could be attributed to the role SmgGDS-607 in regulating prenylation dynamics, rather than clonal differences in the cell lines induced by CRISPR KO, or actual changes in protein abundance attributed to the KO.

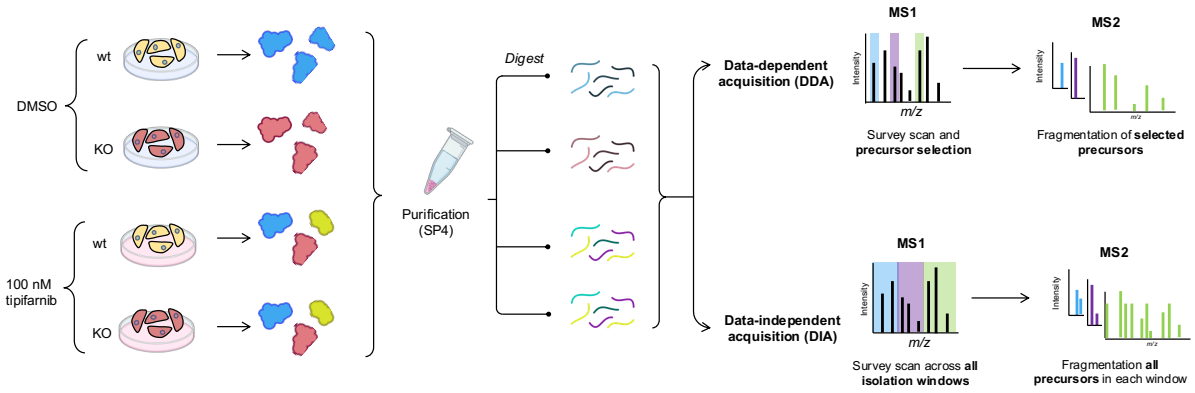

Figure 2.2.17. Workflow for deep proteome profiling of tipifarnib-treated WT and SmgGDS-607 KO cell lines. Treatment strategy and sample processing workflow for whole proteome analysis. SP4 is used to purify lysates and samples are split between data-dependent acquisition (DDA) and data-independent acquisition analyses for benchmarking new approaches to deep proteome profiling in the Tate Group.

Thus, a deep proteome analysis workflow was devised, where the effect of tipifarnib was also evaluated (**Fig. 2.2.17**). Two whole proteome strategies were undertaken in order to account for the Tate Group's transition from data-dependent acquisition (DDA) to data independent acquisition (DIA). In brief, DDA approaches are more traditional and offer broad protein coverage. However, DDA submits only a selection of peptides (precursors) for MS2 fragmentation, whilst DIA submits all generated peptides. While easier to set-up and less computationally intense to analyze, DDA offers less reproducibility, and low abundance peptides are often under-represented. As a result, DIA workflows can benefit from greater accuracy with respect to protein quantification[282].

Whole proteome samples were generated from the above outlined conditions and split between DDA and DIA MS acquisition workflows. Dr. Jack Houghton carried out sample runs and data acquisition, as well as spectral library generation for DIA analysis.

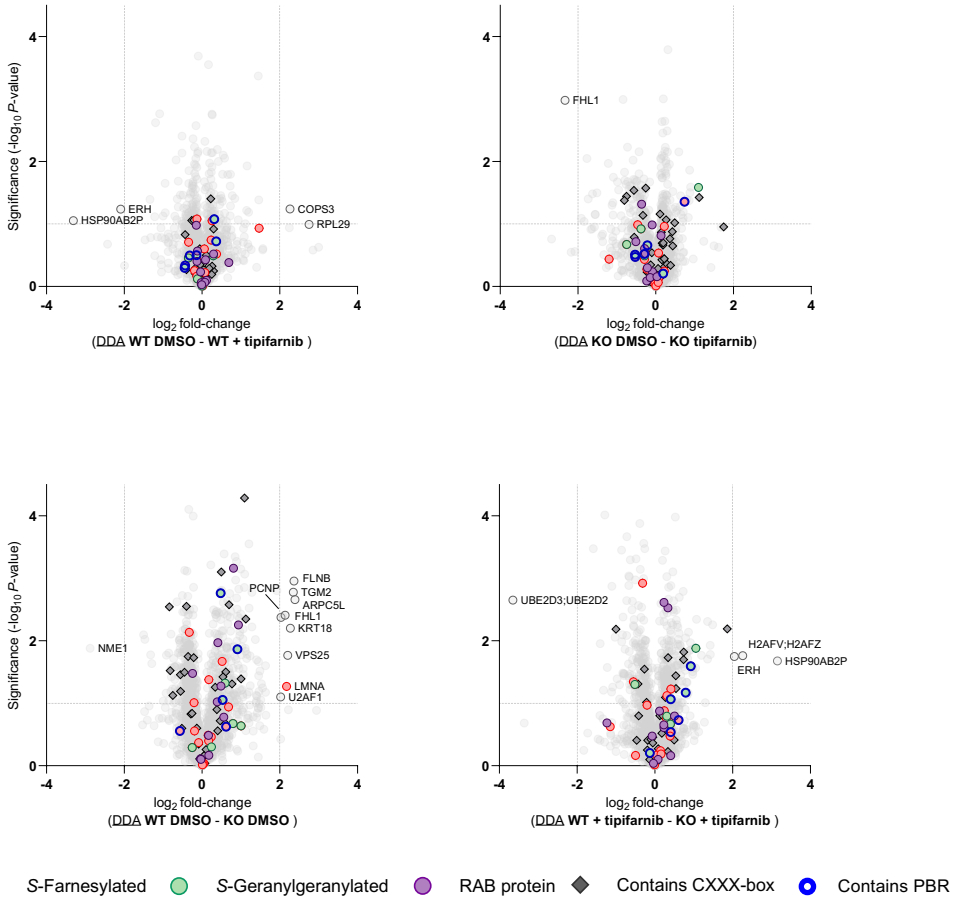

Figure 2.2.18. Whole proteome DDA analysis of H23 WT and SmgGDS-607 KO cell lines in the presence and absence of tipifarnib. Volcano plots showings minimal changes between WT and KO whole proteomes both with and without tipifarnib-treatment (two sample student's t-test; S0 = 0.1, FDR = 0.05, n=3). Substrates are highlighted according to the provided legend.

DDA analysis did not reveal significant changes in in tipifarnib-treated samples apart from COPS3, RPL29, ERH and HSP90AB2P, none of which have a previously established role in prenylation or prenylation-associated proteins. A two-sample t-test between WT and KO revealed that WT cells have a greater abundance of proteins that are related to focal adhesion (GO:0005925), determined by STRING analysis (FDR = 0.0482). This may be significant, as it is now known that acquired resistance to $KRAS^{G12C}$ inhibitors (e.g. sotorasib) is correlated with increased expression of focal adhesion components such as integrin β4 (ITGB4)[283]. Inhibition of SmgGDS-607 could thus potentially be synergistic with $KRAS^{G12C}$-targeting drugs.

Higher abundance of LMNA in WT cells was also noted, however considering that other prenylated proteins remain unchanged between WT or KO samples, this signifies that the overall trend in lower *S*-farnesylation rates observed in probe enrichment studies in SmgGDS-607 KO cells was likely a true finding. Notably, RAP1GDS1 was also not quantified in this study.

DIA analysis was then carried out using the same peptide samples from the previous DDA experiment (**Fig. 2.2.19**).

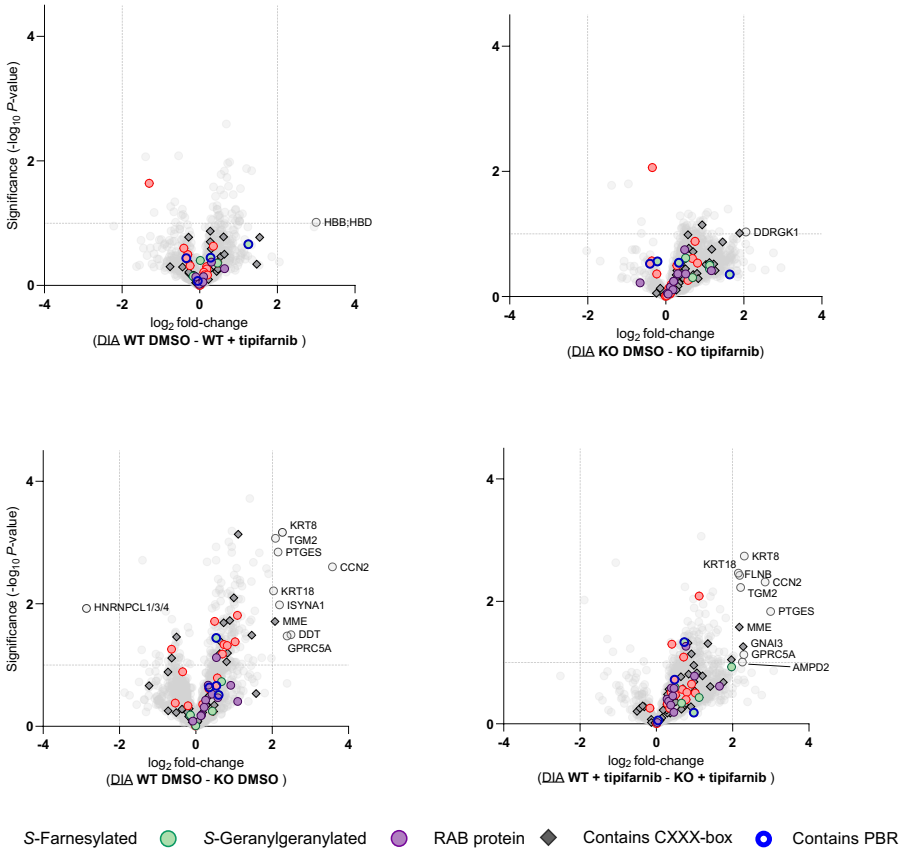

Figure 2.2.19. Whole proteome DIA analysis of H23 WT and SmgGDS-607 KO cell lines in the presence and absence of tipifarnib. Volcano plots showings minimal changes between WT and KO whole proteomes both with and without tipifarnib-treatment (two sample student's t-test; S0 = 0.1, FDR = 0.05, n=3), recapitulating DDA results. Substrates are highlighted according to the provided legend.

The DIA approach identified a total of 1228 more proteins across the experiment (2925 versus 1697 proteins identified using DDA). While this did indicate some improvement over DDA, this was somewhat obscured by the fact that our MS equipment was not optimally functioning at this time, meaning that ID rates in both DIA and DDA were below the standard. Nevertheless, similar conclusions were drawn by DIA analysis – namely that the majority of *S*-prenylated substrates are not differentially enriched in any of the tested conditions. RAP1GDS1 was also identified in this study, and while more abundant in the WT cell line, it did not meet the significance threshold. STRING analysis of substrates that were more abundant in WT cells revealed that the extracellular exosome and extracellular space were enriched GO:cell compartment terms (GO:0070062, GO:005615; FDR = 0.0286). Again, this may indicate that SmgGDS-607 KO has a larger effect on exosome release into the extracellular matrix. The corresponding DDA enriched GO term (i.e focal adhesion) alluded to a proteome change in the junction that anchors cells to the extracellular matrix, of which that protein population has significant overlap with those involved in exosome release (Appendix Fig. **7.5**). However, extensive orthogonal methods are required to substantiate these putative findings and any true biological effect as a result of these differences.

It is perhaps worth noting that regression analysis of corresponding DDA and DIA samples (Appendix Fig. **7.6**) reveal better quantification of *S*-prenylated substrates using DIA. Because the aforementioned statistical analysis revealed no significant enrichment of *S*-prenylated substrates *within* the DDA and DIA datasets, it can be said that DIA is a more reliable workflow to *S*-prenylated protein identification in whole proteome studies. Going forward, DIA would remain the favored workflow in these contexts.

2.2.9. Cell fractionation (membrane-enrichment) to study the influence of tipifarnib and SmgGDS-607 KO on protein localization.

Global prenylation profiling can provide valuable insights into changes in prenylation dynamics in the context of specific perturbations, such as the protein KO (i.e. SmgGDS-607) and drug treatment (tipifarnib) approaches outlined in this chapter. However, enrichment strategies required for such profiling experiments can prove difficult to scale

up or adapt to high-throughput workflows, including those investigated in this thesis (i.e. KingFisher). Moreover, probe incorporation itself can be a bottleneck in the success of these experiments, as not all cell types can reliably uptake YnF and YnGG to a sufficient degree[52]. This may be a consequence of low expression of the enzymes required for phosphorylation of the farnesol and geranylgeraniol moieties as part of the prenyl salvage pathway, which is required for metabolic incorporation of YnF and YnGG probes. This process remains poorly understood[229]. Alternatively, this could also be due to low endogenous metabolic activity of certain cell types, namely primary cells, or even tissue samples. Statins are sometimes used to deplete endogenous isoprenoid pools and pressure cells to utilize the exogenously given probes, however this can result in severe pleiotropic effects that present as artefacts in the acquired data, such as upregulation of RHO proteins[284–286]. Still, while lipid probe profiling has proven fruitful for many applications, optimizing an alternative strategy for understanding prenylation dynamics would be useful, particularly in the use of FTIs in disease-relevant models and patient samples.

One such strategy is *in vitro* prenylation, where lysates are treated with recombinant prenyltransferases and supplemented with a biotinylated isoprenoid analog. Substrates containing prenylation motifs that are found to be not prenylated in the sample (usually due to an experimental perturbation), are then re-prenylated with the biotin analog by the exogenously given machinery[37]. The biotin moiety is then used to enrich re-prenylated substrates for MS or gel-based analysis. This allows deconvolution of substrates that are sensitive to perturbations to prenylation, as this method only reveals substrates that are not prenylated. This also ideally requires a pre-existing knowledge of proteins that are normally prenylated and is not as suitable for the discovery for new substrates. Additionally, because the recombinant prenyltransferases utilized in the assay are mutated to enhance uptake of the isoprenoid analog, this strategy can be relatively inelegant and may not capture the prenylated proteome to a sufficiently biologically relevant degree. Importantly, this protocol still requires an enrichment step that is not currently easily amenable to high-throughput workflows, although work is being

undertaken to improve the use of magnetic bead enrichment, as discussed earlier in the chapter.

Another possible alternative to probe-based labelling is cell fractionation[287,288]. Cell fractionation, resulting in a membrane-enriched fraction, would allow the deconvolution of substrates that partition in and out of membranes as a result of some kind of perturbation; for example, when prenylated proteins delocalize from membranes in the presence of tipifarnib. While this method would not enable a direct differentiation between *S*-farnesylated and *S*-geranylgeranylated substrates, it can be inferred that substrates affected by FTIs would largely be *S*-farnesylated. Furthermore, membrane-enrichment would also enable the study of the localization fate of all proteins affected by FTIs, either directly or indirectly. It is plausible that some *S*-prenylated substrates that are also *S*-palmitoylated, for instance, remain on the plasma membrane or endomembranes to some extent. This would be useful in understanding which FTI-sensitive proteins contribute to certain phenotypes upon the use of FTIs such as tipifarnib, which exhibits dose-limiting toxicities in primary cell models and patient samples, but not demonstrated in immortalized cell lines.

Importantly, cell fractionation does not require the use of probes or bead-based enrichment (**Fig. 2.2.20a**). Instead, cells are lysed using Triton X-114 (TX114), which produces a homogonous lysate at 0°C[287,288]. Above the cloud point of TX114 (20°C), which is the temperature at which a homogenous solution undergoes phase separation, micellar aggregates develop and separate out into two clear phases, with the separation peaking at around 37°C. Cytosolic proteins partition to the top aqueous fraction while membrane-associated proteins are enriched in the bottom hydrophobic fraction. The membrane fraction is then isolated and washed several times to ensure effective removal of cytosolic proteins, and the two fractions are carried forward to detergent removal and proteomic processing. In this case, the fractions are purified by SP4 to remove all traces of TX114 ahead of subsequent reduction, alkylation, and tryptic digest. Resulting peptides are then analyzed by MS-DIA workflows.

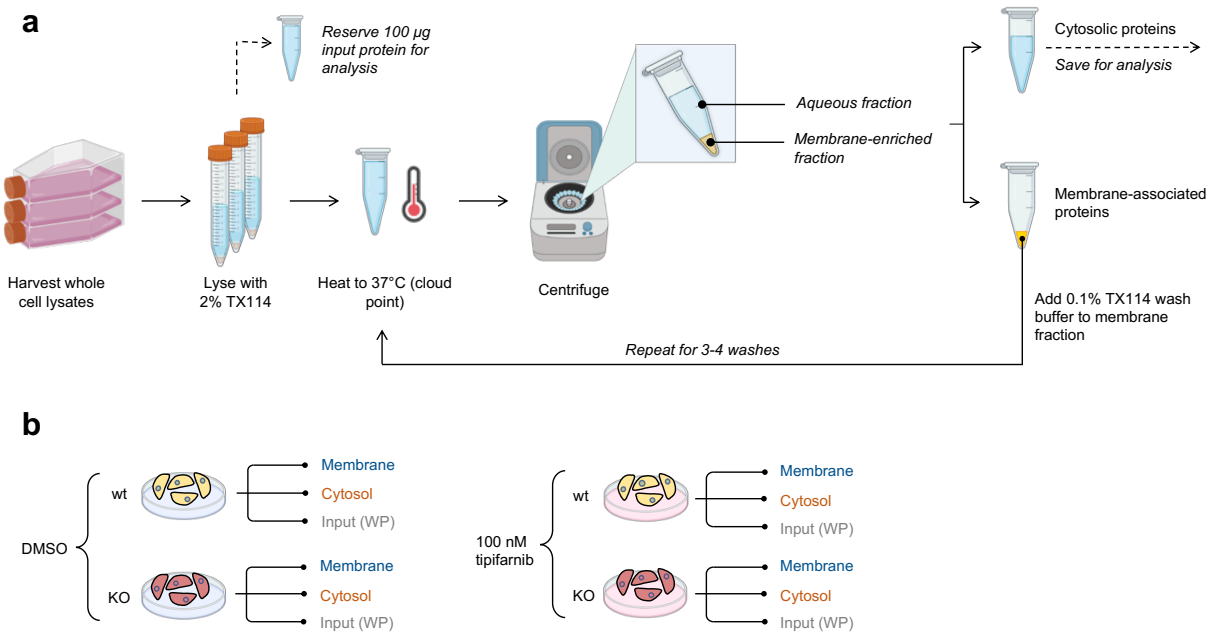

Figure 2.2.20. Cell fractionation as a probe-free alternative to profiling *S*-prenylation dynamics. (a) General schematic of workflow for cell membrane fraction. Cells are pelleted, lysed with 2% TX114 and heated to 37°C to allow for phase separation. Centrifugation forms two distinct phases, with membrane-associated proteins enriched in the lower, detergent phase. Cytosolic proteins are reserved for analysis, whilst the membrane-fraction is washed further to enhance enrichment. Samples are later purified by SP4, digested and analyzed by DIA-MS methods. **(b)** Experimental design of membrane-fractionation experiment. WT and KO cells are treated with tipifarnib (100 nM) or vehicle (DMSO) overnight in triplicate. Samples are harvested the following day for fractionation.

An experiment similar to the whole proteome setup described in the previous section of this chapter was devised, where two parameters were evaluated: a) the ability of SmgGDS-607 to cause membrane delocalization of binding partners and b) the ability of tipifarnib to cause membrane delocalization of *S*-farnesylated substrates (**Fig. 2.2.20b**). Whole proteome (WP), cytosolic and membrane-enriched fractions were produced in triplicate for each condition, and processed for M-analysis. Dr. Jack Houghton carried out sample MS runs and data acquisition, as well as spectral library generation and searching for DIA analysis.

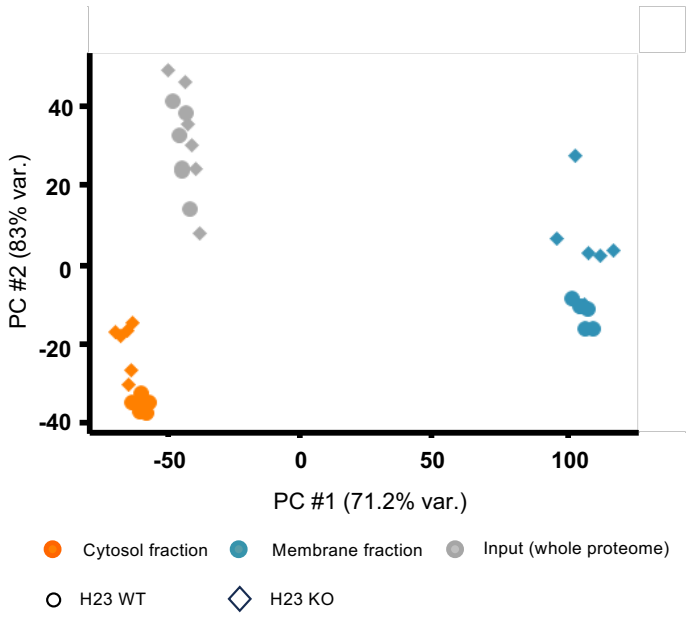

Figure 2.2.21. Principal component analysis (PCA) of whole proteome, cytosolic membrane-enriched fractions. PCA of 36 samples in H23 cell fractionation experiment. Input (whole proteome, grey), cytosolic (orange) and membrane-enriched (blue) fractions cluster independently. Sub-clustering of WT (circle) and KO cells (diamond) was also observed.

An initial principal component analysis (PCA) pleasingly revealed that WP, cytosolic and membrane-enriched fractions clustered together, with subclusters of WT and SmgGDS 607-KO cells also present within the fractions (**Fig. 2.2.21**). This indicated successful and reproducible membrane-enrichment across all the conditions tested. Importantly, annotation and analysis of the enriched protein populations in each fraction would need to be evaluated to verify the efficacy of the fractionation. Thus, STRING (gene ontology) analysis of the proteins enriched in the membrane-associated and cytosolic fractions of WT and KO lines was performed (**Fig. 2.2.22a** and **b**). When looking at cell compartment GO terms (GO:CC), there was highly significant enrichment ($p \leq 0.0001$) of membrane-associated proteins in the membrane-enriched fractions of both cell lines tested, including intracellular organelles and endomembranes. There was also significant GO-term overlap between WT and KO lines, which exhibited the same top ten enriched terms. Corresponding results were found in the analysis of cytosolic fractions, where enriched terms included cytosol, intracellular and nuclear proteins. The overlap between membrane and cytosol-enriched GO-terms, specifically that cytoplasmic proteins were

identified in the membrane-enriched fractions and membrane/organelle proteins were identified in the cytosolic fractions, was not worrying, since GO-terms for proteins can possess multiple compartment annotations, as proteins often change compartments according to various factors, including PTM state. These initial observations indicate that membrane fractionation can be performed reliably with highly significant enrichment of membrane proteins.

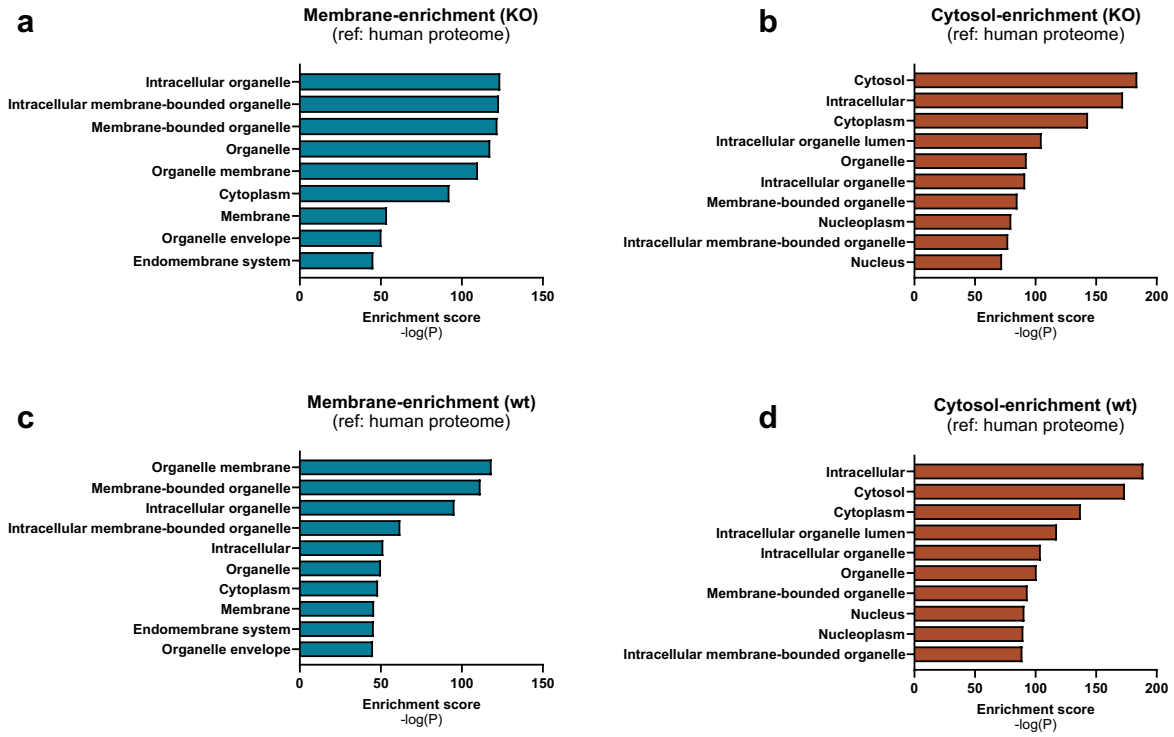

Figure 2.2.22. STRING analysis of membrane-enriched and cytosolic proteins in WT and SmgGDS-607 KO cells. (a, b) KO cellular component overrepresentation analysis, using the STRING whole proteome reference list as a control. **(c, d)** The corresponding analysis performed for WT samples.

Next, two-sample student t-tests (S0 = 0.1, FDR = 0.05) were performed to identify proteins that are significantly enriched in KO and WT cell lines respectively, as well as the effect tipifarnib has on any shifts in protein localization (**Fig. 2.2.23**). Because it is unclear what level of fold-change in a protein's change of localization indicates a significant biological effect, cut-offs were not employed in this preliminary analysis.

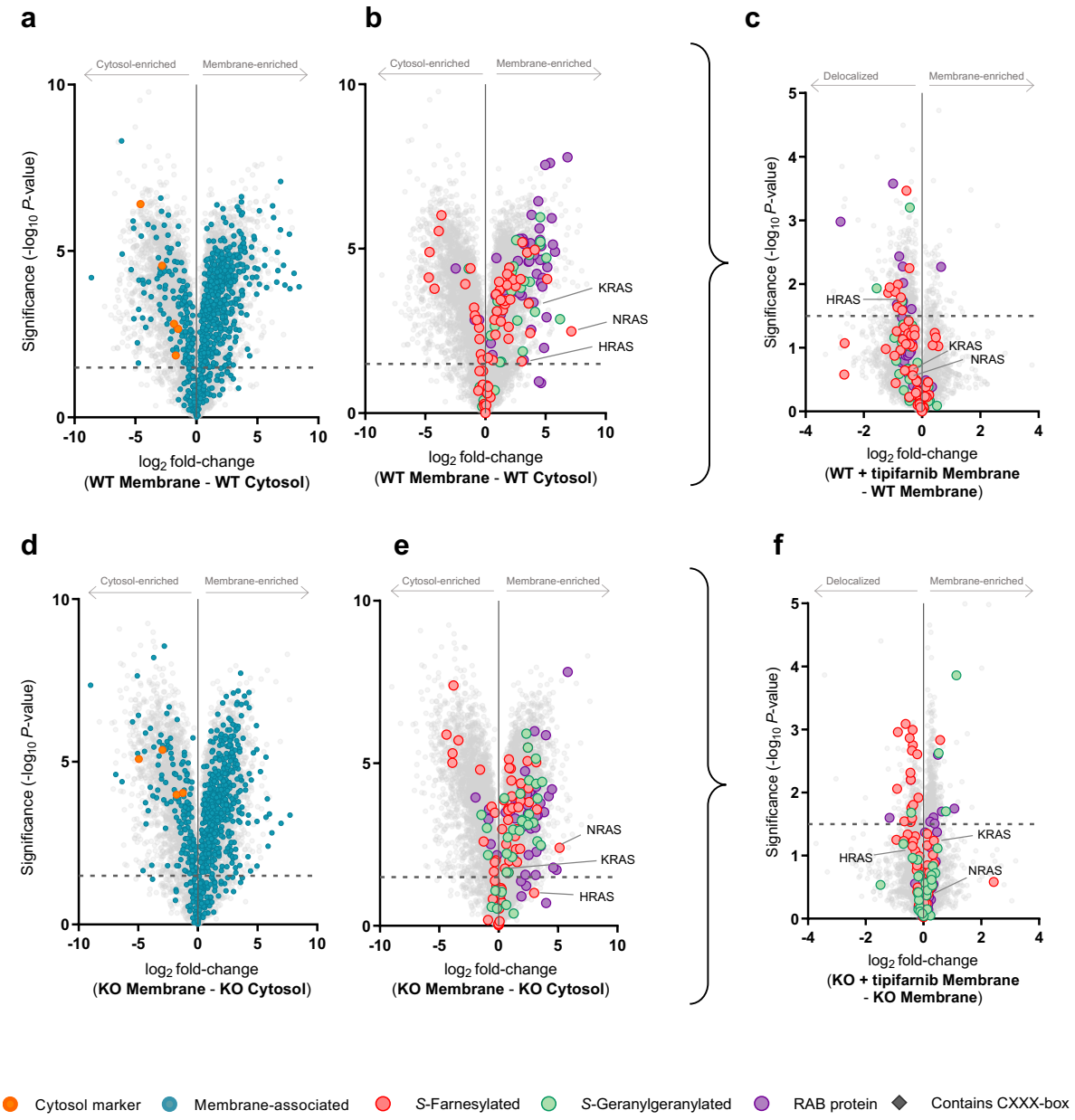

Figure 2.2.23. Membrane-enrichment studies reveal changes in *S*-prenylation dynamics upon tipifarnib treatment. (a) Membrane-enriched fraction compared to cytosol in H23 WT cells. **(b)** highlighting *S*-prenylated proteins demonstrates strong membrane-when compared to cytosol, with few exceptions. **(c)** Shift in *S*-prenylated proteins in the presence of tipifarnib in WT cells, demonstrating that most *S*-prenylated proteins are delocalized upon treatment. Corresponding analyses for SmgGDS-607 KO cells are shown in **(d-f)**. respectively. Substrates are highlighted according to the provided legend.

Analysis of WT membrane fractionation again shows strong enrichment of membrane-associated proteins (annotated using GO:0016020) (**Fig. 2.2.23a**). A set of common

cytosolic markers (GAPDH, BTF3, LDHB and PKM) were chosen over a GO gene set list for cytosolic proteins, as many proteins that are associated with membranes at some point, even contextually, can also be annotated as cytosolic, making it an unreliable annotation for visualizing the efficacy of the fractionation[289].

Annotation of *S*-prenylation revealed that most prenylated proteins were enriched in the membrane fraction, especially RABs and other *S*-geranylgeranylated proteins (**Fig. 2.2.23b**). Expectedly, KRAS, NRAS and HRAS (as well as RRAS and RRAS2) were primarily membrane-associated. Some *S*-farnesylated substrates were found in the cytosolic fraction. This included ALDH9A1, which is known to reside in the cytosol as *S*-farnesylation of the protein is not associated with its localization. Other substrates primarily found in the cytosolic fraction are PEX19, LRRFIP1, BROX and SPDL1.

PEX19 (peroxisomal biogenesis factor 19) is known to be a cytosolic chaperone and has a role in the import of peroxisomal membrane proteins during the formation of peroxisomes[290]. Studies have shown that *S*-farnesylation is required for protein topogenesis and was shown to be dispensable for localization[291]. Thus, PEX19 should be associated more strongly to the cytosolic fraction in this experiment. LRRFIP1 is primarily localized to lysosomes and is only transiently membrane associated[292,293]. BROX (BRO1 Domain and CAAX Motif Containing) is localized to perinuclear condensates, which are expectedly captured in the cytosolic fraction[294]. *S*-farnesylation of SPDL (Spindly-like protein) enables its localization to the kinetochore during mitosis and is not known to readily partition to membranes[295]. RAB proteins, in contrast, are more ubiquitously associated with membranes and endo/exosomes, as was recapitulated in these results[234]. Thus, the presence of these proteins in the cytosolic fraction demonstrates that membrane fractionation is both useful as a standalone experiment, as well as highly complementary to probe-labelling experiments, as it effectively reveals whether *S*-prenylation always leads to membrane-association or not. However, a limitation of this analysis lies in the lack of resolution of the membrane-enriched fraction. That is, it remains unclear whether a protein, for example, resides on an endomembrane

rather than the plasma membrane, which can have significant consequences on downstream signaling and overall biological function.

Comparing the tipifarnib-treated membrane-enriched fractions to the corresponding DMSO control in WT cells reveals which substrates are delocalized from membranes as a result of FT inhibition (**Fig. 2.2.23c**). Expectedly, HRAS was more abundant in the untreated membrane fraction, indicating that it delocalizes from the membrane upon tipifarnib treatment. Again, this is in congruence with the literature on HRAS. KRAS and NRAS are surprisingly shifted towards the untreated membrane as well, albeit less so, despite their ability to undergo alternative prenylation in the presence of tipifarnib. However, it is unclear how significant this shift is from a biological standpoint, as the datapoints were found below the p-value cut-off. It can, for instance, be hypothesized that *S*-geranylgeranylation is a less effective anchor for these RAS proteins, or that their subcellular distribution changes upon prenyl switching, meaning they localize to other membranes not as well represented in this dataset. This could be significant in identifying novel, synergistic vulnerabilities of KRAS and NRAS afforded by tipifarnib treatment due to alternative prenylation. However, further studies on the subcellular localization and interactomes of these proteins in the presence of tipifarnib are required to establish this, which is explored further in later chapters.

Proteins that were shown to persist in tipifarnib-treated membrane samples were ALDH9A1, BROX and CENPE (centromere-associated protein E), which plays a similar role in kinetochore organization as SPDL[296]. Interestingly, RABs and other *S*-geranylgeranylated substrates were also shifted towards the untreated membrane fraction, potentially indicating that the pharmacological inhibition *S*-farnesylation also has a downstream effect on either the biosynthesis of isoprenoids, translocation of these substrates to their membranes, or a downregulation of endosome/exosome formation, where RAB proteins primarily function. Probe-based global *S*-prenylation profiling revealed relatively minimal effects of tipifarnib-treatment on *S*-geranylgeranylated proteins. However, if tipifarnib does indeed influence the biogenesis of endogenous isoprenoids, for example, this would be offset by probe addition in those experiments.

Moreover, these proteins may well be *S*-geranylgeranylated to the same degree with and without tipifarnib, but may not make it to their cognate membranes due to unknown downstream effects brought about by tipifarnib.

Results of the same experiment in SmgGDS-607 KO cells were found to be comparable to the findings from WT cells (**Fig. 2.2.23d**). The same set of *S*-farnesylated proteins (ALDH9A1, PEX19, LRRFIP1, BROX and SPDL1) were also enriched in cytosolic fractions, while RABs and other *S*-geranylgeranylated substrates were more strongly enriched in the membrane fraction (**Fig. 2.2.23e**). KRAS appeared to be less strongly associated to the membrane in the KO cells compared to the WT, however it is unclear how significant this change is. Upon tipifarnib-treatment, KRAS, NRAS and HRAS overall behaved similarly to the WT cell line, which is recapitulated in probe-labelling experiments (**Fig. 2.2.23f**).

When visualizing tipifarnib-sensitivity by fold-change (log_2FC) when compared to DMSO controls, the most sensitive *S*-farnesylated substrates in the WT line were DNAJA4 (DnaJ homolog subfamily A member 4), GNG11 (G Protein Subunit Gamma 11), RHEB (Ras homolog enriched in brain) and HRAS (**Fig. 2.2.24a**). Notably, GNG11, DNAJA4 and HRAS were not identified by the previous probe-labelling experiments outlined in this chapter, therefore it is uncertain to what extent this can be attributed to loss of *S*-farnesylation directly. Strikingly, DNAJA4 exhibited the most extreme difference in tipifarnib-sensitivity between WT and KO cell lines, where it was found to be the least sensitive *S*-farnesylated substrate in KO cells (**Fig. 2.2.24b**). This effect persisted even when normalizing the fold-change to ALDH9A1 (**Fig. 2.2.24c**).

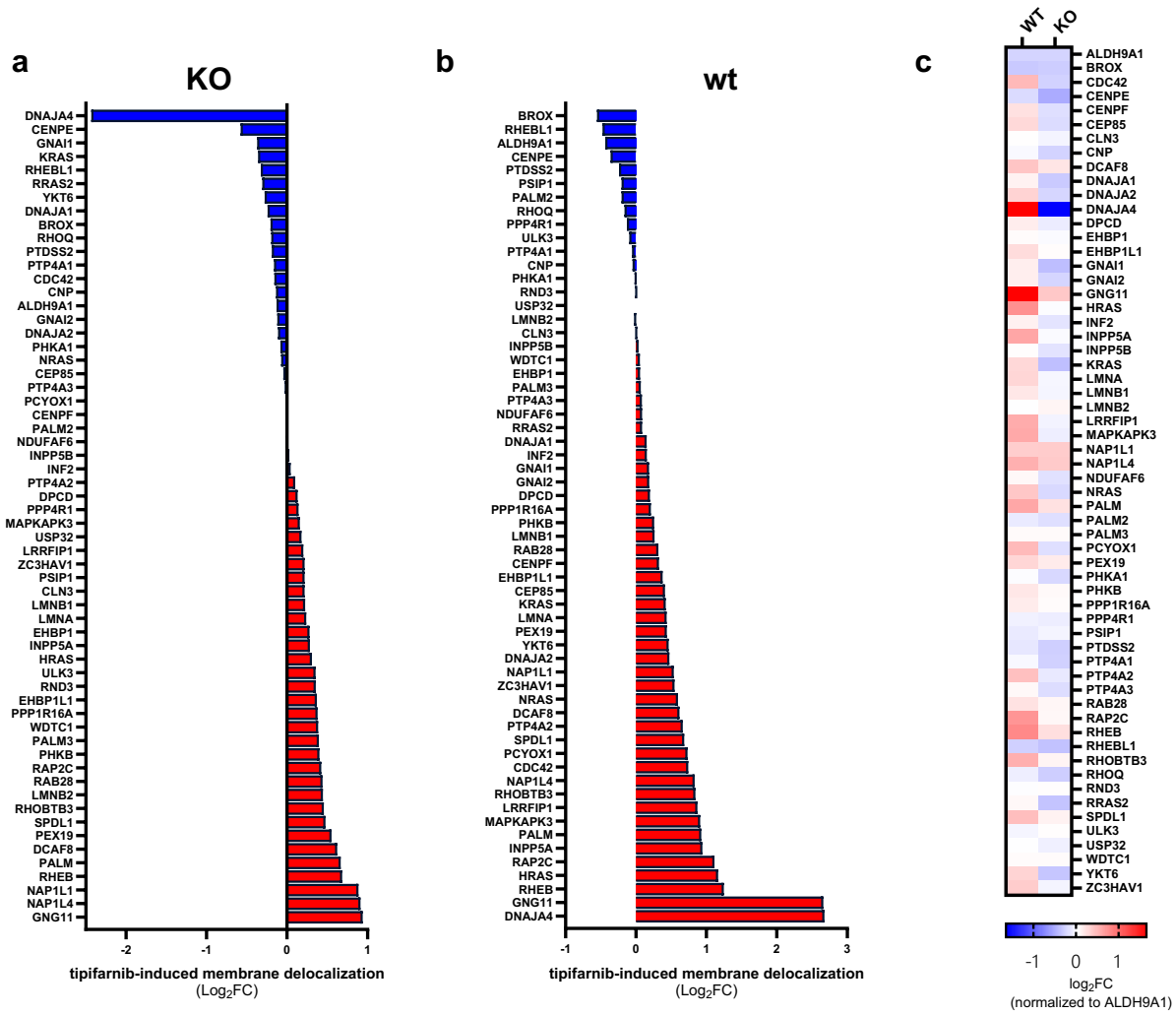

Figure 2.2.24. Tipifarnib-sensitivity as a function of membrane delocalization of *S*-farnesylated substrates. *S*-farnesylated substrates ranked according to their degree of membrane delocalization [log_2FC (Membrane DMSO- Membrane tipifarnib)] for **(a)** SmgGDS-607 KO and **(b)** WT H23 cells. **(c)** Heatmap showing direct comparison of tipifarnib-sensitivity of *S*-farnesylated substrates, normalized to ALDH9A1.

DNAJA4

DNAJA4 is a member of the heat shock protein (HSP40) family that play crucial roles in protein folding and stability, particularly in stres*S*-induced conditions. DNAJA4 was not identified previously in global prenylation experiments and is potentially a novel *S*-prenylated protein, with its modification likely being *S*-farnesylation due to its sensitivity to tipifarnib under WT conditions (CXXX = CQTA). Although DNAJA4 has not been well-

studied in the context of prenylation, it was found to have uncharacteristic roles in regulating cholesterol biosynthesis. Interestingly, DNAJA4 was shown to increase HMG-CoA reductase activity when sterol availability is low. HMG-CoA reductase is the rate-limiting enzyme in the mevalonate pathway and consequently in the biosynthesis of isoprenoids[297–299]. Perhaps in the presence of tipifarnib, DNAJA4 is unable to trigger HMG-CoA reductase activity, resulting in lower availability of endogenous geranylgeranyl for the modification of RABs and other GGTase substrates. In this way, *S*-prenylation of DNAJA4 may function as a novel metabolic marker for lipid biosynthesis. This somewhat supports the hypothesis put forth earlier in this section, where tipifarnib has potentially has an indirect effect on isoprenoid biosynthesis and is echoed by the slight delocalization of *S*-geranylgeranylated substrates demonstrated in this study, the effect of which is offset and camouflaged by the addition of exogenous probes. KO cells could conceivably have an overall lower requirement for the production of isoprenoids, as lower global *S*-farnesylation was demonstrated. Thus, DNAJA4 may play a comparatively minor role in regulating isoprenoid biosynthesis in KO cells, which is somewhat reflected by its lower sensitivity to tipifarnib (using probe-based incorporation as the metric in this context). However, it is unclear exactly what role DNAJA4 plays in KO cells, and further studies are required to elucidate its function as a regulator of isoprenoid biosynthesis. Lipidomic and metabolomic studies, for example, may be useful in achieving this, where the production of endogenous isoprenoids could be monitored in a DNAJA4 KD or KO model, or when DNAJA4 is unable to undergo *S*-prenylation.

Overall, tipifarnib-sensitivity was higher in the WT cell line when compared to the KO, which is recapitulated in the findings of the previous global prenylation profiling experiment. This was logical, considering that the actual fold-change of YnF incorporation between DMSO and tipifarnib treated WT cells is greater due to *S*-farnesylation not being as restrained as it is in the KO cell line.

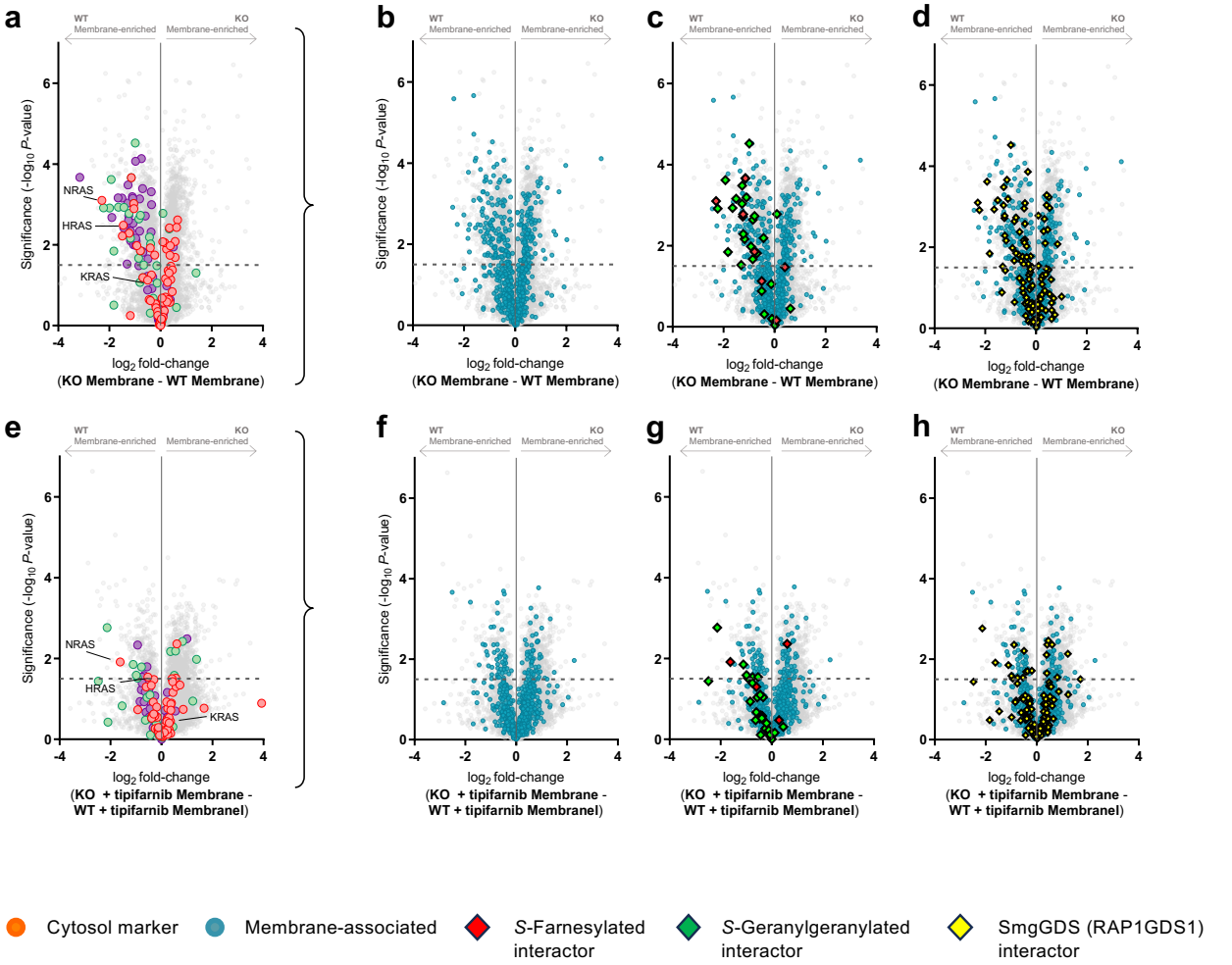

Figure 2.2.25. Membrane delocalization of SmgGDS interactors upon long-form isoform (607) KO. Comparisons of membrane-enriched fractions between H23 WT and SmgGDS-KO cells, showing **(a)** *S*-prenylated substrates, **(b)** membrane-associated proteins, **(c)** *S*-prenylated SmgGDS interactors **(d)** SmgGDS interactors. Corresponding analysis for tipifarnib-treated samples are shown in **(e-h)**, respectively. Substrates are highlighted according to the provided legend. Interactors extracted from BIOGRID.

Differences in membrane-enrichment between the WT and KO cell lines were then investigated (**Fig. 2.2.25a**). Unsurprisingly, KRAS, NRAS and HRAS, as well as RRAS and RRAS2, were more strongly membrane-associated in the WT cell line compared to the KO. However, it was noted that only a subset of other *S*-farnesylated and *S*-geranylgeranylated proteins were more robustly WT membrane-associated. Upon closer analysis it was found that, elegantly, the prenylated proteins that were more enriched in the WT membrane fraction were all known SmgGDS interactors (identified from BIOGRID). When looking at SmgGDS-interactors as a whole, they were more evenly

distributed between WT and KO membrane fractions; notably, the vast majority of interactors that shifted towards the WT fraction were those that canonically *S*-prenylated (**Fig. 2.2.25c** and **d**). When performing the same comparison in the presence of tipifarnib, this observed effect was dampened, however the same trend persisted. PBR-containing substrates are highlighted in the volcano plot in **Fig. 2.2.26a**. Protein fold-changes were also compared in an attempt to quantitatively rank substrates by their responsiveness to SmgGDS-607 KO (**Fig. 2.2.26b)**. RHOG and RAP1A, which were identified to be the most differentially enriched by YnF and YnGG between WT and KO lines, were also among the top-ranking proteins. Non-PBR containing proteins NRAS and HRAS were also found to be enriched in the WT membrane. Although it appears that a PBR may be preferred by SmgGDS-607, it does not appear to be the only criteria for regulated proteins.

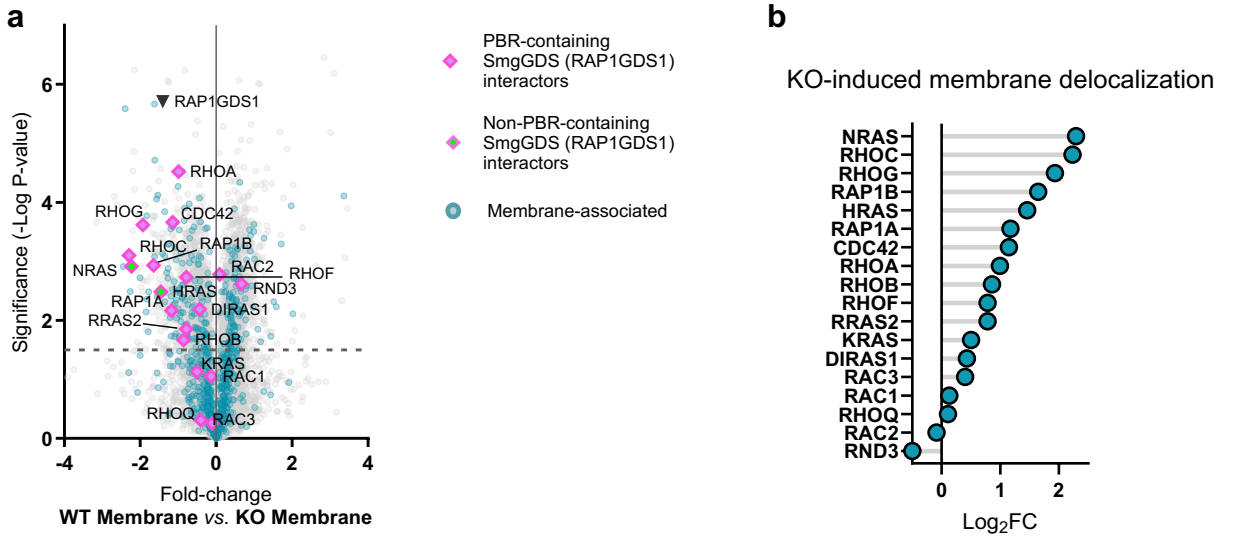

Figure 2.2.26. Membrane delocalization of PBR-containing SmgGDS interactors. (a) Volcano plot highlighting PBR-containing SmgGDS interactors, showing delocalization from membrane upon long-form isoform (607) KO (student t-test, FDR = 0.05, S0=0.1). **(b)** Selected significantly delocalized PBR-containing proteins, ranked by log_2FC (WT vs. KO membrane). Substrates are highlighted according to the provided legend. RAP1GDS1 (SmgGDS) is shown as a black triangle. Interactors extracted from BIOGRID.

In an attempt to deconvolute the effect that SmgGDS-607 has on membrane association more generally, statistical overrepresentation analysis of gene ontology (GO) terms was performed on the substrates that were enriched in the WT membrane fraction when

compared to the corresponding KO sample (**Fig. 2.2.27a**). This revealed that vesicle-mediated transport, endocytosis, protein localization and protein transport were all significantly enriched processes (GO: biological function) in the WT membrane population when compared the KO. When performing background correction using whole-proteome data from this experiment (i.e. all proteins quantified across all fractions, including the input sample), interferon-gamma and other receptor-mediated endocytic responses, as well as RAS signal transduction were upregulated in the WT membrane fraction (**Fig. 2.2.27b**).

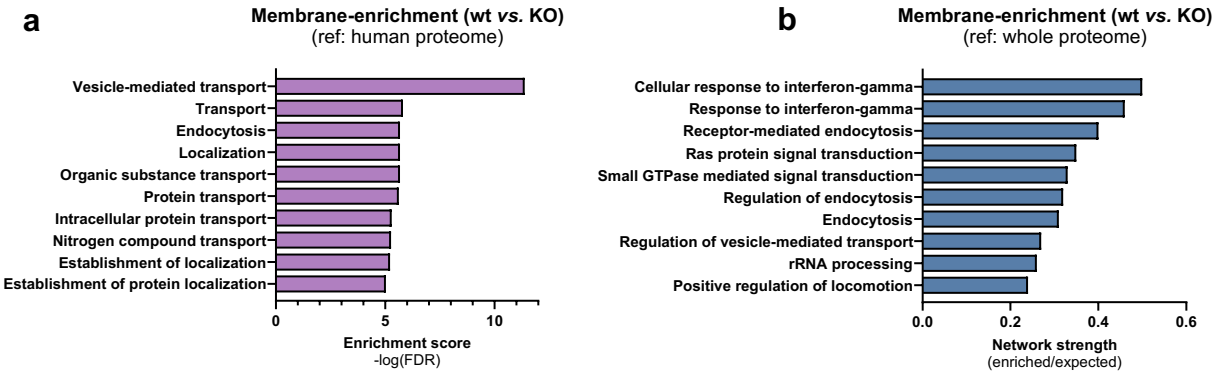

Figure 2.2.27. STRING analysis of proteins enriched in H23 WT membrane fractions. Biological process overrepresentation analysis (performed by STRING) of substrates enriched in WT membranes, compared to the corresponding KO sample. **(a)** shows enrichment against STRING whole human proteome reference list and **(b)** H23 whole proteome list consisting of all proteins identified across the cell fractionation experiment.

Downregulation of interferon-gamma (IFNγ)-specific activation in SmgGDS-607 KO cells may be a significant finding. These results imply that this phenomenon stems from endocytosis, and thereby internalization, of the IFNγ receptor complex (IFNGR), which is initiated by IFNγ-binding[300]. In this case, it is likely that the effect identified by STRING analysis lies in the endocytic component of this process, where RAB and RHO GTPases are known to be key players[234]. Thus, defective *S*-prenylation induced by SmgGDS-607 KO could also lead to attenuated IFNγ-mediated signaling. This may be an important therapeutic advantage in cancers that have high, pathogenic immunogenicity, or more broadly, autoimmune disorders. Relevantly, some studies have shown that IFNγ and RHO inhibitors improve immunogenicity markers of metastatic melanoma, and that statins

appear to emulate this response[301]. Tipifarnib was also previously shown to modulate IFNγ-related signaling and improve outcomes in large granular lymphocytic leukemia, particularly those driven by KRAS and NRAS hyperactivation, although an exact mechanism has not yet been identified[302,303]. SmgGDS-607 KO, either by pharmacological means or by an SSO strategy, could potentially serve as an adjuvant therapy such types of cancer. Further studies are needed to establish and deconvolute this putative effect, as well as to identify the appropriate biomarkers in such cancers.

2.3. Chapter summary and future work

This chapter outlines the development and characterization of an SmgGDS-607 KO system for proteomic profiling, with the aim of uncovering the specific role of this oncogenic splice variant in *S*-prenylation dynamics. Initially, a complex enzyme cooperativity experiment was designed for this purpose, employing dual prenylation probes YnF and YnGG; here, the goal was to discern whether SmgGDS-607 KO functioned as a positive or negative regulator of protein *S*-prenylation by analyzing the dose-dependent incorporation of these probes. However, attempts at this profiling experiment revealed several points of potential optimization, including the use of automation for probe-based protein enrichment, as well as alternative cell lysis and protein purification methodologies. Following systematic benchmarking of these parameters, an optimized protocol was established. This optimized approach enabled highly efficient *S*-prenylated protein profiling in H23 WT and SmgGDS-607 KO cell lines using YnF and YnGG, leading to the identification of 95 canonically *S*-prenylated proteins as well as a selection of novel putative substrates.

Additionally, a proteomic cell fractionation study underscored the value of investigating membrane localization as a complementary method for lipid-PTM profiling. Membrane-enrichment analysis revealed *S*-prenylated substrate delocalization in response to tipifarnib treatment and SmgGDS-607 KO. This demonstrated that known *S*-prenylated SmgGDS interactors were delocalized from the membrane more significantly than other known, non-prenylated interactors. This highlights the role of SmgGDS-607 in the localization of these substrates, as well as pointing to potential therapeutic applications where delocalization of *S*-prenylated SmgGDS 607 interactors is a desired outcome.

Key findings are summarized below.

SmgGDS-607 regulates global *S*-farnesylation and *S*-geranylgeranylation for a selection of small GTPases

Previous studies have putatively shown that SmgGDS-607 KD resulted in reduced rates of global *S*-prenylation. A key finding from this dataset included the observed reduced rate of *S*-farnesylation in SmgGDS-607 KO cells, demonstrated by lower incorporation of YnF, while lower rates of *S*-geranylgeranylation were only shown for a selection of small GTPases (such as RHO family proteins). Interestingly, in a separate experiment, proteomic profiling of membrane-enriched cell fractions indicated that SmgGDS-607 KO also reduced membrane localization of *S*-geranylgeranylated proteins. This was hypothesized to be caused by a reduction in isoprenoid biosynthesis and was not captured in probe-labelling experiments, potentially due to the supplementation of exogenous isoprenoid probes. Delocalization of DNAJA4, a novel *S*-prenylated protein that may have a role in isoprenoid biosynthesis, may also be contributing to this phenomenon. Notably, it is unclear if reduced *S*-farnesylation could similarly be partially attributed to attenuated isoprenoid biosynthesis. Follow-up studies on lipid metabolism would be required to understand this effect, as well as if there is therapeutic merit in these findings.

CXXX-box sequence influences prenylation states, but is not the only determining factor

Upon CXXX-box alignment of YnF and YnGG-enriched substrates, it was demonstrated that while CXXX sequence does influence prenylation state, some exceptions, particularly in the case for alternative prenylation, could not be solely explained by sequence alone. Unfortunately, HRAS was not quantified in this study, which would have been desirable to study in the context of alternative prenylation, as KRAS, NRAS and RRAS2 were all identified and are known to undergo alternative prenylation. Importantly, these all of these RAS proteins bear distinct CXXX-motifs and hypervariable domains (HVDs), and although there is some evidence to suggest that some combination of HVD sequence and the final CXXX amino acid (X_4) contribute to the propensity to switch, it remains likely that other factors play a role in whether a protein can be alternatively prenylated in the presence of FTIs, such as tipifarnib. Identification of other chaperones or interactors that

regulate alternative prenylation, or expose unique vulnerabilities when substrates undergo alternative prenylation, may be a key bottleneck in targeting RAS oncogenicity by way of lipidation. This is explored further in Chapter 5 using proximity-based proteomics to deconvolute the RAS interactome in the presence and absence of tipifarnib.

SmgGDS-607 does not appear to influence alternative prenylation in the presence of tipifarnib

While tipifarnib treatment does clearly cause alternative prenylation for known substrates such as KRAS, NRAS and RRAS2, as well as a small selection of other substrates including PEX19 and LMNB1, SmgGDS-607 did not appear to play a role in this, as KO cells were able to undergo alternative prenylation to a comparable degree.

ALDH9A1 as a control for YnF incorporation

ALDH9A1 was shown to be specifically *S*-farnesylated, however its modification is not FTase-mediated, as tipifarnib treatment did not affect the degree of *S*-farnyeslation of the protein. ALDH9A1 thus serves as a convenient internal control for probe labelling experiments in the presence of an FTI, as it may be used to normalize FTI-sensitivity of other *S*-farnesylated substrates.

Membrane-enrichment proteomics as a readout for perturbations in *S*-prenylation

Cell fractionation proteomics, specifically membrane-enrichment, was shown to be a useful strategy for monitoring membrane delocalization of lipidated substrates, and in this instance, *S*-prenylation. Though this study benefited from complementation of both probe and fractionation approaches, membrane-enrichment proteomics could conceivably be applied to systems where probe-labelling is inefficient, such as primary cells metabolically inactive patient samples. However, cell-compartment specific information, such as whether substrates are differentially trafficked to other endomembranes including the Golgi apparatus or the ER, would be useful to further deconvolute the functional

consequences of tipfarnib treatment or SmgGDS-607 KO, and whether either perturbation introduces a leverageable vulnerability. To this end, RAS activation studies would have also been a valuable readout, though functional enrichment did point to attenuated RAS signaling in KO cells.

SmgGDS-607 KO may putatively be favorable in the context of autoimmune diseases due to associated downregulation of interferon-gamma

Functional enrichment analysis from membrane-enrichment studies revealed that tipifarnib or SmgGDS-607 KO may cause downregulation of interferon-gamma (IFNγ)-specific activation. Although a specific mechanism has not been elucidated, this may in part be attributed to attenuated small GTPase signaling, where RHO and RAB proteins play roles in the endocytic processes crucial for IFNγ-signaling. Although data pointing to this is highly preliminary, it would be interesting to establish and characterize this phenotype further as tipifarnib, and/or SmgGDS-607 splice switching, can be envisioned as potential treatments for autoimmune malignancies or pathogenic immunogenicity in certain cancers.

Chapter 3
Development of a CRISPR-enhanced drug-resistance mutagenesis approach to deconvolute alternative *S*-prenylation dynamics

3.1. Introduction

KRAS, NRAS, and HRAS are important RAS family proteins that share overlapping and ubiquitous signaling cascades, as well as possess a high degree of sequence homology – up to 80%[165] (**Fig. 3.1.1**). These RAS isoforms frequently acquire constitutively activating point mutations, leading to malignant transformation and oncogenesis[304]. RAS mutations are major genetic drivers in cancers that have notoriously high mortality rates, including pancreatic ductal adenocarcinoma (PDAC)[305] and lung adenocarcinoma (LUAD)[306,307], melanoma[308,309], and several hematological cancers[310,311]. This has made them highly sought-after targets in the realm of cancer research. However, efforts to directly target RAS hyperactivation have been fraught with challenges, including the inability to pharmacologically outcompete guanosine substrates that are essential for RAS activation, as well as a lack of hydrophobic surface pockets that can be exploited for ligand development[126]. Many of these drawbacks were deemed insurmountable until the discovery of the first clinically active KRAS inhibitor, AMG-510, in late 2019[125].

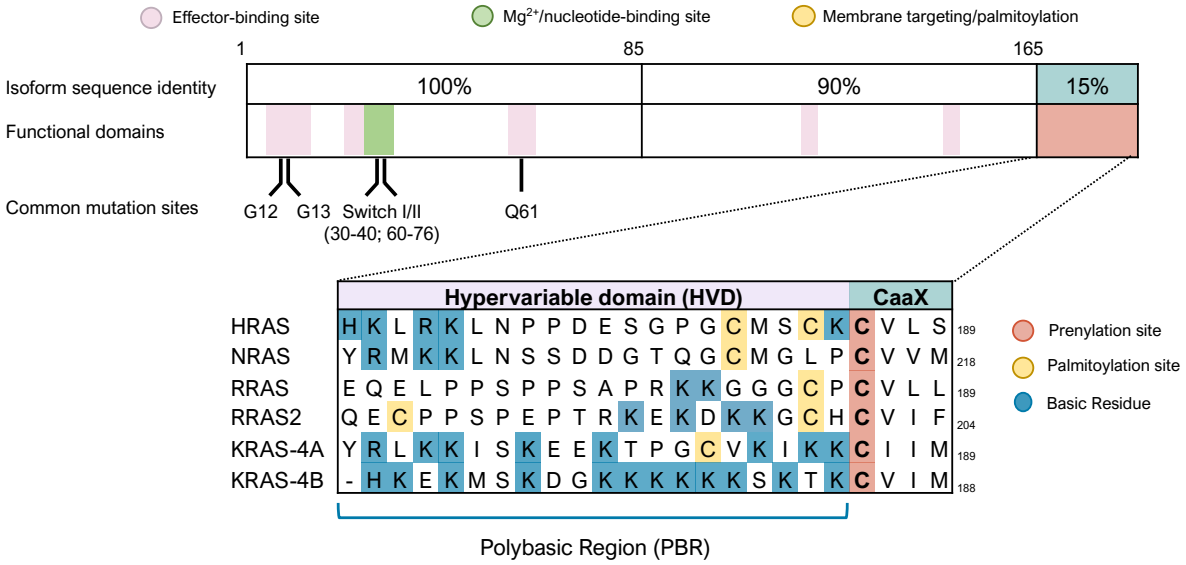

Figure 3.1.1 RAS homology. Alignment and functional annotation of RAS isoform sequences, highlighting sequence homology and divergence at the hypervariable domain (HVD) and CXXX-box, where homology level drops to ~15%.

AMG-510 (sotorasib) is one of several covalent inhibitors designed to target the G12C KRAS mutant frequently encountered in PDAC and LUAD manifestations[125,202,203,312,313]. Adagrasib is a similar second-generation drug that boasts an improved pharmacological profile, including a longer half-life[203]. Both drugs are now available in the clinic. These molecules, which consist of related heterocyclic core scaffolds armed with a cysteine-directed warhead, exploit a cryptic pocket proximal to the point mutation (G12C) found in the inactive (GDP-bound) form of KRAS. Ligand binding promotes nucleophilic attack of the acquired mutant cysteine and irreversibly locks KRAS in its inactive state, resulting in potent antiproliferative effects[314]. While the discovery of sotorasib, adagrasib, and other derivatives has been monumental in the field of KRAS biology and cancer research altogether, acquired resistance has emerged as a significant problem[204]. Several recent studies have described the onset of acquired resistance that develops after sotorasib treatment, which is commonly mediated through a poorly understood, transient drug tolerant state[205]. This refers to the phenomenon where patients who initially respond to a drug relapse following a treatment regime, often due to reversible changes in protein expression[315]. However, prolonged drug exposure can result in the acquisition of mutations, leading to irreversible resistance. In many cases, patients who are partial responders to sotorasib are the most susceptible to this type of acquired resistance; partial responders make up almost 45% of patients treated with this class of KRAS inhibitors[204,205]. More recent studies have shown that the drug tolerant state preceding irreversible resistance was characterized by overexpression of focal adhesion components, driven mostly by integrin β4 (ITGB4)[205]. In the previous chapter, this was briefly discussed in the context of SmgGDS-607 KO, where there was an observed downregulation of focal adhesion pathway, and may indicate that targeting SmgGDS-607 would be synergistic with KRAS inhibition.

In contrast, NRAS and HRAS-driven cancers, as well as other types of KRAS mutant cancers, do not have approved direct, targeted therapies for the reasons previously outlined. To circumvent the difficulties commonly associated with such targeted therapies, RAS downstream signaling pathways have been targeted as way of attenuating the hyperactivated phenotype, which has had varying success in clinical models[199]. At the

same time, strategies targeting the enzymes that post-translationally modify RAS proteins have also been explored as a way of manipulating RAS function[316,317]. To this end, FTIs and similar drugs were developed, initially with limited success[8,3183.]

RAS activating mutations universally preserve CXXX and HVD function, suggesting its ubiquitous essentiality to RAS function, localization, and stabilization. However, despite their overlapping similarities from both functional and primary sequence perspectives, RAS isoforms can markedly differ in their PTM scope, including in *S*-prenylation and *S*-palmitoylation occurrences and dynamics[319]. This is consequently reflected in their responses to FT inhibition; KRAS, NRAS and RRAS2 can compensate for the lack of active FTase in the cell by switching to geranylgeranylation to varying degrees, whilst HRAS remains unprenylated, making it uniquely susceptible to FT inhibition[8,52–54,320]. For this reason, HRAS-driven cancers, such as head and neck squamous cell carcinoma (HNSCC) and acute myeloid leukemia (AML) are being re-investigated as candidates for FTI treatment in the clinic[184,278,321]. Relevantly, the FDA recently granted tipifarnib breakthrough therapy designation for HRAS-driven HNSCC[149,1903.] However, the use of combination therapies with tipifarnib has been prioritized in this context due to dose-limiting myelosuppression and resistance arising from single-agent tipifarnib treatment[151,190,322].

Importantly however, little is known on alternative prenylation or why only a subset of RAS proteins can undergo this switch mechanism. Deconvoluting the criteria required for alternative prenylation may pave the way for other combination therapies. This can be envisioned to be multifaceted; for example, the identification of novel vulnerabilities exposed by *S*-geranylgeranylation of KRAS or NRAS could unveil novel drug targets that work in tandem with tipifarnib. Alternatively, FTI-mediated inhibition of HRAS may be capitalized on, for instance, by the revelation of an adjacent, druggable pathway that engenders its non-prenyl-switching phenotype.

Generally, it can be hypothesized that criteria for alternative prenylation across the proteome arises from either (a) sequence identity, (b) protein-protein interactions, (c)

substrate localization, (d) external regulators stemming from the tumor microenvironment, or some combination of these features. At the level of sequence identity, prenyltransferases have inherent substrate preferences determined by the structures of the CXXX-box binding site. As previously discussed, the prenyltransferase X_4-residue recognition motif in FTase is more polar, whereas the analogous motif in GGTase-I is relatively hydrophobic, which can dictate X-residue preferences[323]. However, the foundational studies that have determined these preferences were primarily conducted *in vitro* and lacked cellular context, where localization, activation-state, and concurrent PTMs may alter these dynamics[25,214,280,324]. Although the use of dual chemical isoprenoid probes (YnF and YnGG) have revealed that alternative prenylation does indeed occur for a subset of proteins, an investigation into the mechanism that engenders this phenomenon has never been conducted in a global, endogenous context. Prenylation switch criteria may serve as a key bottleneck towards new applications of PTIs in the clinic, as well as enable the discovery of new targets in RAS-driven cancers that have long evaded effective therapeutic treatment.

The manual generation of RAS constructs with different HVDs and/or CXXX sequences (i.e. chimera proteins) could be undertaken to deconvolute these criteria. For example, the HRAS CXXX-box could be swapped for the corresponding KRAS motif through a designed plasmid vector, exogenously expressed by transient transfection, and then evaluated using dual chemical isoprenoid probes (YnF and YnGG) in combination with tipifarnib. However, the spectrum of mutations that can be tested using this workflow would remain limited, as scaling up this methodology would require a large number of transfections and construct validations in order to triage all possible mutations in the HVR and CXXX regions alone. Therefore, the functional resolution of HVR and CXXX regions that can be reasonably investigated may be too low to capture relevant chimeras or mutations that facilitate or inhibit prenyl-switching using this strategy.

Instead, a novel protein-centric, drug drug-resistance mutagenesis scanning workflow was developed to address these possible issues and facilitate the capture of prenyl-switching mutations endogenously, without requiring manual generation of RAS chimera

plasmid vectors. This chapter outlines the conception, development, and proposed optimizations of a saturation mutagenesis approach for RAS alternative prenylation, as well attempts at following up associated findings.

3.2. Results and discussion

3.2.1. Conceptualization of a CRISPR-enhanced drug-resistance mutagenesis approach

Inspired by saturation mutagenesis techniques, where random mutations are introduced across a protein of interest to deconvolute sequence-function relationships, a modified scanning mutagenesis approach was devised[325,326]. A recent study showcased a genome-wide mutagenesis scanning technique that can rapidly drive acquired drug resistance mutations in target proteins[325]. Using CRISPR-Cas9 mediated mutagenesis, a single-guide RNA (sgRNA) library was used to induce double-strand breaks (DSBs) targeting essential genes across the genome[3273.] Non-homologous end-joining (NHEJ), an inherently error-prone repair endogenous DNA mechanism, would then allow the acquisition of random, functional in-frame mutations (**Fig. 3.2.1**).

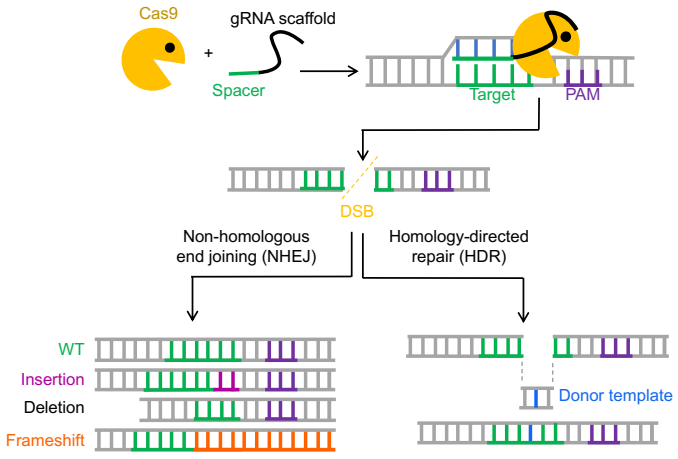

Figure 3.2.1. CRISPR repair pathways. An endonuclease enzyme, most commonly Cas9, is guided to a target cut-site using a single-guide RNA (sgRNA). Cas9 then cuts at 3-4 nucleotides from an adjacent protospacer-adjacent motif (PAM), resulting in a double-strand break (DSB) at the targeted locus. DNA repair then occurs one of two ways, determined by the user. Non-homologous end-joining (NHEJ) relies on error-prone endogenous repair pathways that can result in either an insertion, deletion or frameshift mutation near the cut-site. The user can also provide

a donor-template, which results in homology-directed repair and incorporation of donor sequence to produce a desired mutation.

Under drug selection conditions, mutations that lead to the acquisition of resistance would saturate within the treated cell population over time, which can then be identified and quantified using next-generation sequencing (NGS). These mutations would indicate on-target activity of said drug, thus enabling target deconvolution.

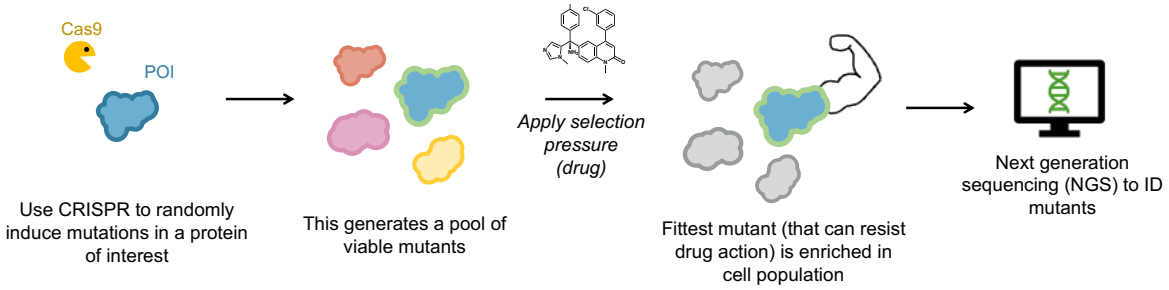

Figure 3.2.2. Protein-centric CRISPR-enhanced **drug-resistance mutagenesis concept.** Cas9 is directed to a specific gene using a designed set of sgRNAs targeting a region of interest (or the entire protein). This generates a pool of viable mutants that are selected for resistance to a drug that otherwise effectively hampers protein activity and results in a phenotype of interest. The fittest mutant is then selected for overtime, which can be analyzed by next-generation sequencing (NGS).

This methodology was adapted to direct Cas9-induced random mutagenesis to specific regions of interest in a single protein, rather than across the genome. Protein-centric drug-resistance mutagenesis scanning could thus yield high resolution data on sequence-function relationships of RAS oncogene HVR and CXXX regions in any cell type, with minimum compromise to the endogenous cellular context that is lost in an overexpression system. When applied to a cell line where proliferation is driven by HRAS, tipifarnib treatment may facilitate the selection for mutations that confer HRAS prenyl-switching capabilities as a mechanism to circumvent FTI-induced toxicity, mimicking whichever unidentified features allow KRAS or NRAS to undergo alternative prenylation (**Fig. 3.2.2**).

Amplicon sequencing of these genes after selection would allow the identification and quantification of these mutations favored under selection conditions, which can serve to

potentially deconvolute the role these regions play in alternative prenylation behavior. High frequency mutations can then be introduced through CRISPR-Cas9 gene editing techniques to re-create the saturated mutation in a cell line of interest and enable validation of alternative prenylation using the dual chemical probe system. These mutations could later be studied to identify potential interactors associated with the gain-of-function mutation using interactomics, which is covered in a later chapter within this thesis. This would allow the deconvolution of chaperones or other interacting proteins that modulate alternative prenylation, which could be exploited for inhibition that is synergistic with FTIs like tipifarnib. Moreover, H23 SmgGDS-607 KO cells may also undergo this mutagenesis approach to decipher the role SmgGDS plays in regulating prenylation of RAS oncogenes, as discussed in the previous chapter. Importantly, this methodology allows the cell to select for the most relevant mutations, rather than rely on a biased selection of a limited set of mutations. Moreover, targeting a single protein would initially require analysis of only specific regions of interest that can be studied through the amplification of a single amplicon, as opposed to sequencing various targeted genes across the genome; this greatly simplifies the workflow and cost of sequencing[328].

3.2.2 Designing a control assay for CRISPR-enhanced drug-resistance mutagenesis

A control, or proof-of-concept, set of conditions was also devised, whereby treatment with a specific $KRAS^{G12C}$ inhibitor (AMG-510, also known as sotorasib) in a $KRAS^{G12C}$-driven cell line may drive resistance through mutagenesis at G12C in order evade covalent-targeted inhibition of KRAS-mediated cell proliferation (**Fig. 3.2.3**).

In the clinic, resistance mutations that commonly arise include non-ligandable G12 mutants (G12D, R or S, for example), or mutations within the liganded pocket that prevent sotorasib or adagrasib binding[204]. Genomic alterations in the RTK-RAS signaling cascade were also found in a subset of patients, as well as the acquisition of other RAS isoform mutations, most frequently via NRAS[204,205]. However, in this instance, a simplified approach was favored, without the goal of replicating known clinical outcomes. In this

case, any mutation away from G12C at this site would be indicative of successful CRISPR-enhanced drug-resistance mutagenesis and would lend confidence to adopting such an approach to tipifarnib-driven HRAS resistance. Amplicon sequencing would additionally simplify this read-out in the first instance.

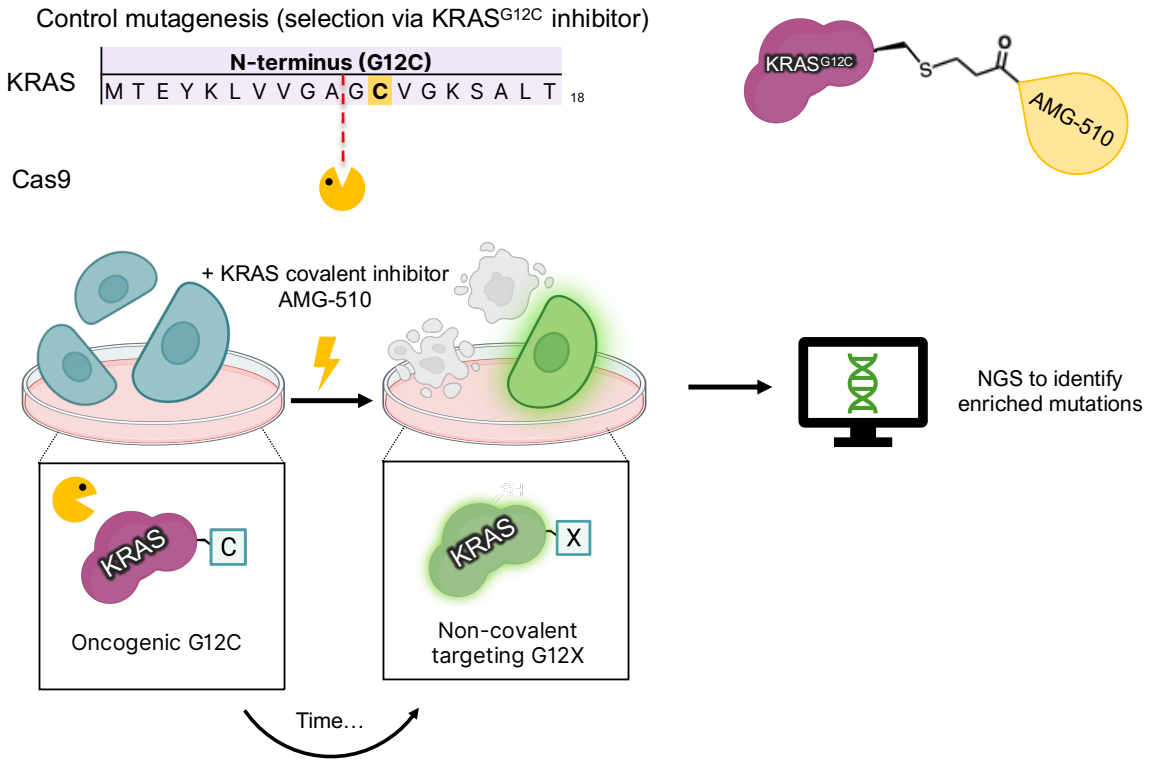

Figure 3.2.3. Strategy for KRAS^{G12C} CRISPR-enhanced drug-resistance mutagenesis. Schematic showing an example sgRNA cut-site and workflow the proposed control screen for drug-resistance mutagenesis. KRAS^{G12C} is covalently modified by AMG-510 which inhibits KRAS GTPase activity. Upon mutagenesis and selection of mutagenized KRAS populations using AMG-510, G12C site is expected to diverge away from G12C to an unmodifiable G12X mutation.

Initially, a set of sgRNAs were designed to target the region around the G12C locus in H23 cells. H23 cells were chosen due to the immediate availability of a stable Cas9 expression line within the Tate lab, thereby only requiring the optimization of sgRNA transfection. Crucially, these H23-Cas9 cells also harbor the KRAS^{G12C} mutation. However, this is presented as a heterozygous mutation, which was confirmed via Sanger sequencing KRAS exon 2 (Appendix Fig. **7.7**). This complicated the design of G12C-directed sgRNAs, however it was hypothesized that the direct targeting of this region on

the G12C strand would still drive resistance via divergence from the Cys, even if WT KRAS activity could compensate this effect to some degree. Thus, 4 sgRNAs were designed that would direct Cas9-mediated DSBs between 6 and 27 base pairs upstream from the G12C site. These DSBs have the potential to drive NHEJ 13 bps up and downstream from each cut-site, which sufficiently covers the region around G12C site [325] (Fig. **3.2.4a**). Unfortunately, the design of sgRNAs downstream of the G12C was not possible due to a paucity of protospacer adjacent motifs (PAMs) beyond this region, which serve as Cas9 recognition motifs and are essential for targeting the enzyme to the desired cut-site. However, this was not expected to affect editing capacity around this region. Additionally, a standard non-targeting sgRNA sequence was also used for control experiments.

The designed sgRNAs oligonucleotides, including the control sgRNA sequence, were obtained and assembled into sgRNA human expression vectors (BPK1520, Addgene) using Golden Gate cloning[329] (**Fig, 3.2.4b**). Briefly, sgRNA oligos (forward and reverse strands) were synthesized with type IIS restriction enzyme overhangs. The annealed sgRNA oligo-duplex, generated by rapid heating and slow cooling of the forward and reverse oligos, is then ligated to the digested destination vector using a standard T4 ligase mix.

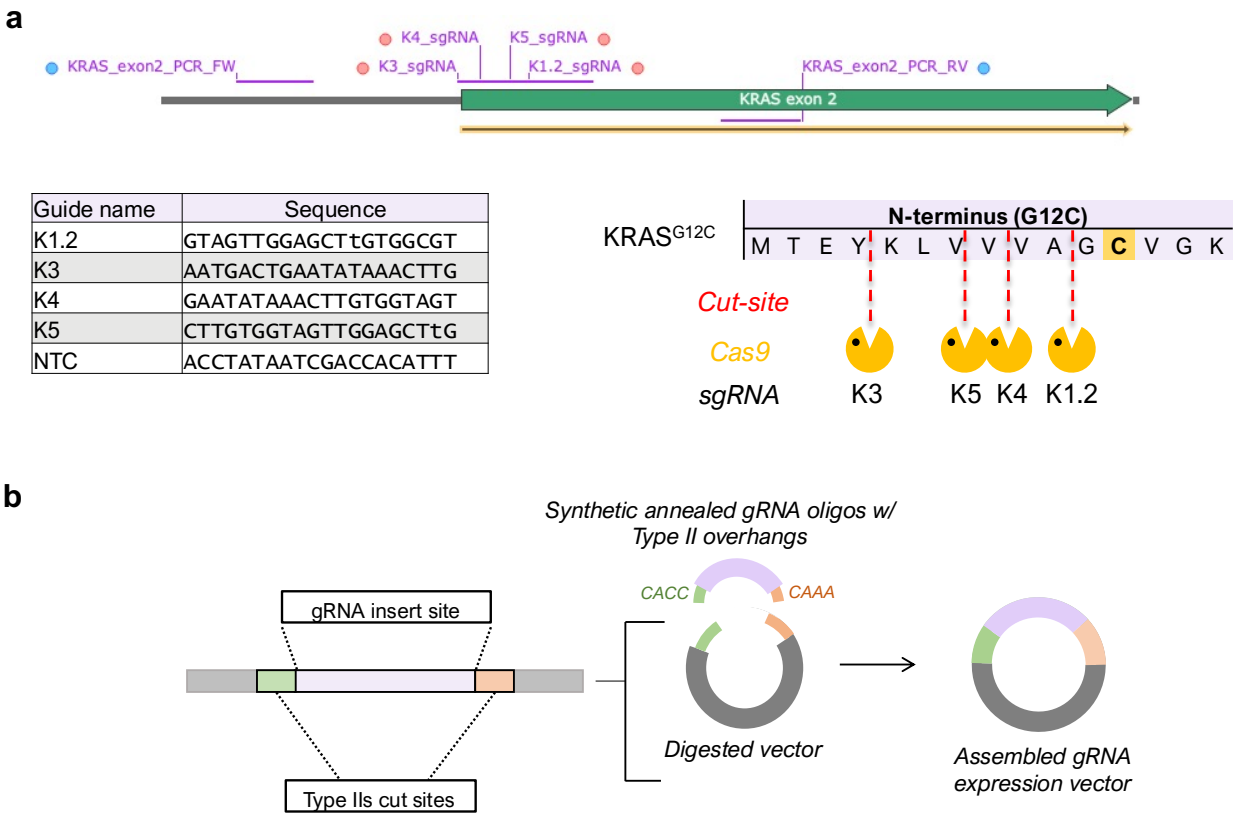

Figure 3.2.4 sgRNA design for KRAS^{G12C} CRISPR-enhanced drug-resistance mutagenesis. **(a)** Schematic and table showing positions and sequences of designed KRAS^{G12C} sgRNAs and control sgRNA (NTC). **(b)** Schematic showing Golden Gate assembly workflow for construction of sgRNA expression vectors.

The assembled vectors were then expanded for use in mutagenesis experiments. However, across this study, expansion of these plasmids proved to be a bottleneck for the screen as the small plasmid size (~2 kb) made them difficult to purify using standard large-scale plasmid purification techniques (i.e. midi- and maxi-preps)[330].

Next, transfection of H23 cells was also optimized to ensure efficient expression of sgRNAs. A model plasmid expressing eGFP was used to optimize transfection. This model plasmid had a similar size to the designed sgRNA plasmids (~2.5 kb), which is one parameter that can affect transfection efficiency. Transfection efficiency was established using two methods. First, H23 cells were transfected with an eGFP plasmid using different

ratios of a standard transfection agent, Lipofectamine 2000 (ThermoFisher), and monitored using live-cell fluorescence imaging (IncuCyte S3). This revealed that transfection efficacy was highest using the lowest DNA:transfection agent ratio and peaked over the course of 24h (**Fig. 3.2.5a**). Cells were then harvested for flow cytometry analysis to confirm optimal DNA:transfection agent ratios for H23 cells. Flow cytometry indicated that 1 µg DNA per 3.25 µL Lipofectamine 2000 was optimal for transfection (1:3.25) in a 48-well plate format, providing up to 81% transfection efficiency (**Fig. 3.2.5b**).

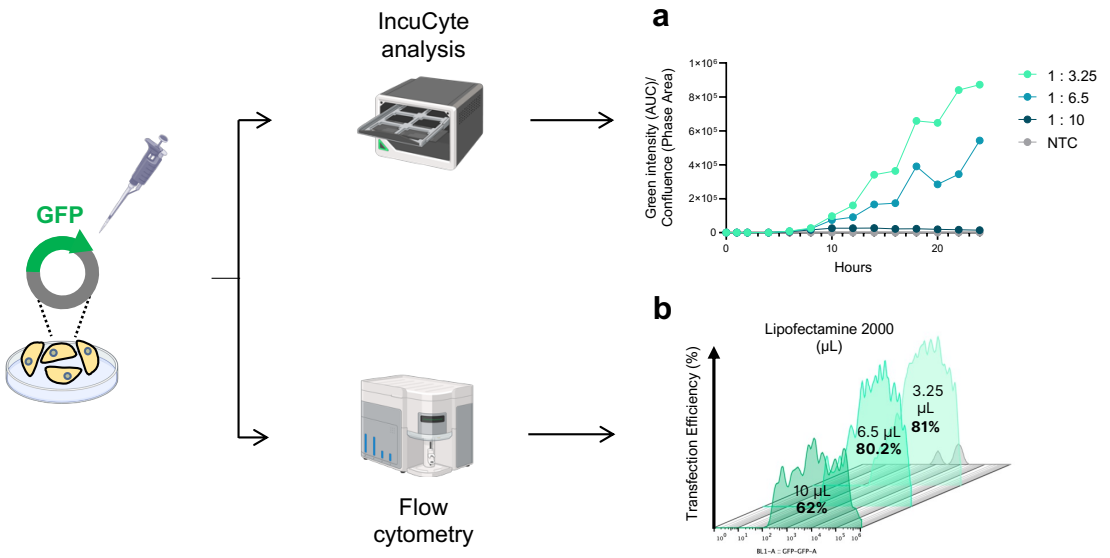

Figure 3.2.5 Optimizing parameters for sgRNA transfection efficiency. Determining sgRNA transfection efficiency using a marker eGFP-expressing plasmid and both **(a)** IncuCyte and **(b)** flow cytometry readouts.

3.2.3 Optimizing KRAS amplicon sequencing for NGS analysis

PCRs utilizing primers with adaptors for Illumina amplicon sequencing were then optimized for $KRAS^{G12C}$ sequencing. These conditions would then be applied to cell samples harvested after mutagenesis and selection. Optimizing amplicon PCRs is essential for robust sequencing data as impurities, side products, or primer dimers greatly reduce the capacity for barcodes to anneal during the second round of amplification directly preceding sequencing[331]. Genomic DNA was extracted using a simple lysis buffer

reported by the Liu lab (described in Methods), only requiring incubation with cells (directly on the culture plate) at 37˚C for 1 hour and subsequent protease inactivation at 80˚C[332]. Genomic DNA PCR amplification was carried out from H23-Cas9 cells and optimized by annealing temperature (**Fig. 3.2.6a**), with 64˚C found to be optimal for the amplicon primers.

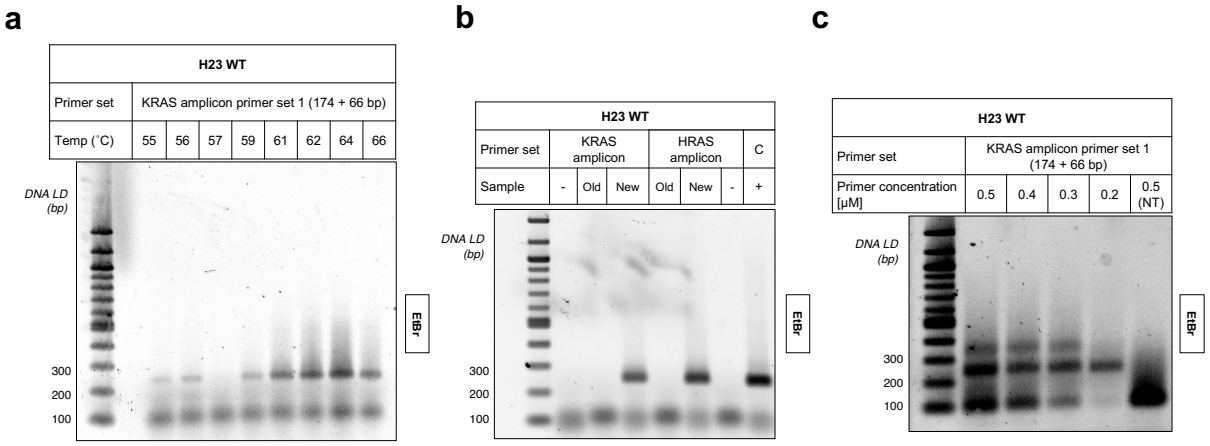

Figure 3.2.6. Optimizing amplicon PCRs for KRAS sequencing. Various optimizations for KRAS amplicon sequencing in H23 cells including **(a)** annealing temperature, **(b)** gDNA extraction mixture stability and **(c)** primer concentration to reduce the formation of primer dimers.

However, primer dimers were still present in the PCR sample, which would complicate sequencing and other downstream analyses. A second set of primers was also tested, however primer dimers persisted and was hypothesized to at least partially arise from the use amplicon adaptors (data not shown). Usually, primer dimers can be removed by simple PCR column purification due to their small size (< 22 bp), however since amplicon PCR primers are larger than typical primers (~ 53 bp), their dimers often are retained in the purified fraction. A common method to reduce primer dimers is to also reduce primer concentration in the PCR reaction[333]. Thus, a titration of primers pairs was performed for KRAS amplicon PCRs, with 0.2 μM final primer concentration found reduce dimers significantly whilst still allowing on-target amplification with the optimized anneal temperature of 64˚C (**Fig. 3.2.6b**). Finally, it was found that PCR amplification from DNA extracted and stored at -20˚C for longer than ~1 week also prevented PCRs, likely due to

the degradation of DNA or generation of contaminants/precipitants upon freeze-thawing (**Fig. 3.2.6c**). Thus, additional care was taken to ensure PCR amplification was performed on the day of extraction for future experiments.

3.2.3 Evaluating mutagenesis efficiency using designed KRAS sgRNAs

Next, sgRNA targeting and induction of mutagenesis was evaluated using a mutagenesis surveyor assay, which is a technique that uses a T7 endonuclease to specifically cleave heteroduplex DNA at NHEJ-induced mutations. These include mismatches and extrahelical loops formed by insertion or deletion (indels) consisting of one or more nucleotides that the T7 endonuclease can specifically bind and cut[334] (**Fig. 3.2.7a**).

Following transfection of the designed KRAS sgRNAs in Cas9-expressing H23 cells, cells were incubated for a further 3 days to allow sufficient mutagenesis to accumulate for analysis. Genomic DNA was then extracted, and the KRAS gene was amplified using the optimized PCR conditions. PCR products were then denatured and re-annealed, accomplished by heating and subsequent rapid cooling, which yielded heteroduplexes that included NHEJ-induced mutations. T7 endonuclease I was then used to specifically digest duplexes that contain mutations, which would saturate near the specified cut-site. The resulting products are then analyzed by gel, where PCR fragments with molecular weights that correspond to the mutation cut-site can be visualized. The presence of primer dimers unfortunately persisted to some extent, complicating analysis as fragments were likely to fall within that region. However, the presence of a new band just above the primer dimer band (~100 bp) indicated successful mutagenesis at the intended site, forming a fragment around (calculated to be ~120 bp) (**Fig. 3.2.7b**). Initially, this was only confirmed for sgRNAs K1.2 and K3 using this T7 assay. Later Sanger sequencing experiments confirmed mutagenesis at the expected sites for the remaining sgRNAs (data not shown).

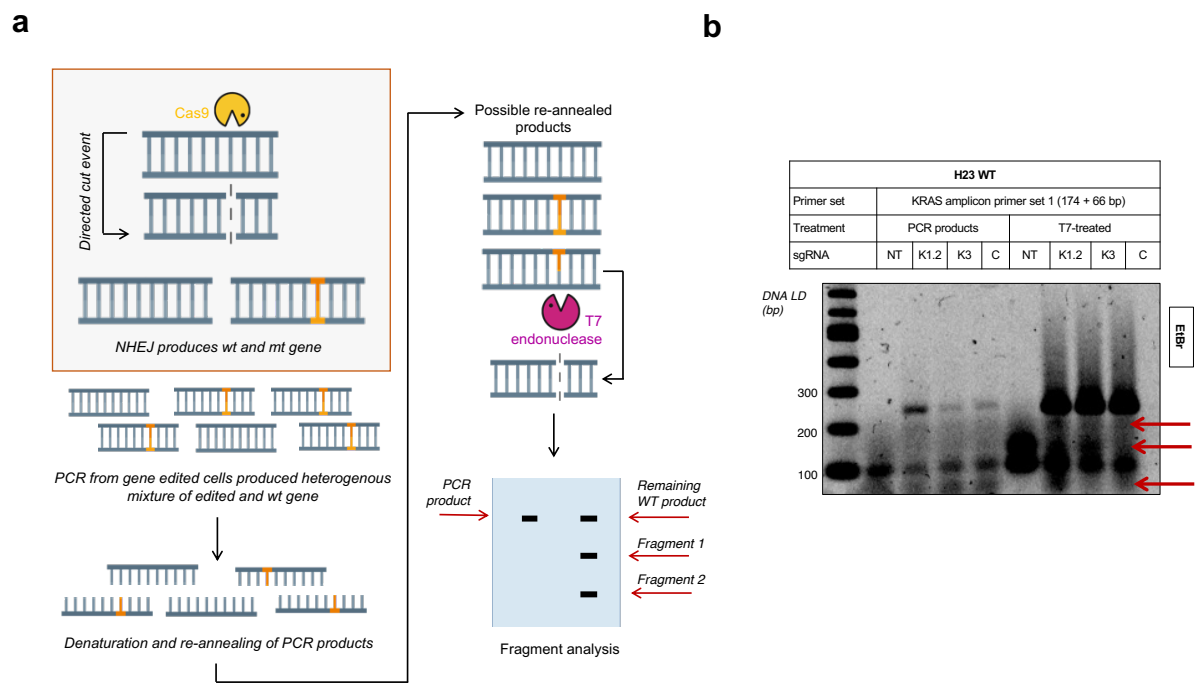

Figure 3.2.7 T7 mutagenesis surveyor assay to validate on-target activity of designed sgRNAs. (a) Schematic of T7 mutagenesis surveyor assay workflow. Mutagenesis of target gene generates various products by NHEJ. PCR of target gene produces various gene products. This results in either homo or heteroduplex formation after denaturation and subsequent annealing of PCR products. Addition of T7 endonuclease specifically cleaves heteroduplexes and results in fragments corresponding to the Cas9 cut-site that can be analyzed by gel. **(b)** T7 mutagenesis surveyor assay results for KRAS-directed sgRNAs (K1.2 and K3).

3.2.4. Optimizing drug selection conditions for CRISPR-enhanced drug-resistance mutagenesis

Drug selection conditions were then optimized for H23-Cas9 cells using both tipifarnib and AMG-510. AMG-510 was primarily used for KRAS^{G12C} selection experiments, as outlined previously, however it was also hypothesized that AMG-510 would also be required to potentiate selection during HRAS-directed mutagenesis. Because H23-Cas9 cells are largely driven by the KRAS^{G12C} mutation, co-treatment with AMG-510 could suppress RAS-rewiring, which refers to RAS signaling pathway reorganization in response to a perturbation, including but not limited to other RAS isoforms dominating the oncogenic response[204]. In this way, AMG-510 co-treatment may allow HRAS mutations to dominate any resistance that may be inaugurated by the assay. A strategy for drug

treatment and selection conditions was thus devised based on H23 growth patterns and sensitivity to the selection drugs (Fig. **3.2.5a**).

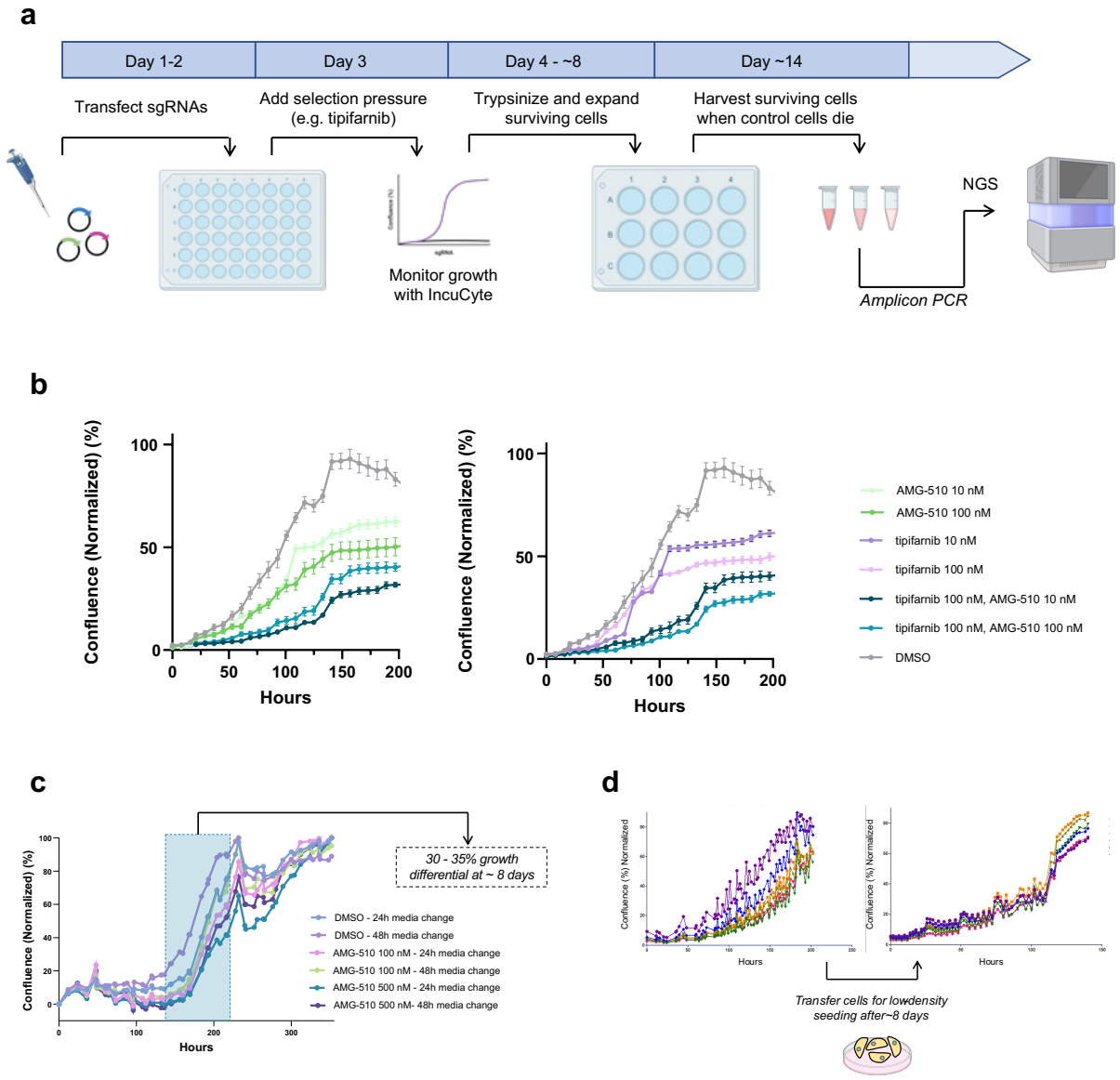

Figure 3.2.8. Workflow and optimization of CRISPR-enhanced drug-resistance mutagenesis in H23 cells. (a) Schematic of devised workflow for 2D drug-resistance mutagenesis. Following transfection of sgRNAs and a subsequent 3-day period to allow accumulation of mutagenized HRAS, a selection pressure (i.e. tipifarnib and/or AMG-510) is added. Confluence is monitored by IncuCyte analysis, whereby cells are transferred to a second phase of selection if confluence is reached during the first phase. Cells are then harvested for NGS analysis once a significant confluence differential between control and mutagenized populations are observed. **(b)** Establishing toxicity of tipifarnib and AMG-510 in H23 cells using

IncuCyte analysis (n=3). (**c)** Determining harvest time-point for H23 cells under selection conditions (representative, n=1). **(d)** Two-phase selection confluence data for $KRAS^{G12C}$ CRISPR-enhanced drug-resistance mutagenesis (500 nM AMG-510; n=1).

Cells were treated with either 10 or 100 nM tipifarnib, AMG-510, or both to observe potential synergy between the two drugs. Cell confluence was measured over time using IncuCyte imaging and analysis, revealing some limited synergy between tipifarnib and AMG-510 (Fig. **3.2.5b**). However, significant toxicity was likely attenuated by the heterozygous, rather than homozygous, presentation of the G12C mutation, meaning that increased expression of WT KRAS could likely emerge as a resistant phenotype, rather than just through direct mutation of the G12C site. It was hypothesized that only a difference in cell proliferation was necessary to enrich for relevant mutations in the first instance, as complete selection was likely not possible with the molecules at hand.

H23 cells were deemed sensitive enough to both treatments to enable selection within a 4 - 8 day window. To confirm this, a mock selection experiment was performed with AMG-510 alone, as these conditions would be used for the initial KRAS control selection experiments. Cells were plated onto 48-well plates. After three days, cells were transferred to 6-well plates with AMG-510 selection media. A higher concentration of AMG-510 (500 nM) was also tested to maximize potential for cell death. Selection media was refreshed every 24 or 48 h to determine long-term selection conditions. Cell death was monitored over ~14 days by confluence analysis using IncuCyte imaging. Analysis of cell viability data revealed that the maximal difference in cell viability between treated and control cells was achieved at around 8 days, which was within the expected timeframe based on initial time-resolved cell viability experiments (Fig. **3.2.5c**). Hence, these conditions would be taken forward to the CRISPR-enhanced drug-resistance mutagenesis screen.

The full CRISPR-enhanced drug-resistance mutagenesis assay was then performed with the optimized conditions (using 500 nM AMG-510). During the selection phase, all conditions achieved confluency within 14 days, partially due to high seeding of cells at

the start of selection (Fig. **3.2.5d**). To mitigate this, mutagenized cells, along with the non-targeting sgRNA (NTC) and untransfected (UT) controls, were harvested and re-seeded at lower densities to resolve differences in proliferation patterns among mutagenized samples. After a further ~ 5 days, an approximate 20% difference in viability was observed between K1.2 and NTC/UT samples, which was deemed sufficient for potential enrichment of any relevant mutations. Genomic DNA from all samples was then collected using the previously described strategy and subjected to amplicon PCR. Unfortunately, after repeated efforts to perform amplicon PCRs on these samples, primer dimers could not be fully resolved, partially due to pandemic-related time-constraints. Samples were thus taken forward to an alternative sequencing strategy to evaluate enriched mutations.

Discordance in Sanger sequencing traces can be attributed to heterozygous products following PCR of genomic DNA, and often arises following mutagenesis. This discordance can be deconvoluted using specialized software to allow an interference of CRISPR-based editing or mutagenesis. EditR[335], an R-based program developed by the Moriarty lab, and ICE (Interference of CRISPR Edits), a program developed by Synthego, use chromatograms generated by capillary fluorescence-based Sanger sequencing to detect areas of significant discordance. Generally, this type of software initially aligns the provided sgRNA sequence to the Sanger chromatogram to calculate if predicted editing matches quality expectations. Sequence traces within the given sgRNA editing region are then compared to traces from the rest of the chromatogram, as well as a control (unedited sample) chromatogram to determine the extent of mutagenesis. The software decomposes the fluorescence signal at each base-call position to predict the edit, which is presented as a percent nucleotide contribution to the signal at that site. Data generated from the initial round of CRISPR-enhanced drug-resistance mutagenesis is summarized in Fig. **3.2.9**.

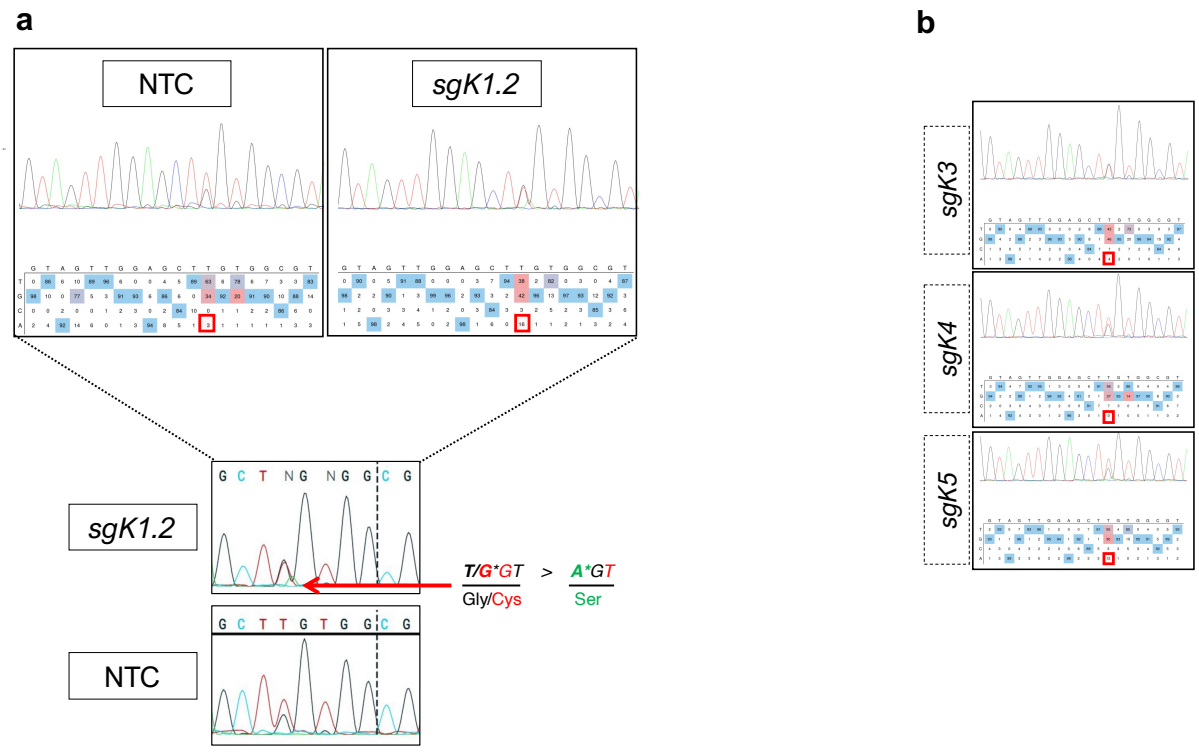

Figure 3.2.9. Sanger sequencing discordance analysis following CRISPR-enhanced drug-resistance mutagenesis of KRAS^{G12C}. **(a)** EditR and ICE analysis revealed the emergence of the G12S AMG-510 resistant mutation in H23 cells. **(b)** EditR analysis of other tested sgRNA, showing only mild enrichment of G12S in K5, and no enrichment in K3 and K4 samples.

Pleasingly, initial analyses of mutagenized samples that underwent selection with AMG-510 revealed a small but significant enrichment of G12S, which is not modifiable by AMG-510 (Fig. **3.2.9a**). The presence of the heterozygous G12C mutation likely diminished the effect of the acquired G12S mutation, which is represented here as an increase from 3% (noise) to 16% overall contribution to the signal at that site. Considering that editing likely only took place on the G12C strand (by design of the sgRNA), this result can be estimated to have almost double the effect in a homozygous G12C population. Moreover, G12S is an expected mutation, given that only a single base change (N to A) at that site is required for -Ser variant to emerge. Further NGS analysis would be necessary to establish this finding, however this result lent enough confidence to the mutagenesis screen set-up to continue with the proposed HRAS model. In the future, it would be important to repeat

this screen in a cell line that was more responsive to AMG-510, as well as harbors the homozygous G12C mutation for clarity of analysis.

Relevantly, a study published after this screen was conducted reported an alternative mutagenesis approach to study drug resistance in a protein-centric manner, dubbed "LentiMutate"[336]. This mutagenesis screen relies on an engineered error prone HIV-1 reverse-transcriptase (RT), which introduces a set of random mutations during integration of a chosen cDNA (of the POI) in lentiviral transduced cells. Random mutagenesis of the re-codonized transgene of interest and subsequent introduction of a drug targeting the transgene resulted in drug-resistant mutations that can specifically be analyzed by NGS in a doxycycline-inducible system. Of note, this system does not rely on the presence of PAM sites for editing, as does CRISPR, and offers more versatility for genes that are "PAM deserts", albeit with less precision. Recodonization of the transgene also allows for more specific amplicon sequencing of the mutagenized target. Among other targets, KRAS and $KRAS^{G12C}$ were tested for drug-resistance against AMG-510. Results demonstrated the emergence of clinically relevant mutations in the G12C line (using H1993 LUAD cells), including G12S. It would be interesting to use such an approach for the proposed CRISPR-enhanced drug-resistance mutagenesis described in this chapter, but due to time constraints this was not possible before completion of the PhD.

3.2.5. CRISPR-enhanced drug-resistance mutagenesis for HRAS alternative prenylation.

Having demonstrated some success in establishing a resistance driven mutagenesis screen in a KRAS model, a similar model for HRAS was designed to deconvolute sequence-related alternative prenylation criteria (Fig. **3.2.10a**). Here, mutagenesis along the length of the HRAS HVD and CXXX-box would introduce a random series of indels that may interfere with any sequence-related features that putatively prevent HRAS from undergoing alternative prenylation in the presence of an FTI (i.e. tipifarnib). Alternatively, mutagenesis could also introduce a feature within this sequence that allows alternative prenylation to occur, analogous to that of KRAS and NRAS. A set of 5 sgRNAs were

designed and assembled in expression vectors using the same workflow as the aforementioned KRAS-directed sgRNAs (Fig. **3.2.10b**).

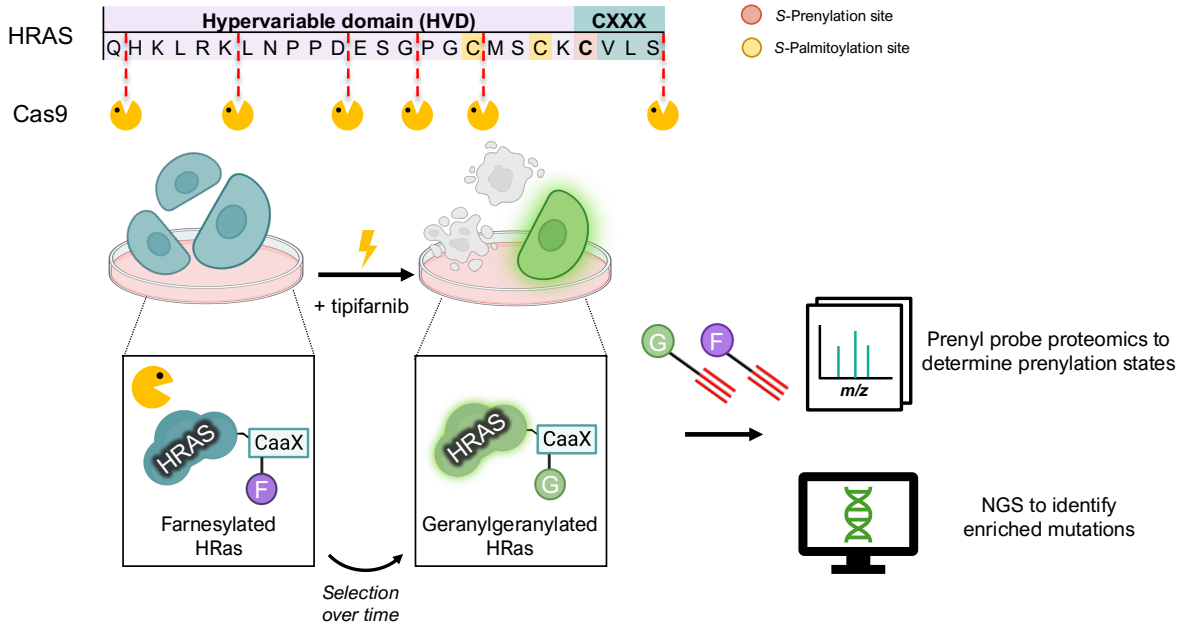

sgRNA	sgRNA Sequence (5'-3')	Cut site (DNA)	Cut site (AA)
H1	AGTGTGTGCTCTCCTGACGC	532636 (+)	QHKLRKLNPPDESGPGCMSCKCVLSX*(INTRON)
H2	ACACTTGCAGCTCATGCAGC	532665 (-)	QHKLRKLNPPDESGPG*CMSCKCVLSX
H3	CCTCCTGATGAGAGTGGCCC	532673 (+)	QHKLRKLNPPDESG*PGCMSCKCVLSX
H4	CUGAACCCUCCUGAUGAGAG	532679 (+)	QHKLRKLNPPD*ESGPGCMSCKCVLSX
H5	AGATCCGGCAGCACAAGCTG	532705 (+)	QHKLRK*LNPPDESGPGCMSCKCVLSX
H6	GCTTCCGCAGCTTGTGCTGC	532712 (-)	Q*HKLRKLNPPDESGPGCMSCKCVLSX

Figure 3.2.10. Strategy for HRAS CRISPR-enhanced drug-resistance mutagenesis. Schematic presenting designed sgRNA cut-sites and workflow for screen. Here, HRAS is unprenylated in the presence of tipifarnib. Upon mutagenesis, a pool of mutagenized HRAS, putatively containing a mutant HRAS that can be alternatively prenylated to resist tipifarnib action. Cells that survive and/or show increased proliferation over control samples can then be taken forward to NGS analysis and dual chemical probe labelling to validate alternative prenylation of HRAS. B) Table showing sequences of designed HRAS sgRNAs and their associated cut-sites.

H23-Cas9 cells remained the cell line of choice, at least initially, due to the convenience of the Cas9 stable expression. Moreover, KRAS oncogenicity was assumed to be attenuated enough to allow HRAS-driving mutations to supersede under AMG-510 and tipifarnib co-treatment conditions.

An analogous set of optimizations were then performed for the HRAS version of the screen. Two sets of amplicon sequencing primers were designed and tested for primer dimers (Fig. **3.2.11a**). Both sets of primers were found to be equally efficient, however the longer set was chosen for future experiments as it provided more coverage of the gene and would also provide a clearer read-out for the T7 surveyor assay. The designed HRAS sgRNAs were then tested for on-target activity in H23-Cas9 cells. The T7 mutagenesis surveyor assay was performed using the optimized transfection conditions outlined previously. Gel analysis of the resulting fragments revealed that all sgRNAs had on-target activity, forming the correct size fragments for each cut-site (Fig. **3.2.11b**).

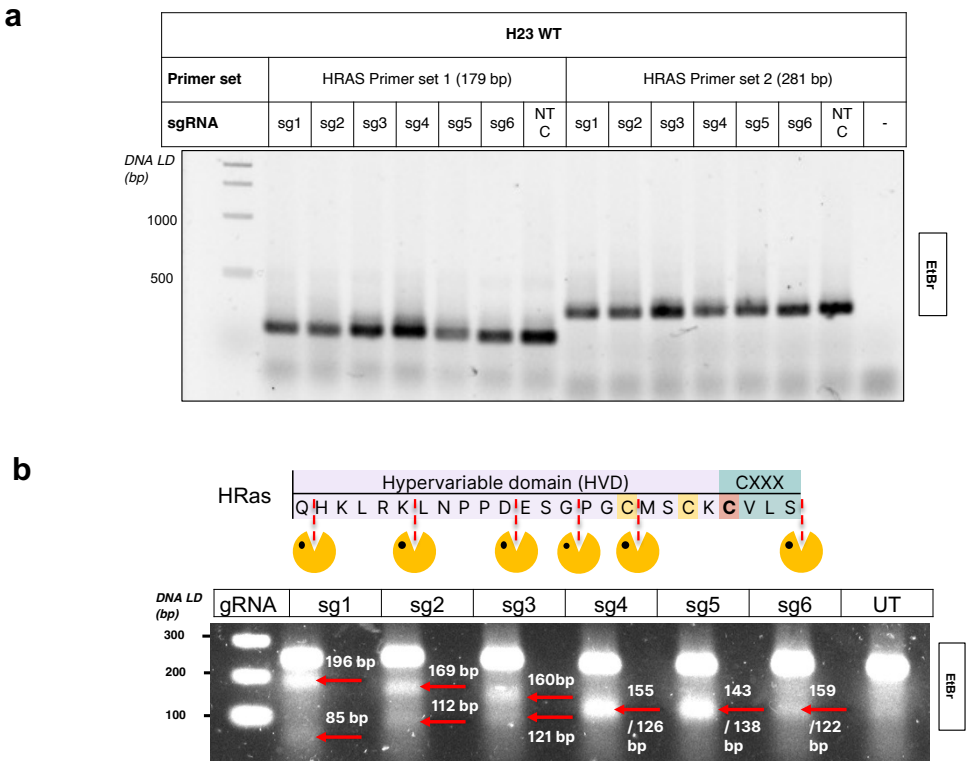

Figure 3.2.11. PCR optimization and validation of sgRNAs for HRAS CRISPR-enhanced drug-resistance mutagenesis. (a) Primer testing for amplicon sequencing of mutagenized HRAS in H23 cells. **(b)** Surveyor T7 assay for designed HRAS sgRNAs in H23 cells, showing successful on target activity for each tested sgRNA.

With validated sgRNAs and selection conditions in hand, the HRAS drug-resistance mutagenesis screen was carried out in H23-Cas9 cells. This was split into two phases. The first was an initial selection round (using 100 nM tipifarnib and 500 nM AMG-510) of

approximately 18 days, until a strong growth differential was observed between the NTC sample and at least one mutagenized sample (i.e. > 30%) (**Fig. 3.2.12a**). While this is recognized to be somewhat of an arbitrary cut-off, a greater than 30% growth differential was found to be comfortably outside the margin of error for cell proliferation studies using the IncuCyte. Similar cut-offs were also employed in other studies that utilize CRISPR-enhanced drug-resistance mutagenesis and also rely on proliferation/cell survival as a read-out[326].

The highest proliferating sample, H2, was subjected to amplicon sequencing while the second phase of selection took place (**Fig. 3.2.12b-d**). For the second phase, all cell samples were harvested and re-plated on larger (6-well) culture plates for another 7 days to allow further enrichment of acquired mutations.

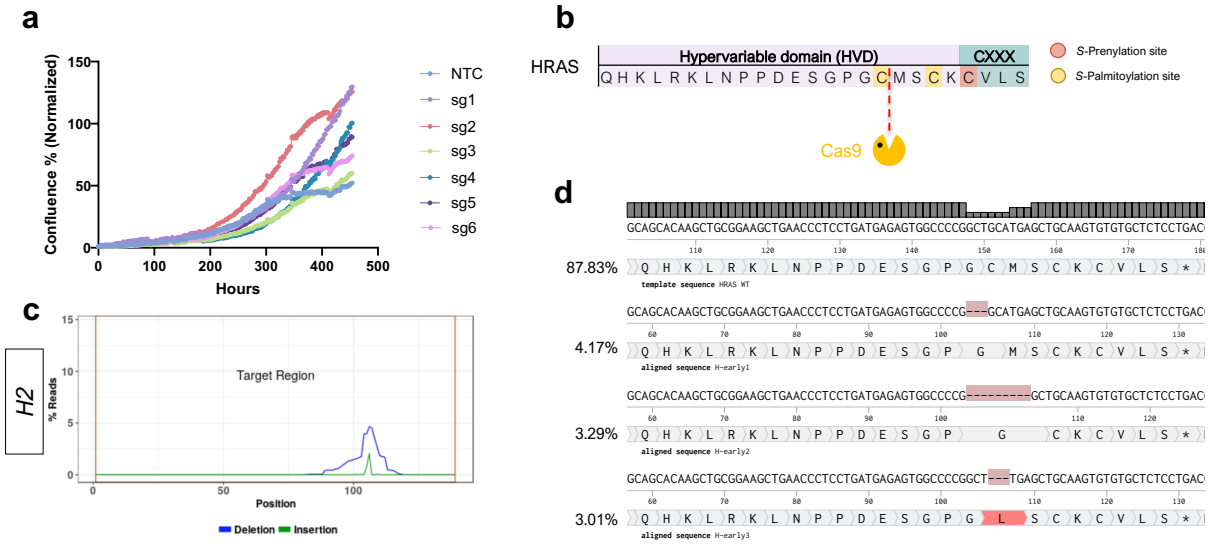

Figure 3.2.12. First phase of resistance mutagenesis screening in H23 cells shows enrichment of *S*-palmitoylation-deficient HRAS mutants. (a) Confluence data over second-phase selection of mutagenized H23 cells using IncuCyte analysis. **(b)** Schematic showing cut-sites of enriched sgRNA-mutagenized samples (H2). **(c)** Indel frequency within target region of H2 sgRNA amplicon-sequenced samples (Genewiz). **(d)** Alignment of enriched amplicon sequences from NGS analysis, showing loss of C181 (Genewiz, Benchling).

The first round of selection revealed H2 to have generated the most favorable mutations upon of AMG-510 and tipifarnib selection. Amplicon sequencing analysis showed that the

loss of the first Cys of the HVD (Cys181) occurred in over 10% of the sample amplicons and was the second highest population after the WT sequence. Cys181 is known to be one of two dynamically *S*-palmitoylated cysteines of HRAS. While it was recognized that this may be a biased or opportunistic result, as loss of that particular Cys may be due to the cut-site being immediately downstream of its codon, H2 was still the highest proliferating sample in the first phase, which may still indicate some significance in the context of the other mutagenized samples. Regardless, loss of Cys181 implied that HRAS was functional without *S*-palmitoylation of that site. Thus, it was conceivable that it could also contribute to a resistant genotype.

After the second phase of enrichment, H5 and H6 samples appeared to proliferate faster than the H2 sample (Fig. **3.2.13a**).

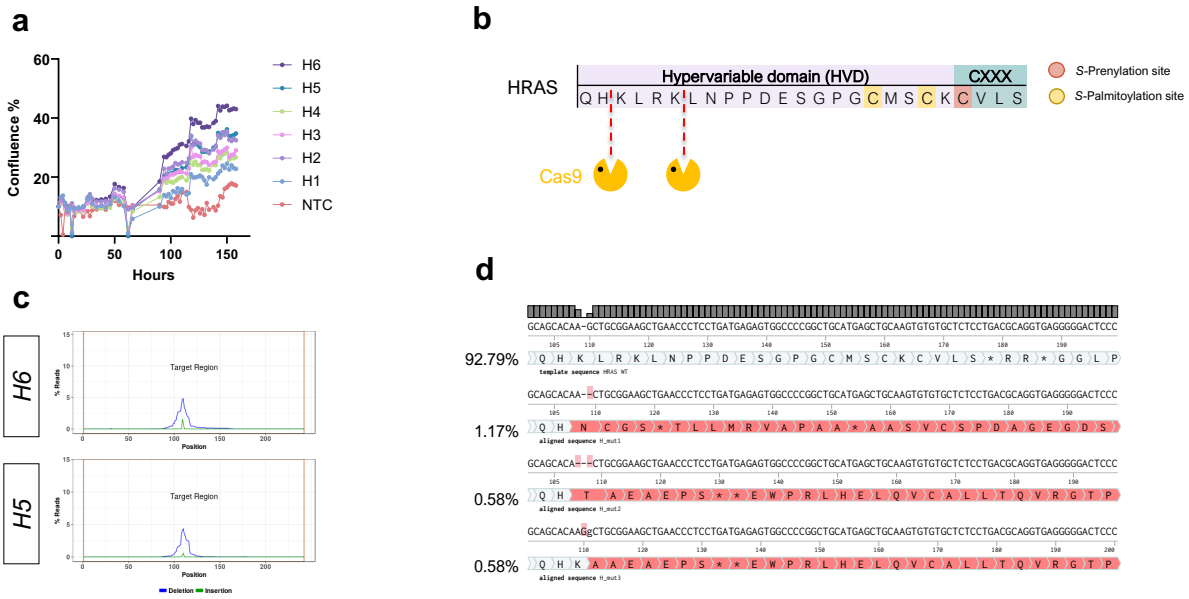

Figure 3.2.13. Second phase of resistance mutagenesis screening in H23 cells shows enrichment of loss-of-function HRAS mutants. (a) Confluence data over second-phase selection of mutagenized H23 cells using IncuCyte analysis. **(b)** Schematic showing cut-sites of enriched sgRNA-mutagenized samples. **(c)** Indel frequency within target region of H5 and H6 sgRNA amplicon sequenced samples (Genewiz). **(d)** Representative alignment of enriched amplicon sequences from NGS analysis, showing truncated loss of function HRAS mutants.

Initially, H5 and H6 sample were harvested for amplicon sequencing. Unfortunately, the harvested H2 sample from this second phase was lost due to sample degradation

(discussed previously in the context of PCR optimization, where long-term sample storage often resulted in an inability to PCR from harvested genomic DNA). Amplicon sequencing of H5 and H6 samples revealed severely truncated mutants, indicating loss of function (Fig. **3.2.13b-d**). This was hypothesized to arise from the lack of HRAS essentiality within the cellular milieu, as KRAS was the major oncogenic driver. This was perhaps compounded by the possibility that AMG-510 treatment did not fully engage the $KRAS^{G12C}$ mutant, or WT KRAS eventually emerged as the dominant driver, which is neither inhibited by AMG-510 nor tipifarnib. While the H2 sample was unable to be sequenced, it was hypothesized that all samples would eventually succumb to the same fate in a system driven by a different RAS isoform, as RAS re-wiring is a recognized phenomenon[337,338]. This may also explain the relatively low enrichment of Cys181del genotype in the initially sequenced H2 sample.

3.2.6. Transitioning to an HRAS-dependent system for CRISPR-enhanced drug-resistance mutagenesis.

In order to avoid the generation of truncated (loss of function) mutants and enhance enrichment of on-target mutations during CRISPR-enhanced drug-resistance mutagenesis, a suitable HRAS-dependent cell line needed to be identified. Thus, a meta-analysis was conducted using data from DepMap, an online platform that amalgamates publicly available CRISPR and drug screening data on a large range of immortalized cell lines[339,340]. This revealed a small subset of cell lines that were both highly dependent on HRAS (as demonstrated by a proteome-wide CRISPR KO screen) and sensitive to tipifarnib (Fig. **3.2.14a**). Of these cell lines, RL952, MELJUSO and T24 were obtained and screened for tipifarnib-sensitivity using IncuCyte analysis. MELJUSO and RL952 cells were found to have desirable EC50s (<100 nM), while T24 cells were not sufficiently tipifarnib sensitive (data not shown) (Fig. **3.2.14b**). Furthermore, the T24 cell line was found to have a relatively low transfection efficiency by flow cytometry analysis (<25%) and was excluded from further experiments in favor of MELJSUO and RL952 (Appendix Fig. **7.8**). Unfortunately, the top candidate cell line NCIH1915, indicated by the scatter plot, could not be obtained for evaluation.

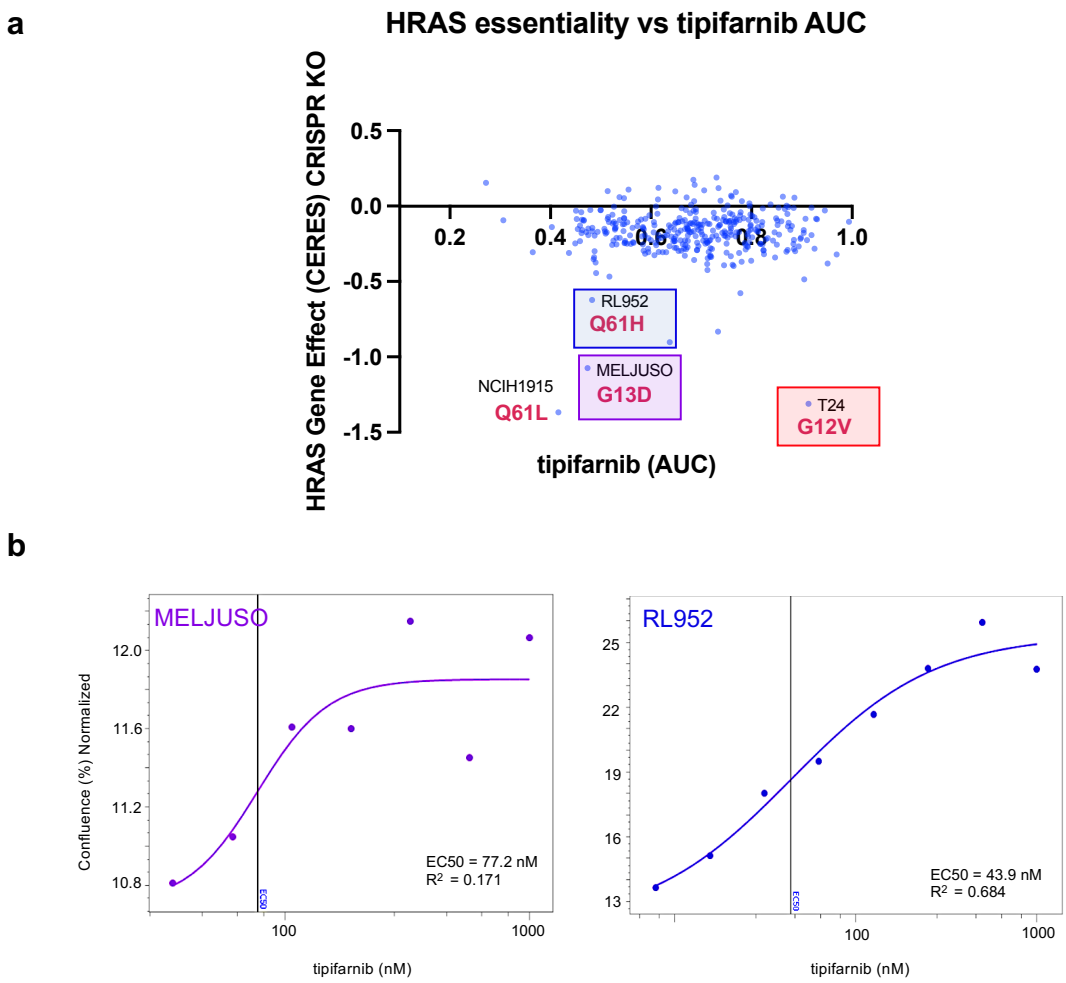

Figure 3.2.14. Second phase of resistance mutagenesis screening in H23 cells shows enrichment of loss-of-function HRAS mutants. (a) meta-analysis of publicly available CRISPR KO screen and tipifarnib sensitivity data identified a small subset of cell lines that exhibit both dependence on HRAS and tipifarnib sensitivity (data curated by DepMap). AUC – area under curve (normalized cell viability values from the PRISM drug repurposing screen). **(b)** Tipifarnib toxicity profiling of two acquired cell lines (MelJuso, RL952). EC50 values generated by IncuCyte analysis and associated software (n=4).

MELJUSO cells (cutaneous melanoma) harbor the G13D HRAS activating mutation and were found to be dependent on HRAS in both CRISPR and RNAi studies (based on publicly available data from DepMap). However, these cells also harbor an activating NRAS mutation, which may prove to be problematic in the same way that the activating $KRAS^{G12C}$ mutation did in the previous H23 model[341]. However, these cells were still taken forward for further experiments. In contrast, RL952 cells (uterine adenosquamous

carcinoma) are exclusively HRAS driven and harbor the Q61H mutation; these cells were also taken forward for mutagenesis experiments[342].

MELJUSO and RL952 cells were also found to have reasonable transfection efficiencies, as determined by live-cell fluorescence imaging analysis conducted with an IncuCyte, the workflow of which was outlined earlier in this chapter (Fig. **3.2.15a,b**). However, use of a newer generation transfection agent (Lipofectamine 3000, ThermoFisher) was necessary to achieve this.

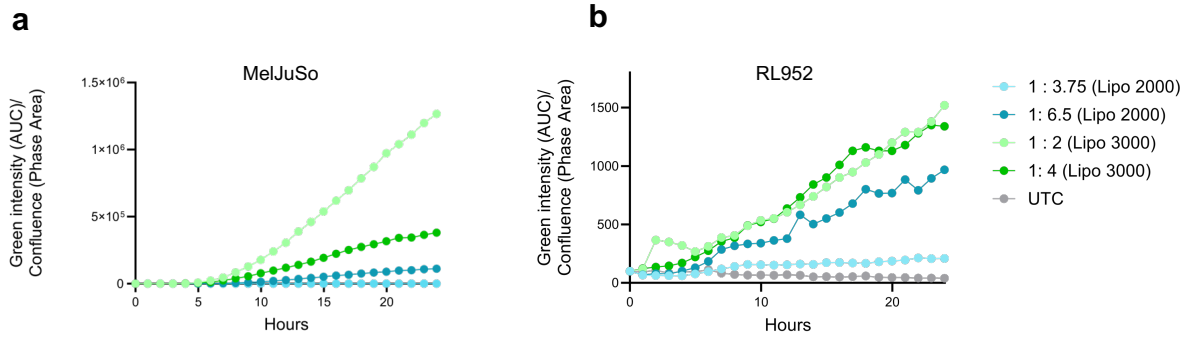

Figure 3.2.15. Evaluating transfection efficiency in MelJuSo and RL952 cell lines. Transfection efficiency and optimal conditions were established in MelJuSo **(a)** and RL952 **(b)** cell lines using an eGFP-plasmid to monitor transfection in an IncuCyte device. Different ratios of the transfection agents Lipofectamine 2000 and 3000 were tested with a set amount of DNA. Efficiency is defined as green fluorescence intensity divided by cell confluence to account for cell death after transfection.

MELJUSO and RL952 cell lines were then stably transduced with a Cas9 construct to allow efficient mutagenesis following transfection with sgRNA-expression vectors (Fig. **3.2.16a**). The selected Cas9 construct also featured a FLAG-tag that could be used to establish successful transduction by Western blot. Briefly, HEK293T cells were transfected with a second-generation LVX Cas9-containing construct, harboring a G418-resistance gene. A packaging vector (HIVpack) and a viral envelope vector (VSV-G) were also co-transfected alongside the Cas9 construct. After virus production, which occurs over 3 days and is terminated by death of the producing HEK293T cells, the virus-containing media was harvested and filtered to remove residual HEK293T cells and associated debris in order to avoid receiving cell contamination. Virus-containing media was then diluted (1:2 and 1:4) with fresh media and Polybrene (hexadimethrine bromide),

a reagent that enhances infectivity of the virus in the receiving cell lines by increasing viral adhesion to the cell surface. Approximately 5 days after transduction, cells were placed under selection (G418, or neomycin) until a non-transduced control population of cells died off (approximately 7 days, data not shown). Afterwards, surviving cells are placed under a maintenance dose of the selection antibiotic, which was a third of the selection dose (250 ng/mL).

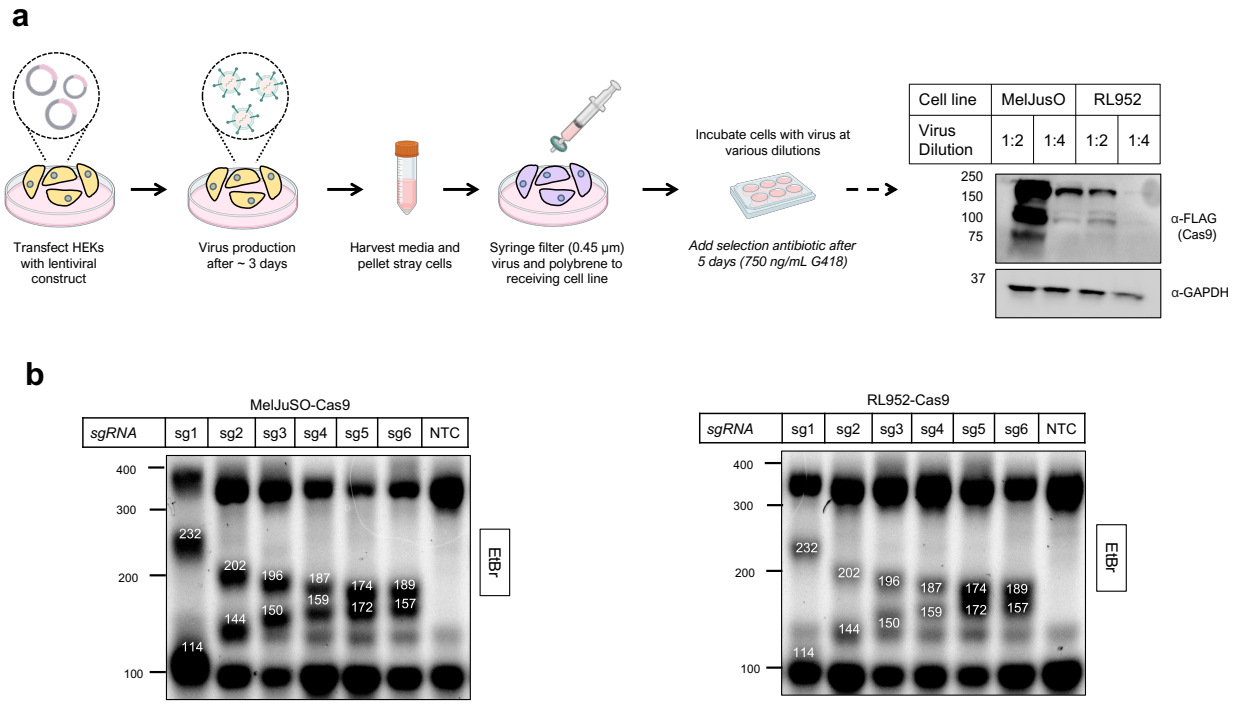

Figure 3.2.16. Generation and validation of HRAS-driven Cas9 cell lines. (a) Schematic demonstrating workflow for the stable transduction of FLAG-Cas9 in HRAS-driven cell lines (MelJuSo and RL952). Western blot (alpha-FLAG) validates successful transduction in both cell lines. **(b)** Surveyor T7 assay validates Cas9 and sgRNA activity in both transduced cell lines.

Western blot analysis of the surviving pools of both cells and their associated viral dilutions (1:2 and 1:4) indicated successful transduction of both MELJUSO and RL952 lines (Fig. **3.2.16a**). Ultimately, cells from the MELJUSO (1:4) population and RL952 (1:2) population were kept for future studies as they exhibited a similar level of Cas9 expression.

Cas9 activity and on-target efficacy of the previously designed HRAS sgRNAs was established using the T7 mutagenesis surveyor assay. Again, all sgRNAs showed on-

target activity, whilst also validating the successful constitutive expression of Cas9 in each of the cell lines (Fig. **3.2.16b**).

These conditions were then taken forward for CRISPR-enhanced drug-resistance mutagenesis. On this iteration of the screen, tipifarnib (100 nM) was used as the sole selection agent, since the $KRAS^{G12C}$ mutant was not present in either cell line. Moreover, there are currently no direct inhibitors of NRAS in the case of the MELJUSO line, meaning that NRAS was left unrestrained in this iteration of the screen[343].

The drug-resistance mutagenesis screen was then conducted using similar parameters to the initial H23 iteration. However, due to issues with IncuCyte use around this time, only starting and end-point images for confluency analysis were taken. The initial phase of the CRISPR-enhanced drug-resistance mutagenesis screen indicated a relatively high indel frequency for MELJUSO cells, and comparatively lower percentages for RL952 cells, as determined by ICE analysis of mutagenized samples taken at day 3 during cell transfer (Fig. **3.2.17a**). This was cautiously attributed to the overall lower transfection efficiency in the RL952 line. It remained possible that Cas9 expression was being lost over time in the RL952 line, however this was not confirmed at the time of the experiment. End-point confluence for each cell line is shown in Fig. **3.2.17b,** which occurred a total of 16 days following addition of the selection drug (100 nM tipifarnib), and approximately 6 days following expansion into 6-well plates. Genomic DNA was extracted from these samples, however, disappointingly, completion of PhD lab work prevented further analysis. Processing and amplicon sequencing analysis of these samples will thus be undertaken in the near future.

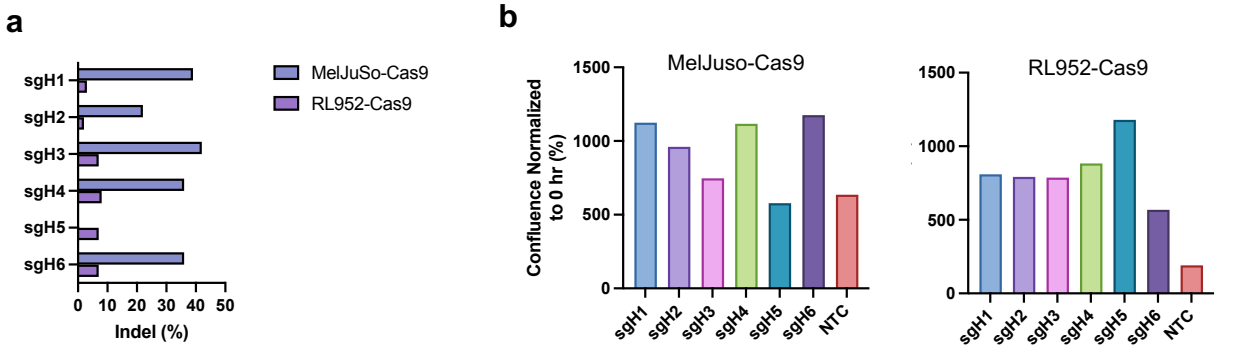

Figure 3.2.17. Drug-resistance mutagenesis of HRAS-driven cell lines. (a) Indel frequency following sgRNA transfection of MelJuSo and RL952-Cas9 cell lines determined by ICE analysis. The MelJuSo sgH5 sequence file was not of sufficient quality for ICE analysis. **(b)** End-point confluence analysis of MelJuSo and RL952-Cas9 lines following CRISPR-enhanced drug-resistance mutagenesis of HRAS (n=1).

3.2.7. Adapting CRISPR-enhanced drug-resistance mutagenesis screening to 3D cell culture models

In vitro 2D cultures (i.e. cell monolayers) offer convenience and scalability in cancer research, particularly for protocols that require complex perturbation regimes, genetic manipulation, or significant amounts of protein. While these models still form the backbone of biological and disease research, they often fail to replicate important features of tumor biology[344]. Monolayers lack the complex cell contacts, hypoxic conditions, cell heterogeneity and altered metabolisms that form the hallmarks of many cancers. The presentation of these features within a studied model can be essential to evaluate tumor dependencies and potential treatments. Although these parameters are usually accounted for in complex xenograft and animal models that sometimes follow initial 2D experiments, these are markedly more difficult to set up and manipulate. By contrast, 3D spheroid models are easily generated by the use of ultra-low adherence plates, where cell aggregation and the secretion of natural extracellular matrix factors drive formation of spheroids in various cell types[345].

Several recent studies have found that tumor dependencies can vary greatly between 2D and 3D models[346,3473.] For example, CREB-binding protein (CREBBP) inhibitors are commonly used as cancer treatments in the clinic, however CRISPR screens in 2D and 3D LUAD models demonstrated that CREBBP KO inhibited growth in 2D while surprisingly promoting growth in 3D models, suggesting that CREBBP-based therapies should be avoided in certain types of cancers[344]. Other studies have shown divergent responses to KRAS inhibition between 2D and 3D models, which is largely governed by hypoxic stressors that are more efficiently captured using 3D models[348]. Consequently, it would also be expected that resistance mechanisms emerge differently between 2D and

3D models, particularly in the case of RAS proteins, which have significant roles in metabolic rewiring and matrix stabilization.

Thus, as an alternative approach, a 3D model for CRISPR-enhanced drug-resistance mutagenesis was conceptualized. Using low adherence U-bottom 96-well plates, spheroids can be formed in a reproducible and relatively high-throughput manner[3473.] IncuCyte imaging and analysis would then be employed for monitoring spheroid formation and subsequent treatment effects, which is often qualitatively visualized by disintegration or regression of the drug-treated spheroid.

MELJUSO and RL952 cells were then tested for tipifarnib responses in spheroid models. This revealed that both cell lines retained sensitivity over the course of an 8-day treatment regime, which included refreshing tipifarnib-containing media every 2 days (Fig. **3.2.18**). MELJUSO cells appeared to be more sensitive to tipifarnib, however since IncuCyte analysis was unable to differentiate spheroid roughness or density, which are features that are relevant in the study of drug responses in 3D, it was difficult to make direct comparisons between cell lines, as well as with their corresponding 2D results. A more downstream approach, such as evaluating RAS activation, would be more appropriate in this regard.

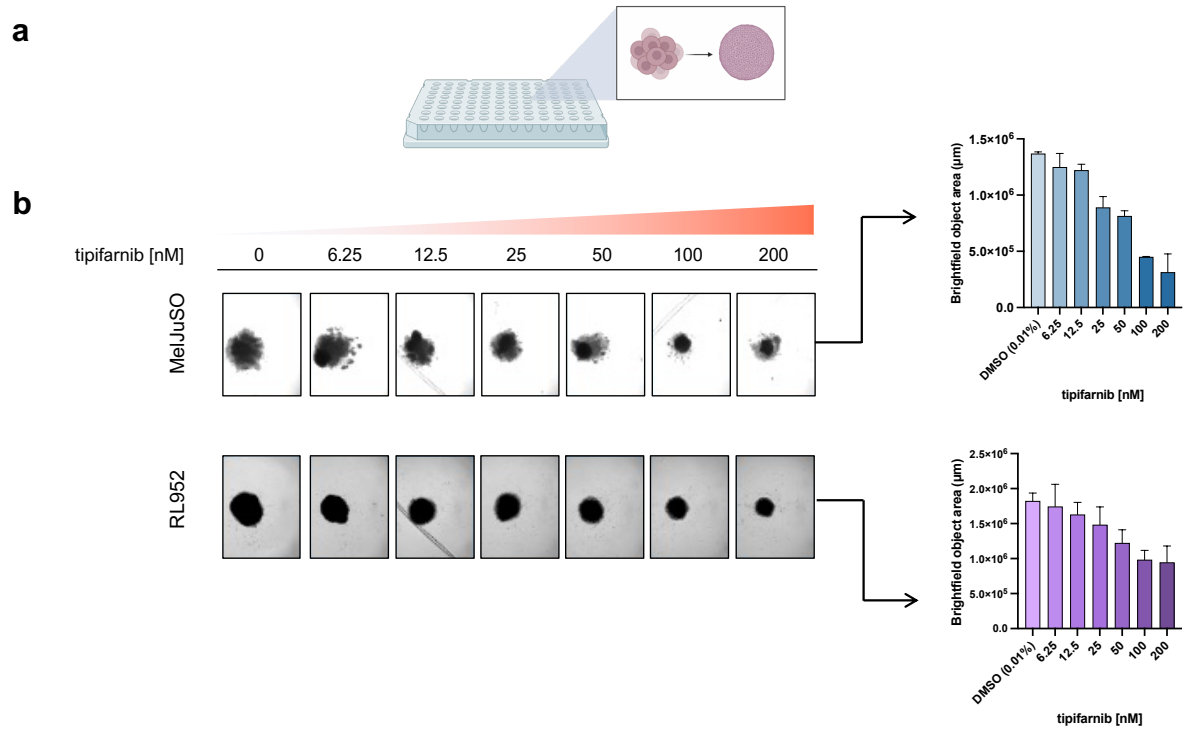

Figure 3.2.18. Establishing tipifarnib toxicity in spheroid models of HRAS-driven cell lines. Tipfiarnib toxicity was evaluated in **(a)** MelJuSo and **(b)** RL952-Cas9 cells using a spheroid assay, whereby following a 3-day spheroid formation period, cells are treated with increasing concentrations of tipifarnib. Spheroid size is then determined using IncuCyte analysis. Images from a representative replicate is shown here. Bar graphs of spheroid size are also provided (right) (n=3).

Having established tipifarnib sensitivity in both HRAS-driven cell lines, a preliminary drug-resistance mutagenesis screen was undertaken. A workflow was devised such that transfection took place before spheroid formation, to ensure homogenous transfection and mutagenesis efficiency across the samples (Fig. **3.2.19a**). After the acquisition of mutations within the standard 3-day period, cells were transferred to the low-adherence U-bottom plates for spheroid formation, which generally occurs within a 2-day period (Appendix **Fig. 7.9**). Following spheroid formation of the mutagenized samples, selection was initiated by addition of 200 nM tipifarnib, which was more aggressive than the 2D treatment to ensure drug penetration. This screen was conducted simultaneously to the aforementioned 2D screen. Consequently, the same mutagenized samples (i.e. sgRNA transfected cells) were split between 2D and 3D models to allow a more direct comparison of enriched acquired mutations.

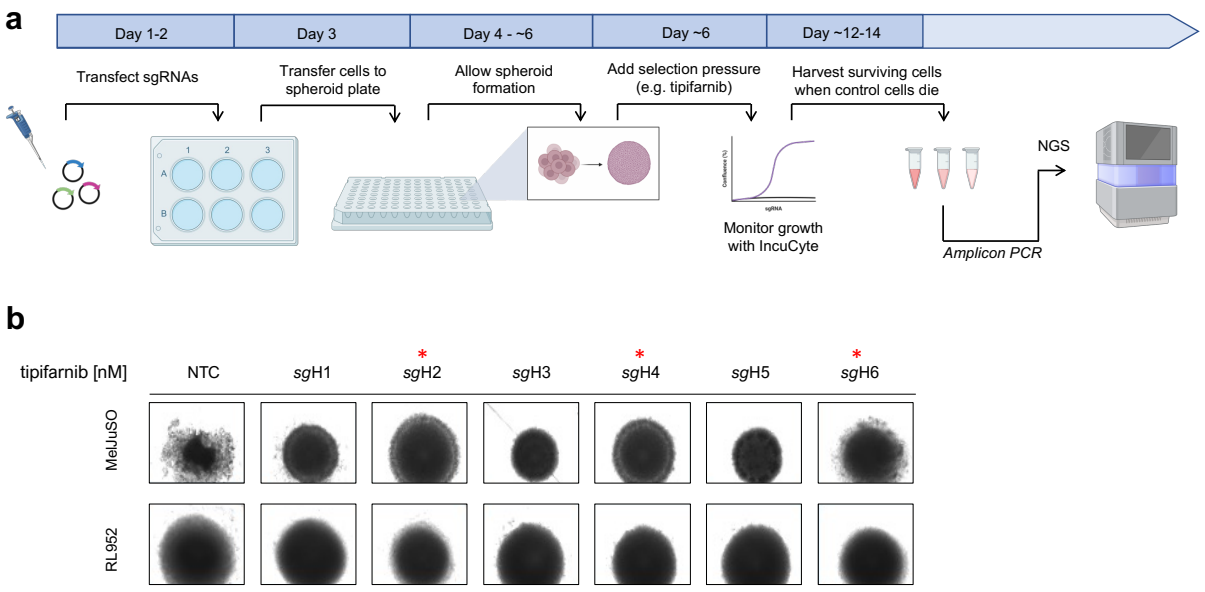

Figure 3.2.19. CRISPR-enhanced drug-resistance mutagenesis as applied to 3D spheroid model. (a) Schematic showing devised workflow of drug-resistance mutagenesis in a novel spheroid model, whereby initial transfection of sgRNA in Cas9-expressing cells results in a mutagenized cell population that are then seeded into spheroid plates. Following spheroids formation, tipifarnib is added and spheroid size is monitored using IncuCyte analysis. After significant growth of mutagenized cells over the control population (NTC), cells are harvested for NGS analysis. **(b)** End-point results of screen in MelJuSo and RL952 cells. MelJuSo selection appeared to be successful due to the observed differential growth between NTC and mutagenized cells (n=1). Red asterisks indicate significant growth over NTC control.

End-point imaging was used to evaluate drug-resistance proliferation, that is, proliferation of mutagenized samples that exceeds that of the control sample. After a ~ 16 day selection period, the NTC MELJUSO sample showed signs of tipifarnib sensitivity, whilst several mutagenized samples continued to proliferate. However, RL952 NTC cells did not exhibit sensitivity, meaning that drug-resistance proliferation was not established for the commensurate mutagenized samples. This was hypothesized to be due to a higher seeding density before selection (for both cell lines), resulting in poorer drug penetration. This may also be compounded by the specific properties of the RL952 spheroids, which visually appeared to be denser and less diffuse compared to the MELJUSO spheroids. Thus, sensitivities established in the previous spheroid assay were hypothesized to be not well replicated in this iteration of the screen. This was also assumed to be the reason for the lower observed MELJUSO cell sensitivity, although some proliferation over the

control sample was demonstrated. Regardless, all samples were harvested for genomic DNA extraction and will be analyzed in the near future, along with the samples from the associated 2D experiment. The screen is also planned to be repeated with lower seeding densities in an attempt to replicate the sensitivities demonstrated in previous experiments. Moreover, as these spheroid selection plates are in a 96-well plate format, replicates can more easily be utilized (compared to 6-well plates for the 2D screen) and will be incorporated in the next iteration of this experiment.

3.2.8. Investigating *S*-prenylation-dependent *S*-palmitoylation in the context of tipifarnib treatment.

In the previous sections of this chapter, some preliminary evidence emerged from the drug-resistance mutagenesis screen that suggested dynamic *S*-palmitoylation of RAS proteins may play a role in alternative prenylation. As HRAS uniquely has two near-adjacent *S*-palmitoylation sites within its HVD, this could be hypothesized to play a role in its interaction with proteins that may prevent alternative prenylation[349]. For example, complete *S*-palmitoylation of HRAS and FBXL2 prevents PDE6D binding as a result of steric hinderance imparted by the lipids[72].

Moreover, FTI treatment may lead to changes in other PTMs including *S*-palmitoylation, which in turn may reveal new vulnerabilities that can be exploited upon tipifarnib treatment, for example. This could be especially significant given that there is a paucity of targeted therapeutics for *S*-palmitoylation, particularly for palmitoyl acyltransferases (PATs), the enzymes that catalyze *S*-palmitoylation[170].

As most studies that have attempted to deconvolute *S*-prenylation criteria (i.e. propensity to be prenylated by either FTase or GGTase) were conducted using either recombinant proteins or overexpression models, it remains to be seen how *S*-palmitoylation dynamics affects prenylation status, or vice-versa in the presence of an FTI. It is important to note that *S*-prenylation is canonically known to occur shortly after translation[350]. This is primarily because PATs are largely membrane-associated, whilst prenyltransferases are

cytosolic and thus have priority access to dual substrate proteins[26,351]. This makes it less probable that *S*-palmitoylation has a direct effect on *S*-prenylation status under normal conditions. Nevertheless, *S*-prenylation dynamics in the presence of tipifarnib, specifically how soon after translation a substrate is alternatively prenylated, remains unexplored. In fact, a small population of unprenylated KRAS has been shown to accumulate after treatment with an FTI, suggesting that alternative prenylation may perhaps be restrained immediately following translation (unpublished data). This also putatively suggests that there may be a mechanism that delivers prenyl-switching substrates, such as KRAS and NRAS, to the GGTase, which in turn is unable accommodate HRAS in the same fashion.

Considering that *S*-prenylation holds a degree of temporal control over subsequent protein modifications, it is somewhat surprising that changes in other types of protein lipidation have not been looked at in the context of prenylation inhibition. Thus, a simple approach was initially designed to investigate the effect tipifarnib has on *S*-palmitoylation (Fig. **3.2.20a**). Here, an acyl-PEG exchange assay was employed, where lysates treated with or without tipifarnib are subjected hydroxylamine treatment[352]. This cleaves the thioester *S*-palmitoyl bond, removing the lipid moiety from its substrate. Maleimide-PEG (here, 10 KDa) then is introduced, which reacts with the newly exposed, previously *S*-palmitoylated cysteine. Subsequent Western blot analysis of a *S*-palmitoylated protein of interest reveals band shifts that correspond to the molecular weight of the added maleimide-PEG group, which in turn reflects the number of *S*-palmitoylation sites on that given protein.

This was initially performed for HRAS, which confirmed that it is doubly *S*-palmitoylated in cells at nearly equimolar concentrations, with the singly *S*-palmitoylated species potentially being slightly more abundant based on band intensity (Fig. **3.2.20b**). However additional replicates and orthogonal validation would be needed to confidently establish this, as HRAS antibodies have been found to exhibit a low-level of pan-RAS binding due to high RAS homology (unpublished data). Interestingly, HRAS *S*-palmitoylation is decreased in the presence of a low concentration of tipifarnib (10 nM), with the singly *S*-palmitoylated species now clearly dominating the HRAS pool. *S*-palmitoylation becomes

more severely restricted at the secondary site with increasing concentrations of tipifarnib (100 nM), however some proportion of the singly *S*-palmitoylated species does appear to remain in the cellular pool. This suggests that at least the second instance of *S*-palmitoylation is dependent on *S*-prenylation. PANC1 cells, as opposed to H23, MELJUSO or RL952 cells, were used here in an attempt to capture KRAS4A *S*-palmitoylated population by Western blot (as they harbor the readily detectable $KRAS^{G12D}$), however these results were not conclusive and likely obscured by detection of the major, non-palmitoylated isoform KRAS4B (data not shown).

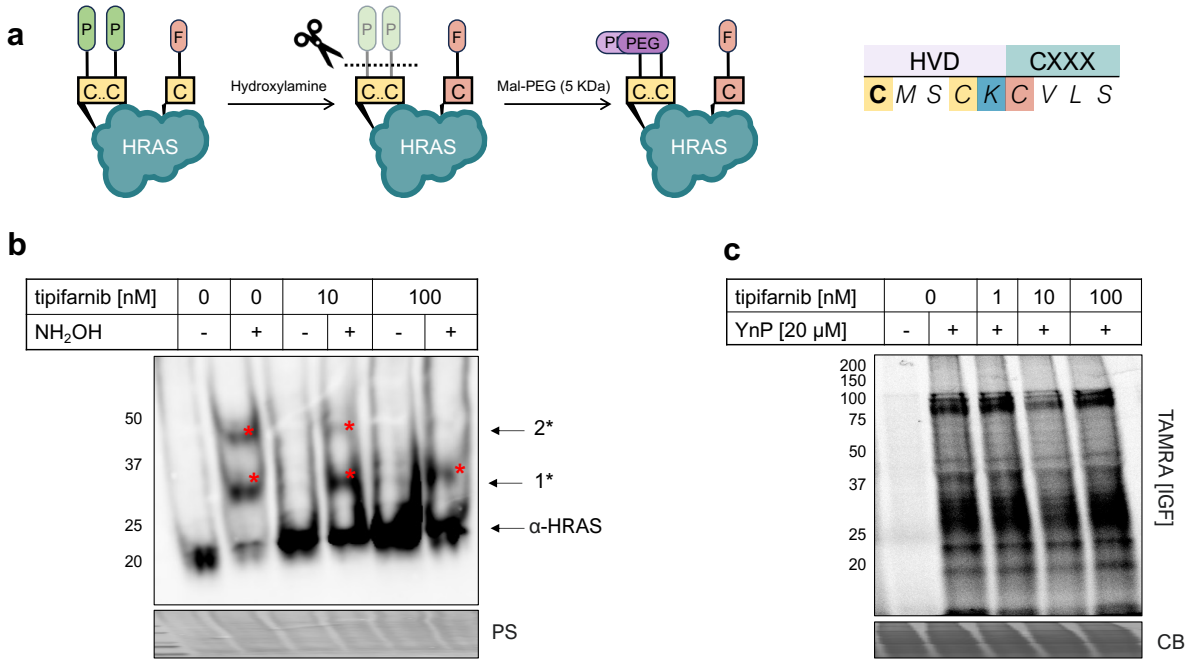

Figure 3.2.20. *S*-palmitoylation dynamics in the presence of tipifarnib. (a) Schematic demonstrating workflow for acyl-PEG exchange (APE), whereby treatment with hydroxylamine cleaves pre-existing *S*-palmitoyl groups on proteins in lysate. Maleimide-PEG (10 kDa) is then added to replace the cleaved groups at *S*-palmitoylated sites. Gel analysis reveals a molecular weight shift in proteins that are endogenously *S*-palmitoylated. HRAS *S*-palmitoylation sites and CXXX-box is shown for reference. **(b)** Acyl-PEG exchange assay for HRAS, showing a shift in molecular weight corresponding to 2 known *S*-palmitoylation sites, and subsequent loss of *S*-palmitoylation upon addition of tipifarnib. **(c)** Global labelling of lysates of YnP-treated cells reveals no obvious changes in profile with increasing concentrations of tipifarnib (AzT; TAMRA in-gel fluorescence).

It is well-established that RAS proteins require a secondary signal for plasma membrane localization, where they exert most, but not all, of their downstream signaling function[234]. For KRAS-4B, this is mediated by a strong polybasic region (PBR) within its HVD, where electrostatic interactions with the inner leaflet of the plasma membrane allow efficient anchoring. For HRAS, NRAS and KRAS-4A however, this step is *S*-palmitoylation dependent, meaning both *S*-prenylation and complete *S*-palmitoylation are necessary for plasma membrane localization. Previous studies have shown that continuous cycles of *S*-palmitoylation (carried out by PATs) and de-palmitoylation (carried out by acyl-protein thioesterases, or APTs) drive RAS endomembrane compartmentalization, and may provide an explanation for how isoform-specific signaling pathways are maintained[349,350,353]. Singly *S*-palmitoylated NRAS for example, has a longer residence time at the Golgi compared to doubly *S*-palmitoylated HRAS under normal conditions[350,354]. Removal of any of the palmitate groups resulted in the redistribution of NRAS and HRAS across cellular endomembranes, including the ER, Golgi, and plasma membrane, which remained in equilibrium in the absence of growth factor signalling. Interestingly, HRAS mutant C184S (singly *S*-palmitoylated at C181) was shown to mimic NRAS Golgi residence times with limited plasma membrane partitioning, whilst the C181S mutant was almost exclusively Golgi resident[350,353]. Tipifarnib treatment in this instance appeared to preferentially reduce *S*-palmitoylation on one HRAS cysteine, however it is unclear which cysteine (C181 or C184), or to what extent this occurs.

It is known however that singly *S*-palmitoylated HRAS at C181 is more efficiently transported to the plasma membrane, albeit less so than doubly *S*-palmitoylated HRAS. Since tipifarnib prevents membrane anchoring of HRAS, it can be hypothesized that C181 is potentially the more sensitive site. This may also support the hypothesis that HRAS is potentially *S*-palmitoylated by two different PATs, or alternatively PATs localized to different cell compartments (ER and Golgi, for example)[355]. Ultimately, these dynamics are important for understanding HRAS trafficking dynamics in the context of FTI treatment, as rewiring of transport and localization patterns can profoundly alter RAS signaling, and endomembrane-localized signaling pathways are functionally distinct from one another[354,355].

To further elucidate what extent *S*-prenylation has on global *S*-palmitoylation, a probe-based approach was employed. Here, PANC1 cells were treated with and without tipifarnib, and labelled with alkyne palmitate (YnPalm, 20 μM) overnight[356]. Cells were harvested and subjected to click ligation to AzT for in gel fluorescence readout. In gel fluorescence did not reveal any major changes to YnPalm incorporation upon increasing concentrations of tipifarnib (Fig. **3.2.20c**). This may partly be associated with the fact that only a small subset of *S*-palmitoylated proteins is also *S*-prenylated (about 3.7%). A list of these proteins is provided in Fig. **3.2.21**.

a

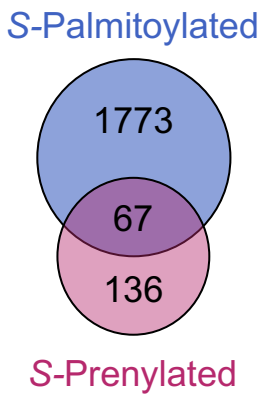

b

F + Palm	GG + Palm	RAB + Palm	F and/or GG + Palm
CNP	ALDH3B1	RAB1A	CDC42
GNAI1	DIRAS2	RAB1B	RAP2A
GNAI2	FBXL2	RAB2A	RRAS2
HRAS	RAC1	RAB2B	YKT6
INF2	RAC2	RAB3A	
INPP5A	RALA	RAB3B	
KRAS	RALB	RAB3D	
LMNA	RAP1A	RAB4A	
LMNB1	RAP1B	RAB4B	
LRRFIP1	RAP2B	RAB5B	
NAP1L1	RHOA	RAB5C	
NME1	RHOB	RAB6A	
NRAS	RHOC	RAB6B	
PALM	RHOG	RAB7A	
PALM2	RRAS	RAB7B	
PCYOX1	UBL3	RAB8A	
PSIP1		RAB8B	
PTGIR		RAB10	
RAP2C		RAB11A	
RHEB		RAB14	
RHOJ		RAB18	
RHOQ		RAB27A	
USP32		RAB35	
		RAB38	

Figure 3.2.21. Meta-analysis of dual *S*-prenylation and *S*-palmitoylation substrates. Substrate co-occurrence of *S*-prenylation and *S*-palmitoylation using data extracted from SwissPalm and a self-curated *S*-prenylation datasets (UniProt). **(a)** Overlap of annotations

showing only a 3.7% co-occurrence rate for dual substrates. **(b)** List of substrates categorized by type of *S*-prenylation.

Because a comparatively small proportion of *S*-palmitoylated proteins was expected to be affected by tipifarnib treatment, an analogous proteomics strategy was used to uncover any effect that was not revealed by in gel fluorescence analysis alone. To this end, a proteomic study of YnPalm-enriched proteins in the presence and absence of tipifarnib was undertaken (Fig. **3.2.22a**). After pre-treatment with tipifarnib (10 and 100 nM), YnPalm was introduced for overnight metabolic labelling in H23 cells. Cells were harvested the next day, and following click ligation to AzB, labelled lysates were subjected to on-bead biotin-neutravidin enrichment (described in Methods). Enriched proteins were digested, and the resultant peptides were processed for label-free quantification (LFQ).

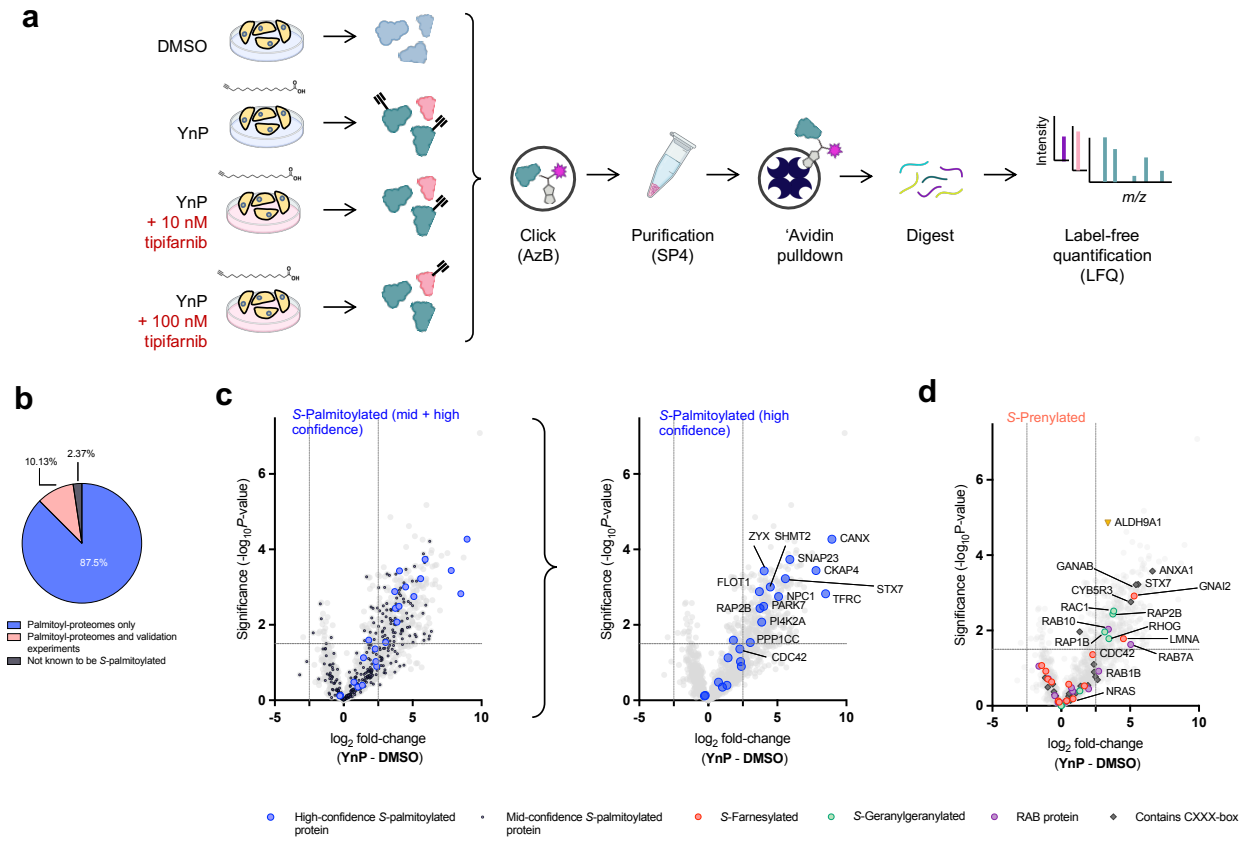

Figure 3.2.22 Global profiling of *S*-palmitoylation in H23 cells using YnPalm-based enrichment. (a) Schematic of YnPalm-based enrichment for proteomic profiling of *S*-palmitoylation. Following a 1-2h pre-treatment with tipifarnib (10 nM, 100 nM), YnP is added to cells for overnight metabolic incorporation. Cells are harvested the next day and lysates are

processed using standard click-ligation (AzB) and enrichment, described in Methods. **(b)** Distribution of *S*-palmitoylation status confidence of significantly enriched substrates (SwissPalm). **(c)** YnP-enrichment versus vehicle (DMSO) control. High and mid-confidence *S*-palmitoylated proteins are highlighted. **(d)** *S*-prenylated proteins enriched using YnP. Log_2FC cut-off set to ±2.5 for LFQ experiments (FDR = 0.05; n=3). See legend for graph annotations.

Initial analysis indicated successful enrichment of *S*-palmitoylated proteins (S0 = 0.1, FDR = 0.05) over the vehicle control (DMSO), with 87.5% of enriched proteins previously found in published palmitoyl-proteomes, and a further 10.7% validated using orthogonal analyses (SwissPalm)[357] (Fig. **3.2.22b** and **c**). High-confidence hits are highlighted in Fig. **3.2.22d**, which included high abundance *S*-palmitoylation markers such as CANX (calnexin). Various *S*-prenylated substrates were also enriched, including LMNA, RAC1, RHOG and RAP1B, among other proteins validated as dual substrates (Fig. **3.2.22e**). Validated dual substrate CDC42 was also enriched, however it did not make the significance cut-off by a small margin. These results are summarized in **Table 3.1**. NRAS was notably not significantly enriched, but this may be obscured by insufficient unique peptide identification, as many NRAS peptides would overlap with KRAS and HRAS peptides, thereby resulting in poor RAS isoform deconvolution. This also likely contributed to the lack of HRAS quantification in this study, which was unfortunate given our specific interest in HRAS *S*-palmitoylation dynamics. Surprisingly, ALDH9A1 was also significantly enriched, perhaps indicating that lipidation of this protein is not isoprenoid specific, as noted in the previous chapter[274].

Table 3.1: Enriched CXXX proteins in YnP dataset

Gene	Accession[1]	Prenyl group	CXXX	Palmitoylated?
ANXA1	P04083	F	CGGN	Validated
GNAI2	P04899	F	CGLF	Validated
LMNA	P02545	F	CSIM	Predicted
RAP2B	P61225	F	CVIL	Validated
NAP1L1	P55209	F	CKQQ	Predicted
ALDH9A1	P49189	F	N/A	N/A
RAP1B	P61224	F/GG	CQLL	Validated
CDC42*	P60953	F/GG	CVLL/CCIF	Validated
RAB7A	P51149	GG	*CSC	Validated
RAB10	P61026	GG	*KCC	Predicted
RHOG	P84095	GG	CILL	Predicted
RAC1	P63000	GG	CLLL	Validated
GANAB	Q14697-3	ND	CCWC	Validated
CYB5R3	P00387	ND	CFVF	Predicted
STX7	O15400-2	ND	CMLM	Validated

[1]Uniprot accession ID; ND = not determined

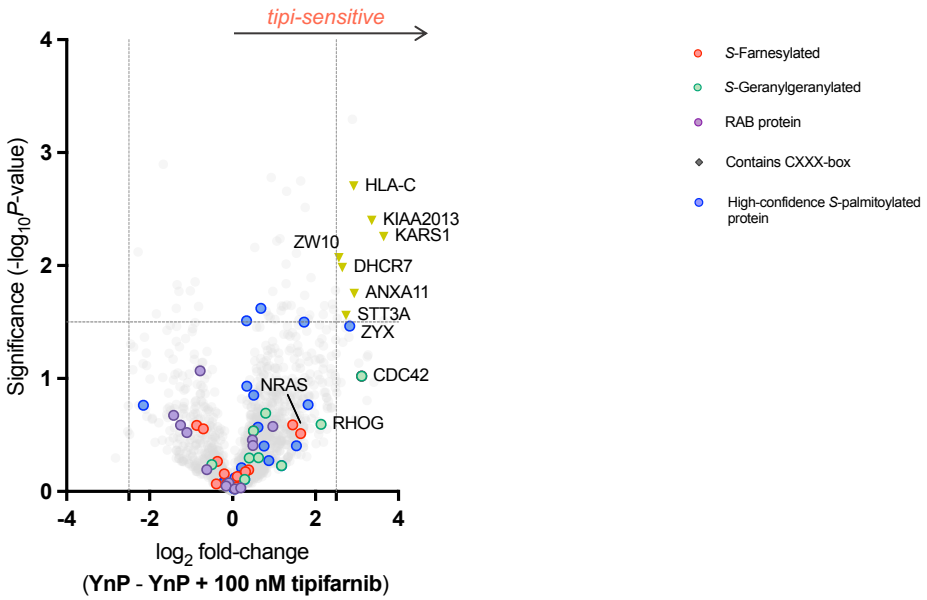

Figure 3.2.23. Tipifarnib-sensitive *S*-palmitoylated substrates in H23 cells. Volcano plot showing tipifarnib-sensitive YnP substrates (upper right quadrant, highlighted as yellow triangles). Log_2FC cut-off set to ±2.5 for LFQ experiments (student t-test; S0 = 0.01; FDR = 0.05; n=3). See legend for graph annotations.

Tipifarnib sensitivity was then investigated using both statistical analyses and profile plots (fold-change over background/control). A student t-test (YnP vs. YnP + 100 nM tipifarnib) revealed several substrates whose level of *S*-palmitoylation decreased upon tipifarnib treatment (Fig. **3.2.23**). Unexpectedly, most of these proteins are not *S*-prenylated. However, they were all identified in at least 2 publicly available palmitoyl proteome datasets (SwissPalm). These proteins (ZW10[358], ANXA11[358], KARS1[359], DHCR7[360], HLA-C[361], STT3A[362]) are also known to be associated with ER/Golgi trafficking or lipid biogenesis, which may suggest some downstream effect caused by tipifarnib-induced delocalization other *S*-prenylated proteins that are involved in these processes. For example, *S*-farnesylation of SPDL1 is required for ZW10 localization at the kinetochore during mitosis[295]. FTI-induced SPDL1 mislocalization may also result in destabilization or mislocalization of ZW10 that in turn affects its *S*-palmitoylation status. It may also be possible that changes in protein expression affect the results of the YnP pulldown, however preliminary analysis of whole proteome data (from Chapter 2) does not indicate changes in abundance of these proteins upon tipifarnib treatment.

Profile plots of YnP enrichment with increasing concentration of tipifarnib demonstrate that while several *S*-prenylated proteins do not exhibit changes in *S*-palmitoylation status upon tipifarnib treatment (such as LMNA and GNAI2), a small subset of *S*-farnesylated proteins lose YnP modification, including NAP1L1, CDC42, RRAS and NRAS (Fig. **3.2.24a-d**; Fig. **3.2.25a**). Interestingly, YnP-enrichment of RHOG, a canonically *S*-geranylgeranylated protein, was also observed to be depleted in tipifarnib-treated samples. While YnGG-labelling of RHOG was not significantly affected by tipifarnib treatment in the previous chapter, SmgGDS-607 KO significantly decreased both YnGG and low-abundance YnF labelling in H23 cells. Furthermore, membrane fractionation experiments revealed that RHOG was among the most significantly membrane delocalized proteins upon tipifarnib treatment, despite it not being canonically *S*-farnesylated. Though it is unclear what exactly engenders RHOG sensitivity to tipifarnib, it remains an interesting phenomenon and may have implications on the application of FTIs to other non-RAS-driven cancers. For example, loss of RHOG increases T-cell receptor signaling pathways in the absence of external stimuli[363]. RHOG inhibition, perhaps by way of delocalization, could theoretically enhance therapeutic modalities that require strong T-cell activation, such as in chimeric antigen receptor (CAR)-T cell therapy[364]. While RHOG is relatively understudied compared to other RHO proteins, including its role in T-cell activation, uncovering trends such as this provides some basis for investigating novel applications of FTIs to other diseases or treatment modalities.

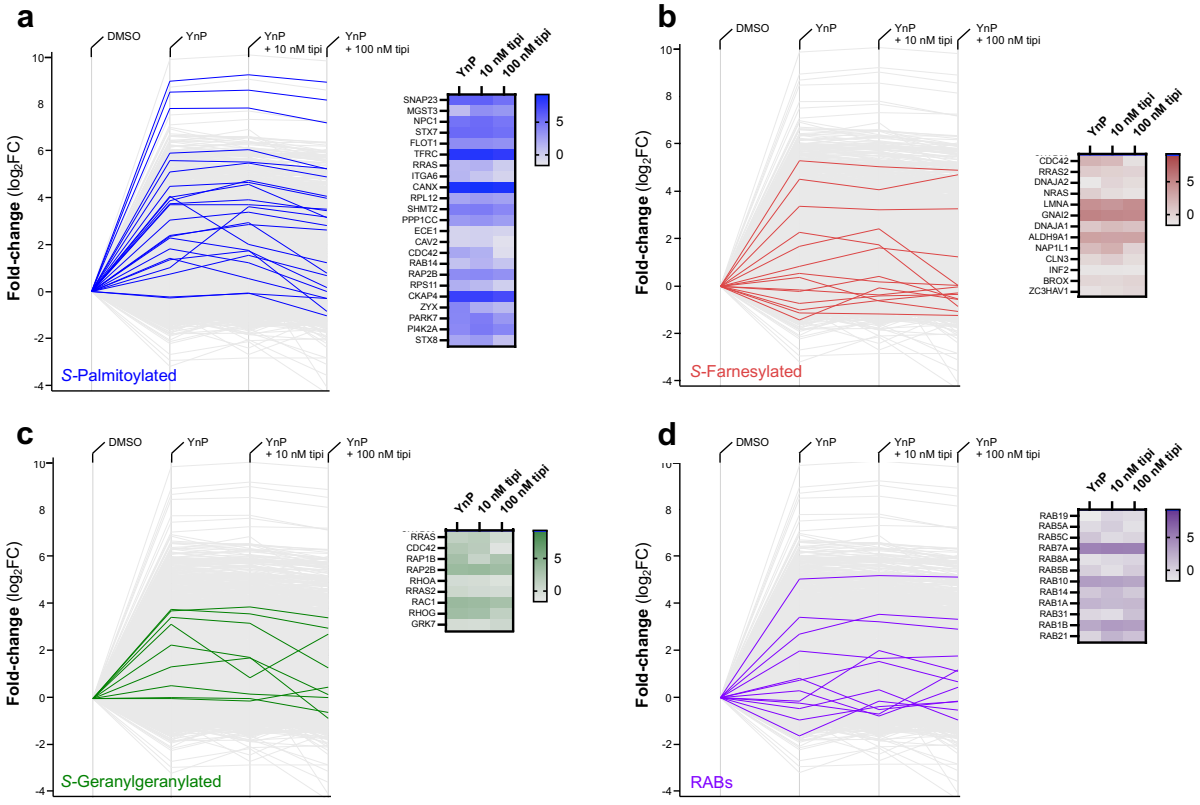

Figure 3.2.24. Global profiling of *S*-palmitoylation in H23 cells reveals FTI-induced changes in *S*-palmitoylation dynamics. Global enrichment profiles using YnP-enrichment. Annotations categorized substrates as **(a)** high-confidence *S*-palmitoylated proteins, **(b)** *S*-farnesylated, **(c)** *S*-geranylgeranylated and **(d)** RAB proteins. Heat-maps (colored by log_2FC) are provided to the right of each profile plot, representing a selection of known substrates (n=3).

As discussed previously, several *S*-palmitoylated proteins were also found to exhibit a level of tipifarnib sensitivity in this experiment. If this is a true finding, it would be expected that the *S*-palmitoylation status of these proteins depends on the activity of *S*-farnesylated substrates that are delocalized by tipifarnib, similar to the case previously put forth for ZW10. Using hierarchical clustering analysis (Pearson correlation; Perseus software), a large cluster of tipifarnib-sensitive proteins was identified within the dataset (Fig. **3.2.25a** and **b**). Among these proteins were RHOG, CDC42 and NRAS, which were previously noted to be tipifarnib-sensitive. STRING analysis of these proteins revealed statistical overrepresentation (FDR = 3.2E-02) of retrograde vesicle-mediated transport from the Golgi to the ER (biological process; GO:0006890), which could conceivably be mediated by a variety of *S*-farnesylated substrates. However, the majority of other proteins were

found to be related to cytoplasmic translation (FDR = 7.93e-05), which may be an indication that there was a considerable level of non-specific enrichment (i.e. high abundance ribosomal proteins).

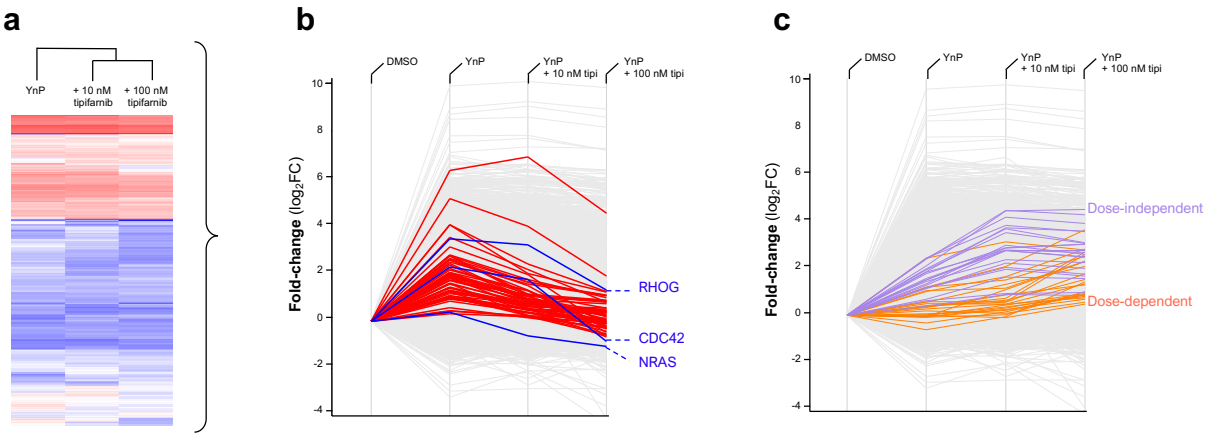

Figure 3.2.25 Hierarchical clustering analysis of YnPalm dataset reveals *S*-palmitoylated substrates sensitive to tipifarnib treatment. (a) Heatmap representing summary data of hierarchical clustering**. (b)** Profile plot highlighting substrates that exhibit decreased YnP-enrichment with increasing concentrations of tipifarnib (shown in red). RHOG, CDC42 and NRAS are highlighted *S*-prenylated proteins (shown in blue). **(c)** Profile plot highlighting substrates that exhibited increased YnP -enriched upon tipifarnib treatment. Dose -dependent cluster shown in orange, and dose-independent cluster show in purple. (n=3)

Interestingly, hierarchical clustering analysis also revealed both tipifarnib dose-dependent and independent increase in YnPalm labelling (Fig. **3.2.24c**). Among these, LYPLA1, the acyl-protein thioesterase for HRAS, was found to have increased YnPalm-enrichment with higher concentrations of tipifarnib. LYPLA1 is primarily a cytosolic APT, however can transiently localize to the Golgi or plasma membrane and has been suggested to regulate its own *S*-palmitoylation status[365]. It could be hypothesized that LYPLA1 differentially regulates its *S*-palmitoylation status when HRAS is unprenylated, such as by stabilizing *S*-palmitoylation rates for HRAS by sequestering itself in an inaccessible membrane compartment. However, extensive validation would be required to validate this phenomenon. For now, these remain interesting questions put forth by this hypothesis-generating experiment and await further investigation.

3.2.9. Revisiting RAS chimera proteins to investigate *S*-prenylation and *S*-palmitoylation interplay.

At the onset of this project, initial attempts at recapitulating RAS lipidation using overexpression models proved challenging. From unpublished reports, this was hypothesized to arise from the accumulation of delocalized “dead” RAS protein in the cytosol, which is said to be the result of overwhelming existing lipidation machinery by high RAS overexpression (unpublished data). Moreover, the production of various chimeric proteins was expected to be challenging, largely due to the COVID-19 pandemic which severely restricted our capacity for large scale vector generation.

We chose to revisit this strategy towards the end of the project in order to have a validation system in place for RAS *S*-prenylation dynamics. For example, this system would provide the basis for the generation of RAS chimeras that have switched-out HVDs or CXXX-boxes (e.g., HRAS with KRAS HVD; KRAS with HRAS CXXX-box, etc.). *S*-palmitoylation mutants could also be studied, including the previously discussed HRAS C181S and C184S mutants, to better understand their roles in RAS trafficking and localization. This would also provide a better model for the aforementioned acyl-exchange assay, since tagged RAS proteins could be more reliably identified by Western blot, without the caveat that many RAS antibodies exhibit a degree of isoform non-specificity.

Thus, a vector assembly strategy was devised, where KRAS-4A KRAS-4B, NRAS and HRAS genes were cloned into Flp-In T-Rex™ vectors (Invitrogen)[366]. This expression system allows the stable integration of a gene of interest from a single, stably integrated *Flp* Recombination Target (FRT) site at a transcriptionally active genomic locus under the control of a tetracycline inducible system. This allows isogenic and inducible expression of a protein of interest, giving temporal control over protein expression as well as control over the amount of protein expressed within a given timeframe. As a result, the Flp-In TRex system significantly reduces variability across experiments and attenuates overexpression of a given construct, which can lead to undesirable pleiotropic effects. For

example, overexpression of HRAS not only results in mislocalized protein, but can induce cellular senescence, which can hamper the metabolic incorporation of lipid probes[367].

Designed vectors could then be initially tested by transient transfection for proper expression and protein labelling by lipid probes, and then triaged to stable cell line production. Generation of Flp-In TRex cell lines also requires less time than typical stable cell line production (e.g. lentiviral transduction, monoclonal selection) as simple polyclonal selection results in a pseudo-monoclonal population of cells due to the ubiquity of the FRT site integration. That is, the integration of a transgene is only possible at one site in the genome, which is identical across all cells.

Initially, KRAS-4A, KRAS-4B, NRAS and HRAS WT genes were cloned into Flp-In TRex vectors using Gibson assembly. These were then mutated to create a) an *S*-prenylation control mutant (SXXX) and b) *S*-palmitoylation mutants using site-directed mutagenesis (SDM) (Fig. **3.2.26a**). An extended set of plasmids containing RAS chimeras were designed and synthesized in a similar manner (Appendix **Table 7.8a** and **b**). Initial benchmarking of these constructs was envisioned to be carried out using a medium-throughput technique shown in Fig. **3.2.26b**. Briefly, constructs would be transfected in 12-well plates, and after 24h, tetracycline would be used to induce low level expression. Following an optional tipifarnib pre-treatment (1-2h), lipid probes would be added and metabolically incorporated overnight. The next day, cells would be harvested and click ligated to a reporter molecule (AzT or AzTB), and processed on 96-well plates in a KingFisher device (discussed in the previous chapter and in Methods). TAMRA readout via in-gel fluorescence would then reveal incorporation patterns of the probes, which can be further validated using an enrichment protocol (using the KingFisher).

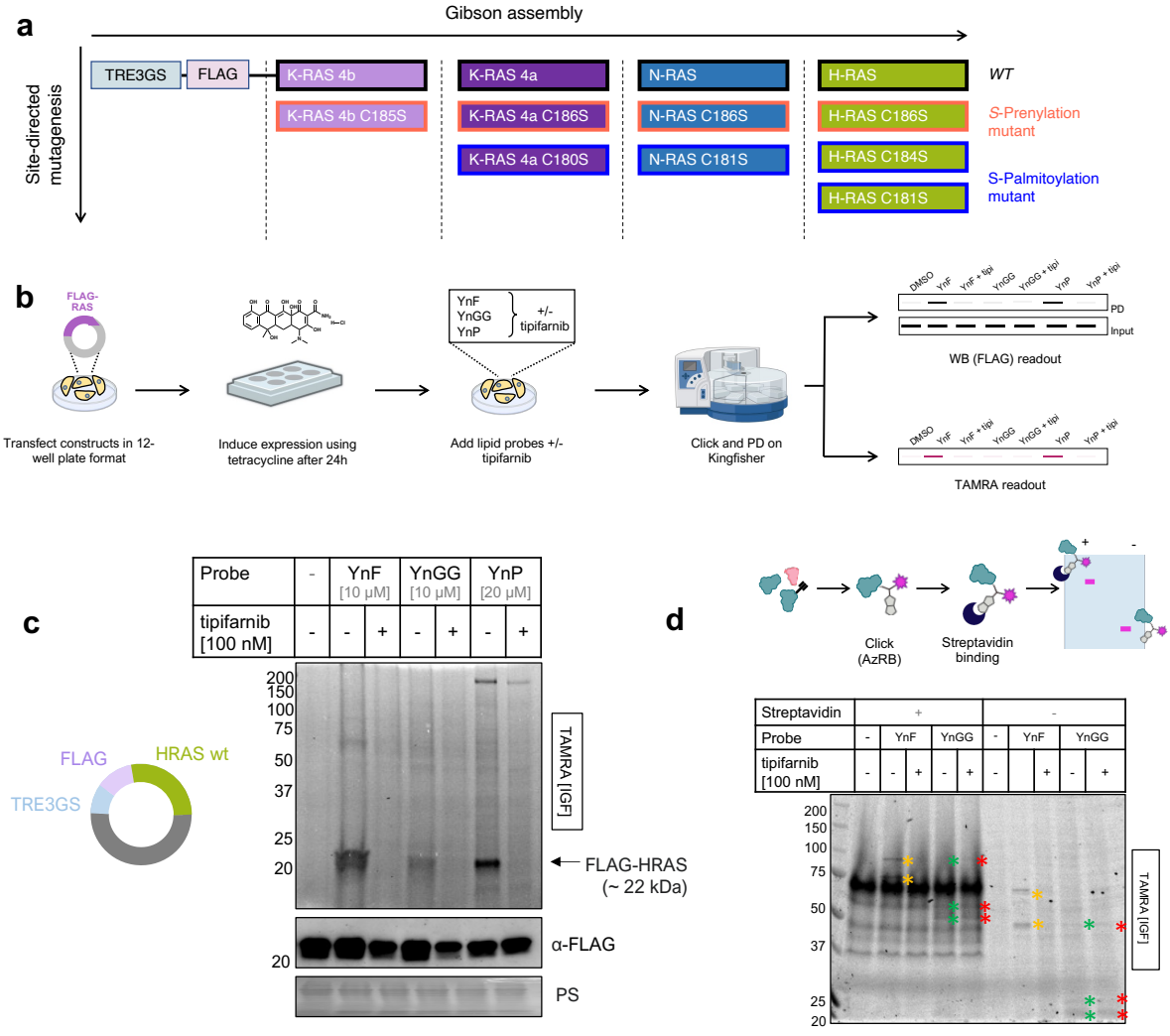

Figure 3.2.26. Designing RAS lipidation mutants to validate role of *S*-palmitoylation in alternative prenylation. **(a)** design of RAS isoform plasmids and corresponding lipidation mutants using Gibson assembly and site-directed mutagenesis, respectively. **(b)** construct validation strategy using a probe labelling and KingFisher-assisted click-ligation clean-up and/or bead-based enrichment. **(c)** Probe labelling profile using an in-gel fluorescence (IGF) readout (TAMRA) of the designed HRAS WT construct. Probe labelling pattern demonstrates loss of YnF, as well as YnP, labelling upon tipifarnib treatment. **(d)** Streptavidin shift assay of YnF and YnGG-treated H23 cells (schematic shown on top). TAMRA fluorescence indicated successful shift of lipid-modified proteins (same color astricks show protein shift), albeit with a low signal-to-noise ratio.

Initial labelling experiments of an HRAS WT construct (Fig. **3.2.26**) revealed the expected incorporation pattern for each lipid probe tested (YnF, YnGG, YnPalm). A low level of

YnGG labelling was noted, which may be attributed to high levels of expression of HRAS in this experiment. More optimizations and validation experiments, including determining optimal tetracycline-induced expression levels for RAS constructs. Unfortunately, testing of the plasmids was hindered by several technical issues brought about by the KingFisher, and were unable to be resolved before completion of the PhD.

An alternative approach was also investigated in place of enrichment experiments, where addition of recombinant streptavidin protein in AzTB ligated probe-treated lysates results in a molecular weight shift in labelled protein (Fig. **3.2.26d**). This assay, dubbed "streptavidin shift", allows the assessment of probe incorporation without the need for bead-based enrichment, which can be more cumbersome to optimize and carry out[368]. Whilst bead-based biotin-Avidin enrichment protocols can require up to 3 hours for pull-down, followed by several washing steps, streptavidin shift assays only requires the addition of streptavidin protein to AzTB click-ligated lysate and subsequent gel loading for analysis.

This was tested initially on probe-treated H23 cells and is envisioned to be utilized in other lipid-probe experiment models if successful. While some shift in labelled protein was observed with the expected molecular weight (~28 kDa), the in-gel fluorescence signal was massively obscured by background fluorescence cast by excess streptavidin protein. However these results do imply that a similar streptavidin shift model can be employed in place of bead-based enrichment protocols, especially in the context of evaluating several protein constructs as described here. Further efforts validate these constructs were paused after completion of PhD work and will be returned to in the near future.

3.3. Chapter summary and future directions

This chapter outlines attempts at deconvoluting alternative prenylation criteria in an unbiased manner. To this end, a drug drug-resistance mutagenesis assay was designed to tease out sequence-related features within the HRAS HVD and CXXX-box that result in noncanonical alternative prenylation of HRAS. This is envisioned to emulate the unknown sequence criteria of KRAS, NRAS and RRAS that allow each of these isoforms to undergo alternative prenylation, while WT HRAS cannot.

Development of a drug-resistance mutagenesis approach to study alternative prenylation of HRAS

The assay strategy was first benchmarked using a $KRAS^{G12C}$ model, where mutagenesis around the G12C mutation under selection with AMG-510, a G12C-directed covalent inhibitor, would result in an anticipated G12X mutation, diverting away from the modifiable cysteine at that site. Initial attempts at this appeared to be successful, giving enough confidence to carry out the HRAS screen in H23 cells. This proved to be difficult as selection was hampered by $KRAS^{G12C}$, the primary oncogenic driver in H23 cells, despite efforts in attenuating KRAS activity using AMG-510. Still, initial results revealed that *S*-palmitoylation of C181 may putatively be related to the inability for HRAS to undergo alternative prenylation. In an attempt to optimize the drug-resistance mutagenesis screen, HRAS-driven cell lines were identified, benchmarked and subjected to the same screen using tipifarnib as the sole selection agent. Unfortunately, results from the screen, as well as a 3D spheroid-based screen run in parallel, were unable to be analyzed before the end of the PhD, but will be revisited at a later time to determine whether optimizations were successful.

A major caveat to this type of screening lies in the nature of selection taking place. That is, relying solely on changes in proliferation, rather than complete cell death in the control population and proliferation of the mutagenized, selected population, can prove difficult

in the absence of a significantly cytotoxic drug. This increases unwanted background signal from remaining unselected cells, which dilutes the population of cells harboring mutations that result in the desired phenotype (i.e. alternatively prenylated HRAS). Additionally, it is not known whether an alternatively prenylated HRAS results in a significant increase in proliferation under tipifarnib selection, which can further complicate downstream analyses.

In an attempt to mitigate these issues, an alternative screen was proposed that does not rely on selection via proliferation and cell death. Because the only expected phenotype of an alternatively prenylated (i.e. *S*-geranylgeranylated) HRAS is plasma membrane localization of HRAS, a screen was designed to sort cells based on plasma membrane anchoring of a target protein (Fig. **3.3.1a**). Here, HRAS conjugated to a fluorescent protein (yellow fluorescent protein or YFP) is stably expressed using an isogenic Flp-In system (as described earlier in this chapter). Within that same construct, a self-cleaving T2A peptide joins a membrane anchoring conjugated to another fluorescent protein (cyan fluorescent protein or CFP) that can undergo fluorescence resonance energy transfer (FRET) with the corresponding fluorescent protein on HRAS[369]. The T2A sequence (EGRGSLLTCGDVEENPGP) placed between two protein-coding genes on a single vector allows both constructs to be stably expressed as two independent proteins in what is known as a polycistronic expression system[370]. Close proximity of the two proteins at the plasma membrane would generate a FRET signal when HRAS is localized to the membrane under normal, wildtype conditions. Upon the application of tipifarnib, for example, the FRET signal would then be lost. Thus, a regain of FRET signal after mutagenesis selection with tipifarnib would indicate HRAS alternative prenylation. Cells expressing such a mutagenized protein would not need to over-proliferate to saturate the signal. Instead, FRET producing cells can be isolated and pooled using flow cytometry and then subjected to NGS analysis. This system could also be used to investigate protein localization to the plasma membrane in a high-throughput manner, allowing the study of various drug or genetic perturbations in this context.

BIOGRID analysis of publicly available interactomics data revealed Tyrosine-protein kinase Lyn (LYN) to be an appropriate plasma membrane marker, which is anchored by *N*-myristoylation rather than *S*-palmitoylation or *S*-prenylation and should remain undisturbed by tipifarnib treatment[371] (Fig. **3.3.1b**). Moreover, only the *N*-myristoylated N-terminus of LYN would be required for this assay, which may reduce bulkiness and potential steric hinderance of interactions with the target FRET partner. Several studies have also reported the use of LYN11 was a membrane marker[372,373]. Vectors containing WT HRAS and an unprenylated background control (C186S), as well as the corresponding KRAS benchmarking controls to establish the threshold for FRET signals needed for selection, were thus designed (Fig. **3.3.1c**). Generation of these plasmids, however, proved time-consuming as high homology between fluorescent proteins within a single vector resulted in recombination during Gibson assembly (data not shown). After several optimizations, the initial KRAS plasmids were generated for benchmarking and will be tested in the near future.

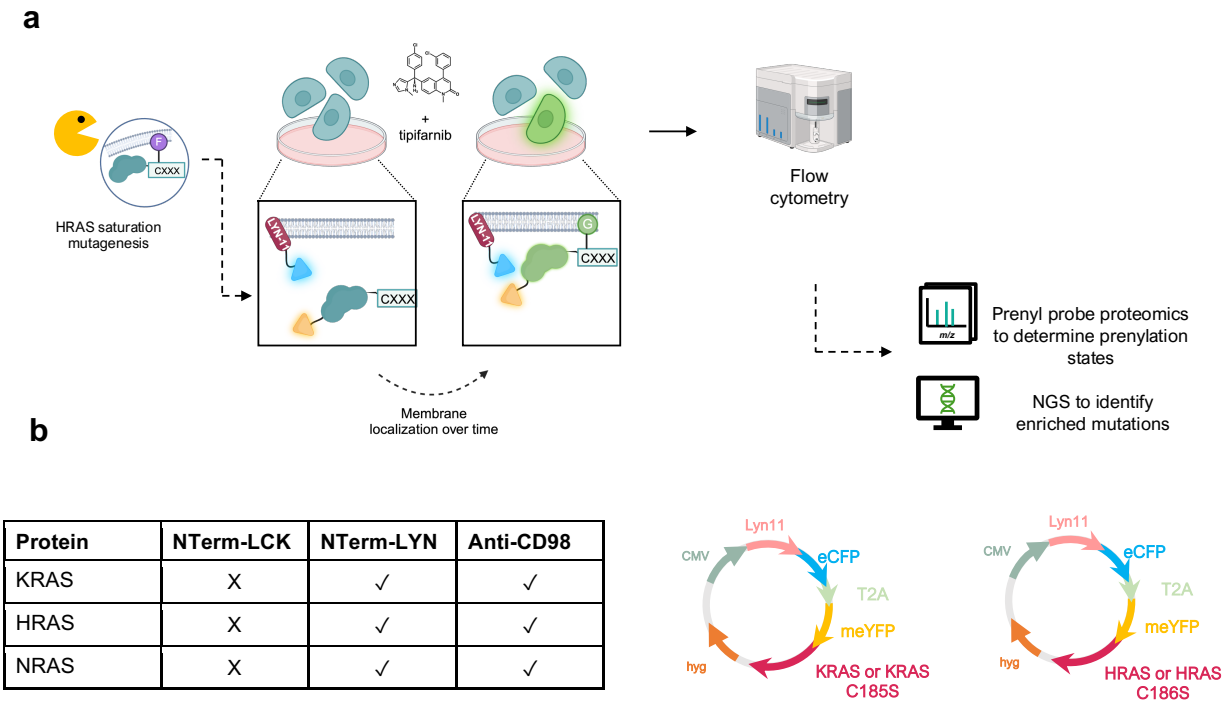

Protein	NTerm-LCK	NTerm-LYN	Anti-CD98
KRAS	X	✓	✓
HRAS	X	✓	✓
NRAS	X	✓	✓

Figure 3.2.27. Development of a membrane localization readout for drug-resistance mutagenesis. (a) Schematic for a FRET-based readout, indicating plasma membrane localization. Regain of plasma membrane localization upon the generation of an alternatively prenylated HRAS (following drug-resistance mutagenesis) results in a FRET signal that can be

sorted for using flow cytometry. Subsequent NGS and proteomic analysis would reveal the mutagenesis engendering the alternative prenylation phenotype and confirm alternative prenylation for HRAS, respectively**. (b)** Summary of BIOGRID analysis of membrane-anchored RAS interactors. A CD98 approach was briefly considered but abandoned for the more straightforward LYN approach.

Investigating *S*-palmitoylation dynamics in the presence of the FTI tipifarnib

Preliminary results from drug-resistance mutagenesis of HRAS implied that *S*-palmitoylation may be putatively involved in the inability of HRAS to undergo alternative prenylation in the presence of tipifarnib. Initial endeavors to follow up these preliminary results included global profiling of *S*-palmitoylation in the presence of tipifarnib. Global profiling was thus undertaken using YnPalm, an alkyne palmitoyl probe, in low (10 nM) and high (100 nM) tipifarnib conditions, revealing that several proteins lost some degree of YnPalm labelling in the presence of tipifarnib. While HRAS was unfortunately not quantified in this study, *S*-palmitoylation was decreased for NRAS, CDC42 and RHOG with increasing concentration of tipifarnib, which is in accordance with the hypothesis that many proteins require *S*-prenylation prior to *S*-palmitoylation. A subset of dual substate proteins (i.e. both *S*-prenylated and *S*-palmitoylated) were also found to not be affected by tipifarnib treatment, including LMNA. This implied that for some proteins, localization imparted by *S*-prenylation is not necessary to facilitate their delivery to their respective PAT.

Several *S*-palmitoylated proteins were also found to be tipifarnib sensitive. This is hypothesized to arise from a dependence on the proper localization of *S*-farnesylated proteins impeded by the application of tipifarnib. At the same time, hierarchical clustering analysis also revealed tipifarnib dose-dependent and independent increases in *S*-palmitoylation. This includes the APT for HRAS, LYPLA1, which may indicate a phenomenon by which LYPLA1 sequesters itself in an inaccessible cell component by preserving its *S*-palmitoylation status, thereby increasing the *S*-palmitoylation half-life of HRAS when it cannot be *S*-prenylated in the presence of tipifarnib. Although these phenomena currently remain hypothetical, revealing new FTI-related vulnerabilities in the

context of *S*-palmitoylation, for which no targeted therapeutics exist, may pave the way for use of FTIs, such as tipifarnib, in other disease contexts.

While tipifarnib-sensitivity of *S*-palmitoylated substrates, including HRAS and NRAS, may also be explained by off-target inhibition of their modifying PATs, this remains unlikely due to structural disparities between prenyltransferases and PATs, supported by this distinct mode of inhibition of tipifarnib and similar FTIs. Moreover, tipifarnib doses used in this study remained strictly within the nanomolar range, with the maximum doses used experimentally dictated by previous proteomic studies (i.e. dose needed for complete inhibition of farnesylation of canonical substrates)[52]. Still, although widely considered to be a highly selective and potent molecule, there is a distinct paucity of studies on tipifarnib off-targets. Profiling off-target binding of tipifarnib would be interesting to investigate in this context, perhaps using a label-free approach, such as proteomic cellular thermal shift assays (CETSA)[374].

It is also acknowledged that some missteps were taken throughout this study, partially owing to the interface of the COVID-19 pandemic. Chief among these was the delay in developing a vector-based validation system for chimeric RAS proteins, which would allow a direct elucidation of the roles the HVR and CXXX-box play in alternative prenylation of RAS isoforms. While the drug-resistance mutagenesis approach provided an interesting avenue to explore a relatively unbiased assessment of alternative prenylation criteria, validation using an orthogonal system perhaps should have been prioritized in hindsight. Nevertheless, this part of the project remains ongoing and will be established in the near future. CRISPR generation of *S*-palmitoylation mutants would then be undertaken should more evidence related to its role in alternative prenylation arise.

Chapter 4
RAS interactome studies to identify novel tipifarnib-associated vulnerabilities

4.1. Introduction

As echoed throughout this thesis, high degrees of RAS protein homology, though suggestive of functional redundancy, do not necessarily translate to complete functional overlap. Distinct RAS isoforms (KRAS, NRAS and HRAS, among others) have persisted throughout over 400 million years of evolution, strongly implying the existence of isoform-specific roles[160]. Although RAS proteins are known to have overlapping activators and downstream effectors, various reports have confirmed independent signaling pathways and intracellular processing events that are driven by single isoforms[353,375,376]. Moreover, RAS mutations emerge preferentially across various cell and tissue types in cancer, which supports the notion that isoforms may have differential functions depending on the cellular milieu and external stimuli[127] (Fig. **4.1.1**) For example, KRAS mutations are disproportionately found in pancreatic (PDAC), colorectal (CRC), and lung (LUAD) cancers, whilst NRAS mutations primarily drive melanoma and AML, and HRAS mutations are most common in HNSCC, lymphoid and bladder cancers[127].

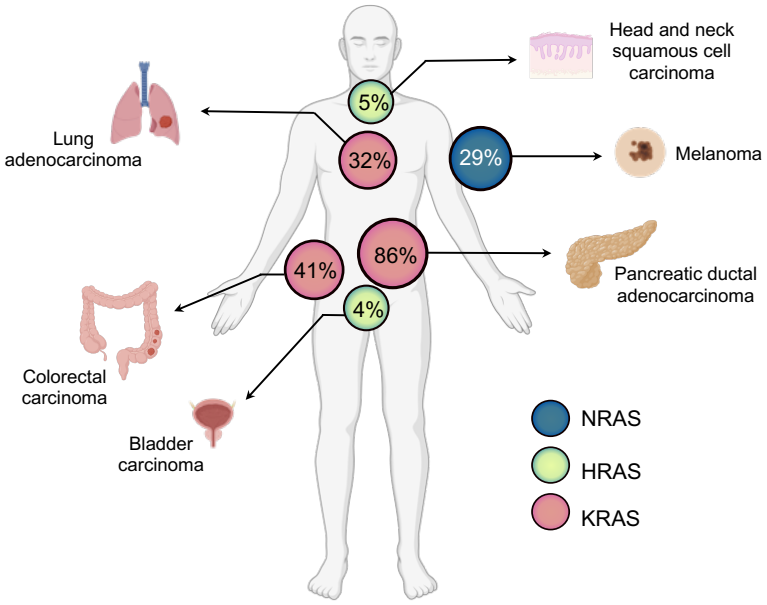

Figure 4.1.1. Distribution of RAS isoform drivers in human cancers. RAS isoform mutations and associated oncogenesis emerge non-proportionally across different cancer/tissue types. Percentage is proportion of a particular RAS isoform-driver in a given cancer type[198]. Figure made with BioRender.

The emergence of RAS isoform-specific pathways has often been studied as a function of subcellular distribution and membrane partitioning dynamics, which is primarily mediated by PTMs – specifically protein lipidation[74,376]. As discussed previously, RAS isoform homology decreases significantly near the C-terminus where *S*-prenylation and *S*-palmitoylation lipidation sites are concentrated, defining an area comprising a short stretch of amino acids that is aptly named to hypervariable domain (HVD). Indeed, RAS proteins have divergent lipidation dynamics, including non-parallel responses to lipidation-targeted therapeutics (i.e. FTIs). *S*-prenylation is thought to be the base lipidation event for RAS proteins and largely understood to take place soon after translation. This modification prompts RAS trafficking to the ER where a series of post-prenylation processing events (endoproteolysis and carboxyl methylation of the CXXX-motif) occurs, which is followed by other subcellular trafficking events, primarily through anterior and retrograde transport from the Golgi[234]. The Golgi also harbors PATs that *S*-palmitoylate KRAS4A, NRAS and HRAS, which directly impacts their residence time on cellular membranes[355].

Disrupting any of these lipidation events can also alter the dynamics of subsequent lipidation events, further impacting the subcellular distribution of substrate proteins. For example, the previous chapter demonstrated that tipifarnib, an FTI, also prevents *S*-palmitoylation of HRAS and NRAS, as well as other proteins. This, in turn, reflects on interacting proteins that are implicated in the mediation of RAS signaling events that are frequently dysregulated in cancer.

Protein-protein interactions (PPIs), particularly in the case of RAS proteins, dictate downstream function and have direct consequences on metabolism, proliferation and secretory events that are fundamental in the study of cancer[377]. The range of possible PPI events can be seen to be dictated, at least in part, by subcellular localization. Deconvoluting these interactors may thus reveal novel vulnerabilities associated with a singular RAS isoform that can be exploited for therapeutic intervention. This is especially relevant in the identification of synergistic drug combinations, whereby the application of one drug may uncover a different, novel druggable vulnerability. In the same way,

interactome studies may also aid in the prediction and targeting of resistance pathways. For example, interactome studies have revealed a novel interaction between KRAS and JAK1 upon application of sotorasib, a $KRAS^{G12C}$ inhibitor[378]. This may justify the use of JAK1 inhibitors, such as abrocitinib, as a way to discourage resistance emerging through the JAK-STAT pathway, which has been shown to be another common driver of PDAC. At the same time, JAK1 inhibitors may potently synergize with $KRAS^{G12C}$ inhibitors in certain contexts. Ultimately, the interactome may harbor various clues to early resistance pathways that evade other analytical methods.

FTIs have surprisingly limited toxic effects in pre-clinical models and have been generally well-tolerated in many clinical trials, with their main shortcomings centered on inefficacy in the treatment of certain RAS-driven cancers, as well as hematological toxicities associated with higher doses necessary to achieve treatment goals[379]**.** With tipifarnib's recent breakthrough therapy designation by the FDA in HRAS-driven cancers, the use of FTIs is actively being re-evaluated in the clinic[149]. Understanding which contexts FTIs demonstrate the most benefit, as well as identifying potential synergistic therapies, has become a key goal that may be achieved in deciphering the interactome of *S*-prenylated proteins implicated in disease. Alternative prenylation remains a significant hurdle in the application of FTIs in RAS-driven cancers for which no concrete mechanism has been established.

It can be hypothesized that isoform-specific interacting proteins may have a role in dictating alternative prenylation events. For example, a positive regulator may facilitate the delivery or binding of GGTase-I to KRAS and NRAS, or conversely an HRAS-specific interactor may inhibit alternative prenylation in the presence of an FTI. Whilst alternative prenylation may be engendered through a sequence-specific effect, as explored in the previous chapter, this may still result in a differential interactome that harbors therapeutically actionable vulnerabilities. Furthermore, *S*-geranylgeranylated KRAS or NRAS may also localize differently to its *S*-farnesylated form, which also exposes it to a potentially druggable interactome that is otherwise inaccessible without the use of FTIs (Fig. **4.1.2**).

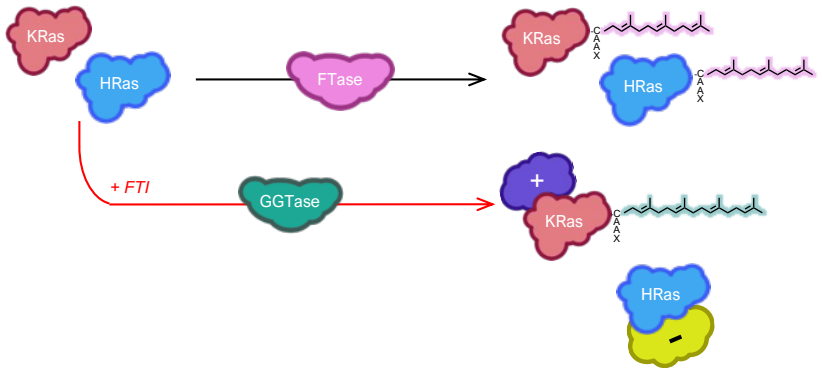

Figure 4.1.2. Deconvoluting alternative RAS prenylation through interactome studies. Interactors of RAS isoforms may modulate differential alternative prenylation dynamics, manifesting as positive regulators for KRAS or NRAS alternative prenylation (KRAS shown here for brevity), or negative regulators for HRAS, which does not undergo alternative prenylation.

This chapter describes the application of proximity-labelling techniques in an effort to deconvolute RAS isoform-specific interactomes in the presence and absence of tipifarnib. Interactomics may thus aid in the identification of regulators of alternative prenylation events, or reveal novel druggable vulnerabilities in the context of FTI treatment.

4.2. Results and discussion

4.2.1. Validation and optimization of APEX2 proximity labelling strategy

Protein function is inextricably linked with subcellular localization and the interactions that transpire within the cellular environment. Global profiling of PPIs has enabled the mapping of complex protein interaction networks, significantly contributing to our understanding of protein function and uncovering areas for therapeutic intervention[377]. Consequently, interactomics methodologies have greatly advanced over the last decade, and currently encompass a wide range of techniques[380].

Interactome mapping has been traditionally accomplished through affinity-purification mass spectrometry techniques (AP-MS), where interacting proteins are captured by co-precipitation of the protein of interest (POI)[381]. This requires ectopic expression of the POI engineered to include an affinity element; purification/precipitation of the POI is achieved using the affinity binder immobilized on resin, resulting in the concurrent enrichment of stable interactors that are then analyzed by MS. While AP-MS remains a useful technique in the realm of interactomics, dynamic and weak interactions are often loss upon cell lysis and sample processing, which require the use of detergents and partially denaturing conditions[382]. While this can be mitigated using crosslinking reagents, this also greatly increases background due to the capture of false positives, significantly decreasing the dynamic range of such techniques[380,382].

Proximity labelling (PL) emerged as a complementary approach to AP-MS to address some of these shortcomings. Directed evolution has afforded engineered enzymes that can efficiently tag surrounding biomolecules, which is most commonly achieved through the catalytic activation of biotin and biotin-derivatives, generating a short-lived reactive species that can covalently react with biomolecules. When appended to a POI by way of genetic fusion (i.e. bait), interacting and spatially proximal endogenous biomolecules (i.e. prey) are biotinylated and can be enriched using standard pulldown techniques. This

allows the capture of both stable and transiently interacting proteins and nucleic acids (i.e. DNA, RNA) *in situ*, with some techniques established for *in vivo* applications (BioID, TurboID). Moreover, because the generated reactive biotin species are largely membrane impermeant, PL can also be applied to the specific study of organelle interactomes. A summary of proximity labelling techniques is provided in Table **4.2.1**.

Table 4.1. Comparison of commonly used proximity labelling techniques

	Wildtype Enzyme	**Molecular Weight (kDa)**	**Substrate**	**Labelling time**	**Labelling radius**	**Advantages**	**Limitations**
BioID	Biotin Ligase (BirA)	35	Biotin	6 – 24h	~10 nM	Amenable to *in vivo* applications	Very low catalytic activity; poor temporal resolution
TurboID	Biotin Ligase (BirA)	35	Biotin	30 – 60 min	~10 nM	Amenable to *in vivo* applications; highest activity BirA ligase	High catalytic activity/promiscuous
MiniTurboID	Biotin Ligase (BirA)	28	Biotin	10 – 60 min	~20 nM	Smallest BirA ligase; higher temporal resolution; reduced background	Reduced catalytic activity
APEX2	Ascorbate Peroxidase	28	Biotin phenol (w/ addition of H_2O_2)	≤1 min	~10 – 15 nM	Quick labelling time; temporal resolution	Toxicity of peroxide; high catalytic activity/promiscuous
LOV-Turbo	Biotin Ligase (BirA)	50	Biotin	30 min – 5 min	N.D.	High spatial and temporal control; wide dynamic range	Inactive on some cell components; larger size
MicroMap*	None (Iridium catalyst)	N/A	Diazirine	5 – 15 min	< 4 nM	Can be used to study liganded proteins; no ectopic expression or enzyme	Toxic catalyst; variable labelling times; known ligand required; requires synthetic ligation of catalyst to protein ligand

Various studies on RAS interactomes have been reported, most commonly through the use of AP-MS and BioID[378,383–387]. However, RAS protein-protein interactions are highly dynamic and compartmentalized, potentially requiring the use of more temporally constrained techniques to capture the most relevant interactors upon the introduction of a perturbation, such as drug treatment. APEX2 is currently the most temporally constrained PL technique, with labelling taking place in as little as 1 minute once initiated[388]. APEX2 is an engineered biotin peroxidase that oxidizes exogenously fed biotin-phenol into a reactive phenoxyl radical in the presence of hydrogen peroxide (Fig. **4.2.1a**). This can be further controlled using an inducible expression system, such as those afforded by TRex Flp-In cells, described in the previous chapter[366]. To this end, APEX2-RAS TRex Flp-In cell lines were generated to study the interactomes of KRAS, $KRAS^{G12D}$, NRAS and HRAS, and how they may adapt in the presence of tipifarnib (Fig.

4.2.1a). In theory, such a technique would not only capture the interactome of these RAS isoforms upon tipifarnib treatment, but may also contextualize them in subcellular locations when unprenylated, in the case of HRAS, or alternatively prenylated, in the case of KRAS and NRAS. It has also been established, from literature and the previous chapter, that FTI treatment also affects downstream *S*-palmitoylation dynamics, which could also be of interest in this context.

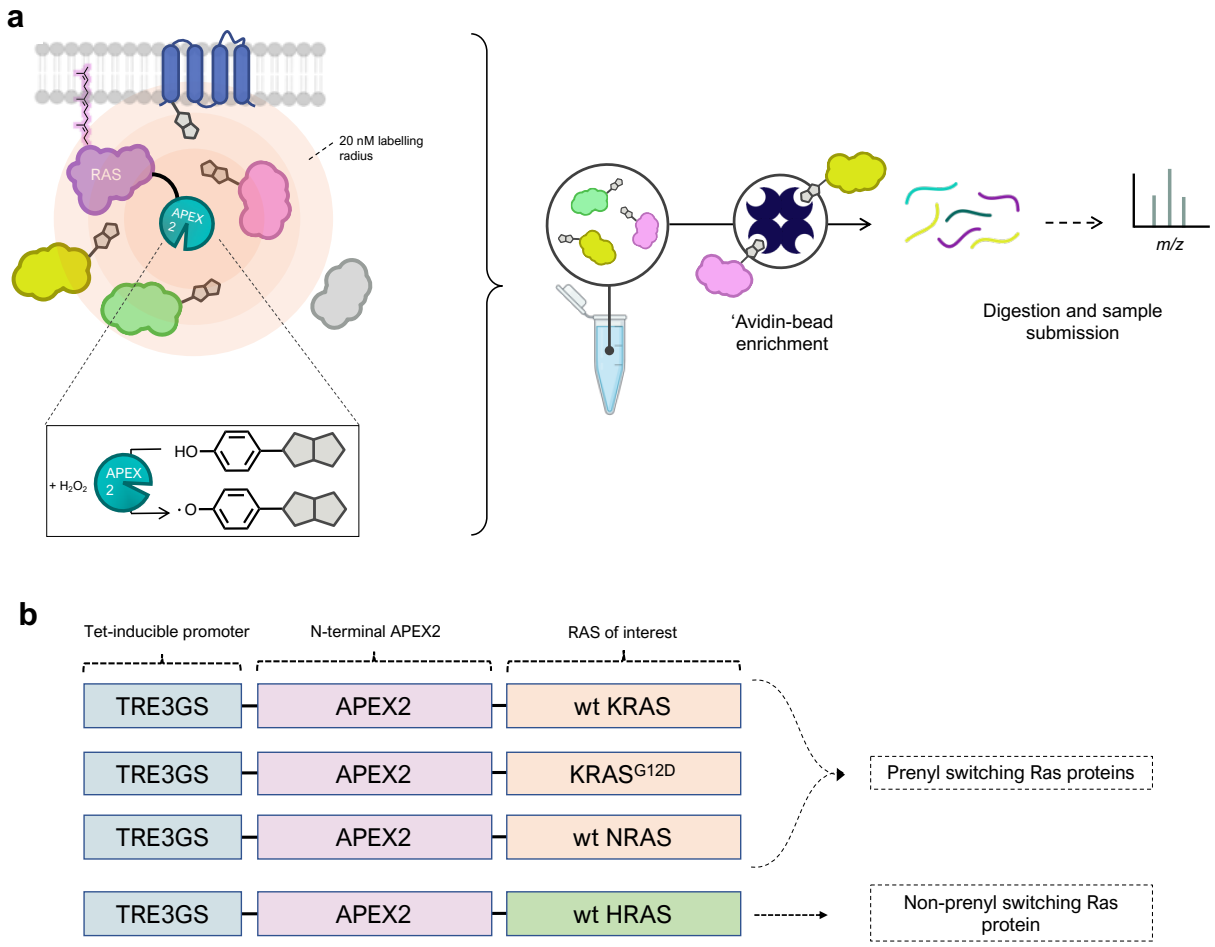

Figure 4.2.1. APEX2 proximity labelling offers high temporal control for RAS interactome capture. (a) APEX2 biotin peroxidase is genetically fused to a protein of interest (shown as RAS here), which utilizes exogenously given biotin-phenol to label proximal proteins within a ~20 nM radius, only upon addition of hydrogen peroxide, in which labelling is allowed to occur for up to 1 min. Biotinylated proteins in cell lysates are then isolated using 'avidin-bead based enrichment, after which enriched proteins are digested and analyzed by MS-methods. **(b)** Designed APEX2-RAS fusion constructs used through these studies. Constructs, which cloned into TRex Flp-In

vector backbones, include a Tet-inducible promoter and an N-terminal fusion to prevent RAS mislocalization by obstruction of the membrane targeting motifs on the protein C-terminus.

These APEX2-RAS cell lines were designed and generated by Dr. Andreas Damianou (University of Oxford) (Appendix Fig**. 7.10**). Critically, the APEX2 enzyme was fused to the RAS N-terminus to avoid the disruption of RAS localization by obscuring the HVD and CXXX-box at the protein C-terminus. Other features included a flexible linker to reduce potential steric hinderance of the APEX2 enzyme, as well as a FLAG-tag for convenient detection by Western blot.

Because high overexpression was found to result in aggregated, mislocalized protein, induction experiments were initially carried out to determine a reasonable tetracycline dose for expression of the construct, as well as to as establish an induction duration that allowed all cell lines to have comparable expression levels (unpublished data). Tetracycline was titrated from the maximum recommended dose, for 6 h and 16 h induction periods (Fig. **4.2.2**). These durations were chosen as their corresponding harvest time points are expected to be convenient for experiment planning, offering either a same-day treatment and harvest protocol, or an overnight treatment and next day harvest.

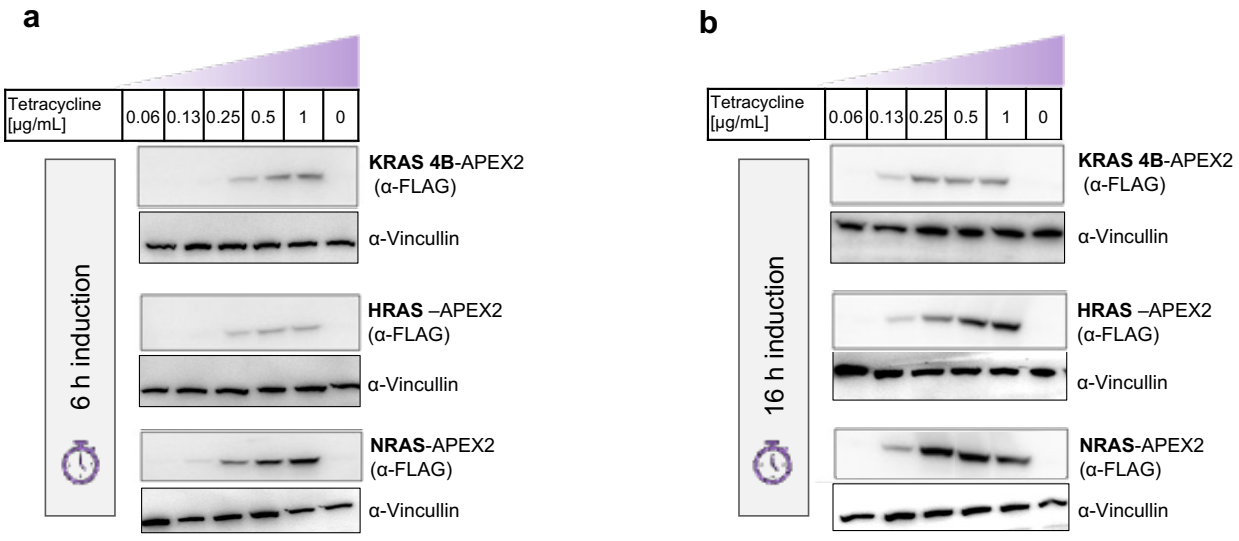

Figure 4.2.2. Optimizing APEX2-RAS induction conditions for proximity labelling experiments. Western blot analysis of APEX2-RAS (FLAG) induction upon tetracycline-

treatment is dose-dependent and time-dependent, with labelling tested at 6h **(a)** and 16h **(b)** induction times.

Both strategies induced APEX2-RAS expression in a relatively dose-dependent manner, however the 16h timepoint exhibited higher expression consistency between the cell lines, which was deemed more desirable. Thus, 0.5 µg/mL tetracycline with a 16h induction period was chosen for all APEX2-RAS experiments going forward.

Biotinylation conditions were then tested for each cell line using the workflow outlined in Fig. **4.2.3a**. Briefly, expression was induced for 16h (overnight), after which biotin-phenol was added to cells for 1h before initiating hydrogen peroxide labelling. Because hydrogen peroxide is toxic to cells, it was paramount to quench and remove as much reagent as possible without prematurely lysing or lifting adherent cells during wash steps. Biotinylation can then be visualized by Western blot through the use of HRP-conjugated Neutravidin to evaluate the labelling efficacy and distribution of signal. Biotinylation should only occur in induced, biotin-phenol and hydrogen peroxide treated cells; any residual biotinylation observed when any of these elements is omitted should be associated with endogenously biotinylated proteins, and not saturate the signal. These conditions were tested in each cell line, demonstrating that labelling only occurred in the presence of all APEX2 labelling components, with minimal biotin signal observed in uninduced, no biotin and no hydrogen peroxide conditions (Fig. **4.2.3b**).

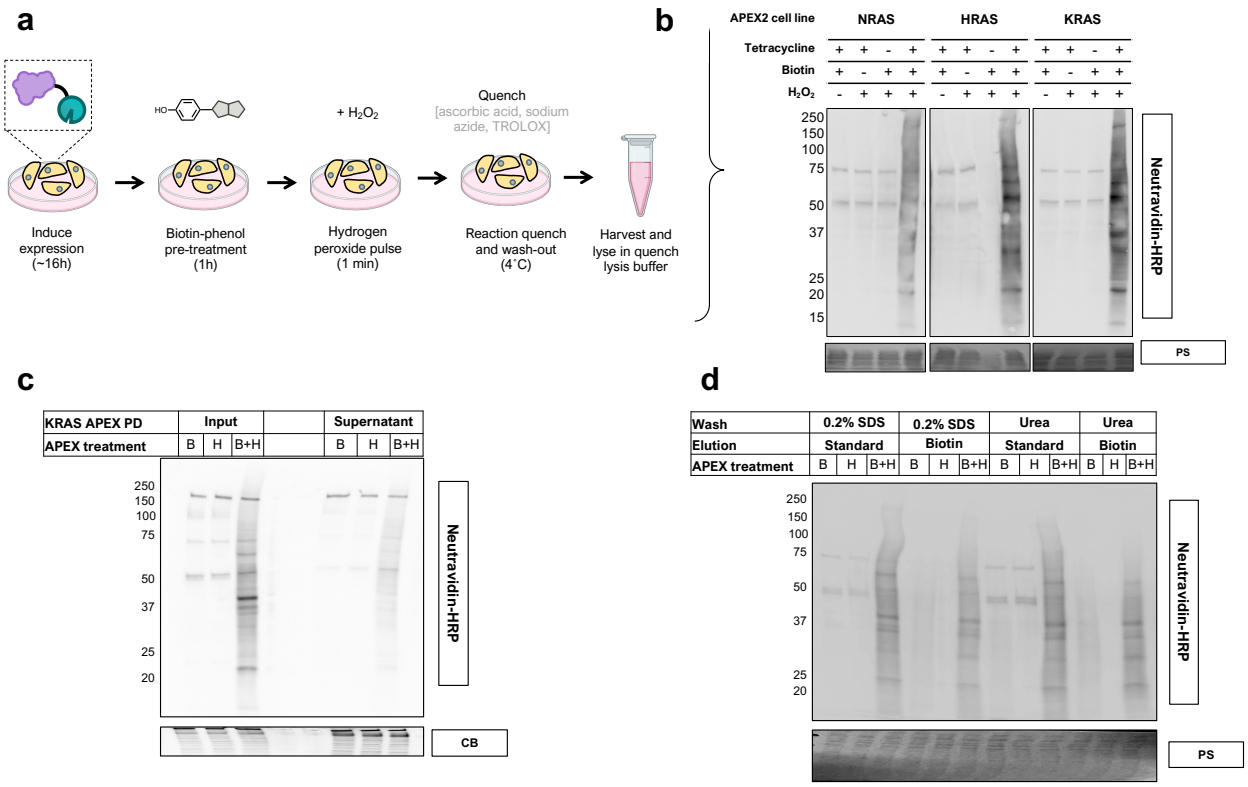

Figure 4.2.3. Validation of APEX2-RAS biotinylation and optimization of interactor enrichment. (a) Schematic summarizing the APEX2 biotinylation workflow in cells. This begins with construct induction using tetracycline (~16h), followed by biotin-phenol treatment (1h). Hydrogen peroxide is added to initiate labelling for 1 min, after which labelling is quench by the addition of a buffer containing ascorbic acid, sodium azide and TROLOX. Cells are washed with this buffer multiple times before harvesting and lysing in a buffer containing quench reagents. **(b)** Western blot (Neutravidin-HRP) validation of APEX2-RAS cell line biotinylation, where biotinylation is only observed in the presence of all APEX2 labelling components. **(c)** Western blot (Neutravidin-HRP) of input and enrichment of biotinylated proteins following APEX2 labelling in the APEX2-KRAS cell line. Depletion is observed in the supernatant samples (B = biotin, H = hydrogen peroxide). **(d)** Optimization of wash and elution steps during enrichment of biotinylated proteins, using both normal (0.2% SDS) and denaturing (Urea + 0.2% SDS) wash buffers, as well as biotin-supplemented elution, using the same input samples in panel (c). Blot represents eluted proteins. CB – Coomassie blue; PS – Ponceau S stain

The two bands observed at 75 and 50 kDa are generally observed in background conditions throughout PL labelling experiments and correspond to those reported in the literature, likely representing high abundance biotin-binding proteins, such as pyruvate carboxylase (PC)[389].

Next, pulldown/enrichment conditions from APEX2-RAS lysates were optimized. Using the APEX2-KRAS cell line as a proof-of-concept, biotinylated lysates as well as the associated controls were tested for depletion of biotinylated proteins from the supernatant. This confirmed that biotinylated proteins were modestly depleted following magnetic 'avidin-bead based enrichment (Fig. **4.2.3c**). Pulldown wash conditions were also investigated, with standard (0.2% SDS) and denaturing (urea + 0.2% SDS) conditions tested, as well as the use of biotin to enhance elution by outcompeting 'avidin binding by biotinylated proteins (Fig. **4.2.3d**). Urea-supplemented pulldown washes did not appear to reduce background, however the use of biotin appeared to marginally reduce background in both 0.2% SDS and urea washed pulldown samples. However, this was not found to be significant enough to deviate from the standard proteomic enrichment protocols employed in the Tate Group, but could be explored as a future optimization should enrichment prove to be poor by proteomic analysis. A caveat to this brief study was that enrichment experiments were performed using magnetic beads, which were not used for proteomic sample preparation, where instead agarose-beads are used to avoid contaminants. However, as both types of beads employ 'avidin-biotin enrichment, it was deemed similar enough to draw conclusions for agarose-bead enrichment. Further optimization using agarose-beads can be conducted in the future if necessary.

4.2.2. Validation of APEX2-RAS fusion *S*-prenylation status and response to tipifarnib.

In order to capture the most relevant RAS interactome in the presence and absence of tipifarnib, it was essential that the designed APEX2-RAS fusion constructs are appropriately *S*-prenylated and respond to tipifarnib analogously to the endogenous proteins. That is, KRAS and NRAS constructs should undergo alternative prenylation, while HRAS should remain unprenylated upon tipifarnib treatment. Thus, alternative prenylation was investigated using the dual isoprenoid probe system (YnF and YnGG) (Fig. **4.2.4a**). Here, tipifarnib was added alongside tetracycline to saturate the amount of unprenylated or alternatively prenylated protein, as *S*-prenylation occurs shortly after translation and is retained throughout the lifetime of a RAS protein, which is reported to

be approximately 48 hours. Isoprenoid probes (YnF or YnGG) were added the next day for another overnight incubation for metabolic labelling. Cells are then harvested the following day, click ligated to AzTB, purified by SP3 using a KingFisher device and analyzed by in-gel fluorescence. Because of the size of the conjugated reporter agent (1.2 kDa), a slight band shift can be observed for successfully probe-labelled proteins, particularly in the case of ectopically expressed proteins, which tend to dominate the signal.

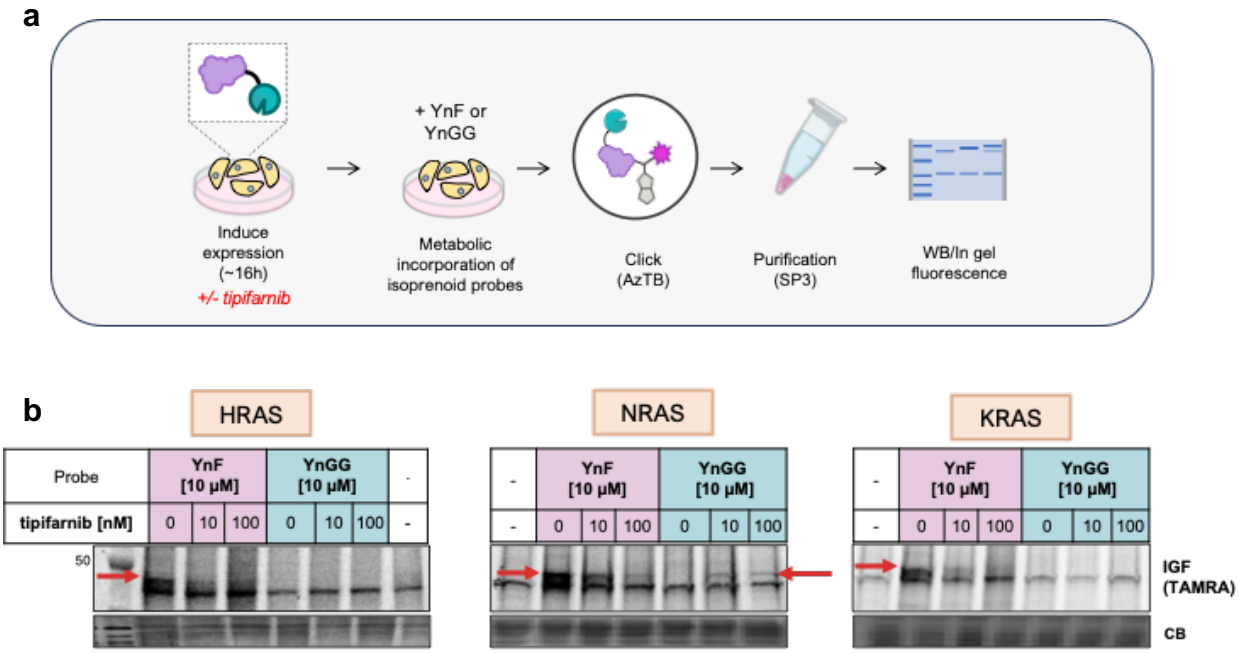

Figure 4.2.4. Validation of *S*-prenylation status of APEX2 constructs. (a) schematic depicting workflow for isoprenoid probe (YnF/YnGG; 10 µM) incorporation studies in APEX2 cell lines. Construct expression is induced by addition of tetracycline simultaneous to optional addition of tipifarnib (100 nM) to evaluate alternative prenylation capacity. Cells are then subjected to metabolic incorporation of isoprenoid probes, after which cells are harvested, lysed and subjected to click ligation to a reporter agent (AzTB), purified using SP3 to remove excess click reagents, and analyzed by in-gel fluorescence (TAMRA). **(b)** Results of probe incorporation experiments with and without tipifarnib in APEX2-RAS cell lines. Red arrow indicates mass-shifted probe labelled APEX2-RAS construct. Band in control lane (no probe) is background signal.

Whilst NRAS and HRAS APEX2 constructs were appropriately labelled with YnF under normal conditions, and respectively alternatively prenylated and unprenylated in the presence of tipifarnib in a dose-dependent manner, KRAS remained unprenylated (Fig. **4.2.4b)**. While it is not exactly unexpected that the fusion of a large enzyme to a RAS protein may affect its behavior, including alternative prenylation, it was surprising that APEX2-NRAS still retained the ability to undergo alternative prenylation whilst APEX2-KRAS did not.

To confirm this, an analogous pulldown experiment was undertaken where the same treatment strategy was employed, however lysates were instead subjected to 'avidin-based bead enrichment using a KingFisher device and analyzed by Western blot (α-FLAG) (Fig. **4.2.4a** and **b)**. APEX2-KRAS^{G12D} was tested alongside HRAS, NRAS and KRAS constructs to test whether this was a KRAS-specific phenomenon. Pulldown results confirmed that APEX2-KRAS was unable to undergo alternative prenylation, whilst APEX2-KRAS^{G12D} did. While this phenomenon was difficult to rationalize, it was hypothesized that such a construct may be helpful in identifying alternative prenylation drivers or inhibitors, since the APEX2-fusion appeared to disrupt whatever process facilitates alternative prenylation for this construct. It was thus kept as a potential control in following experiments.

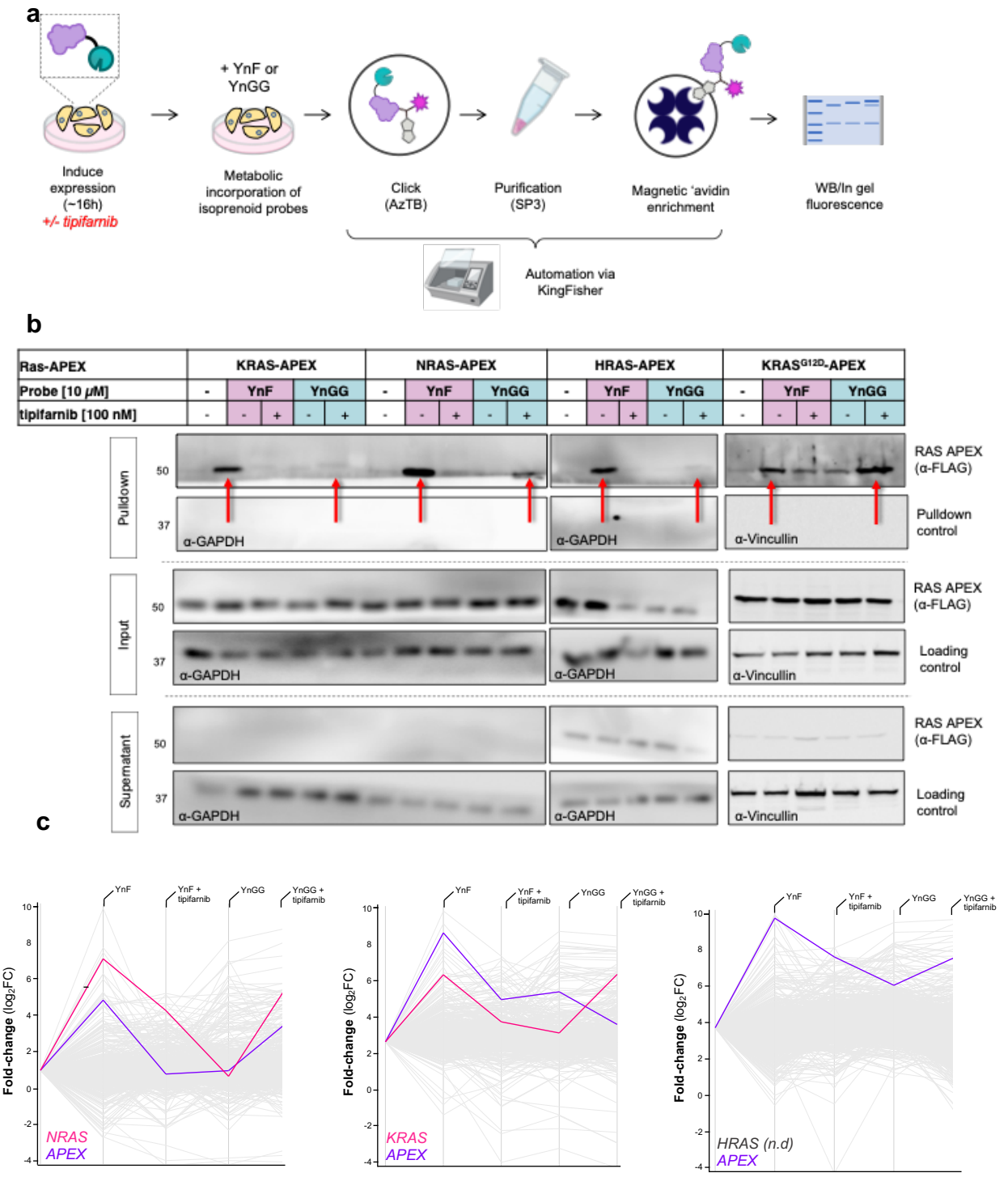

Figure 4.2.5. Validation of alternative prenylation status for APEX2-RAS constructs. (a) Schematic depicting workflow for enrichment of probe-labelled APEX2-RAS constructs with and without tipifarnib (100 nM). Induction, tipifarnib treatment, metabolic labelling with YnF or YnGG were performed as described in Fig. 4.2.4a. Here, click ligation of resultant lysates to AzTB was conducted on a 96-well plate, which was then subjected to SP3 purification and magnetic 'avidin-bead enrichment, which were all performed using a KingFisher device to increase the throughput

of construct validation. Samples were then analyzed by Western blot (α-FLAG). **(b)** Western blot analysis of YnF or YnGG-enriched APEX2-RAS constructs, confirming alternative prenylation for NRAS and $KRAS^{G12D}$, and lack thereof for KRAS and HRAS constructs. **(c)** Profile plots from proteomic analysis of probe-enriched constructs in the presence or absence of tipifarnib for APEX2-NRAS, KRAS and HRAS, with APEX2-construct and RAS-only derived peptides highlighted separately. HRAS-only derived peptides were not identified in this experiment (n=1).

Alternative prenylation was also investigated using proteomics to partially differentiate between APEX2-fusion and endogenous RAS protein *S*-prenylation dynamics in a more quantitative manner. However, identification overlap was expected seeing that RAS sequences were identical to the fused APEX2-RAS construct, and overexpression, even if attenuated using an inducible TRex Flp-In expression system, still might saturate the signal. Using the previously described induction and treatment workflows described in Fig **4.2.4a** and **4.2.5a**, resultant lysates were click ligated to AzRB and subjected to 'avidin agarose bead-based enrichment, as opposed to magnetic beads employed in KingFisher workflows. Enriched proteins were digested and analyzed by label-free quantification (LFQ) (DDA; n =1), with separate searches set up for APEX2 peptides, RAS-peptides, and APEX2-RAS fusion peptides. Results again confirmed that both NRAS and APEX2-derived peptides undergo alternative prenylation. Confusingly, KRAS-derived peptides appeared to undergo alternative prenylation as well, whilst APEX2-derived peptides did not. Furthermore, HRAS was not quantified in the APEX2-HRAS sample, which was foreseen considering the paucity of possible unique tryptic HRAS peptides, making it substantially more difficult to assign in proteomic analysis. The associated APEX2-derived peptides, however, exhibited a mild uptake of YnGG in the tipifarnib-treated condition, which again was unexpected. It was hypothesized that this mild uptake was associated with some background labelling or inefficient pulldown, as this was performed in a single replicate initially. While this experiment is set to be repeated in the near future, the results from the initial gel-based pulldown experiments were used to assign alternative prenylation capacity to NRAS and $KRAS^{G12D}$, and lack thereof for HRAS and KRAS constructs.

4.2.3. APEX2-KRAS^{G12D} interactome benchmarking study

With conditions for biotinylation and enrichment in hand, as well as having validated YnF and YnGG labelling of APEX2-RAS constructs, a preliminary proteomic investigation was devised. Here, only one APEX2-RAS construct was selected to simplify the workflow and identify suitable background controls for proteomic analysis. At least 38 proteins in the human proteome harbor biotin-binding motifs that may be captured using PL techniques, necessitating the use of appropriate background controls that should ideally be tailored to the individual experiment (data mined from UniProt)[390]. APEX2-KRAS^{G12D} was chosen due to its capacity to undergo alternative prenylation and funneled into the workflow outlined in Fig. **4.2.6**.

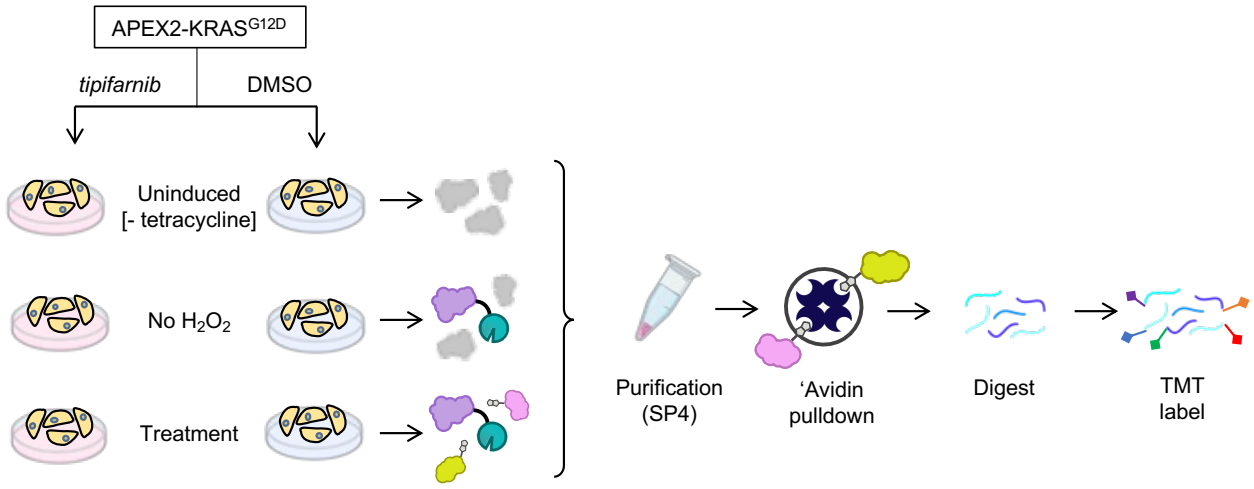

Figure 4.2.6. Proteomic strategy for profiling APEX2-KRAS^{G12D} isoform interactors. APEX2-KRAS^{G12D} cells were subject to PL in the presence and absence of tipifarnib (100 nM) using the same APEX2 labelling strategy described in Fig. **4.2.3.** Uninduced (no tetracycline) and no H_2O_2 controls samples were prepared to identify a suitable background control for data analysis. Sample were prepared in triplicate, harvested and lysed, purified using SP4 and subject to 'avidin enrichment using Neutravidin-agarose beads. Following pulldown, samples were digested on-bead, and resultant peptides were TMT-labelled (6-plex), pooled and analyzed by mass spectrometry.

Cells were induced and treated with either tipifarnib (100 nM) or DMSO simultaneously for ~ 16h (overnight). Uninduced (no tetracycline), no biotin and no hydrogen peroxide

controls were prepared alongside biotinylated, treated samples. The following day, biotin-phenol was added for 1h before initiating biotinylation by addition of hydrogen peroxide. Cells were labelled for 1 min before quenching the reaction and washing out hydrogen peroxide at 4˚C. Cells were then harvested through agitation and lifting, and lysed in Falcon tubes after collection. Purification from quench reagent components and excess biotin was then carried out using SP4, and 20 µg of each sample was reserved for quality control analysis via Neutravidin blotting (Fig. **4.2.7a**). Samples were confirmed to have the correct biotinylation patterns and tipifarnib treatment did not seem to significantly affect labelling efficacy. Processed lysates were then subjected to 'avidin agarose bead-based enrichment using a standard protocol (described in Methods). Following tryptic digest, peptides were TMT labelled (6-plex), pooled, and fractionated prior to MS submission.

Proteomic analysis revealed enrichment of known KRAS interactors, including KRAS and APEX2 identified constructs, which serve as one class of positive controls for PL experiments as the enzyme constructs undergo a high degree of self-biotinylation (Fig. **4.2.7b**). APEX2, RAS and APEX2-RAS sequences were considered as separate search entries during proteomic analysis. Here, high-confidence interactors defined as proteins identified twice or more in published interactome datasets (complied using BIOGRID)[249]. STRING analysis of enriched proteins revealed functional enrichment of RHO-signaling pathways and signal transduction. This is in accordance with canonical RAS signaling, which both stimulate and functionally overlap with RHO signaling[391]. Moreover, high-affinity binders (ARAF1, BRAF and RAF) were significantly enriched, however due to high sequence homology, proteomic analysis was unable to differentiate between these isoforms[392].

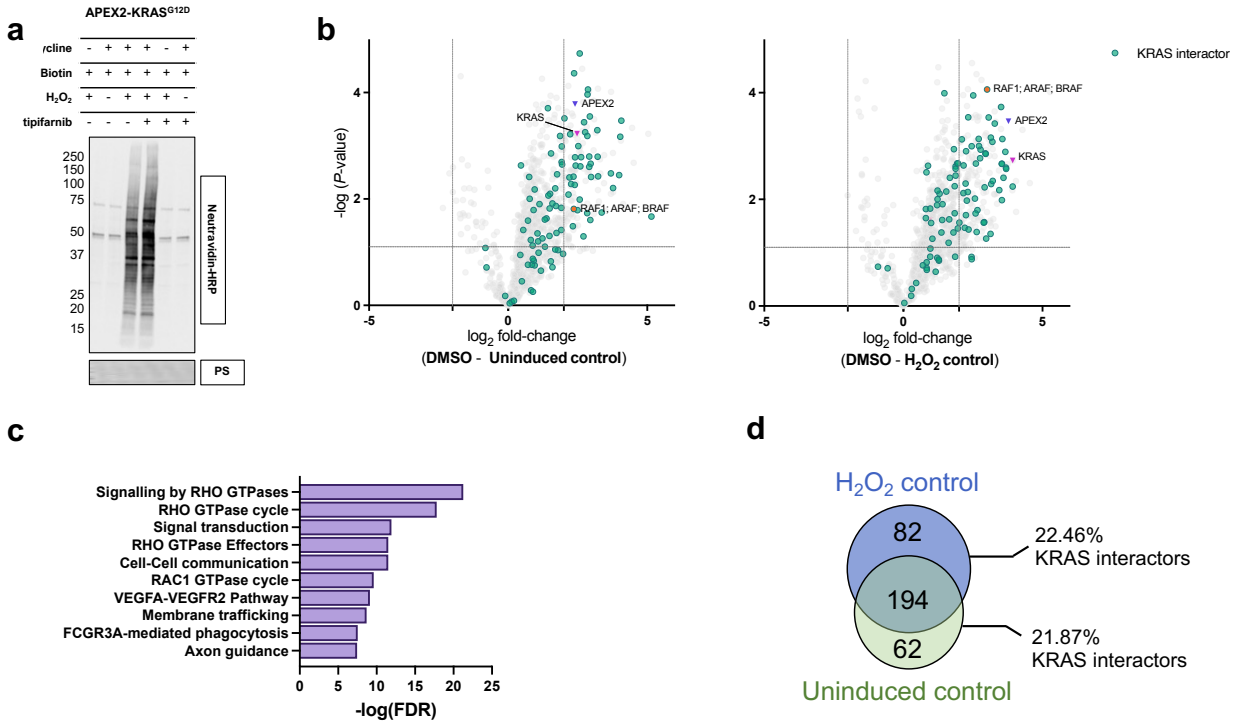

Figure 4.2.7. Preliminary proteomic analysis of APEX2-KRAS^{G12D} interactome. (a) Quality control biotinylation analysis via Western blot (Neutravidin-HRP) of a representative replicate of APEX2-KRAS^{G12D} samples, confirming appropriate biotinylation patterns in controls and PL samples. **(b)** Volcano plots depicting APEX2-KRAS^{G12D} interactor-enrichment (student t-test; FDR = 0.05; ratio = 1.5), compared to two different controls (uninduced and $H2O_2$ controls). High-confidence KRAS interactors (curated from BIOGRID data) are highlighted in teal. RAF1/ARAG/BRAF is highlighted in orange. KRAS-only and APEX2-construct derived peptides are highlighted in magenta and purple, respectively. **(c)** Functional enrichment analysis (STRING) of enriched proteins identified in APEX2-KRAS^{G12D} interactome analysis (GO: biological function). Data is representative of both control analyses in panel **b**. **(d)** Venn diagram comparing enriched proteins using both control analyses in panel **b**.

Background correction using the “no hydrogen peroxide” sample did not significantly differ from the uninduced sample purely by interactors identified. While H_2O_2 control sample correction yielded 272 proteins significantly enriched (p-value > 0.01; ratio = 1.5), only 22.46% of these proteins were annotated as high-confidence KRAS interactors. The uninduced control background correction resulted in 226 enriched proteins, with a similar percentage of known interactors – 21.67%. Notably, 70.56% of these interactors were shared between the two conditions. Overall, both controls appeared to function similarly within this dataset. It was decided that the H_2O_2 control was potentially the most appropriate in this context, as controlling for background without any expression of the

construct may not account for changes in signal transduction that are stimulated by expression by the APEX2-RAS fusion protein. Therefore, not correcting for this background signal may result in an artefactual enrichment of RAS-related proteins that are not necessarily directly captured by PL.

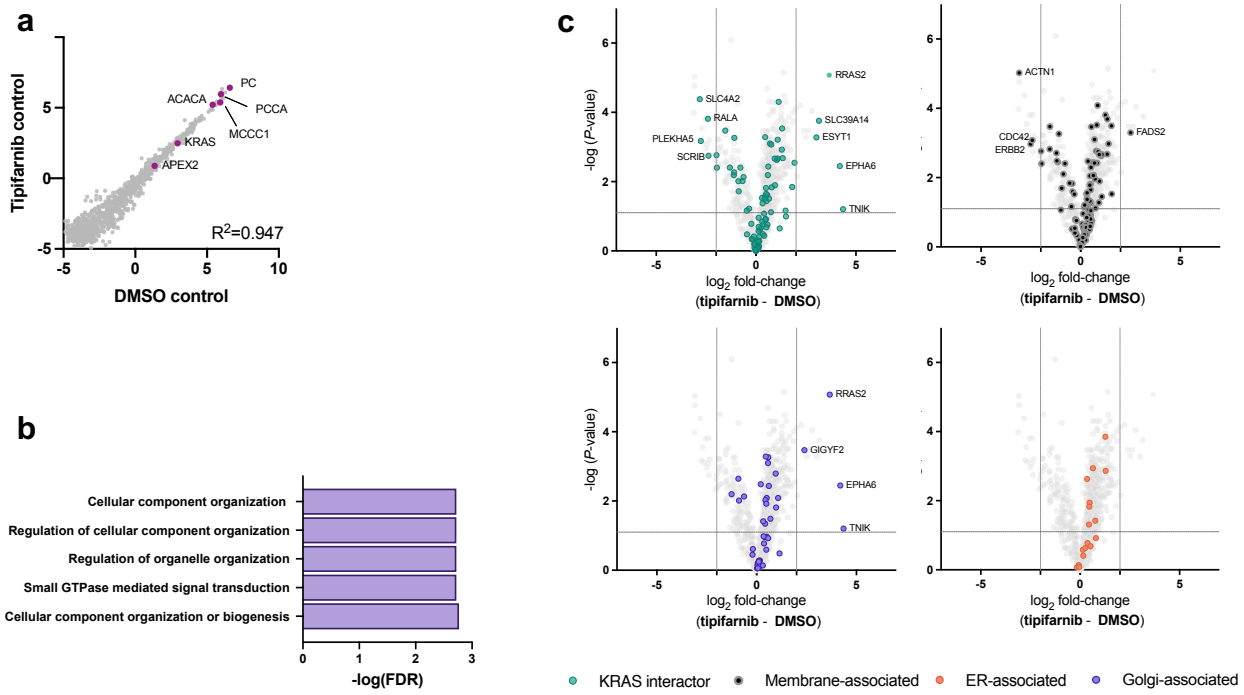

Figure 4.2.8. Proteomic analysis of APEX2-KRAS^{G12D} interactome in the presence of tipifarnib. (a) Correlation analysis of background-corrected (H_2O_2 control) tipifarnib and DMSO-treated APEX2-KRAS^{G12D} samples. **(b)** Functional enrichment analysis (STRING) of DMSO-enriched (ergo, tipifarnib downregulated) (GO: biological function). **(c)** Volcano plots of high-confidence KRAS interactor and cell component annotations of tipifarnib vs DMSO interactome analysis (student t-test; S0 = 0.1, FDR = 0.05; ratio = 1.5). See legend for annotations.

Next, the effects on tipifarnib on the KRAS^{G12D} interactome were investigated. Firstly, correlation analysis between the two background controls (tipifarnib and DMSO) was conducted to avoid artefactual skewing of the data following background correction (Fig. **4.2.8a**). Background controls were found to have a high correlation coefficient (0.947), making them appropriate for use in the data analysis pipeline. Somewhat expectedly, few proteins were observed to be differentially enriched between tipifarnib and DMSO treated samples. STRING analysis of the DMSO-treated enriched proteins showed enrichment

of cell component organization and GTPase-mediated signal transduction pathways, meaning that tipifarnib treatment may correspondingly have some effect on KRAS-signaling capacity (Fig. **4.2.8b**). Among the known high-confidence RAS-binders, RALA[393], SCRIB[394], SLC4A2[395], and PLEKHA5[396] were differentially enriched in DMSO-treated samples, meaning interactions with these proteins are potentially reduced upon tipifarnib treatment (Fig. **4.2.8c**). These are potentially interesting hits in the context of KRAS-mediated oncogenesis. RALA (RAS-related protein A) is a small protein of the RAS small GTPase family and plays a central role in anchorage-independent cell proliferation in KRAS-mutated cancers[393]. Knockdown of RALA has been shown to strongly attenuate proliferation via RAS signaling pathways, particularly in LUAD and pancreatic cancer models[397]. SCRIB (Scribble) is an *S*-palmitoylated protein implicated in the activation of GTPases and is generally localized to the plasma membrane under normal conditions[398]. A recent report demonstrated that application of $KRAS^{G12C}$ inhibitor sotorasib resulted mislocalization of SCRIB through attenuated KRAS signaling, which in turn reactivates MAPK signaling, leading to adaptive resistance[394]. Therefore, it may be possible that alternatively prenylated KRAS loses some interaction with SCRIB. Although it is unclear how these may serve as a druggable vulnerabilities, FTI-mediated loss of SCRIB and RALA interactions may be an interesting route to combinatorial therapies in RAS-driven cancers. Furthermore, SLC4A2 (solute carrier family 4 member 2) was known to be upregulated in KRAS-mutant CRCs, and recently published meta-analysis identified it as a potential novel immunotherapy target in KRAS-driven LUAD[395].

Tipifarnib-enriched KRAS interactors included RRAS2, which canonically shares signal transduction pathways with KRAS[399,400]. It may be possible that alternatively prenylated RAS proteins converge on membranes or specific membrane-domains, resulting in the capture of RRAS2 in the KRAS tipifarnib-treated interactome. EPHA6 (ephrin type-A receptor 6) is receptor tyrosine-kinase that is important for cell-cell communication and is a known predictive biomarker of resistance in KRAS and EGFR-driven cancers[401,402]. Tyrosine-kinase inhibitors (TKIs) have been shown to have some inhibitory action on EPHA6, making potential inhibitors readily available for testing in the context of investigating FTI synergy[403]. TNIK (NCK-interacting kinase) is another tyrosine-kinase

that regulated WNT signaling transduction for which an inhibitor also exists[404,405].

In an attempt to deconvolute the microenvironment of *S*-farnesylated and *S*-geranylgeranylated (i.e. alternatively prenylated) KRAS, differentially interacting proteins were annotated based on cell localization (plasma membrane, Golgi, and ER) (Fig. **4.2.8d-f**). Overall, more interactors were enriched in tipifarnib-treated samples, potentially making this analysis slightly skewed. Nonetheless, there was an observed minor increase in Golgi and ER-associated interactors in the tipifarnib-treated samples compared to the DMSO control. This may indicate that alternatively prenylated KRAS has increased residence at these cell compartments, which is partially supported by reports of small levels of unprenylated KRAS accumulation before its eventual re-localization via *S*-geranylgeranylation (unpublished data). However, further validation would be required to confirm these trends, either through time-resolved imaging of KRAS during tipifarnib-treatment, or cell fractionation analysis across several early timepoints, for example.

These identified differentially interacting proteins may serve as useful starting points for deconvoluting novel druggable vulnerabilities elicited through tipifarnib treatment in KRAS-driven cancers. Further validation is required to understand how this may be leveraged, either through CRISPR-KO/siRNA screens conducted in the presence and absence of tipifarnib, or lower throughput validation techniques for particular targets, either through siRNA knockdown or drug treatment for proteins that have existing inhibitors[406].

4.2.4. APEX2-RAS interactome study in the presence and absence of tipifarnib

After validating an interactomics workflow for APEX2- $KRAS^{G12D}$ using a relatively small-scale study, a larger study was devised with the remaining APEX2-RAS constructs (KRAS WT, NRAS and HRAS) (Fig. **4.2.9a**). Here, the same treatment strategy and proteomic sample was employed. Key differences from the previously outlined workflow for $KRAS^{G12D}$ included the use of larger culture dishes (15 cm vs 10 cm) to increase protein yields across the experiment, as the previous study was affected by cell loss

during quenching/washing steps following hydrogen peroxide-initiated labelling. Moreover, TMT 15-plex was used instead of 6-plex to capture a full replicate of each of the cell lines within a single TMTplex with minimal TMT-channel signal crosstalk [265](discussed in the previous chapter).

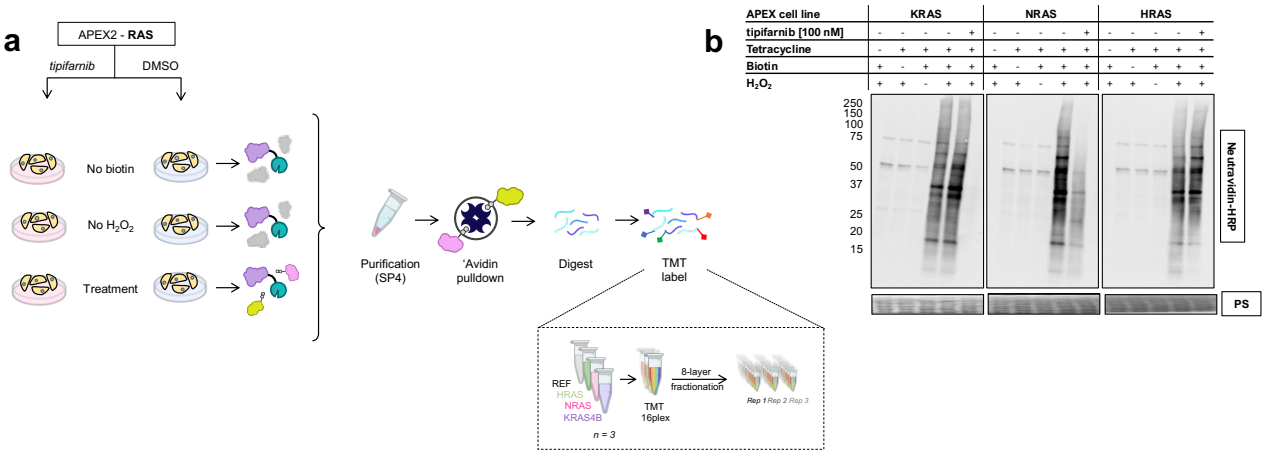

Figure 4.2.9. Proteomic strategy for profiling APEX2-RAS isoform interactors. (a) Schematic depicting sample generation and proteomic sample processing of APEX2-RAS PL constructs. Workflow is analogous to Fig. 4.2.6. TMT-labelled was conducting using a 15-plex, including a reference (pooled) sample to enhance peptide quantification and allow multi-batch TMT comparisons. TMT-labelled samples are then fractionated using a high-pH 8-layer fractionation kit (Pierce, ThermoFisher), and submitted for MS-analysis. **(b)** Quality control biotinylation analysis via Western blot (Neutravidin-HTP) of a representative replicate of prepared APEX2-RAS samples, confirming appropriate biotinylation patterns in controls and PL samples. PS – Ponceau S stain

Following PL sample generation (described in Methods), 20 µg of lysate was reserved for quality control analysis as in the APEX2-KRAS^{G12D} study, which revealed the expected biotinylation patterns for each cell line (Fig. **4.2.9b**). All lysates were generated on the same day, however due to the sheer amount of samples (54 in this case) requiring proteomic processing, samples were subjected to 'avidin bead-based enrichment in batches based on replicates. Principal component analysis (PCA) revealed clear batch effects as a result, thereby necessitating the use of batch correction computational approaches (Fig. **4.2.10**). PCA was used as a benchmarking parameter for computational processing, revealing that reference scaling, COMBAT-based batch correction and KNN (cluster-based imputation), resulted in the most significant reduction in batch effects

(shown in the upper left quadrant of **Fig. 4.2.10**)[407]. This workflow was thus incorporated in our proteomic analysis. One significant caveat to this study was the loss of one NRAS replicate, which was addressed by the creation of a "false replicate" using a combination of the remaining replicates. The study will thus be repeated for higher quality data in the near future, however for the time-being this was determined to be appropriate for the acquisition and analysis of preliminary data.

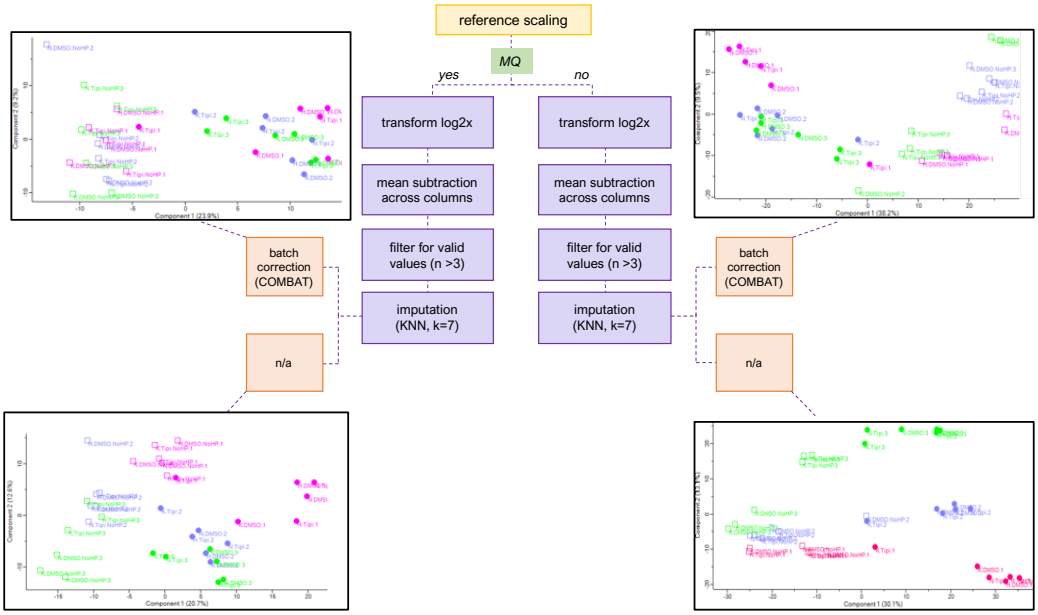

Figure 4.2.10. Data analysis workflow of APEX2-RAS interactome study using multi-batch TMT labelling. Data analysis depicted as go/no go workflow and benchmarked using principal component analysis (PCA) of all samples. Lower right quadrant PCA shows clustering based on TMT-batch (which are organized as replicates), indicating batch effects. Batch effects are mitigated by the use of reference scaling and batch correction using the COMBAT algorithm (all data processed using R and Peresus software). K-next neighbor (KNN) imputation is performed for all datasets to mitigate presence of missing values, particularly in PL control samples.

As a first attempt at deconvoluting the large amount of proteomic data generated, analysis of APEX2-KRAS samples was undertaken using a similar cell component annotation strategy. APEX2-KRAS was significantly enriched along with KRAS-derived peptides, signifying successful labelling and enrichment **Fig. 4.2.11a**. High-confidence interactors were also significantly enriched, however RAF1/ARAF/BRAF were notably absent throughout this study, across all APEX2-RAS cell lines.

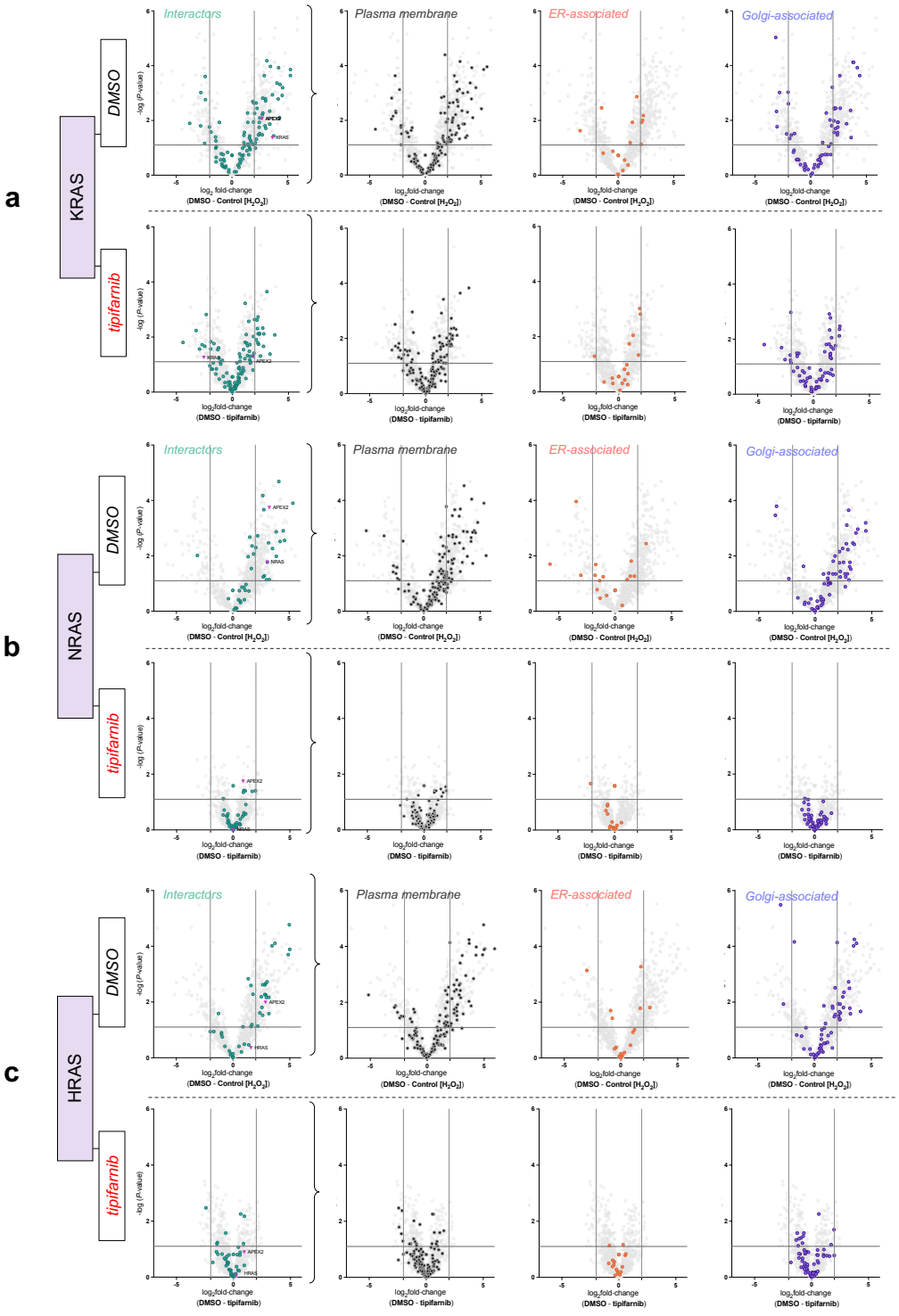

Figure 4.2.11. Proteomic analysis of APEX2-RAS interactomes in the presence and absence of tipifarnib. Volcano plots of high-confidence KRAS **(a),** HRAS **(b)** and NRAS **(c)** interactor and cell component annotations of tipifarnib vs DMSO interactome analysis (student t-test; S0 = 0.1, FDR = 0.05; ratio = 1.5). See legend for annotations.

Generally, cell component analysis observations of APEX2-KRAS did not appreciably recapitulate the findings from the APEX2-KRAS^{G12D}, in that there was an observed increase in Golgi-associated proteins in the DMSO-enriched sample when compared to the tipifarnib sample – the opposite was found in the KRAS^{G12D} dataset. This may be associated with our initial finding that the APEX2-KRAS construct does not undergo alternative prenylation, whereas APEX2-KRAS^{G12D} does. Therefore, as the protein localization may be altered as a result of alternative prenylation, this may in turn be reflected in the captured interactome. STRING analysis of differentially enriched tipifarnib interactors revealed functional enrichment (biological process) of cellular component (GO:0016043; FDR = 0.00022) and cytoskeletal organization (GO:0007010; FDR = 0.00030), while DMSO-enriched interactors exhibited functional enrichment of protein stabilization (GO:0050821; FDR = 3.64e-07) and cellular process (GO:0009987; FDR = 3.64e-07). It is relatively unclear how this may point to biological effects associated with tipifarnib treatment, however it this trend was reversed in the APEX2-KRAS^{G12D} proteomic analyses, further implying that this KRAS construct was responding in the same manner as KRAS^{G12D}.

Similar conclusions were drawn by the APEX2-NRAS and HRAS interactomes (Fig. **4.2.11b** and **c**), where enrichment of both respective fusion constructs, including the APEX2-derived peptides, were found to be significant. In the case of HRAS, HRAS-derived peptides were not found significantly enriched, however as discussed previously, this was expected due to issues resolving unique HRAS peptides. There were overall fewer observed differentially enriched proteins between tipifarnib and DMSO in HRAS and NRAS interactomes, which also may be reflective of either subtle changes in the interactome upon FTI treatment, or that the dynamic range of the interactome enrichment on this occasion was not sufficient to capture these differentials. When comparing DMSO and tipifarnib-enriched interactomes in the APEX2-HRAS cell line, SCAMP2 (Secretory carrier-associated membrane protein 2) was significantly enriched in the DMSO population. SCAMP2 is part of a large class of Golgi-resident proteins that play key roles in the regulation of anterograde trafficking between the Golgi and plasma membrane[408,409]. This may support the notion that HRAS is not trafficked to the plasma

membrane in the presence of tipifarnib, and may also shed light on potentially important regulators up or downstream of this process, whereby SCAMP2 putatively does not interact with unprenylated HRAS. Notably, SCAMP2 was not differentially enriched in the analogous NRAS and KRAS tipifarnib vs DMSO interactome analyses, which is in keeping with the fact that SCAMP2 is known interactor of HRAS, but not KRAS or NRAS (BIOGRID)[249]. However, it is unclear if SCAMP2, or its associated membrane trafficking pathway, plays a role in alternative prenylation, and requires substantial further validation.

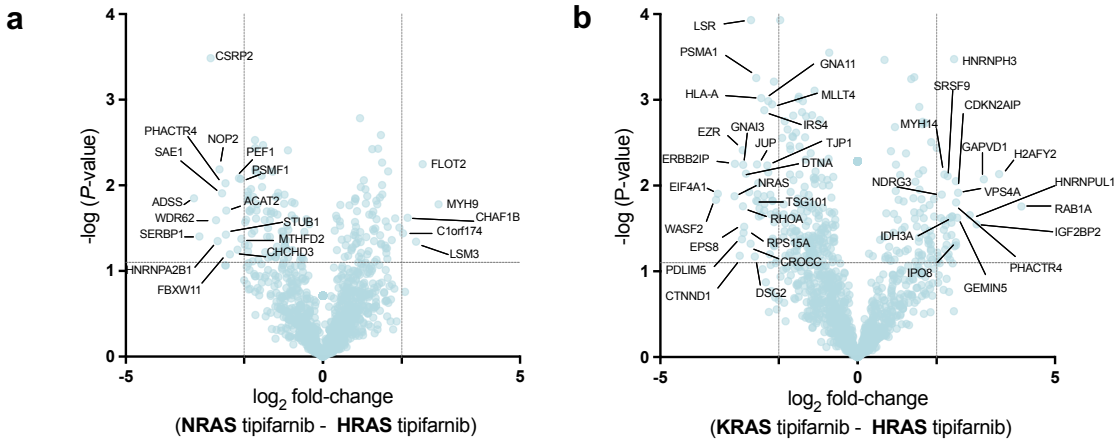

Figure 4.2.12. Comparison between alternatively and non-alternatively prenylated interactomes. Volcano plots of **(a)** NRAS *vs* HRAS **(b)** KRAS *vs* HRAS **(c)** interactome comparisons (student t-test; FDR = 0.05; ratio = 1.5). Differentially enriched proteins are labelled.

When comparing the NRAS tipifarnib-treated interactome with that of HRAS, HRAS exhibited an enrichment of several high-abundance proteosome, histone, and ribosomal proteins, which may be the result of non-specific enrichment (Fig. **4.2.12a**). On the other hand, NRAS-tipifarnib enriched proteins included FLOT2 (Flotillin-2), a highly conserved *S*-palmitoylated protein implicated in signal transduction pathways associated with vesicular trafficking and known to be associated with mediating RAS interactions with effectors at the plasma membrane[410–412]. This again may serve to emphasize that HRAS is not signaling at the plasma membrane as effectively as NRAS, which is alternatively prenylated in the presence of tipifarnib. Making the same comparison with KRAS tipifarnib-treated interactome revealed differential enrichment of GAPVD1 (GTPase-activating protein and VPS9 domain-containing protein 1) in the KRAS population, a

known GTPase-activating protein (GAP) for RAB proteins, and potentially for RAS proteins[161,413]. It remains possible that a different set of GAPs activate alternatively prenylated RAS, perhaps as a result of protein localization or presence of a more hydrophobic/larger prenyl group (when compared to farnesyl). This has not yet been investigated and may present an unexplored avenue to target RAS activation potentiated by tipifarnib/FTI treatment. However, targeting GAPs directly would likely not be efficient owing to their wide-ranging substrate scope in the cell, as well as homology with other GAPs essential for cellular function[163].

It was not immediately obvious how the majority of other differentially enriched proteins relate to alternative prenylation states and their associated interactomes, and analysis was further complicated by the level of noise in the data, as well as the fact that KRAS in this context does not appear to undergo alternative prenylation for reasons that currently remain unknown. When comparing the APEX2-KRAS^{G12D} interactome with APEX2-KRAS, 105 significantly enriched proteins (30.9% of KRAS; 37.2% of KRAS^{G12D}) were shared between the two datasets (Fig. **4.2.13a**). A greater proportion of KRAS^{G12D} interactors were found to be known high-confidence KRAS interactors compared to the KRAS interactome (21.27% *vs* 11.47%). This may signify that the quality of data generated for this experiment was somewhat lower than the previously undertaken KRAS^{G12D} interactome profiling. Comparisons between differentially enriched proteins from all resolved interactomes from this experiment (HRAS, NRAS and KRAS) revealed a modest degree of overlap, however functional enrichment studies did not offer immediately actionable insights into what may be modulating alternative prenylation (Fig. **4.2.13b**). It was noted, however, that fewer overlapping enriched proteins were identified in the tipifarnib-treated interactomes, which could be followed up on using orthogonal screening techniques, such as the use of genetic screens (i.e. CRISPR or RNAi), as discussed previously (Fig. **4.2.13c**).

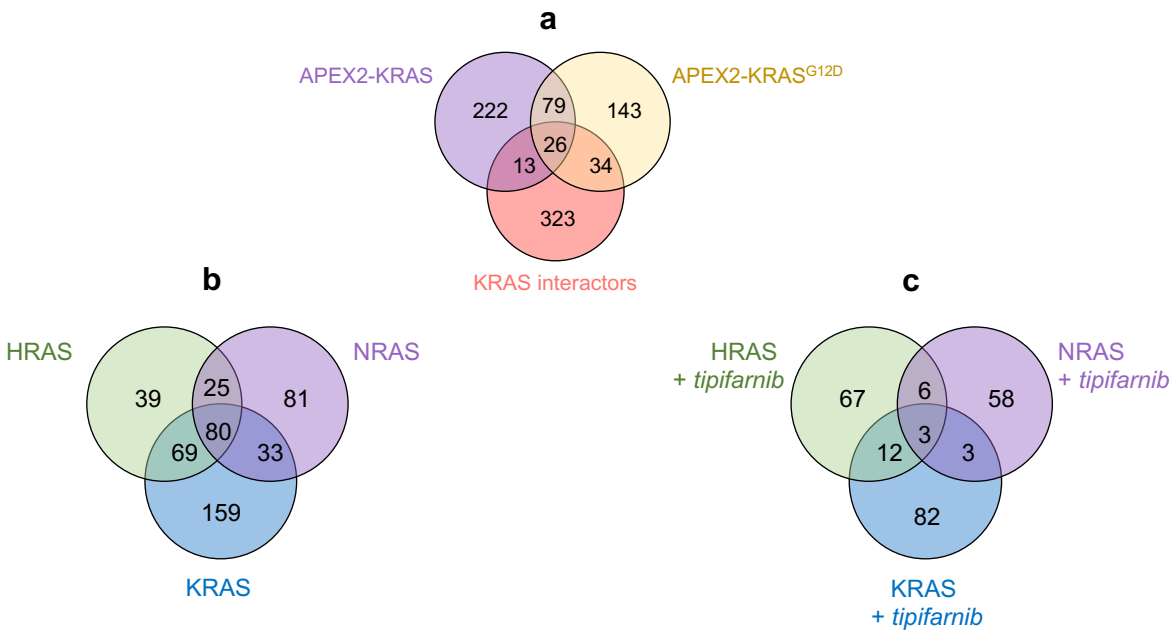

Figure 4.2.13. Comparisons between APEX2-RAS isoform datasets. (a) Venn diagram depicting overlap of significantly enriched proteins in APEX2-KRAS (purple) and APEX2-KRAS^{G12D} (yellow) datasets, with known high-confidence KRAS interactors (red). **(b)** Venn diagram depicting overlap of significantly enriched proteins in DMSO-treated APEX2-RAS isoform datasets. **(c)** Venn diagram depicting overlap of significantly enriched proteins in tipifarnib-treated APEX2-RAS isoform datasets. (HRAS = green; NRAS = purple; KRAS = blue)

Overall, it was understood from this analysis that deconvoluting potentially interesting hits was obscured by the noise in the data, which could be associated with the nature of APEX2 labelling. Moreover, the use of hydrogen peroxide, although brief, does introduce a level of cellular stress that may be captured in the labelled samples, and consequently not in the H_2O_2 control samples. These putative artifacts could potentially be attenuated by the introduction of more replicates, however this is much more difficult to incorporate in APEX2 PL experiments due to the level of speed and precision required during labelling and wash steps. Moreover, the peculiarities of the KRAS construct did not instill a lot of confidence in this dataset, at least for KRAS-related comparisons. Though more complex data analysis strategies could be undertaken to further deconvolute this data, there was limited time during the PhD to contribute further to this endeavor. However, this will be revisited in the near future. Therefore, while we explored resolutions and potential improvements to the APEX2 protocol, as well as other data analysis techniques, alternatives were explored for interactome mapping of RAS isoforms in the presence and absence of tipifarnib.

4.2.5. Transitioning to a MiniTurboID interactome profiling strategy

APEX2 labelling is generally promiscuous when compared to other PL methods, due to the transient and high-speed nature of labelling. It is also appreciated that RAS signaling is particularly complex and highly context-specific, necessitating the recruitment of multiple effectors and interactors to execute downstream function, with over 1000 interactors identified for RAS proteins in published datasets (BIOGRID). It was hypothesized that longer labelling times, afforded by PL methods like MiniTurboID, would result in the accumulation of signals that average out background signal that is not necessarily directly associated with tipifarnib treatment, as well as intensifying signals that are potentially more relevant to the perturbation of interest[414].

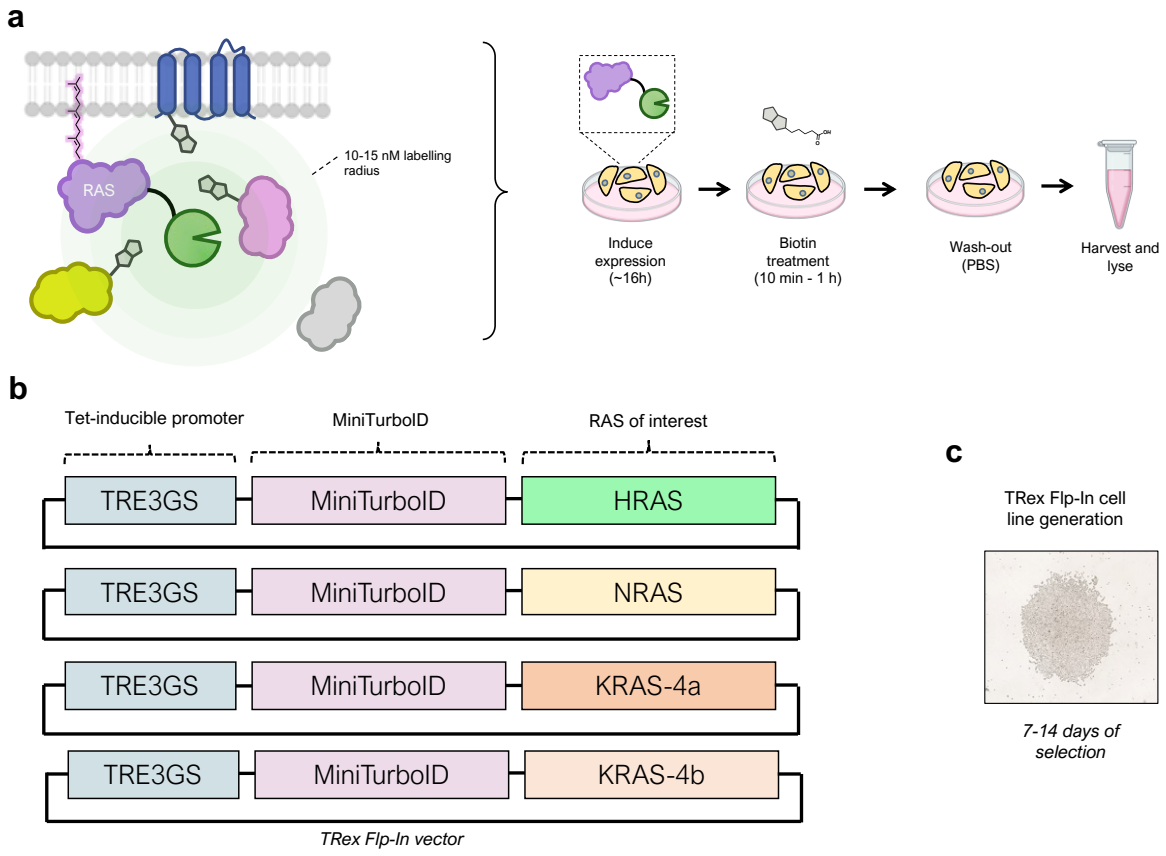

Figure 4.2.14. MiniTurboID proximity labelling strategy for RAS interactome mapping. (a) MiniTurboID biotin ligase is genetically fused to a protein of interest (shown as RAS here), which utilizes exogenously given and endogenous biotin to label proximal proteins within a ~10-15 nM radius upon induction of construct expression, with a typical labelling window of 10 min – 1 h. Biotinylated proteins in cell lysates are then isolated using 'avidin-bead based enrichment, after

which enriched proteins are digested and analyzed by MS-methods. **(b)** Designed MiniTurboID-RAS fusion constructs. RAS isoforms were cloned into TRex Flp-In vector backbones, including a Tet-inducible promoter and an N-terminal fusion to prevent RAS mislocalization by obstruction of the membrane targeting motifs on the protein C-terminus. **(c)** Example of selected foci or "island" generated during selection of MiniTurboID-RAS TRex Flp-In cell lines**.** Cell line generation was performed alongside Erika Bernardini.

Herein, an analogous MiniTurboID system was developed to complement the APEX2 constructs (Fig. **4.2.14a**). MiniTurboID is a biotin ligase, as opposed to biotin peroxidase, that harbors intrinsic biotin activation capacity[414]. Biotin is converted to a reactive biotin ester (biotin-AMP) that can covalent bind to surrounding biomolecules within a slightly smaller labelling radius when compared to APEX2 (10-15 nM *vs* 20 nM for APEX2)[380]. Labelling is induced by the introduction of biotin, ideally in low-biotin media, such as standard DMEM, to avoid background labelling. This is appreciably less laborious than APEX2 labelling, as no additional induction, quench or washing steps are required. Importantly, this makes MiniTurboID more amenable to the inclusion of more conditions and replicates as required. Sufficient labelling is usually observed from 10 mins of exogenous biotin addition, however the labelling period can be extended in the interest of accumulating more signal, where relevant.

MiniTurboID constructs were designed using TRex Flp-In vector backbone as the APEX2 constructs, including the same flexible linker and FLAG-tag (Fig. **4.2.14b**). Constructs were assembled using Gibson assembly. Stable TRex Flp-In cells were generated using a standard protocol[366]. Briefly, the MiniTurboID construct was transfected alongside a Flp recombinase expression vector (pOG44), which facilitates insertion of the gene of interest in engineered FRT sites present in the host cell line (HEK TRex Flp-In, ThermoFisher). After cells recover from transfection, the selection antibiotic (hygromycin B) is added to select for cells harboring the gene of interest. This eventually results in isogenic cell foci on the selection plate (shown in Fig. **4.2.14c**) that are harvested, pooled and passaged together.

Unfortunately, generation of the HRAS line failed on the first attempt, which was hypothesized to arise from poor plasmid purity (as later deduced from Sanger

sequencing, data not shown). The remaining cell lines were carried forward. Following cell line generation, induction tests were performed using tetracycline using just a 16 h timepoint for convenience (Fig. **4.2.15a**). Induction was monitored by Western blot (α-FLAG), as in previous APEX2 experiments.

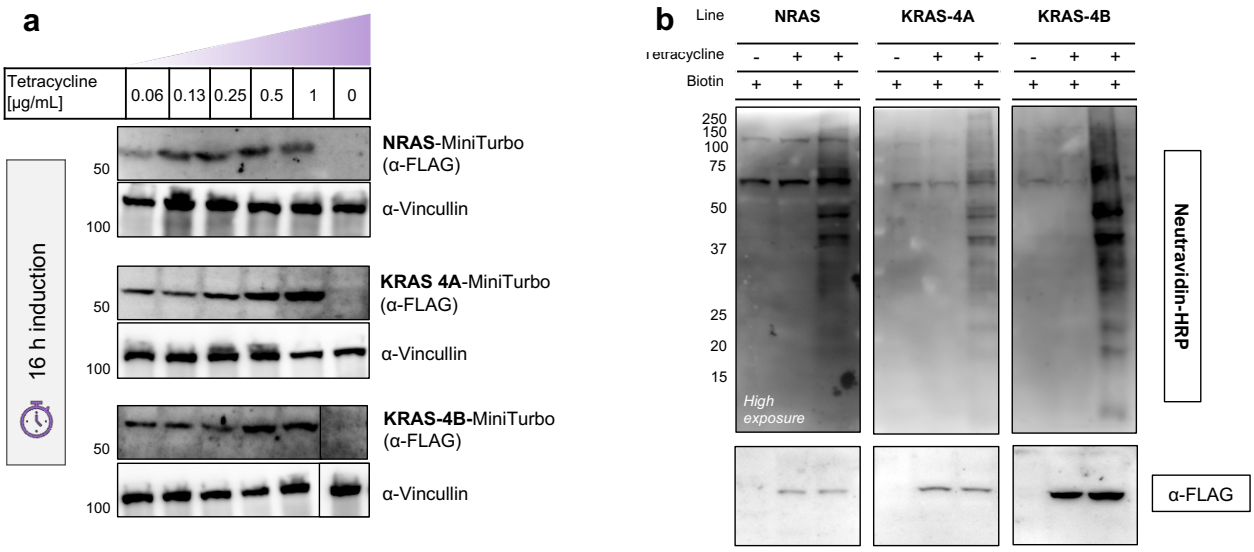

Figure 4.2.15. Testing MiniTurboID-RAS constructs for proximity labelling experiments. (a) Western blot analysis of MiniTurboID-RAS (FLAG) induction upon tetracycline-treatment is dose-dependent. **(b)** Western blot (Neutravidin-HRP) validation of biotinylation patterns of MiniTurbo-NRAS, KRAS4A and KRAS4B constructs, where biotinylation is only observed upon induction (tetracycline) and biotin.

Induction of each of the constructs was successful and exhibited the expected molecular weight (~ 51 kDa). A tetracycline concentration of 0.5 µg/mL was chosen for experiments going forward, as this appeared to be the lowest tested concentration that demonstrated consistent expression across all three cell lines. Next, biotinylation tests were conducted, which consisted of a 16 h induction period and 1 h labelling period, initiated by addition of 250 µM biotin (Fig. **4.2.15b**). Correct biotinylation patterns were observed for all cell lines. The NRAS cell line exhibited weak labelling, however this was likely due to lower protein loading. Overall, the observed biotinylation signal from these experiments were relatively weak compared to APEX2, which was anticipated due to the less promiscuous nature of MiniTurboID PL. This was expected to aid in the reduction of background that proved to be problematic in APEX2 experiments.

Attempts at discerning *S*-prenylation patterns for these cell lines, as was performed for the APEX2 constructs, were made; however, due to issues with pulldown and labelling experiments at this time, *S*-prenylation and alternative prenylation were not confirmed for these constructs before the end of the PhD. Despite this, proteomic samples were prepared in parallel to *S*-prenylation validation experiments, which enabled preliminary insights in to the MiniTurboID interactomes while we resolved issues with probe labelling and enrichment (Fig. **4.2.16**).

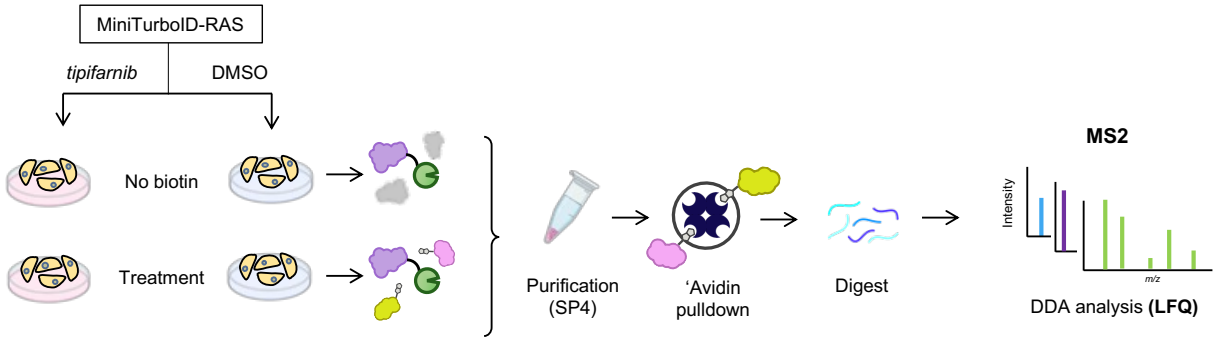

Figure 4.2.16. Proteomic strategy for profiling MiniTurboID-RAS isoform interactors. Schematic depicting sample generation and proteomic sample processing of MiniTurbo-RAS constructs were subject to PL in the presence and absence of tipifarnib (100 nM). Uninduced (no tetracycline) controls samples alongside labelled samples. Samples were prepared in triplicate, harvested and lysed, purified using SP4 and subject to 'avidin enrichment using Neutravidin-agarose beads. Following pulldown, samples were digested on-bead, and resultant peptides were analyzed by mass spectrometry (LFQ, using a DDA acquisition workflow on a TIMS-TOF device).

Additionally, at this time the Tate Group transitioned to a newer MS technology (TIMS-TOF), enabling the acquisition of higher quality proteomic data from lower amounts of protein, and resulted in the improvement of peptide quantification without the need for TMT-labelling[415,416].Samples were thus submitted without TMT-labelling or fractionation, in contrast to the previous iterations of PL (APEX2) experiments. It was noted, however, that this would complicate comparisons with APEX2 data.

Unfortunately, due to issues with proteomic sample submission, NRAS, as well as KRAS4B + tipifarnib MiniTurboID sample data were not fully acquired. As a result, this initial analysis was focused on comparing KRAS4A and KRAS4B MiniTurboID

interactomes. KRAS4A is considered to be a minor splice variant of KRAS, with 4B being more dominant[417]. However, recent reports have shifted this paradigm with the finding that KRAS4A was expressed in equal amounts of KRAS4B in various types of colorectal cancer. Moreover, KRAS4A membrane targeting is additionally regulated by *S*-palmitoylation and is required for stable plasma membrane localization whilst KRAS4B has an inbuilt membrane targeting motif, consisting of a stretch of basic amino acids near the C-terminus (polybasic region, or PBR) that facilitates stabilizing electrostatic interactions with the negatively charged inner leaflet of the plasma membrane[418]. As they are directed to the membrane through distinct mechanisms, these splice variants possess different interactomes[384]. For example, one recent study found that KRAS4A is a direct regulator of HK1 (hexokinase 1), which is both a known GTPase effector and a key enzyme in the initiation of glucose metabolism[181]. KRAS4A interacts with HK1 by virtue of its distinct subcellular localization, which can be targeted to the outer mitochondrial membrane when *S*-palmitoylation is suppressed, in converse to KRAS4B, which is a non-interactor and cannot differentially regulate its second membrane-targeting signal, which is inbuilt. This is significant, in that KRAS4A may play a dominant role in metabolic rewiring. Revealing these types of differentials may contribute to a better understanding of how to target membrane localization in RAS-driven cancers, lending itself to the development of new therapeutic modalities.

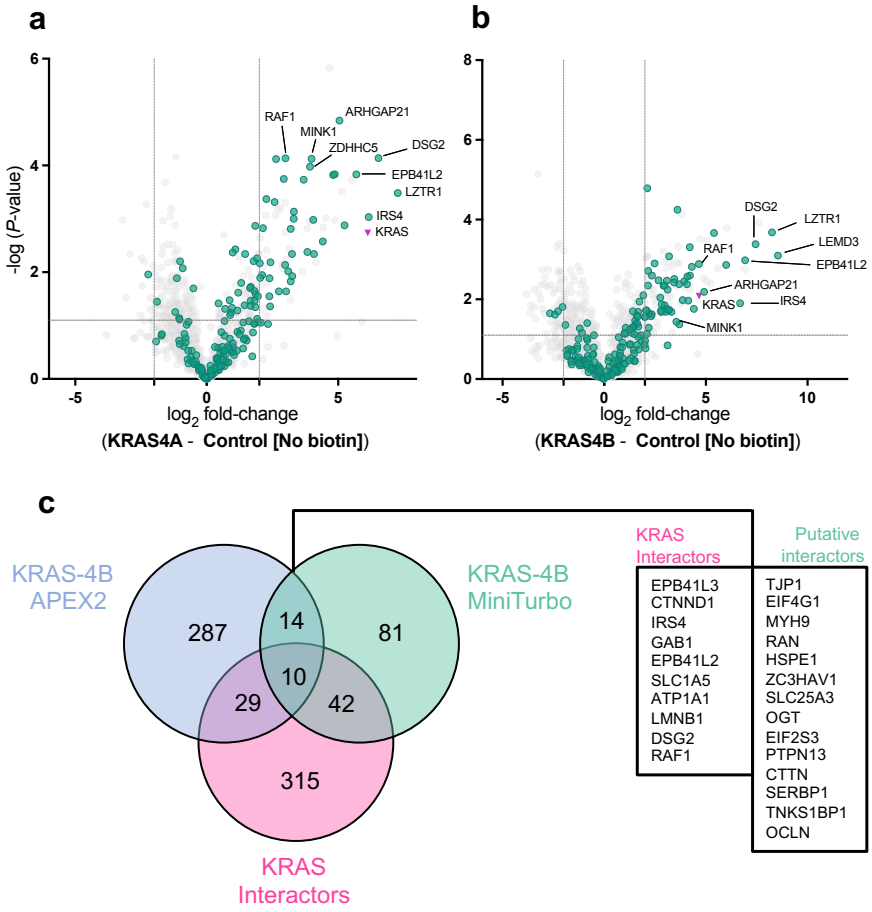

Figure 4.2.17. Proteomic analysis of MiniTurboID-KRAS4A and 4B interactomes. Volcano plots depicting **(a)** MiniTurbo-KRAS4A and **(b)** KRAS4B interactor-enrichment (student t-test; S0 = 0.1, FDR = 0.05; ratio = 1.5), compared to a background controls (no biotin). High-confidence KRAS interactors (curated from BIOGRID data) are highlighted in teal. A selection of interactors are labelled. KRAS is highlighted in magenta. **(c)** Venn diagram showing overlap of previous APEX2-KRAS4B (blue), MiniTurboID-KRAS4B (teal) and high-confidence KRAS interactors (red).

Initial proteomic analysis of MiniTurboID PL demonstrated successful enrichment of KRAS (by way of self-biotinylation), as well as various high-confidence KRAS interactors, including LZTR1 (Leucine Zipper Like Post Translational Regulator 1), a key interactor that regulates the ubiquitination of KRAS, which was notably absent in the previously described APEX2 studies (Fig. **4.2.17a** and **b**). Moreover, MiniTurboID-KRAS4B had a higher proportion of high-confidence KRAS interactors in the enriched population when compared to the previous APEX2-KRAS4B experiment (35.37% *vs* 11.47%), meaning that the background in the enriched population appeared to be significantly reduced in the MiniTurboID experiment (Fig. **4.2.17c**).

Comparing the MiniTurboID KRAS4A interactome with that of KRAS4B revealed several differentially enriched proteins (Fig. **4.2.18**). Perhaps most notably, ZDHHC5, a PAT with a relatively unexplored substrate scope, was significantly enriched in the KRAS4A population, along with LYPLA2, which was enriched but didn't meet the significance cut-off[419]. As discussed previously, KRAS4A is an *S*-palmitoylated alternative splice variant of the *KRAS* gene, while the major splice variant KRAS4B is not *S*-palmitoylated. ZDHHC5 is a member of the DHHC class of PATs that are primarily concentrated at the Golgi and ER[420]. ZDHHC5 is one of the few PATs characterized to have plasma membrane localization, and is known to promote retrograde transport from the plasma membrane and recycling endosomes to the Golgi[419]. Moreover, while ZDHHC5 has been identified in several published PL and AP-MS RAS interactome studies, including in the APEX2 PL experiments outlined in this chapter, it has yet to be established as a *bona fide* PAT for RAS proteins[249]. Instead, ZDHHC9 has long been considered to be the major PAT for NRAS and HRAS, and no PAT has been definitely assigned to KRAS4A. ZDHHC9 is a primarily Golgi-resident PAT closely related to ZDHHC5, and both share an accessory protein, GOLGA7, that regulates PAT activity[421,422]. It is also well-established that ZDHHCs, of which 23 have been identified, harbor a high level of redundancy across target substrates, as loss of a single ZDHHC can often be compensated by the activity of another. In fact, *S*-palmitoylated RAS persists even upon genetic deletion of multiple ZDHHCs[423]. It remains possible that ZDHHC5 functions as an alternative or complementary PAT for RAS at the plasma membrane, acting to re-palmitoylate substrates that are subject to de-palmitoylation by APTs in the cytosol. This may be part of a larger contribution to the complex trafficking dynamics of RAS proteins, where dynamic *S*-palmitoylation largely dictates which membrane RAS signals from, directly impacting the nature of signaling and downstream consequences of RAS activity.

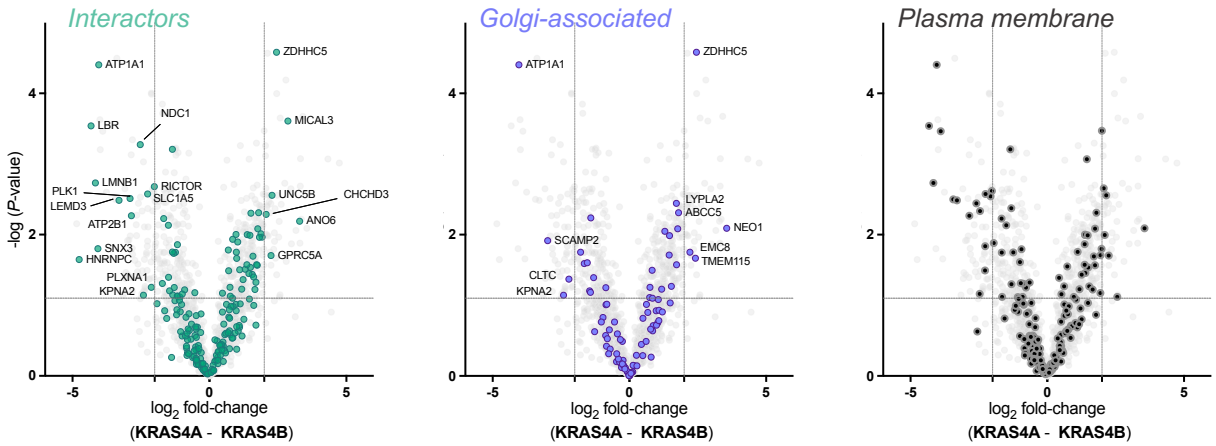

Figure 4.2.18. Comparison of MiniTurboID-KRAS4A and 4B interactomes. Volcano plots comparing MiniTurbo-KRAS4A *vs* KRAS4B interactomes, with proteins annotated by high-confidence KRAS interactor (teal), Golgi-association (purple), and plasma membrane-association (black) (student t-test; S0 = 0.1, FDR = 0.05; ratio = 1.5).

In the same vein, enrichment of LYPLA2 (Acyl-protein thioesterase 2) in the KRAS4A interactome also supports the validity of the MiniTurboID system, as KRAS4A is subject to de-palmitoylation while KRAS4B is not. LYPLA2 is an APT putatively implicated in HRAS de-palmitoylation, however as with many palmitoylation-related enzymes, its substrate scope has not yet been profiled[424]. LYPLA2 is a closely related to LYPLA1 (~68% homology), which has also been classified as a putative RAS APT for which dual and isoform-specific inhibitors have been described[189,425]. While inhibition of ZDHHCs remains challenging due to high homology, redundancy, and functional essentiality across the PAT family, APTs have been suggested as potential therapeutic targets for modulation of RAS activity[189]. It could be hypothesized that APT inhibition sustains RAS signaling at the plasma membrane due to stabilization of the *S*-palmitoylated species, however somewhat counterintuitively, APT inhibition has instead been shown to reduce RAS signaling and cell proliferation. Pharmacological stabilization of RAS at the plasma membrane through APTi triggers RAS redistribution across cellular membranes, resulting in attenuated signaling. Therefore, APTi may be a novel therapeutic modality for KRAS4A-driven cancers.

Other potentially notable findings include the enrichment of MICAL3 in the KRAS4A interactome, an epithelial to mesenchymal transition (EMT) regulator frequently overexpressed in non-smoker LUAD, however it is unclear how this may be tied with isoform-specific KRAS interactions[426,427]. In the KRAS4B interactome, specific enrichment of ATP1A1 was observed. ATP1A1 (sodium/potassium-transporting ATPase subunit alpha) is a transmembrane protein that has been found to be overexpressed in KRAS-driven cancers[428]. Surface exposed domains of ATP1A1 undergo homophilic interactions between cancer cells and fibroblasts, which triggers activin A secretion. Activin A then saturates in the tumor-stroma interface and modulates heterogeneity in the tumor microenvironment through EMT modulation, leading to tumor invasion and metastasis. A separate study also found that KD of ATP1A1 causes cell death in 3D models of KRAS-driven cancers, but not in 2D, which supports this mechanism[429]. Again, how KRAS4B-specific interactions with ATP1A1 engender this phenomenon has not yet been investigated, however can be another incentive to therapeutically delocalize RAS in metastatic cancer.

Comparing the MiniTurbo-KRAS4A tipifarnib-treated interactome with the corresponding DMSO-treated control revealed fewer differentially enriched proteins (Fig. **4.2.19**). Tipifarnib-treatment generally had a similar effect across APEX2 interactome experiments. Here, this phenomenon may partially be due to anchoring stability imparted by alternative prenylation, as geranylgeranyl is more hydrophobic than farnesyl. However, few conclusions can be drawn prior to validation of *S*-prenylation states of these MiniTurboID constructs, which is forthcoming.

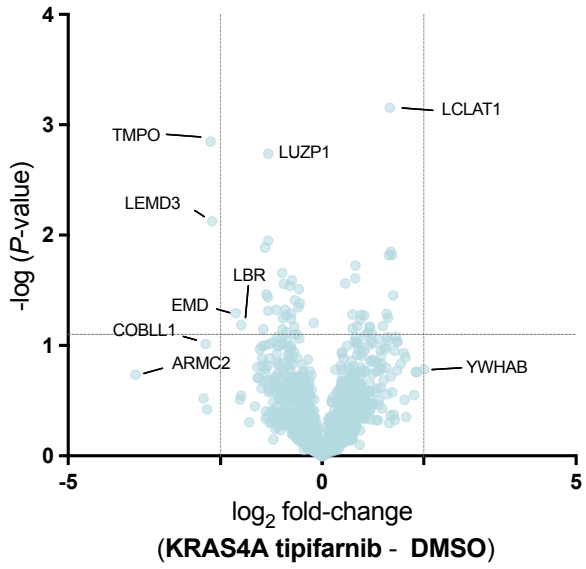

Figure 4.2.19. Proteomic analysis of MiniTurboID-KRAS4A interactome in the presence of tipifarnib. Volcano plot comparing DMSO and tipifarnib-treated MiniTurbo-KRAS4A interactomes (student t-test; S0 = 0.1, FDR = 0.05; ratio = 1.5). A selection differentially enriched proteins are labelled.

TMPO was found to be enriched in the DMSO-treated interactome, a protein involved in the nuclear organization and a known LMNA interactor, which is *S*-farnesylated[430]. This may mean that this PL approach also captures tipifarnib-associated effects potentially unrelated or adjacent to the POI, however at this stage it cannot be confirmed if this is indeed the case, or if this is a significant disadvantage altogether. Nevertheless, LCLAT1 may be a potentially interesting tipifarnib-specific interaction. LCLAT1 is an ER-resident acyltransferase responsible for acylating phosphoinositides, which are signaling lipid molecules that embed in cellular membranes and recruit proteins in a phosphorylation-dependent fashion[431]. Acylated phosphoinositides promote different signaling cascades to their non-acylated counterparts[432]. LCLAT1 in particular has been shown to regulate AKT-signaling in this manner, an important component of downstream KRAS activity. However, as with other interactors identified throughout this chapter, orthogonal validation would be necessary to establish this interaction, in this context, the role of tipifarnib-treated KRAS4A. Other differentially enriched interactors identified have ill-defined ties to KRAS or other known RAS functions. As this data is preliminary and the PL experiment is planned to be repeated with the other MiniTurboID constructs following *S*-prenylation

state validation, these proteins can be further investigated if enriched in the next iteration of this experiment.

4.3. Chapter summary and future directions

This chapter outlines two different PL approaches to study the RAS interactome in the presence and absence of tipifarnib in an effort to identify novel tipifarnib-potentiated therapeutic targets. APEX2 PL provided a model to capture a "snapshot" of the RAS interactome, as APEX2 labelling is the most temporally constrained compared to other developed PL methods. This proved to be potentially detrimental from an analytical standpoint, as reproducibility and high background labelling hindered the deconvolution of both known RAS interactors, as well as useful starting points for novel tipifarnib-associated interactions. Retrospectively, APEX2 labelling was also putatively deemed to be less informative than other PL methods that are less promiscuous and utilize longer labelling times, as the accumulation of signal following tipifarnib treatment was perhaps more likely to capture high-confidence interactors, as well as saturate the most relevant interactions. Moreover, when validating *S*-prenylation dynamics for these constructs, APEX2-KRAS did not undergo alternative prenylation as expected, which was a major caveat within this system to which an explanation has yet to be determined.

To this end, an analogous MiniTurboID was employed to complement the APEX2 model. MiniTurboID constructs for KRAS4A, KRAS4B, NRAS and HRAS were designed, however due to time constraints, only KRAS4A and KRAS4B constructs reached the proteomic analysis stage. This revealed that *S*-palmitoylation-related interactors were differentially enriched for KRAS4A when compared KRAS4B, and served to help validate the MiniTurboID system, since KRAS4A is known to be the *S*-palmitoylated KRAS splice variant. While *S*-prenylation dynamics have yet to be validated for any of the MiniTurbo ID constructs, this result instilled a degree of confidence in this PL methodology and will be carried forward to future interactome studies. Moreover, MiniTurboID appeared to be more efficient at capturing known KRAS interactors, with less background than the analogous APEX2 studies. However, as samples were run on a more advanced mass spectrometer, it was difficult to make direct comparisons. It would certainly be worth repeating these APEX2 experiments to run on this spectrometer for comparative studies.

Throughout this chapter, potential hits that have differential interactions with RAS isoforms in the presence of tipifarnib were identified, some of which had precedence related to RAS function from the literature. This includes RALA and SCRIB, which were observed to have lost some degree of interaction with $KRAS^{G12D}$ upon tipifarnib treatment. However, even after further optimizations to reduce background in proteomic studies, it remains likely that several proteins will have this kind of differential enrichment elicited by tipifarnib-treatment, necessitating a mid to high-throughput method to validate these interactors and establish potential synergy with tipifarnib-treatment. This can be envisioned to be a genetic perturbation screen, where CRISPR-KO or RNAi of these hit interactors can be conducted in presence and absence of tipifarnib. Moreover, if a hit interactor has a known on-target drug, this may be directly used to establish potential synergy. Other types of PL methodologies can be employed to complement this work, including secretome studies, whereby Golgi or ER-anchored PL-enzymes biotinylate proteins that are processed for secretion and eventually reach the extracellular environment[433]. Biotinylated proteins are then isolated from the culture media, rather than by cell lysis, to capture the labelled secretome. This can be done in the presence or absence of tipifarnib, allowing the profiling of secreted factors affected by tipifarnib-treated that may have implications in the modulation of the tumor microenvironment.

Despite the need for optimization of these experimental workflows, including but not limited to construct validation, background correction, and data analysis, interactome profiling demonstrates a viable approach to profile differential interactors of RAS isoforms afforded by tipifarnib-treatment, and may help reveal novel therapeutic modalities for RAS-driven cancers.

Chapter 5
Conclusions and future perspectives

Together, these studies have offered potentially actionable insights into *S*-prenylation dynamics upon the application of tipifarnib, a highly potent FTI that is currently under clinical investigation. SmgGDS, for example, appears to play a significant role in overall *S*-farnesylation dynamics, however it is unclear how synergy with an FTI may be envisioned. Instead, SmgGDS splice variant targeting may confer some benefits of FTI activity without the associated toxicities, as KO of the long-form "oncogenic variant" appear to have a milder, more targeted effect on global *S*-prenylation. It is remains unclear exactly what role SmgGDS plays during this process. It can be hypothesized that SmgGDS clients all the quantified *S*-farnesylated substrates to the FTase, or that SmgGDS enhances *S*-farnesylation by binding the FTase directly. The initial proposed pseudo-enzyme kinetic study (**Fig**. 2.2.5) may serve to deconvolute this mechanism, which may now be achievable given the described optimizations to the global prenylation profiling workflow. Additionally, validation of other findings within the dataset, including novel prenylated substrates and the role of DNAJA4 in regulating cholesterol biosynthesis, may be interesting to pursue, in an effort to further characterize the impact FTIs on cells and how this may translate to a therapeutic benefit. Somewhat disappointingly however, SmgGDS appeared to play no role in alternative prenylation.

The use of the drug-resistance driven CRISPR mutagenesis assay however, drew attention to a feature of RAS proteins that may contribute to differential propensities for alternative prenylation across RAS isoforms. *S*-palmitoylation may play a significant role in this, and it remains to be investigated how genetic deletion of *S*-palmitoylation sites impact alternative prenylation. *S*-palmitoylation was also widely affected by tipifarnib, perhaps revealing new opportunities to attenuate the activity of any one of the identified substrates for therapeutic benefit. This is significant considering that few drugs for PATs have been identified, and functional redundancies within the major PAT family (ZDHHCs) make drug discovery challenging in this context. Validation of these substrates as potential drug targets for tipifarnib will thus be undertaken with these goals in mind. For example, the use of APT inhibitors with FTIs may synergize against NRAS. Additionally, it remains possible that tipifarnib may have some off-target effects on PATs or other palmitoylation-associated machinery, however this was not conclusively determined by

this study and is largely unsupported by the current literature. It remains an interesting possibility however, potentially best investigated by off-target binding profiling of tipifarnib

Finally, this study has also shown that interactomics can be useful in both contextualizing protein localization in response to drug treatment, as well as revealing new interactors that result from delocalization of the protein of interest, which may be exploited for therapeutic benefit. Although the complexity and wealth of this data encumbers the identification of a set of actionable candidate proteins, further refinement of our interactomics techniques, such as the introduction of the MiniTurboID system, may pave the way for more robust sets of candidate proteins. These candidate proteins are envisioned to either play a role in alternative prenylation, or represent a novel druggable modality only revealed by application of an FTI. Synergy can then be evaluated by a genetic perturbation screen couple with tipifarnib, as a CRISPR or RNAi screen targeting candidate proteins in a specific RAS-isoform driven cancer.

Overall, these studies have explored and optimized a range of systems-wide techniques that can interrogation lipidation at a greater depth than chemical probe-based profiling alone. These techniques can be highly complementary and serve to deconvolute cross-talk between PTMs and interacting proteins that are largely inaccessible by other techniques in isolation.

Chapter 6

Materials and methods

6.1. General procedures

6.1.1. Cell culture

PANC-1 (CRL-1469) and AsPC-1 (CRL- 1682) were obtained from ATCC. EA.hy926 (CRL- 2922), HEK293T (CRL-3216), T24 (HTB-4), RL952 (CRL-1671) were acquired through the Francis Crick Institute after STR (short tandem repeat) profile authentication. TRex Flp-In HEK293 cells were obtained from ThermoFisher. MelJuSo (CVCL_1403) cell were a gift from Prof. David Holden at Imperial College London. Cas9-NCI-H23 -/- SmgGDS-607 and Cas9-NCI-H23 WT cells were obtained from the Sweet- Cordero Lab at the University of San Francisco. All cells were cultured in DMEM (Gibco, 11965118), RPMI-1640 (Gibco, 11875101), DMEM-GlutaMax (Gibco, 61965026), DMEM/Ham's F12 (Gibco, 12634010); McCoy's 5A (Gibco, 16600082).

Media was supplemented with 10% (v/v) Fetal Bovine Serum (FBS) (Gibco, 10270-106. Lot: 2260082) according to distributor protocols (ATCC). TRex Flp-In cell lines were cultured with DMEM-GlutaMax (Gibco, 61965026) with 10% Corning™ Fetal Bovine Serum Tetracycline Negative (15393691). Mycoplasma testing was performed regularly via PCR (LookOut® Mycoplasma PCR Detection Kit, Sigma-Aldrich). Cells were maintained in a humidified incubator (37℃, 5% CO2).

Generally, cells were seeded on plates 16-24h prior to experimentation. Trypsin-EDTA 0.25% (Gibco; 25200056) was used to lift cells for passaging or seeding. Cryogenically preserved cell stocks were using a standard protocol. Harvested cells (2—5e10^6 cells) were resuspended in culture medium with 10% FBS and 10% DMSO. Cells were frozen in a Mr. Frosty™ overnight at -80℃ and transferred to a -150℃ freezer for long-term storage. Cell stocks were thawed rapidly in a 37℃ water bath, transferred to a 15 mL Falcon tubes containing 5 mL of fresh media, and centrifuged to collect (5 min at 150 × *g*). Cells were resuspended in 10 mL of fresh media and seeded into a T25 flask. For TRex Flp-In cells, thawed cells were immediately resuspended in fresh media in a T75 flask.

Media was changed after cells adhered (~6-16h) and passaged accordingly. Cell viability/number was regularly checked using Trypan blue exclusion (ThermoFisher).

6.1.2. Compounds and antibiotics

Compounds and antibiotics. All drug compounds and chemical probes were dissolved in pure DMSO (Sigma-Aldrich) and stored at -20℃. Antibiotics were stored in sterile-filtered water (0.22 μM) and frozen in aliquots. Thawed stocks of antibiotics (Hygromycin B, Zeocin, Blasticidin, Ampicillin, Kanamycin, G418/neomycin, Spectinomycin) were not reused.

6.1.3. Cell lysis

Cells were lysed in an optimized buffer formulation: 50 mM HEPES (Sigma-Aldrich) pH 7.5, 150 mM NaCl (Sigma-Aldrich), 1% NP-40 (Calbiochem), 0.2% SDS (Sigma-Aldrich), and EDTA-free protease inhibitors 1X (Tablet, Roche), 250 U/μL Benzonase (Millipore). Alternative formulations were 50 mM HEPES (Sigma-Aldrich) pH 7.5, 150 mM NaCl (Sigma-Aldrich), 1% SDS (Sigma-Aldrich), and EDTA-free protease inhibitors 1X (Tablet, Roche), 250 U/μL Benzonase (Millipore). Lysis buffer was sterile filtered through a 0.22 μM filter prior to use when appropriate. Cells were washed with PBS, and cold lysis buffer was added to the plate. Plates were incubated at 4℃ for 20 mins before cell scraping and lysate harvesting. Samples were then incubated with gentle shaking at RT for 10 mins to allow Benzonase digestion. Ultrasonication was occasionally used for highly concentrated lysates to aid dissolution. Samples were finally centrifuged (14,000 × *g*, 5 min, 4℃) to remove cellular debris. A protein concentration assay was then performed (Bio-Rad) to normalize lysate concentrations (1-2 mg/mL).

6.1.4. SDS-PAGE

Lysates were normalized to 1-2 mg/mL using the original lysis buffer formula, when appropriate, using a standard DC protein assay protocol (Bio-Rad). Samples were then diluted 1:4 with 4x Laemmli loading buffer (Bio-Rad) containing 20% beta-mercaptoethanol. Samples were boiled for 5-10 mins at 95℃ and allowed to cool to RT before loading 10-14 µL (approximately 10-20 µg) on a 10 or 15 ladder gel. Most gels were 12%, apart from gels ran to resolve SmgGDS isoforms, which were 7% polyacrylamide. Gels were either hand-casted using a Bio-Rad kit (NAT1268) or purchased pre-casted (Bio-Rad, 4561046, 4561084, 4561086DC). Proteins were separated by gel electrophoresis at 120V in a TRIS-Glycine buffer (Bio-Rad NAT1258) at RT. Samples were analyzed by Coomassie blue staining (InstantBlue, Abcam, ab119211) when necessary, using the manufacturer's protocol.

6.1.5. In-gel fluorescence

Following click ligation to azide-TAMRA (AzT) or azide-TAMRA biotin (AzTB), samples were run using the SDS-PAGE protocol outlined above. Resultant gels were imaged using a Typhoon FLA 9500 imager (GE healthcare) using the 532/575 nm excitation/emission wavelengths (TAMRA). Ladders (Cy5) were imaged using 635/670 nm excitation/emission wavelengths. Alternatively, a LICOR Odyssey device was used with the corresponding settings.

6.1.6. Western blot

Following SDS-PAGE, proteins were transferred to either nitrocellulose (0.45 µm, Amersham Protran, GE Healthcare) or PVDF (0.25 µm, Bio-Rad) using a standard protocol with a Trans-Blot Turbo System (25 mM Tris, 190 mM glycine, 20% MeOH or ethanol; Bio-Rad) (25V, 2.5A, 7 min, mixed molecular weight). Following transfer, membranes were analyzed by Ponceau solution staining (Sigma-Aldrich). Membranes

were washed using Tris-buffer (50 mM Tris pH 7.4, 150 mM NaCl) supplemented with 1.0% Tween-20 (TBST). Prior to Western blot with the primary antibody, membranes were blocked with 5% nonfat milk (Sigma-Aldrich) or 5% bovine serum albumin (BSA) (Sigma-Aldrich). Afterwards, membranes were incubated with the primary antibody in blocking solution overnight at 4℃ or 1-2 h at RT. Membranes were washed with TBST (3 x 7 mins, gentle shaking) and then incubated with secondary antibody (HRP-conjugate) when appropriate, for 1-2h at RT. Membranes were washed again with TBST following secondary antibody incubation TBST (3 x 7 mins, gentle shaking) prior to imaging. Membranes were then incubated with 200-500 µL Luminata Crescendo Western HRP substrate (Milipore) to develop chemiluminescence signal and imaged using and ImageQuant LAS 4000 or the LICOR Odyssey device. Images were processed and analyzed using Image J (NIH). Antibodies and dilutions used are found in the Appendix (Chapter 7).

6.2. Protein purification techniques

6.2.1 Chloroform-Methanol (TCM) protein precipitation

Protein was precipitated using $CHCl_3$ (2 volumes), MeOH (0.5 volumes), and dH_2O (1 volume), all relative to sample lysate volume. The samples were vortexed and centrifuged (14,000 × *g*, 5 min, 4℃). The top layer was removed, ensuring the resulting precipitate at the phase interface was not disturbed, and the remaining volume was carefully removed. The precipitate was then washed twice with MeOH (500 µL) using the centrifugation steps as described, resuspending the precipitate through vortexing and sonication each time. MeOH was removed and the pellet was left to air-dry for 5 min at RT. The protein pellet was the resuspended in 2% SDS (w/v) in HEPES (50 mM, pH 7.5) to $1/10^{th}$ of the initial sample volume, with several cycles of sonication and vortexing. The resuspended samples were then diluted to 0.2% SDS (w/v) by addition of HEPES (50 mM, pH 7.5). All Eppendorf vessels were of Lo-Bind grade.

6.2.2. SP4 protein precipitation

Protein was precipitated by addition of 4 volumes of acetonitrile (MeCN, LC-MS grade when appropriate) per 1 volume of sample. Sample was vortex gently for 5 seconds before centrifugation for 5 mins at 500 – 16,000 *x g*. For larger amounts of material (i.e. > 200 µg protein), sample were transferred to protein LoBind Falcon tubes (Eppendorf) and centrifuged at 1000 *x g* for 5-10 mins. After centrifugation, the supernatant (MeCN) was removed by pouring gently, avoiding disruption of the pellet. Samples were then washed with and 80% ethanol solution, >10x initial precipitation volume (LC/MS grade when appropriate). Samples were resuspended by ultrasonication and vortexing, and centrifuged at max speed for 5 mins to pellet protein. Supernatant were gently poured out and replaced with maximum vessel volume of 80% EtOH, for a total of 3 washes. Samples were finally resuspended either in 0.2% SDS, 50 mM HEPES (pH 8), 50 mM HEPES (pH 8), or 25 mM ammonium bicarbonate (pH 8), depending on downstream application.

6.2.3. Probe sonication

Protein samples were dissolved using a Fisherbrand 505 probe sonicator when appropriate (i.e. high input, large material samples). Samples were sonicated using a 20% amplitude, 1 sec pulse cycle, at a volume greater than 200 µL. Probe was washed with sequentially with MeCN and proteomic grade H_2O between each sample.

6.2.4. SP3 precipitation

A 1:1 combination (400uL:400uL) of two different types of carboxylate- functionalized SP3 beads, both with a hydrophilic surface (Sera-Mag Speed Beads, GE Life Sciences, (45152105050250, 50mg/mL) and (65152105050250, 50mg/mL), was prepared fresh before each precipitation. Beads were mixed and washed in water using a magnetic rack prior to processing. Beads were then resuspended in 1 mL of water and 25 uL aliqouts were added to each well (30 wells) of the 96-well plate containing 100 µg of protein

(100uL, 1 mg/mL) of protein lysate samples to achieve an approximate ratio of 1:10 (µg of protein/g of SP3 beads). To initiate binding, absolute ethanol (552 µL) was added to each well to achieve a final concentration 80% ethanol (v/v). The deep-well plate was then incubated at RT for 15 min shaking and then transferred to a Thermo Kingfisher bead-based enrichment system to exchange the buffer and remove click reagents, using the program entitled “SP3 bead protein clean up from click reaction. During this program, the beads were rinsed twice with 500 µL of 90% ethanol without releasing the magnetic beads from the magnet. For elution, the beads were released and mixed in 200 µL of 50 mM 0.2% SDS HEPES buffer (deep well plate). Protein concentration was determined at this point to measure retention of protein on SP3 beads.

6.3. Cell treatments

6.3.1. YnF/YnGG/YnP probe treatment.

Cells were plated at the appropriate densities for dish/vessel (recommendations from ThermoFisher) and left to adhere overnight (~16 h). Media was changed prior to probe treatment. 10 µM of either probe was added to the cells and left to metabolically incorporate overnight based on previous optimizations. YnP was given at 20-30 µM based on lab recommendations. The next day, barring any additional treatment, cells were washed using DPBS (3 times, max vessel volume) and harvested using the appropriate lysis buffer. For tipifarnib-treatment, 100 nM was added to cells 1-2h prior to probe treatment, unless otherwise stated.

6.3.2. siRNA knockdown of SmgGDS isoforms.

PANC-1 cell were plated onto 48-well plates at 0.03 x 106 cells/well and incubated overnight. The following day, cells were transfected with 25 nM BD, IL and C1 siRNAs (sequences reported in Appendix) (ThermoFisher Scientific) using RNAiMax (ThermoFisher Scientific) according to the manufacturer’s protocol. Cells were incubated

for 24 h prior to harvesting. Lysates were normalized and processed for western blot for evaluation.

6.3.3. Transfection optimization

Cells were plated onto 24-well plates at 0.05 x 10^6 cells/well and incubated overnight. The following day, cells were transfected with pmaxGFP® (Lonza Biosciences) using Lipofectamine 2000 (Thermo Scientific) at varying concentrations. Cells were imaged using phase imaging and 488nm laser light for GFP signal detection over 24 h using an IncuCyte S3® device (Sartorius). Images were taken every ~4 -8 h. After 24 h, cells were washed in PBS and resuspended in flow cytometry buffer (1% FBS, 1 mM EDTA in PBS) and analyzed using an Attune NxT Flow Cytometer (Thermo Scientific).

6.3.4. CRISPR-mutagenesis drug selection optimization

Cells were plated on 96- well plates at 0.01 x 10^6 cells/well and incubated overnight. The following day, cells were treated with increasing concentrations of AMG-510 and/or tipifarnib using media supplemented with SYTOX^{TM} Green (250 nM, Thermo Scientific). Cells were imaged using phase imaging and 488nm laser light for GFP signal detection over 8-14 days using an IncuCyte S3® device (Sartorius). Images were taken every 4-12 h. Media with selection drug was refreshed every 2-3 days. EC50s were calculated using the IncuCyte S3 analysis software (Sartorius) using the Hill Equation ($n \geq 3$).

6.3.5. Spheroid formation

Corning Ultra-Low Attachment (ULA) 96-well plates (4520) were used to form spheroids. Cells were seeded into the well at 200 µL at an optimized density (see Appendix). Spheroid formation was monitored using an IncuCyte S3® device (Sartorius). For drug treatments and media changes, only the top 100 µL was changed as to not disturb the spheroid at the bottom of the well.

6.3.6. Lentiviral transduction – Cas9 cell lines

Low-passage HEK293T cells were seeded into 6-well plates and cultured overnight. The next day, culture media was replaced with fresh medium. Lentiviral plasmid pLVX-Cas9-Neo (2 µg; Addgene 104996) was transfected alongside viral envelope plasmid pCMV-VSV-G (0.66 µg; Addgene 8454) and viral packaging vector psPAX2 (1.34 µg; Addgene 12259) using Lipofectamine 2000 (10 µL per well) following the manufacturer's instructions. After 24h, media was changed again and virus production was allowed to proceed for 2-3 days. Viral media was then harvested and filtered (0.22 µm filter). Viral media was diluted 1:2 and 1:4 with fresh media, and Polybrene (Millipore) was added to a final concentration of 10 µg/mL to each dilution. This transduction media was then added to the receiving cell lines (RL952 and MelJuSo) at both dilutions on 6-well plates. A non-transduced control was kept on the same plate. After 24h, transduction media was replaced with fresh media. Transduction proceeded for 72h before the addition of selection media (0.75 - 1 µg/µL G418/Neomycin [Sigma-Aldrich]). Selection proceeded until control well cells died, around 5 – 7 days. Samples were harvested and screen by Western blot (FLAG-HRP) for expression of Cas9 construct.

6.3.7. TRex Flp-In cell line generation

Flp-In™ T-REx™ 293 Cell Line (Invitrogen™) was transfected with the target plasmid (pcDNA™5/FRT/TO backbone with gene of interest) and pOG44 Flp-Recombinase Expression Vector (ThermoFisher) at a 1:9 (w/w) ratio using Lipofectamine 2000 following the manufacturer's protocol. After 24h, media was changed with complete media (DMEM + GlutaMax; 10 µg/m Blasticidin). After another 24h, cells were expanded in 4 10cm dishes for each plasmid transfected. The following day, media is replaced with complete media + 100 µg/mL Hygromycin B. Media was then changed on all four plates every 3 days with complete media with Hygromycin B. After about two weeks, cell foci will appear. Foci are then harvested, pooled and cultured together. A sample was then analyzed by Western blot to check for construct expression under tetracycline control.

6.4. Cell/membrane fractionation

6.4.1. Pre-condensation of TX114

To purify standard TX114 (Sigma Aldrich) from hydrophilic components found in the detergent, condensation of pure TX114 was performed. Pre-condensation was performed in DPBS (1X) in a 50 mL Falcon Tube (3 mL TxX14 to 47 mL DPBS). Buffer was homogenized and clarified on ice, for two cycles. Solution was then incubated in a 37˚C water bath to allow phase separation by gravity. Clarification was done overnight. The next day, the aqueous phase was discard and fresh DPBS was added up to 50 mL. This cycle was repeated 2-3 more times (over 2-3 days). This results in a 2% TX114 solution. Purified detergent was stored in the dark at 4˚C.

6.4.2. Cell treatment and harvest

H23 cells were treated in T175 flasks with DMSO or 100 nM tipifarnib overnight (~16h). Cells were washed 2X with DPBS and harvested by trypsinization. Cells were then pelleted by centrifugation (5 min at 150 × *g*), washed once more with DPBS and pelleted for a final time. Pellets were flash frozen with liquid nitrogen and stored in the -80˚C.

6.4.3. Cell lysis

Pelleted cells were thawed at RT and 1 mL of TX114 lysis buffer was added (0.1% TX114). Cells were mixed into lysis buffer and vortexed briefly to resuspend all cells. Lysis proceeded for 30 mins at 4˚C. Benzonase (25U/µL) was added and incubated with lysate for 10 mins shaking at RT. Samples were then centrifuged at maximum speed (5 min, 4˚C) to clarify and remove cell debris. Supernatants (95%) were transferred to LoBind Eppendorf tubes.

6.4.4. Phase separation

Lysates were the incubated at 37˚C (heating block; StarLab) for 10 mins to allow the detergent phase to partially precipitate. Samples are then centrifuged at max speed for 10 mins at RT. Aqueous phase was isolated and saved in another LoBind Eppendorf (cytosol sample). A prepared 0.1% TX114 wash buffer was added to the original volume, homogenized, and clarified on ice. This cycle was repeated 3-4 times to isolate the membrane fraction. Samples were then subject to SP4 precipitation to remove traces of TX114 detergent prior to proteomic sample preparation. Protein was quantified by the DC assay (Bio-Rad) and subject to whole proteome sample preparation. Proteomic samples were analyzed by TIMS-TOF (Bruker) mass spectrometry using a DIA method.

6.5. Molecular cloning

6.5.1. Agarose gel electrophoresis

Powdered agarose (Gibcon, Ultrapure) was dissolved in a 1X TAE buffer (40mM Tris, 20mM acetate, 1mM EDTA) by heating. GelRed (Biotium, 1:10000) was added to the heated agarose solution and poured into a gel cast. After the gel was set, samples dissolved in DNA purple loading buffer (NEB, 1:6) were added to each well. DNA was separated using electrophoresis (70-100V). Gel was imaged using Typhoon FLA 9500 imager (GE healthcare) at 300 nm/ 600 nm excitation/emission wavelength.

6.5.2. DNA purification

All DNA vectors were column purified by Mini (12123), Midi (12143) or Maxi (12162) - Prep using the Qiagen Spin DNA purification system. Midi and Maxi-prep kits were of the HiSpeed variety. Samples were stored in DNAase-free water (autoclaved) or TE buffer (10 mM Tris, 0.1 mM EDTA) at -20˚C.

6.5.3. Genomic DNA extraction

Cells plated on 48-well plates were incubated overnight. The following day, media was removed and cells were washed once with PBS. Lysis buffer (150 µL; 10 mM Tris-HCl, pH 7.5; 0.05% SDS; 25 µg/ml proteinase K [New England Biosciences]) was added into each well. Cells were incubated with lysis buffer (1 h, 37 °C), followed by a proteinase K inactivation step (30 min, 80 °C). Samples were then taken to PCR or stored at -20℃.

6.5.4. Gibson assembly (NEB HiFi)

DNA fragments generated by PCR or restriction digest were purified by column or gel purification. For 2-3 fragments, ~0.04 pmol of each fragment was used, with a 2-fold molar excess of the insert, or a 5-fold molar excess when the insert was less than 200 bp. Samples were incubated with 10 µL of the HiFi Master Mix (NEB), and added to a total of 20 µL per reaction. Samples were incubated for 15 min – 2 hours, and stored at -20˚Cor taken directly to transformation. Gibson assembly protocols were designed using NEB Builder 2.0. Primers were obtained from ThermoFisher or SigmaAldrich (standard HPLC purity).

6.5.5. Bacterial transformation

NEB 5-alpha Competent *E. coli* (high efficiency for assembly cloning; C2987H) 20 µL – 50 µL was thawed on ice for 10 mins. 1-2 µL of assembled or sub-cloned vector sample was added to each tube on ice, very gently flicked to mix, and incubated for 30 mins. Samples were heat-shocked using a heat block (Eppendorf) at 42˚C for 45 seconds. Samples were transferred back to ice to recovered. 200 µL of RT outgrowth media (SOC) was added to each tube, and incubated at 37˚C, shaking, for 1 hours. Samples were pipetting, spread on selection plates and grown at 37˚C overnight. For lentiviral constructs, NEB Stable Competent *E. coli* (C3040H) cell were used. Outgrowth steps

were performed at 30˚C instead of 37˚C. NEB® 10-beta/Stable Outgrowth Medium was also used in place of standard SOC.

6.5.6. HRAS and KRAS genomic PCRs

Primers for amplicon sequences were designed for $KRAS^{G12C}$ and HRAS using PrimerBLAST (NCBI) and adapted to include Illumina amplicon sequencing adapters (Forward sequencing read: 5'- ACACTCTTTCCCTACACGACGCTCTTCCGATCT-3'; Reverse sequencing read: 5'- GACTGGAGTTCAGACGTGTGCTCTTCCGATCT-3'). Primers are reported in the SI. PCRs were conducted using genomic DNA (gDNA) extracted from H23 cells according to the following protocol: pCas9-H23 WT cells plated on 48-well plates were incubated overnight. The following day, media was removed and cells were washed once with PBS. Lysis buffer (150 µL; 10 mM Tris-HCl, pH 7.5; 0.05% SDS; 25 µg/ml proteinase K (New England Biosciences)) was added into each well. Cells were incubated with lysis buffer (1 h, 37 °C), followed by a proteinase K inactivation step (30 min, 80 °C). Samples were then taken to PCR or stored at -20℃.

6.5.7. NGS sample preparation

Samples were analyzed by Illumina multiplexed amplicon deep sequencing (GeneWiz, UK). Samples were generated by PCR using the above protocol. Samples were in some cases purified by gel using the NEB DNA Gel Extraction Kit to ensure purity (T1020S).

6.5.8. sgRNA design and preparation

Single guide RNAs (sgRNAs)were designed using the Synthego CRISPR design tool (Synthego) and verified manually. gRNAs directed towards $KRAS^{G12C}$ whose binding site includes the point mutation were manually mutated to accommodate the change in DNA sequence in the target system. The designed gRNAs were synthesized with the appropriate overhangs for the vector backbone. sgRNAs were cloned via golden gate

assembly into a human U6- promoter sgRNA expression plasmid (BPK1520). BPK1520 was a gift from Keith Joung (Addgene plasmid #65777; RRID: Addgene_65777). Briefly, the vector backbone was digested using BsmBI (New England Biosciences) and gel purified. The insert (sgRNA) oligonucleotides were annealed and then ligated to the vector. The product was transformed into DH5-alpha high-efficiency competent cells (50 µL, New England Biosciences) using the manufacturer's recommended protocol. Transformed bacteria were grown on Ampicillin selection plates overnight. Several colonies were miniprepped (QIAprep Spin Miniprep kit, Qiagen) or midiprepped (QIAPrep Highspeed Plasmid kit, Qiagen) according to the manufacturer's protocol, and sequenced by Sanger sequencing (Genewiz, UK). Mutants were generated using the appropriate primers designed using NEBaseChanger via site-directed mutagenesis (Q5^{TM} SDM kit, New England Biosciences). sgRNA are reported in the Appendix. Resulting plasmids were prepped and sequenced as described.

6.5.9. T7 mutagenesis surveyor assay

Cells were plated on 48-well plates at 0.01 x 106 cells/well and incubated overnight. The following day, cells were transfected with the designed U6-plasmids containing sgRNAs directed towards HRas (preparation of plasmids is described in the previous section) using Lipofectamine 2000 (Thermo Scientific) under optimized conditions. The next day, media was changed, and cells were incubated for another 2-3 days. gDNA was then extracted from cells using the protocol previously described. Mutagenesis was detected using the EnGen® Mutation Detection Kit (New England Biosciences). Briefly, gDNA extracts were subject to PCR to amplify the target locus (HRAS) using the designed amplicon-adaptor primers described previously. Heteroduplexes of mutation-containing sites were formed from the PCR products by heating (95℃), followed by slow cooling to RT. Heteroduplexes were then subject to T7 endonuclease I digest. Afterward, proteinase K digestion was performed to inactivate the endonuclease. Digested products were then separated via DNA agarose gel electrophoresis (2.0% agarose gel, stained with Gel-

Red® (Sigma-Aldrich) and analyzed using a TyphoonTM FLA 9500 biomolecular imager (GE Healthcare).

6.5.10. Site-directed mutagenesis (SDM)

A NEB Q5 Site-directed mutagenesis kit (E0554) was used for all SDM applications. PCRs were performed using conditions recommended by Tm Calculator (NEB). Primers were designed by NEBBaseChanger (NEB). Resulting samples were transformed according to the aforementioned protocol using High-Efficiency competent cells. Vectors were isolated using column purification (QIAGEN Miniprep). Samples were sequenced to confirm mutations (Sanger sequencing, GeneWiz, UK).

6.6. Proximity Labelling protocols

6.6.1. APEX2 proximity labelling

HEK293 FRT cells containing the construct of interest were induced to a 0.5 µg/mL tetracycline overnight (~16h) on 10 or 15 cm dishes. The next day, cells were incubated with 500 µM of biotinyl tyramide (biotin phenol; Tocris) for 30 minutes to 1 hour. To initiate proximity labelling reaction, 1 mM H_2O_2 was added for exactly 40 second, after which an ice cold quench buffer (10 mM sodium ascorbate, 10 mM sodium azide, 5 mM Trolox in DPBS) was added to the cells. Cells were gently washed with quench buffer (pouring buffer out each time to avoid disrupting cells). Cells were then harvestesd by gentle lifting using the quench buffer and collected into a Falcon tube. Cells were pelleted, flash frozen using liquid nitrogen and stored at -80˚C until lysis. For lysis, 1% SDS in quench buffer (supplemented with 1X EDTA-free protease inhibitor cocktail tablet [Roche]) was added to cell pellets and mixed thoroughly. Lysis proceeded for 30 mins at 4˚C with gentle shaking. Benzonase 250 U/µL was added to each sample and incubated at RT for 10

mins shaking (250 rpm). Cells were additional ultrasonicated to assist DNA shearing and lysis. Samples were then clarified by centrifugation (max speed, 5 mins).

6.6.2. MiniTurbo proximity labelling

MiniTurboID expressing HEK FRT cells were induced with 0.5 µg/mL tetracycline overnight (16 h) on a 10 cm dish. The next day, 250 µM biotin (Sigma Aldrich) was added to cells for 1 hour to initiate labelling. Cells were then placed on ice and washed with ice cold DPBS 4 times. Cells were harvested and lysed using a standard lysis buffer (1% SDS formulation).

6.7. Bioorthogonal reactions

6.7.1. Acyl-PEG Exchange

Cells were treated with or with tipifarnib (100 nM) overnight (~16 h) and lysed in TEA lysis buffer (50mM triethanolamine, pH 7.3, 150 mM NaCl, 5 mM EDTA, 4% SDS,1X protease EDTA-free inhibitor cocktail [Roche]). Lysis proceeded for 30 mins on ice and resultant lysates were clarified by centrifugation (max speed, 10 mins). Supernatants were transferred to a LoBind Eppendorf tube. Approximately 200 µg of lysate was carried forward for each condition. Samples were treated with TCEP (neutralized, 200 mM, pH 7.4) for 30 mins with rotation to reduce disulfide bonds. Afterwards, 2.5 µL 1M NEM (*N*-Ethylmaleimide Tocris) was then added for 2 hours to block non-palmitoylated thiols within the sample. Excess NEM was removed by 2 iterations of TCM/MeOH precipitation. Proteins were resuspended in 60 µL TEA buffer and split into two aliquots. One aliquot was treated with 90 µL 1M hydroxylamine (Sigma Aldrich) in 0.2% Triton X-100/TEA buffer for 1 hour with rotation in order to remove the *S*-palmitoylation from cysteines within the sample. The other aliquot served as a negative control sample and was treated with 90 µL in 0.2% Triton X-100/TEA buffer for 1 hour. Excess hydroxylamine was removed

by 2 iterations of TCM/MeOH precipitation. Proteins were resuspended in 30 µL TEA buffer and incubated with 60uL of 1.33 mM 10 kDa methoxypolyethylene glycol maleimide (mPEG-Mal, Sigma-Aldrich) for 2 hours at RT with rotation. A final TCM/MeOH precipitation yielded the final labelled sample. All samples were then dissolved to 1X Laemmli loading buffer and loaded onto a 12% for Western blot analysis of *S*-palmitoylated proteins.

6.7.2. Click reaction (CuAAC)

Lysates were normalized to 1-2 mg/mL using lysis buffer and incubated with click reagent mixture, prepared as follows (6 µL click reagent mixture per 100 µL of lysate):

- **Capture reagent** (AzTB – gel-based assays, AzRB or AzB– proteomics): 1 µL (10 mM in DMSO), final concentration 100 µM (1 volume)
- **$CuSO_4$**: 2 µL (50 mM in dH2O), final concentration 1 mM (2 volumes)
- **TCEP:** 2 µL (50 mM in dH2O), final concentration 1 mM (2 volumes)
- **TBTA:** 1 µL (10 mM in dH2O), final concentration 100 µM (1 volume)

The click-reagent mixture was prepared, vortexed, and incubated for 2 mins. The mixture was then added to the normalized lysates and shaken for 1 h at room temperature, after which the reaction was quenched by addition of EDTA (5 mM final concentration). For gel-based analysis, protein was precipitated using CHCl3 (2 volumes), MeOH (0.5 volumes), and dH_2O (1 volume), all relative to sample lysate volume. The samples were vortexed and centrifuged (14,000 × *g*, 5 min, 4℃). The top layer was removed, ensuring the resulting precipitate at the phase interface was not disturbed, and the remaining volume was carefully removed. The precipitate was then washed twice with MeOH (500 µL) using the centrifugation steps as described, resuspending the precipitate through vortexing and sonication each time. MeOH was removed and the pellet was left to air-dry for 5 min at RT. The protein pellet was the resuspended in 2% SDS (w/v) in HEPES (50 mM, pH 7.5) to $1/10^{th}$ of the initial sample volume, with several cycles of sonication and vortexing. The resuspended samples were then diluted to 0.2% SDS (w/v) by addition of HEPES (50 mM, pH 7.5).

6.7.3. Protein enrichment (pull-down; gel analysis)

Following sample protein (150 µg) ligation to capture reagent AzTB or AzT and workup (as described in previous section). Approximately 10 µg input protein was reserved for analysis. The remaining protein samples (100 µg) were incubated with pre-washed (0.2% SDS, 50 mM HEPES, pH 7.5; x3). Streptavidin Magnetic Beads (New England Biolabs, 30 µL beads per 100 µg protein) for 2 h at RT, with gentle shaking. The supernatant was removed and kept for analysis. Beads were washed with 0.2% (w/v) SDS in HEPES pH 7.5 (500 µL, x3) and eluted by boiling in 1x Laemmeli sample loading buffer supplemented with 5% (v/v) beta-mercaptoethanol (95 °C, 10 min). Proteins were separated by SDS-PAGE and analyzed by in-gel fluorescence using a Typhoon FLA 9500 biomolecular imager (GE Healthcare), followed by subsequent western blot analysis.

6.7.4. Streptavidin shift assay

Following metabolic lipid probe labelling (YnF, YnGG or YnP) in cells and subsequent harvest, resultant lysates were click ligated to AzTB. Samples were then purified by TCM/MeOH or SP4. Proteins were resuspended in 1X Laemelli buffer supplemented with 10% beta-mercaptoethanol. Samples were boiled for 10 mins and left to cool completely to RT. Each experimental sample was split into two aliquots. A final concentration of 100 µM recombinant streptavidin (Jackson Immunoresearch, 016-000-084) was added to one aliquot, while 0.2% SDS was added to the other. Samples were mixed and incubated for 10 mins at RT, before loading onto a 12% gel for SDS-PAGE and western blot/in-gel fluorescence analysis.

6.8. Proteomics methods

6.8.1. Protein enrichment (pull-down; proteomic analysis)

Following sample protein (600 µg) ligation to capture reagent AzRB or AzB (biotin-PEG3-azide) and workup OR proximity labelling – workup was performed by SP4 as described

in the previous section. Samples were incubated with pre-washed (0.2% SDS, 50 mM HEPES, pH 7.5; x3) Pierce NeutrAvidin (60 µL beads per 1 mg protein, ThermoFisher) for 2 h at RT, with gentle shaking. The supernatant was removed and kept for analysis. Beads were washed with 1.0% (w/v) SDS in HEPES pH 7.5 (500 µL, x3), and then with 50 mM HEPES pH 8.0 (500 µL, x3). TCEP (5 mM in HEPES pH 8.0) and chloroacetamide (10 mM in HEPES pH 8.0) were added and samples were incubated at room temperature for 15 min, with gentle shaking. Sequence grade trypsin (0.2 µg, Promega) was added to the bead suspension and incubated overnight (37℃, 1,200 rpm). The following day, beads were pelleted by centrifugation (5,000 × *g*), and the supernatant was transferred to a separate microcentrifuge tube (Eppendorf, Protein LoBind). The resulting peptides were quantified with Pierce Quantitative Fluorometric Peptide Assay (Thermo Scientific) according to the manufacturer's protocol.

6.8.2. TMT-labelling

Peptides were then chemically labelled with 6,10 or 15-plex TMT reagents (~ 44 µg per sample dissolved in dry MeCN; Thermo Scientific), which was adjusted according to peptide yield from digest determined from the aforementioned quantification assay, and incubated for 2 h at RT with gentle shaking. For a reference sample, equimolar amounts of each sample were combined prior to labelling. The reaction was quenched upon addition of 5% (w/v) hydroxylamine (1 µL). Labelled peptides were pooled into the experimentally designed TMTplexes and evaporated in a SpeedVac (Thermo Scientific) at 45℃ until dryness. Dried peptides were resuspended in 150 µL 1.0% (v/v) TFA in proteomic-grade water and adjusted to < 4 pH using TFA. Samples were cleared by centrifugation (14,000 × *g*, 5 min, RT), and then fractionated using the Pierce High pH Reversed-Phase Peptide Fractionation Kit (ThermoFisher Scientific) according to the manufacturer's protocol. Fractionated samples were evaporated to dryness, and resuspended in peptide reconstitution buffer (0.5% TFA (v/v), 2.0% MeCN (Optima-grade) in proteomic-grade water). Samples were filtered using Durapore® filters (x3) fitted into 20 µL plastic pipette tips directly into MS vials (4000 × *g*, 5 min) on the day of analysis. Samples were analyzed using a QExactive Orbitrap spectrometer or Eclipse Orbitrap spectrometer (ThermoFisher).

6.8.3. Whole proteome sample preparation

Protein lysate was subjected to reduction (5 mM final concentration TCEP - tris(2-carboxyethyl)phosphine) alkylation (10 mM final concentration CAA - chloroacetamide) for 10 - 45 mins at room temperature with shaking (600 rpm)/ TCEP and CAA stocks were prepared with 25 mM ammonium biocarbonate. Sample pH was adjusted to pH 8 as needed. 10-20 µg of each sample was carried forward to SP4 precipitation. Following precipitation, samples were taken forward to tryptic digest. Stock trypsin was freshly prepared (1 µg/µL in 25 mM ammonium bicarbonate) and 25 µL of trypsin solution was added to each sample (protein pellet). Samples were digested overnight (~8-16h). Resultant peptides were quantified using NanoDrop analysis (Nanodrop One, ThermoFisher) and evaporated to dryness using a SpeedVac. Samples were then rehydrated in at least 20 µL rehydration solution ((0.5% TFA (v/v), 2.0% MeCN (Optima-grade) in proteomic-grade water) and filtered through 3X Durapore (Millipore) filters into an MS submission vial prior to analysis.

6.8.5. Eclipse TMT 180 min – DDA LC/MS protocol

Peptides were analysed by liquid chromatography with mass spectrometry using an Eclipse Orbitrap coupled to Ultimate3000 LC (Thermo Fisher) (ThermoFisher Scientific) equipped with a 100-*µ*m internal dimension × 2-cm Acclaim PepMap 100 Precolumn (ThermoFisher Scientific) and a 75-*µ*m internal dimension × 50-cm, 2-*µ*m particle Acclaim PepMap RSLC C18 analytical column (ThermoFisher Scientific). Analytical solvents A (0.1% FA) and B (80% acetonitrile plus 0.1% FA and 1% DMSO). Peptides were separated by a 120 min analytical gradient which was 5%–35% solvent B over 180 minutes, rising to 99% solvent B over 20 minutes, followed by a 30 minute wash at 99% solvent B. Columns were held at 45°C. Data were acquired in a data-dependent manner with the following settings: MS1 acquisition settings: 380–1500 m/z window, 120,000 resolution, 3x10e6 automatic gain control (AGC) target, 60 ms maximum injection time;

MS2 acquisition settings: 17,500 resolution, high-energy collisional dissociation fragmentation (CID 35), 1x10e6 AGC target, 50 ms maximum injection time. CID collision energy was set to 35% with an isolation window of 0.7 m/z. Isobaric Tag Loss exclusion was set to 18 to 5 m/z low to high exclusion mass width. MS3 (ddMS3 OT HCD) was set to an isolation window of 2 m/z. Activation HCD (65%). Orbitrap resolution was set to 50000, with a scan range of 100-500 m/z/ Maximum injection time of 105 ms. 10 dependent scans were made.

6.8.6. LFQ whole proteome 120 min – DIA LC/MS protocol

Peptides were analysed by liquid chromatography with mass spectrometry using Q Exactive coupled to an Easy-nLC 1000 HPLC (ThermoFisher Scientific) equipped with a 100-*μ*m internal dimension × 2-cm Acclaim PepMap 100 Precolumn (ThermoFisher Scientific) and a 75-*μ*m internal dimension × 50-cm, 2-*μ*m particle Acclaim PepMap RSLC C18 analytical column (ThermoFisher Scientific). Analytical solvents A (0.1% FA) and B (80% acetonitrile plus 0.1% FA). Peptides were separated by a 120 min analytical gradient which was 5%–35% solvent B over 90 minutes, rising to 99% solvent B over 10 minutes, followed by a 17 minute wash at 99% solvent B. Columns were held at 45°C. Data were acquired in a data-independent manner with the following settings: MS1 acquisition settings: 4050–1650 m/z window, 70,000 resolution, 3x10e6 automatic gain control (AGC) target, 78 ms maximum injection time; MS2 acquisition settings: 17,500 resolution, high-energy collisional dissociation fragmentation (NCE 28), 1x10e6 AGC target, 41 ms maximum injection time. 23 DIA windows, with an isolation width of 22 m/z, were cycled though at 22 m/z intervals, starting with a centre of 411 m/z though to 895 m/z, and one further window with an isolation width of 744 m/z centred on 1278 m/z.

6.8.7. LFQ whole proteome Evosep – timsTOF - DIA LC/MS protocol

Peptides were analyzed by nanoLC-MS/MS using an Evosep One (Evosep) coupled with a timsTOF HT(Bruker) equipped with an 8cm, 150µm, 1.5µm analytical column (Evosep). 200ng peptides were separated by the Evosep 30SPD workflow (Analytical solvents A: 0.1% FA and B: acetonitrile plus 0.1% FA). Column was held at 40°C. Data were acquired

in data-independent acquisition PASEF mode with the following settings: m/z range from 100 m/z to 1700 m/z, ion mobility range from 1/K0 = 1.30 to 0.85 Vs/cm2 using equal ion accumulation and ramp times in the dual TIMS analyser of 100 ms each. Each cycle consisted of 8 PASEF ramps covering 21 mass steps each wit25 Da windows each with 2/3 non-overlapping ion mobility windows covering the 475 to 1000 m/z range and 0.85 and 1.26 Vs/cm2 ion mobility range. The collision energy was lowered as a function of increasing ion mobility from 59 eV at 1/K0 = 1.6 Vs/cm2 to 20 eV at 1/K0 = 0.6 Vs/cm2.

6.8.8. Evosep – timsTOF - DDA LC/MS protocol

Peptides were analyzed by nanoLC-MS/MS using an Evosep One (Evosep) coupled with a timsTOF HT (Bruker) equipped with an 8cm, 150µm, 1.5µm analytical column (Evosep). 200ng peptides were separated by the Evosep 30SPD workflow (Analytical solvents A: 0.1% FA and B: acetonitrile plus 0.1% FA). Column was held at 40°C. Data were acquired in data-dependent acquisition PASEF mode with the following settings: m/z range from 100 m/z to 1700 m/z, ion mobility range from 1/K0 = 1.30 to 0.85 Vs/cm2 using equal ion accumulation and ramp times in the dual TIMS analyzer of 100 ms each. The collision energy was lowered as a function of increasing ion mobility from 59 eV at 1/K0 = 1.6 Vs/cm2 to 20 eV at 1/K0 = 0.6 Vs/cm2. Isolation width was lowered as a function of decreasing m/s from 3 m/z at 800 m/z to 2 m/z at 700 m/z. Active exclusion was applied for 0.4 min. Each cycle consistent of 4 PASEF ramps (total cycle time 0.53 sec) with 2.75 ms measuring time allowed for each selected precursor.

6.8.9. MaxQuant data analysis

Raw data was processed using MaxQuant (v. 1.6.17.0 or 2.0.3). UniProt Human Reference Proteome (August 2020; Jan 2022) was used as the search database for protein identification. Cysteine carbamidomethylation was set as a fixed modification to reflect the products of alkylation during proteomic sample preparation. Methionine

oxidation and protein N-terminal acetylation were set as variable modifications. Trypsin/P was indicated as the digestion enzyme, with up to 2 missed cleavages and a minimum of 6 residues per peptide allowed. Unique and razor peptides were selected for protein identification and quantification. Reporter ion MS2-based quantification was employed, with defined TMT 6, 10 or 16-plex on lysine residues and peptide N-termini as isobaric labels. All other parameters were set to default. Resulting data was further analysed using Perseus (v 1.6.14 or 2.0.7). Reporter ion MS3-based quantification was employed for Eclipse acquired data.

6.8.10. Fragpipe data analysis

ddaPASEF Bruker .d files were processed using Fragpipe with the built-in “LFQ MBR” workflow. Default settings, other than MaxLFQ min ions was set as 1, were used. Briefly, Bruker .d files were searched using MSFragger (version 3.8) with the following parameters: strict trypsin digestion; up to 2 missed cleavages allowed; precursor ion tolerance: 20 ppm; trimming of protein N-terminal methionine; oxidation (M) and N terminal acetylation as variable modifications; carbamidomethylation (C) as a fixed modification; Human database (Downloaded from UniProt 13 July 2023 containing 20552 proteins) with decoys (50%) and contaminants added with inbuilt fragpipe tool. MSFragger search results were processed using Percolator (version 3.5) for peptide-spectrum match validation, followed by Philosopher (version 5.0.0) for protein and FDR filtering. Label-free quantification values were calculated using the MaxLFQ algorithm using IonQuant (version 5.0.0) with match between runs enabled and min ions set as 1.

6.8.11. DIA-NN data analysis

diaPASEF Bruker .d files were processed using library-free analysis in DIA-NN (version 1.8.1) using the following parameters: Human database (Downloaded from UniProt 13 July 2023 containing 20552 proteins and 246 common contaminants); “deep learning-based spectra and RTs prediction” was enabled; trypsin with 1 missed cleavages; N-term

Excision, C carbamidomethylation, Oxidation and N terminal Acetylation were enabled with maximum 2 variable modifications; MBR was enabled; quantification strategy set to “Robust LC (high precision)”; heuristic protein inference was disabled; Mass and MS1 accuracy set to 0.

6.8.12. Perseus data analysis

Data processed by DIA-NN, FragPipe or MaxQuant were uploaded to the Perseus platform workspace (v 1.6.2.3, 2.0.1.3). Protein groups and intensity values were filtered by “potential contaminant”, “reverse peptides” and “only ID by site” annotations. For LFQ analysis, replicates for each condition were grouped together. Intensity values were log2 transformed and filtered to require at least 2 valid values per condition, where relevant and at least 1 unique/razor peptides for each protein entry. For TMT analysis, TMT intensity values were grouped based on multiplex set and experimental conditions. Intensity values were log2 transformed and filtered to require at least 2 valid values per condition, where relevant and at least 1 unique/razor peptides for each protein entry. The mean values within each row (TMT set) were subtracted from the matrix. Subtraction of the median values across TMT channels was then performed to normalize across conditions. TMT labelling efficiency was calculated to be >70% for analysis.

Imputation was performed with either MinDet or KNN algorithms when necessary and to perform principal component analysis. KNN cluster number was determined by the square root of total number of samples analyzed. A two-sample t-test was performed across all quantified proteins to determine level and significance of enrichment between control and experimental samples, as relevant (n=3, Permutation-based FDR=0.01, S0=1). Cut-offs were determined based on biological relevance. Fold-change values were plotted against adjusted p-values in a volcano plot. For profile plots, Pearson correlation or Euclidian distance algorithm was used for hierarchal clustering analysis. COMBAT batch correction was performed as needed (i.e. for multiplex TMT samples). Volcano plots were plotted using GraphPad Prism (v. 9 and 10).

6.8.13. Quality control analysis workflow

PTXQC (Proteomics (PTX) quality control (QC)) analysis (R package) was performed LC-MS data generated with the MaxQuant software suite according to the package instructions. Skyline (MacCoss Lab Software) analysis was performed to identify common MS contaminants according to standard software instructions.

6.8.14. Functional enrichment analysis

STRING functional enrichment analysis was performed using the online tool (STRING.db) or by using the Cytoscape platform. Statistical overrepresentation analysis was performed using the top 75% or 25% of enriched substrates on either side of an enrichment plot. Human whole proteome reference (2020-2023) was used as background unless stated otherwise. PTM annotations were curated from SwissPalm (*S*-palmitoylation) or manually curated (*S*-prenylation) based off in house experimental data. Statistical analysis and p-values were determined using the Fisher's Exact test. The false discovery rate (FDR) was calculated by the Benjamin-Hochberg procedure and log10 transformed for plotting, as necessary.

Bibliography

1. Bradley, D. The evolution of post-translational modifications. *Curr Opin Genet Dev* **76**, 101956 (2022).
2. Nilsen, T. W. & Graveley, B. R. Expansion of the eukaryotic proteome by alternative splicing. *Nature* **463**, 457–463 (2010).
3. Losada de la Lastra, A., Hassan, S. & Tate, E. W. Deconvoluting the biology and druggability of protein lipidation using chemical proteomics. *Current Opinion in Chemical Biology* Preprint at https://doi.org/10.1016/j.cbpa.2020.10.002 (2021).
4. Ramazi, S. & Zahiri, J. Post-translational modifications in proteins: resources, tools and prediction methods. *Database* **2021**, (2021).
5. Aebersold, R. *et al.* How many human proteoforms are there? *Nature Chemical Biology 2018 14:3* **14**, 206–214 (2018).
6. Liddy, K. A., White, M. Y. & Cordwell, S. J. Functional decorations: post-translational modifications and heart disease delineated by targeted proteomics. *Genome Med* **5**, 20 (2013).
7. Losada de la Lastra, A., Hassan, S. & Tate, E. W. Deconvoluting the biology and druggability of protein lipidation using chemical proteomics. *Curr Opin Chem Biol* **60**, 97–112 (2021).
8. Cox, A. D., Der, C. J. & Philips, M. R. Targeting RAS Membrane Association: Back to the Future for Anti-RAS Drug Discovery? *Clin Cancer Res* **21**, 1819 (2015).
9. Prescher, J. A. & Bertozzi, C. R. Chemistry in Living Systems. *Nat Chem Biol* **1**, 13–21 (2005).
10. Jiang, H. *et al.* Protein Lipidation: Occurrence, Mechanisms, Biological Functions, and Enabling Technologies. *Chem Rev* **118**, 919–988 (2018).
11. Tate, E. W., Kalesh, K. A., Lanyon-Hogg, T., Storck, E. M. & Thinon, E. Global profiling of protein lipidation using chemical proteomic technologies. *Current Opinion in Chemical Biology* Preprint at https://doi.org/10.1016/j.cbpa.2014.10.016 (2015).

12. Hang, H. C. *et al.* Chemical probes for the rapid detection of fatty-acylated proteins in mammalian cells. *J Am Chem Soc* **129**, 2744–2745 (2007).
13. Hang, H. C. & Linder, M. E. Exploring Protein Lipidation with Chemical Biology. *Chem Rev* **111**, 6341 (2011).
14. Emenike, B., Nwajiobi, O. & Raj, M. Covalent Chemical Tools for Profiling Post-Translational Modifications. *Front Chem* **10**, 868773 (2022).
15. Parker, C. G. & Pratt, M. R. Click Chemistry in Proteomic Investigations. *Cell* **180**, 605 (2020).
16. Wright, M. H. *et al.* Protein myristoylation in health and disease. *J Chem Biol* **3**, 19–35 (2010).
17. Palsuledesai, C. C. & Distefano, M. D. Protein prenylation: Enzymes, therapeutics, and biotechnology applications. *ACS Chem Biol* **10**, 51–62 (2015).
18. Ducker, C. E., Upson, J. J., French, K. J. & Smith, C. D. Two N-myristoyltransferase isozymes play unique roles in protein myristoylation, proliferation, and apoptosis. *Molecular Cancer Research* **3**, 463–476 (2005).
19. Lowther, W. T. & Matthews, B. W. Structure and function of the methionine aminopeptidases. *Biochimica et Biophysica Acta (BBA) - Protein Structure and Molecular Enzymology* **1477**, 157–167 (2000).
20. Grocin, A. G., Serwa, R. A., Sanfrutos, J. M., Ritzefeld, M. & Tate, E. W. Whole proteome profiling of N-myristoyltransferase activity and inhibition using sortase A. *Molecular and Cellular Proteomics* (2019) doi:10.1074/mcp.RA118.001043.
21. Wright, M. H. *et al.* Validation of N-myristoyltransferase as an antimalarial drug target using an integrated chemical biology approach. *Nat Chem* **6**, 112–121 (2014).
22. Wright, M. H., Paape, D., Price, H. P., Smith, D. F. & Tate, E. W. Global profiling and inhibition of protein lipidation in vector and host stages of the sleeping sickness parasite trypanosoma brucei. *ACS Infect Dis* **2**, 427–441 (2016).
23. Wright, M. H. *et al.* Global analysis of protein N-myristoylation and exploration of N-myristoyltransferase as a drug target in the neglected human pathogen leishmania donovani. *Chem Biol* **22**, 342–354 (2015).

24. Thinon, E. *et al.* Global profiling of co- and post-translationally N-myristoylated proteomes in human cells. *Nat Commun* (2014) doi:10.1038/ncomms5919.
25. Maurer-Stroh, S., Washietl, S. & Eisenhaber, F. Protein prenyltransferases. *Genome Biol* **4**, 1–9 (2003).
26. Linder, M. E. & Deschenes, R. J. Palmitoylation: policing protein stability and traffic. *Nat. Rev. Mol. Cell Biol.* **8**, 74–84 (2007).
27. Greaves, J. *et al.* Molecular basis of fatty acid selectivity in the zDHHC family of S-acyltransferases revealed by click chemistry. *Proc Natl Acad Sci U S A* (2017) doi:10.1073/pnas.1612254114.
28. Lanyon-Hogg, T., Faronato, M., Serwa, R. A. & Tate, E. W. Dynamic Protein Acylation: New Substrates, Mechanisms, and Drug Targets. *Trends in Biochemical Sciences* Preprint at https://doi.org/10.1016/j.tibs.2017.04.004 (2017).
29. Omerovic, J., Laude, A. J. & Prior, I. A. Ras proteins: paradigms for compartmentalised and isoform specific signalling. *Cell Mol Life Sci* **64**, 2575 (2007).
30. Prior, I. A. & Hancock, J. F. Ras trafficking, localization and compartmentalized signalling. *Semin Cell Dev Biol* **23**, 145 (2012).
31. Prior, I. A., Hood, F. E. & Hartley, J. L. The frequency of ras mutations in cancer. *Cancer Res* **80**, 2669–2974 (2020).
32. Scott Reid, T., Terry, K. L., Casey, P. J. & Beese, L. S. Crystallographic analysis of CaaX prenyltransferases complexed with substrates defines rules of protein substrate selectivity. *J Mol Biol* (2004) doi:10.1016/j.jmb.2004.08.056.
33. Hougland, J. L. *et al.* Identification of Novel Peptide Substrates for Protein Farnesyltransferase Reveals Two Substrate Classes with Distinct Sequence Selectivities. *J Mol Biol* **395**, 176–190 (2010).
34. Jung, D. & Bachmann, H. S. Regulation of protein prenylation. *Biomedicine and Pharmacotherapy* **164**, (2023).
35. Reigard, S. A. *et al.* Interplay of isoprenoid and peptide substrate specificity in protein farnesyltransferase. *Biochemistry* **44**, 11214–11223 (2005).

36. Yokoyama, K., McGeady, P. & Gelb, M. H. Mammalian Protein Geranylgeranyltransferase-I: Substrate Specificity, Kinetic Mechanism, Metal Requirements, and Affinity Labeling. *Biochemistry* **34**, 1344–1354 (1995).
37. Kalinin, A. *et al.* Expression of mammalian geranylgeranyltransferase type-II in Escherichia coli and its application for in vitro prenylation of Rab proteins. *Protein Expr Purif* **22**, 84–91 (2001).
38. Kuchay, S. *et al.* GGTase3 is a newly identified geranylgeranyltransferase targeting a ubiquitin ligase. *Nat Struct Mol Biol* (2019) doi:10.1038/s41594-019-0249-3.
39. Shirakawa, R. *et al.* A SNARE geranylgeranyltransferase essential for the organization of the Golgi apparatus. *EMBO J* **39**, e104120 (2020).
40. Bloch, K. The biological synthesis of cholesterol. *Science (1979)* **150**, 19–28 (1965).
41. Rodwell, V. W., Nordstrom, J. L. & Mitschelen, J. J. Regulation of HMG-CoA Reductase. *Adv Lipid Res* **14**, 1–74 (1976).
42. Slater, E. E. & MacDonald, J. S. Mechanism of Action and Biological Profile of HMG CoA Reductase Inhibitors: A New Therapeutic Alternative. *Drugs* **36**, 72–82 (1988).
43. Reiner, Ž. Statins in the primary prevention of cardiovascular disease. *Nature Reviews Cardiology 2013 10:8* **10**, 453–464 (2013).
44. Liao, J. K. Isoprenoids as mediators of the biological effects of statins. *J Clin Invest* **110**, 285 (2002).
45. Oesterle, A., Laufs, U. & Liao, J. K. Pleiotropic Effects of Statins on the Cardiovascular System. *Circ Res* **120**, 229–243 (2017).
46. Yeganeh, B. *et al.* Targeting the mevalonate cascade as a new therapeutic approach in heart disease, cancer and pulmonary disease. *Pharmacol Ther* **143**, 87–110 (2014).
47. Seabra, M. C., Reiss, Y., Casey, P. J., Brown, M. S. & Goldstein, J. L. Protein farnesyltransferase and geranylgeranyltransferase share a common alpha subunit. *Cell* **65**, 429–434 (1991).

48. Taylor, J. S., Reid, T. S., Terry, K. L., Casey, P. J. & Beese, L. S. Structure of mammalian protein geranylgeranyltransferase type-I. *EMBO J* **22**, 5963 (2003).
49. Long, S. B., Hancock, P. J., Kral, A. M., Hellinga, H. W. & Beese, L. S. The crystal structure of human protein farnesyltransferase reveals the basis for inhibition by CaaX tetrapeptides and their mimetics. *Proc Natl Acad Sci U S A* (2001) doi:10.1073/pnas.241407898.
50. Long, S. B., Casey, P. J. & Beese, L. S. The basis for K-Ras4B binding specificity to protein farnesyl- transferase revealed by 2 Å resolution ternary complex structures. *Structure* (2000) doi:10.1016/S0969-2126(00)00096-4.
51. Roberts, P. J. *et al.* Rho family GTPase modification and dependence on CAAX motif-signaled posttranslational modification. *Journal of Biological Chemistry* **283**, 25150–25163 (2008).
52. Storck, E. M. *et al.* Dual chemical probes enable quantitative system-wide analysis of protein prenylation and prenylation dynamics. *Nat Chem* **11**, 552–561 (2019).
53. Fiordalisi, J. J. *et al.* High Affinity for Farnesyltransferase and Alternative Prenylation Contribute Individually to K-Ras4B Resistance to Farnesyltransferase Inhibitors. *Journal of Biological Chemistry* **278**, 41718–41727 (2003).
54. Whyte, D. B. *et al.* K- and N-Ras Are Geranylgeranylated in Cells Treated with Farnesyl Protein Transferase Inhibitors. *Journal of Biological Chemistry* **272**, 14459–14464 (1997).
55. Ashby, M. CaaX converting enzymes. *Curr. Opin. Lipidol.* **9**, 99–102 (1998).
56. Manolaridis, I. *et al.* Mechanism of farnesylated CAAX protein processing by the integral membrane protease Rce1. *Nature* **504**, 301–305 (2013).
57. Winter-Vann, A. M. & Casey, P. J. Post-prenylation-processing enzymes as new targets in oncogenesis. *Nature Reviews Cancer 2005 5:5* **5**, 405–412 (2005).
58. Roberts, P. J. *et al.* Rho family GTPase modification and dependence on CAAX motif-signaled posttranslational modification. *Journal of Biological Chemistry* **283**, 25150–25163 (2008).
59. Backlund, P. S. Post-translational Processing of RhoA. *Journal of Biological Chemistry* **272**, 33175–33180 (1997).

60. Guo, Z. *et al.* Structures of RabGGTase–substrate/product complexes provide insights into the evolution of protein prenylation. *EMBO J* **27**, 2444–2456 (2008).
61. Alexandrov, K., Horiuchi, H., Steele-Mortimer, O., Seabra, M. C. & Zerial, M. Rab escort protein-1 is a multifunctional protein that accompanies newly prenylated rab proteins to their target membranes. *EMBO Journal* **13**, 5262–5273 (1994).
62. Alexandrov, K. *et al.* Characterization of the ternary complex between Rab7, REP-1 and Rab geranylgeranyl transferase. *Eur J Biochem* **265**, 160–170 (1999).
63. Maurer-Stroh, S. *et al.* Towards Complete Sets of Farnesylated and Geranylgeranylated Proteins. *PLoS Comput Biol* **3**, e66 (2007).
64. Michaelson, D. *et al.* Differential localization of Rho GTPases in live cells: regulation by hypervariable regions and RhoGDI binding. *J. Cell Biol.* **152**, 111–126 (2001).
65. Scheffzek, K., Stephan, I., Jensen, O. N., Illenberger, D. & Gierschik, P. The Rac–RhoGDI complex and the structural basis for the regulation of Rho proteins by RhoGDI. *Nature Struct. Biol.* **7**, 122–126 (2000).
66. Hancock, J. F. & Hall, A. A novel role for RhoGDI as an inhibitor of GAP proteins. *EMBO J.* **12**, 1915–1921 (1993).
67. Takahashi, K. *et al.* Direct interaction of the Rho GDP dissociation inhibitor with ezrin/radixin/moesin initiates the activation of the Rho small G protein. *J. Biol. Chem.* **272**, 23371–23375 (1997).
68. Boulter, E. *et al.* Regulation of Rho GTPase crosstalk, degradation and activity by RhoGDI1. *Nature Cell Biol.* **12**, 477–483 (2010).
69. Dirac-Svejstrup, A. B., Sumizawa, T. & Pfeffer, S. R. Identification of a GDI displacement factor that releases endosomal Rab GTPases from Rab-GDI. *EMBO Journal* **16**, 465–472 (1997).
70. Ozdemir, E. S., Jang, H., Gursoy, A., Keskin, O. & Nussinov, R. Arl2-Mediated Allosteric Release of Farnesylated KRas4B from Shuttling Factor PDEδ. *J Phys Chem B* **122**, 7503 (2018).
71. Renata, Z. *et al.* Ras-GRF, the activator of Ras, is expressed preferentially in mature neurons of the central nervous system. *Molecular Brain Research* **48**, 140–144 (1997).

72. Liang, D. *et al.* Palmitoylation and PDE6δ regulate membrane-compartment-specific substrate ubiquitylation and degradation. *Cell Rep* **42**, 111999 (2023).
73. Chandra, A. *et al.* The GDI-like solubilizing factor PDEδ sustains the spatial organization and signalling of Ras family proteins. *Nature Cell Biology 2012 14:2* **14**, 148–158 (2011).
74. Onken, B., Wiener, H., Philips, M. R. & Chang, E. C. Compartmentalized signaling of Ras in fission yeast. *Proc Natl Acad Sci U S A* **103**, 9045–9050 (2006).
75. Zhang, H., Constantine, R., Frederick, J. M. & Baehr, W. The prenyl-binding protein PrBP/δ: A chaperone participating in intracellular trafficking. *Vision Res* **75**, 19–25 (2012).
76. Riou, P. *et al.* 14-3-3 proteins interact with a hybrid prenyl-phosphorylation motif to inhibit G proteins. *Cell* **153**, 640–653 (2013).
77. Berg, T. J. *et al.* Splice variants of SmgGDS control small GTPase prenylation and membrane localization. *J. Biol. Chem.* **285**, 35255–35266 (2010).
78. Hamel, B. *et al.* SmgGDS is a guanine nucleotide exchange factor that specifically activates RhoA and RhoC. *Journal of Biological Chemistry* **286**, 12141–12148 (2011).
79. Schuld, N. J. *et al.* The Chaperone Protein SmgGDS Interacts with Small GTPases Entering the Prenylation Pathway by Recognizing the Last Amino Acid in the CAAX Motif. *J Biol Chem* **289**, 6862 (2014).
80. Jennings, B. C., Lawton, A. J., Rizk, Z. & Fierke, C. A. SmgGDS-607 Regulation of RhoA GTPase Prenylation Is Nucleotide-Dependent. *Biochemistry* **57**, 4289–4298 (2018).
81. García-Torres, D. & Fierke, C. A. The chaperone SmgGDS-607 has a dual role, both activating and inhibiting farnesylation of small GTPases. *Journal of Biological Chemistry* **294**, 11793–11804 (2019).
82. Brandt, A. C., Koehn, O. J. & Williams, C. L. SmgGDS: An Emerging Master Regulator of Prenylation and Trafficking by Small GTPases in the Ras and Rho Families. *Front Mol Biosci* **8**, 685135 (2021).

83. Berg, T. J. *et al.* Splice variants of SmgGDS control small gtpase prenylation and membrane localization. *Journal of Biological Chemistry* **285**, 35255–35266 (2010).
84. Shimizu, H. *et al.* Structure-based analysis of the guanine nucleotide exchange factor SmgGDS reveals armadillo-repeat motifs and key regions for activity and GTPase binding. *Journal of Biological Chemistry* **292**, 13441–13448 (2017).
85. Brandt, A. C. *et al.* Splice switching an oncogenic ratio of SmgGDS isoforms as a strategy to diminish malignancy. *Proc Natl Acad Sci U S A* **117**, 3627–3636 (2020).
86. Laufs, U. & Liao, J. K. Targeting Rho in Cardiovascular Disease. *Circ Res* **87**, 526–528 (2000).
87. Gendaszewska-Darmach, E., Garstka, M. A. & Błażewska, K. M. Targeting Small GTPases and Their Prenylation in Diabetes Mellitus. *J Med Chem* **64**, 9677–9710 (2021).
88. Seabra, M. C. Ophthalmic Genetics New insights into the pathogenesis of choroideremia: a tale of two REPs New insights into the pathogenesis of choroideremia: a tale of two REPS. *Ophthalmic Genet* **17**, 43–46 (1996).
89. Worman, H. J. Prelamin A prenylation and the treatment of progeria. *J Lipid Res* **51**, 223–225 (2010).
90. Glenn, J. S., Watson, J. A., Havel, C. M. & White, J. M. Identification of a Prenylation Site in Delta Virus Large Antigen. *Science (1979)* **256**, 1331–1333 (1992).
91. Gisselberg, J. E., Zhang, L., Elias, J. E. & Yeh, E. The prenylated proteome of Plasmodium falciparum reveals pathogen-specific prenylation activity and drug mechanism-of-action. *Molecular and Cellular Proteomics* **16**, S54–S64 (2017).
92. Ayong, L., DaSilva, T., Mauser, J., Allen, C. M. & Chakrabarti, D. Evidence for prenylation-dependent targeting of a Ykt6 SNARE in Plasmodium falciparum. *Mol Biochem Parasitol* **175**, 162–168 (2011).
93. Huang, W. H., Chen, C. W., Wu, H. L. & Chen, P. J. Post-translational modification of delta antigen of hepatitis D virus. *Curr Top Microbiol Immunol* **307**, 91–112 (2006).

94. Berndt, N., Hamilton, A. D. & Sebti, S. M. Targeting protein prenylation for cancer therapy. *Nature Reviews Cancer 2011 11:11* **11**, 775–791 (2011).
95. Saeedi, P. *et al.* Global and regional diabetes prevalence estimates for 2019 and projections for 2030 and 2045: Results from the International Diabetes Federation Diabetes Atlas, 9th edition. *Diabetes Res Clin Pract* **157**, (2019).
96. Donath, M. Y. Targeting inflammation in the treatment of type 2 diabetes: Time to start. *Nat Rev Drug Discov* **13**, 465–476 (2014).
97. Forrester, S. J., Kikuchi, D. S., Hernandes, M. S., Xu, Q. & Griendling, K. K. Reactive Oxygen Species in Metabolic and Inflammatory Signaling. *Circ Res* **122**, 877 (2018).
98. Gendaszewska-Darmach, E., Garstka, M. A. & Błażewska, K. M. Targeting Small GTPases and Their Prenylation in Diabetes Mellitus. *J Med Chem* **64**, 9677–9710 (2021).
99. Møller, L. L. V., Klip, A. & Sylow, L. Rho GTPases-emerging regulators of glucose homeostasis and metabolic health. *Cells* **8**, (2019).
100. Kowluru, A. Friendly, and not so friendly, roles of Rac1 in islet β-cell function: Lessons learnt from pharmacological and molecular biological approaches. *Biochem Pharmacol* **81**, 965 (2011).
101. Sahajpal, N., Kowluru, A. & Kowluru, R. A. The Regulatory Role of Rac1, a Small Molecular Weight GTPase, in the Development of Diabetic Retinopathy. *J Clin Med* **8**, (2019).
102. Duluc, L. & Wojciak-Stothard, B. Rho GTPases in the regulation of pulmonary vascular barrier function. *Cell Tissue Res* **355**, 675–685 (2014).
103. Li, M. *et al.* The Emerging Role of Rho Guanine Nucleotide Exchange Factors in Cardiovascular Disorders: Insights Into Atherosclerosis: A Mini Review. *Front Cardiovasc Med* **8**, 782098 (2022).
104. Nohria, A. *et al.* Statins Inhibit Rho Kinase Activity in Patients with Atherosclerosis. *Atherosclerosis* **205**, 517 (2009).
105. Nicholls, S. J. *et al.* Statins, High-Density Lipoprotein Cholesterol, and Regression of Coronary Atherosclerosis. *JAMA* **297**, 499–508 (2007).

106. Coussa, R. G. & Traboulsi, E. I. Choroideremia: A review of general findings and pathogenesis. *Ophthalmic Genet* **33**, 57–65 (2012).
107. Köhnke, M. *et al.* Rab GTPase Prenylation Hierarchy and Its Potential Role in Choroideremia Disease. *PLoS One* **8**, e81758 (2013).
108. Preising, M. N. & Ayuso, C. Rab escort protein 1 (REP1) in intracellular traffic: A functional and pathophysiological overview. *Ophthalmic Genet* **25**, 101–110 (2004).
109. Seabra, M. C., Ho, Y. K. & Anant, J. S. Deficient geranylgeranylation of Ram/Rab27 in choroideremia. *Journal of Biological Chemistry* **270**, 24420–24427 (1995).
110. Larijani, B., Hume, A. N., Tarafder, A. K. & Seabra, M. C. Multiple Factors Contribute to Inefficient Prenylation of Rab27a in Rab Prenylation Diseases. *Journal of Biological Chemistry* **278**, 46798–46804 (2003).
111. Abbouda, A., Avogaro, F., Moosajee, M. & Vingolo, E. M. Update on Gene Therapy Clinical Trials for Choroideremia and Potential Experimental Therapies. *Medicina (B Aires)* **57**, 1–14 (2021).
112. Merideth, M. A. *et al.* Phenotype and Course of Hutchinson–Gilford Progeria Syndrome. *https://doi.org/10.1056/NEJMoa0706898* **358**, 592–604 (2008).
113. Eriksson, M. *et al.* Recurrent de novo point mutations in lamin A cause Hutchinson–Gilford progeria syndrome. *Nature 2003 423:6937* **423**, 293–298 (2003).
114. De Sandre-Giovannoli, A. *et al.* Lamin A truncation in Hutchinson-Gilford progeria. *Science (1979)* **300**, 2055 (2003).
115. Corrigan, D. P. *et al.* Prelamin A endoproteolytic processing in vitro by recombinant Zmpste24. *Biochemical Journal* **387**, 129–138 (2005).
116. Sinensky, M. *et al.* The processing pathway of prelamin a. *J Cell Sci* **107**, 61–67 (1994).
117. Casasola, A. *et al.* Prelamin A processing, accumulation and distribution in normal cells and laminopathy disorders. *Nucleus* **7**, 84–102 (2016).

118. Wang, Y. *et al.* Blocking farnesylation of the prelamin A variant in Hutchinson-Gilford progeria syndrome alters the distribution of A-type lamins. *Nucleus* **3**, (2012).
119. Murtada, S. Il *et al.* Lonafarnib improves cardiovascular function and survival in a mouse model of Hutchinson-Gilford progeria syndrome. *Elife* **12**, (2023).
120. Dominici, S. *et al.* Different prelamin A forms accumulate in human fibroblasts: a study in experimental models and progeria. *Eur J Histochem* **53**, 6 (2009).
121. Yang, S. H., Andres, D. A., Spielmann, H. P., Young, S. G. & Fong, L. G. Progerin elicits disease phenotypes of progeria in mice whether or not it is farnesylated. *J Clin Invest* **118**, 3291 (2008).
122. Suzuki, M. *et al.* FDA approval summary for lonafarnib (Zokinvy) for the treatment of Hutchinson-Gilford progeria syndrome and processing-deficient progeroid laminopathies. *Genetics in Medicine* **25**, 100335 (2023).
123. FDA Approves First Treatment for Hutchinson-Gilford Progeria Syndrome and Some Progeroid Laminopathies | FDA. https://www.fda.gov/news-events/press-announcements/fda-approves-first-treatment-hutchinson-gilford-progeria-syndrome-and-some-progeroid-laminopathies.
124. Völkert, M., Wagner, M., Peters, C. & Waldmann, H. The chemical biology of Ras lipidation. *Biol Chem* **382**, 1133–1145 (2001).
125. Canon, J. *et al.* The clinical KRAS(G12C) inhibitor AMG 510 drives anti-tumour immunity. *Nature 2019 575:7781* **575**, 217–223 (2019).
126. Punekar, S. R., Velcheti, V., Neel, B. G. & Wong, K. K. The current state of the art and future trends in RAS-targeted cancer therapies. *Nature Reviews Clinical Oncology 2022 19:10* **19**, 637–655 (2022).
127. Cox, A. D., Fesik, S. W., Kimmelman, A. C., Luo, J. & Der, C. J. Drugging the undruggable RAS: Mission Possible? *Nature Reviews Drug Discovery 2014 13:11* **13**, 828–851 (2014).
128. Jackson, J. H. *et al.* Farnesol modification of Kirsten-ras exon 4B protein is essential for transformation. *Proceedings of the National Academy of Sciences* **87**, 3042–3046 (1990).

129. Willumsen, B. M., Christensen, A., Hubbert, N. L., Papageorge, A. G. & Lowy, D. R. The p21 ras C-terminus is required for transformation and membrane association. *Nature 1984 310:5978* **310**, 583–586 (1984).
130. Nagase, T. *et al.* Effect of farnesyltransferase overexpression on cell growth and transformation. *Int. J. Cancer* **80**, 126–133 (1999).
131. Soriano, O., Alcón-Pérez, M., Vicente-Manzanares, M. & Castellano, E. The Crossroads between RAS and RHO Signaling Pathways in Cellular Transformation, Motility and Contraction. *Genes (Basel)* **12**, (2021).
132. Etienne-Manneville, S. & Hall, A. Rho GTPases in cell biology. *Nature* **420**, 629–635 (2002).
133. Haga, R. B. & Ridley, A. J. Rho GTPases: Regulation and roles in cancer cell biology. *Small GTPases* **7**, 207–221 (2016).
134. Shen, M. *et al.* Farnesyltransferase and geranylgeranyltransferase I: structures, mechanism, inhibitors and molecular modeling. *Drug Discov Today* **20**, 267–276 (2015).
135. Karasic, T. B., Chiorean, E. G., Sebti, S. M. & O'Dwyer, P. J. A Phase I Study of GGTI-2418 (Geranylgeranyl Transferase I Inhibitor) in Patients with Advanced Solid Tumors. *Target Oncol* **14**, 613–618 (2019).
136. Wang, M. & Casey, P. J. Protein prenylation: unique fats make their mark on biology. *Nature Reviews Molecular Cell Biology 2016 17:2* **17**, 110–122 (2016).
137. Marchwicka, A., Kamińska, D., Monirialamdari, M., Błażewska, K. M. & Gendaszewska-Darmach, E. Protein Prenyltransferases and Their Inhibitors: Structural and Functional Characterization. *International Journal of Molecular Sciences 2022, Vol. 23, Page 5424* **23**, 5424 (2022).
138. Vogt, A. *et al.* A non-peptide mimetic of Ras-CAAX: selective inhibition of farnesyltransferase and Ras processing. *J Biol Chem* **270**, 660–664 (1995).
139. Reid, T. S. & Beese, L. S. Crystal Structures of the Anticancer Clinical Candidates R115777 (Tipifarnib) and BMS-214662 Complexed with Protein Farnesyltransferase Suggest a Mechanism of FTI Selectivity†. *Biochemistry* **43**, 6877–6884 (2004).

140. Hunt, J. T. *et al.* Discovery of (R)-7-cyano-2,3,4,5-tetrahydro-1-(1H-imidazol-4-ylmethyl)-3-(phenylmethyl)-4- (2-thienysulfonyl)-1H-1,4-benzodiazepine (BMS-214662), a farnesyltransferase inhibitor with potent preclinical antitumor activity. *J Med Chem* **43**, 3587–3595 (2000).
141. Njoroge, F. & Girijavallabhan, V. Discovery and Advancement of Farnesyl Transferase Inhibitors as Potential Anticancer Therapeutic Agents: SCH 66336 a Case Study. *Current Medicinal Chemistry-Immunology, Endocrine & Metabolic Agents* **1**, 185–198 (2005).
142. Vasudevan, A. *et al.* Potent, highly selective, and non-thiol inhibitors of protein geranylgeranyltransferase-I. *J Med Chem* **42**, 1333–1340 (1999).
143. Tan, K. T. *et al.* Design, synthesis, and characterization of peptide-based rab geranylgeranyl transferase inhibitors. *J Med Chem* **52**, 8025–8037 (2009).
144. Bon, R. S. *et al.* Structure-Guided Development of Selective RabGGTase Inhibitors. *Angewandte Chemie International Edition* **50**, 4957–4961 (2011).
145. Haney, S. L. *et al.* Preclinical investigation of a potent geranylgeranyl diphosphate synthase inhibitor. *Invest New Drugs* **36**, 810–818 (2018).
146. Stigter, E. A. *et al.* Development of selective, potent RabGGTase inhibitors. *J Med Chem* **55**, 8330–8340 (2012).
147. Reid, T. S. & Beese, L. S. Crystal structures of the anticancer clinical candidates R115777 (Tipifarnib) and BMS-214662 complexed with protein farnesyltransferase suggest a mechanism of FTI selectivity. *Biochemistry* **43**, 6877–6884 (2004).
148. Kazi, A. *et al.* Dual farnesyl and geranylgeranyl transferase inhibitor thwarts mutant KRAS-driven patient-derived pancreatic tumors. *Clinical Cancer Research* **25**, 5984–5996 (2019).
149. FDA Grants Fast Track Designation to Tipifarnib for the Treatment of Patients with HNSCC. https://www.cancernetwork.com/view/fda-grants-fast-track-designation-tipifarnib-treatment-patients-hnscc.
150. Harousseau, J. L. *et al.* A phase 2 study of the oral farnesyltransferase inhibitor tipifarnib in patients with refractory or relapsed acute myeloid leukemia. *Blood* **109**, 5151–5156 (2007).

151. Hanna, G. J. *et al.* A phase 1/2 trial to evaluate the safety and antitumor activity of tipifarnib and alpelisib for patients with PIK3CA-mutated/amplified and/or HRAS-overexpressing recurrent/metastatic head and neck squamous cell carcinoma. *https://doi.org/10.1200/JCO.2022.40.16_suppl.TPS6104* **40**, TPS6104–TPS6104 (2022).
152. Yam, C. *et al.* A phase II study of tipifarnib and gemcitabine in metastatic breast cancer. *Invest New Drugs* **36**, 299–306 (2018).
153. Akula, M. K. *et al.* Protein prenylation restrains innate immunity by inhibiting Rac1 effector interactions. *Nat Commun* (2019) doi:10.1038/s41467-019-11606-x.
154. Kim, E. *et al.* Disruption of the mouse Rce1 gene results in defective Ras processing and mislocalization of Ras within cells. *J. Biol. Chem.* **274**, 8383–8390 (1999).
155. Bergo, M. O. *et al.* Inactivation of Icmt inhibits transformation by oncogenic K-Ras and B-Raf. *Journal of Clinical Investigation* **113**, 539 (2004).
156. Winter-Vann, A. M. *et al.* A small-molecule inhibitor of isoprenylcysteine carboxyl methyltransferase with antitumor activity in cancer cells. (2005).
157. Marín-Ramos, N. I. *et al.* A Potent Isoprenylcysteine Carboxylmethyltransferase (ICMT) Inhibitor Improves Survival in Ras-Driven Acute Myeloid Leukemia. *J Med Chem* **62**, 6035–6046 (2019).
158. Wang, M. *et al.* A small molecule inhibitor of isoprenylcysteine carboxymethyltransferase induces autophagic cell death in PC3 prostate cancer cells. *Journal of Biological Chemistry* **283**, 18678–18684 (2008).
159. Sun, W. T. *et al.* Inhibition of isoprenylcysteine carboxylmethyltransferase augments BCR-ABL1 tyrosine kinase inhibition-induced apoptosis in chronic myeloid leukemia. *Exp Hematol* **44**, 189-193.e2 (2016).
160. García-España, A. & Philips, M. R. Origin and Evolution of RAS Membrane Targeting. *Oncogene 2023 42:21* **42**, 1741–1750 (2023).
161. van dam, T. J. P., Bos, J. L. & Snel, B. Evolution of the Ras-like small GTPases and their regulators. *Small GTPases* **2**, 4–16 (2011).

162. Milburn, M. V. *et al.* Molecular Switch for Signal Transduction: Structural Differences Between Active and Inactive Forms of Protooncogenic ras Proteins. *Science (1979)* **247**, 939–945 (1990).
163. Vigil, D., Cherfils, J., Rossman, K. L. & Der, C. J. Ras superfamily GEFs and GAPs: validated and tractable targets for cancer therapy? *Nature Reviews Cancer 2010 10:12* **10**, 842–857 (2010).
164. Vetter, I. R. & Wittinghofer, A. The Guanine Nucleotide-Binding Switch in Three Dimensions. *Science (1979)* **294**, 1299–1304 (2001).
165. Castellano, E. & Santos, E. Functional Specificity of Ras Isoforms: So Similar but So Different. *Genes Cancer* **2**, 216 (2011).
166. Hancock, J. F., Paterson, H. & Marshall, C. J. A polybasic domain or palmitoylation is required in addition to the CAAX motif to localize p21ras to the plasma membrane. *Cell* **63**, 133–139 (1990).
167. Boyartchuk, V. L., Ashby, M. N. & Rine, J. Modulation of Ras and a-factor function by carboxyl-terminal proteolysis. *Science (1979)* **275**, 1796–1800 (1997).
168. Choy, E. *et al.* Endomembrane trafficking of ras: The CAAX motif targets proteins to the ER and Golgi. *Cell* **98**, 69–80 (1999).
169. Laude, A. J. & Prior, I. A. Palmitoylation and localisation of RAS isoforms are modulated by the hypervariable linker domain. *J Cell Sci* **121**, 421–427 (2008).
170. Ko, P.-J. & Dixon, S. J. Protein palmitoylation and cancer. *EMBO Rep* **19**, e46666 (2018).
171. Schroeder, H. *et al.* S-acylation and plasma membrane targeting of the farnesylated carboxyl- terminal peptide of N-ras in mammalian fibroblasts. *Biochemistry* **36**, 13102–13109 (1997).
172. Shahinian, S. & Silvius, J. R. Doubly-Lipid-Modified Protein Sequence Motifs Exhibit Long-Lived Anchorage to Lipid Bilayer Membranes. *Biochemistry* **34**, 3813–3822 (1995).
173. Lynch, S. J. *et al.* The Differential Palmitoylation States of N-Ras and H-Ras Determine Their Distinct Golgi Sub-compartment Localizations. *J Cell Physiol* **230**, 610 (2015).

174. Leventis, R. & Silvius, J. R. Lipid-binding characteristics of the polybasic carboxy-terminal sequence of K-ras4B. *Biochemistry* **37**, 7640–7648 (1998).
175. Grecco, H. E. & al., et. Signaling from the living plasma membrane. *Cell* **144**, 897–909 (2011).
176. Schmick, M., Kraemer, A. & Bastiaens, P. I. H. Ras moves to stay in place. *Trends Cell Biol* **25**, 190–197 (2015).
177. Lakshman, B. *et al.* Quantitative biophysical analysis defines key components modulating recruitment of the GTPase KRAS to the plasma membrane. *Journal of Biological Chemistry* **294**, 2193–2207 (2019).
178. Muñoz-Maldonado, C., Zimmer, Y. & Medová, M. A Comparative Analysis of Individual RAS Mutations in Cancer Biology. *Front Oncol* **9**, 1088 (2019).
179. Ren, J. G. *et al.* RAB27B controls palmitoylation-dependent NRAS trafficking and signaling in myeloid leukemia. *J Clin Invest* **133**, (2023).
180. Cuiffo, B. & Ren, R. Palmitoylation of oncogenic NRAS is essential for leukemogenesis. *Blood* **115**, 3598–3605 (2010).
181. Amendola, C. R. *et al.* KRAS4A directly regulates hexokinase 1. *Nature 2019 576:7787* **576**, 482–486 (2019).
182. Santra, T. *et al.* An Integrated Global Analysis of Compartmentalized HRAS Signaling. *Cell Rep* **26**, 3100-3115.e7 (2019).
183. Asati, V., Mahapatra, D. K. & Bharti, S. K. PI3K/Akt/mTOR and Ras/Raf/MEK/ERK signaling pathways inhibitors as anticancer agents: Structural and pharmacological perspectives. *Eur J Med Chem* **109**, 314–341 (2016).
184. Untch, B. R. *et al.* Tipifarnib Inhibits HRAS-Driven dedifferentiated thyroid cancers. *Cancer Res* **78**, 4642–4657 (2018).
185. Smith, A. E. *et al.* Tipifarnib Potentiates the Antitumor Effects of PI3Kα Inhibition in PIK3CA- and HRAS-Dysregulated HNSCC via Convergent Inhibition of mTOR Activity. *Cancer Res* **83**, (2023).
186. Lin, D. T. S. & Conibear, E. ABHD17 proteins are novel protein depalmitoylases that regulate N-Ras palmitate turnover and subcellular localization. *Elife* **4**, e11306 (2015).

187. Remsberg, J. R. *et al.* ABHD17 regulation of plasma membrane palmitoylation and N-Ras-dependent cancer growth. *Nature Chemical Biology 2021 17:8* **17**, 856–864 (2021).
188. Kathayat, R. S., Elvira, P. D. & Dickinson, B. C. A fluorescent probe for cysteine depalmitoylation reveals dynamic APT signaling. *Nat Chem Biol* (2017) doi:10.1038/nchembio.2262.
189. Dekker, F. J. *et al.* Small-molecule inhibition of APT1 affects Ras localization and signaling. *Nat Chem Biol* **6**, 449–456 (2010).
190. Ngan, H. L., Law, C. H., Choi, Y. C. Y., Chan, J. Y. S. & Lui, V. W. Y. Precision drugging of the MAPK pathway in head and neck cancer. *npj Genomic Medicine 2022 7:1* **7**, 1–10 (2022).
191. Mendoza, M. C., Er, E. E. & Blenis, J. The Ras-ERK and PI3K-mTOR Pathways: Cross-talk and Compensation. *Trends Biochem Sci* **36**, 320 (2011).
192. Coussy, F. *et al.* Combination of PI3K and MEK inhibitors yields durable remission in PDX models of PIK3CA-mutated metaplastic breast cancers. *J Hematol Oncol* **13**, 1–10 (2020).
193. Siddiqui, F. A. *et al.* PDE6D Inhibitors with a New Design Principle Selectively Block K-Ras Activity. *ACS Omega* **5**, 832–842 (2020).
194. Canovas Nunes, S. *et al.* Validation of a small molecule inhibitor of PDE6D-RAS interaction with favorable anti-leukemic effects. *Blood Cancer Journal 2022 12:4* **12**, 1–14 (2022).
195. Canovas Nunes, S. *et al.* Validation of a small molecule inhibitor of PDE6D-RAS interaction with favorable anti-leukemic effects. *Blood Cancer Journal 2022 12:4* **12**, 1–14 (2022).
196. Papke, B. *et al.* Identification of pyrazolopyridazinones as PDEδ inhibitors. *Nature Communications 2016 7:1* **7**, 1–9 (2016).
197. Leung, E. L. H. *et al.* Inhibition of KRAS-dependent lung cancer cell growth by deltarasin: blockage of autophagy increases its cytotoxicity. *Cell Death & Disease 2018 9:2* **9**, 1–15 (2018).

198. Moore, A. R., Rosenberg, S. C., McCormick, F. & Malek, S. RAS-targeted therapies: is the undruggable drugged? *Nature Reviews Drug Discovery 2020 19:8* **19**, 533–552 (2020).
199. Khan, I., Rhett, J. M. & O'Bryan, J. P. Therapeutic targeting of RAS: New hope for drugging the "undruggable". *Biochimica et Biophysica Acta (BBA) - Molecular Cell Research* **1867**, 118570 (2020).
200. Ostrem, J. M., Peters, U., Sos, M. L., Wells, J. A. & Shokat, K. M. K-Ras(G12C) inhibitors allosterically control GTP affinity and effector interactions. *Nature 2013 503:7477* **503**, 548–551 (2013).
201. Skoulidis, F. *et al.* Sotorasib for Lung Cancers with KRAS p.G12C Mutation . *New England Journal of Medicine* **384**, 2371–2381 (2021).
202. Hong, D. S. *et al.* KRAS G12C Inhibition with Sotorasib in Advanced Solid Tumors . *New England Journal of Medicine* **383**, 1207–1217 (2020).
203. Jänne, P. A. *et al.* Adagrasib in Non–Small-Cell Lung Cancer Harboring a KRAS G12C Mutation . *New England Journal of Medicine* **387**, 120–131 (2022).
204. Awad, M. M. *et al.* Acquired Resistance to KRAS G12C Inhibition in Cancer . *New England Journal of Medicine* **384**, 2382–2393 (2021).
205. Mohanty, A. *et al.* Acquired resistance to KRAS G12C small-molecule inhibitors via genetic/nongenetic mechanisms in lung cancer. *Sci Adv* **9**, eade3816 (2023).
206. Edelstein, R. L. & Distefano, M. D. Photoaffinity Labeling of Yeast Farnesyl Protein Transferase and Enzymatic Synthesis of a Ras Protein Incorporating a Photoactive Isoprenoid. *Biochem Biophys Res Commun* **235**, 377–382 (1997).
207. Furfine, E. S., Leban, J. J., Landavazo, A., Moomaw, J. F. & Casey, P. J. Protein Famesyltransferase: Kinetics of Famesyl Pyrophosphate Binding and Product Release. *Biochemistry* **34**, 6857–6862 (1995).
208. Pompliano, D. L. *et al.* Steady-State Kinetic Mechanism of Ras Farnesyl: Protein Transferase. *Biochemistry* **31**, 3800–3807 (1992).
209. Reigard, S. A. *et al.* Interplay of isoprenoid and peptide substrate specificity in protein farnesyltransferase. *Biochemistry* **44**, 11214–11223 (2005).
210. Parker, C. G. & Pratt, M. R. Click Chemistry in Proteomic Investigations. *Cell* **180**, 605 (2020).

211. Kho, Y. *et al.* A tagging-via-substrate technology for detection and proteomics of farnesylated proteins. *Proc Natl Acad Sci U S A* **101**, 12479–12484 (2004).
212. Labadie, G. R., Viswanathan, R. & Poulter, C. D. Farnesyl Diphosphate Analogues with ω-Bioorthogonal Azide and Alkyne Functional Groups for PFTase-Catalyzed Ligation Reactions. *J Org Chem* **72**, 9291 (2007).
213. Rose, M. W. *et al.* Evaluation of geranylazide and farnesylazide diphosphate for incorporation of prenylazides into a CAAX box-containing peptide using protein farnesyltransferase*. *The Journal of Peptide Research* **65**, 529–537 (2005).
214. Wang, Y. C., Dozier, J. K., Beese, L. S. & Distefano, M. D. Rapid Analysis of Protein Farnesyltransferase Substrate Specificity Using Peptide Libraries and Isoprenoid Diphosphate Analogues. *ACS Chem Biol* **9**, 1726 (2014).
215. Berndt, N. & Sebti, S. M. Measurement of protein farnesylation and geranylgeranylation in vitro, in cultured cells and in biopsies, and the effects of prenyl transferase inhibitors. *Nature Protocols 2011 6:11* **6**, 1775–1791 (2011).
216. Broncel, M. *et al.* Multifunctional Reagents for Quantitative Proteome-Wide Analysis of Protein Modification in Human Cells and Dynamic Profiling of Protein Lipidation During Vertebrate Development. *Angew Chem Int Ed Engl* **54**, 5948 (2015).
217. Broncel, M. *et al.* Multifunctional reagents for quantitative proteome-wide analysis of protein modification in human cells and dynamic profiling of protein lipidation during vertebrate development. *Angewandte Chemie - International Edition* (2015) doi:10.1002/anie.201500342.
218. Palsuledesai, C. C., Ochocki, J. D., Markowski, T. W. & Distefano, M. D. A combination of metabolic labeling and 2D-DIGE analysis in response to a farnesyltransferase inhibitor facilitates the discovery of new prenylated proteins. *Mol Biosyst* **10**, 1094–1103 (2014).
219. DeGraw, A. J. *et al.* Evaluation of Alkyne-Modified Isoprenoids as Chemical Reporters of Protein Prenylation. *Chem Biol Drug Des* **76**, 460–471 (2010).
220. Jeong, A. *et al.* In Vivo Prenylomic Profiling in the Brain of a Transgenic Mouse Model of Alzheimer's Disease Reveals Increased Prenylation of a Key Set of Proteins. *ACS Chem Biol* **17**, 2863–2876 (2022).

221. Gisselberg, J. E., Zhang, L., Elias, J. E. & Yeh, E. The prenylated proteome of Plasmodium falciparum reveals pathogen-specific prenylation activity and drug mechanism-of-action. *Molecular and Cellular Proteomics* **16**, S54–S64 (2017).
222. Suazo, K. F., Schaber, C., Palsuledesai, C. C., Odom John, A. R. & Distefano, M. D. Global proteomic analysis of prenylated proteins in Plasmodium falciparum using an alkyne-modified isoprenoid analogue. *Scientific Reports 2016 6:1* **6**, 1–11 (2016).
223. Ivanov, S. S., Charron, G., Hang, H. C. & Roy, C. R. Lipidation by the host prenyltransferase machinery facilitates membrane localization of Legionella pneumophila effector proteins. *Journal of Biological Chemistry* **285**, 34686–34698 (2010).
224. Das, D. *et al.* Flexible and General Synthesis of Functionalized Phosphoisoprenoids for the Study of Prenylation in vivo and in vitro. *ChemBioChem* (2012) doi:10.1002/cbic.201100733.
225. Berry, A. F. H. *et al.* Rapid Multilabel Detection of Geranylgeranylated Proteins by Using Bioorthogonal Ligation Chemistry. *ChemBioChem* **11**, 771–773 (2010).
226. Patrício, M. I., Barnard, A. R., Cox, C. I., Blue, C. & MacLaren, R. E. The Biological Activity of AAV Vectors for Choroideremia Gene Therapy Can Be Measured by In Vitro Prenylation of RAB6A. *Mol Ther Methods Clin Dev* **9**, 288–295 (2018).
227. Palsuledesai, C. C. *et al.* Metabolic Labeling with an Alkyne-modified Isoprenoid Analog Facilitates Imaging and Quantification of the Prenylome in Cells. *ACS Chem Biol* **11**, 2820–2828 (2016).
228. DeGraw, A. J. *et al.* Evaluation of Alkyne-Modified Isoprenoids as Chemical Reporters of Protein Prenylation. *Chem Biol Drug Des* **76**, 460–471 (2010).
229. Verdaguer, I. B., Crispim, M., Hernández, A. & Katzin, A. M. The Biomedical Importance of the Missing Pathway for Farnesol and Geranylgeraniol Salvage. *Molecules* **27**, (2022).
230. Kloog, Y., Elad-Sfadia, G., Haklai, R. & Mor, A. Ras Chaperones: New Targets for Cancer and Immunotherapy. *Enzymes (Essen)* **33**, 267–289 (2013).

231. Wang, M. & Casey, P. J. Protein prenylation: Unique fats make their mark on biology. *Nat Rev Mol Cell Biol* **17**, 110–122 (2016).
232. Troutman, J. M., Andres, D. A. & Spielmann, H. P. Protein farnesyl transferase target selectivity is dependent upon peptide stimulated product release. *Biochemistry* **46**, 11299–11309 (2007).
233. Prior, I. A. & Hancock, J. F. Ras trafficking, localization and compartmentalized signalling. *Semin Cell Dev Biol* **23**, 145 (2012).
234. Wang, M. & Casey, P. J. Protein prenylation: Unique fats make their mark on biology. *Nature Reviews Molecular Cell Biology* Preprint at https://doi.org/10.1038/nrm.2015.11 (2016).
235. Dharmaiah, S. *et al.* Structural basis of recognition of farnesylated and methylated KRAS4b by PDEd. *Proc Natl Acad Sci U S A* **113**, E6766–E6775 (2016).
236. Chandra, A. *et al.* The GDI-like solubilizing factor PDEδ sustains the spatial organization and signalling of Ras family proteins. *Nature Cell Biology 2012 14:2* **14**, 148–158 (2011).
237. Klein, C. H. *et al.* PDEδ inhibition impedes the proliferation and survival of human colorectal cancer cell lines harboring oncogenic KRas. *Int J Cancer* **144**, 767–776 (2019).
238. Cox, A. D., Der, C. J. & Philips, M. R. Targeting RAS Membrane Association: Back to the Future for Anti-RAS Drug Discovery? *Clinical Cancer Research* **21**, 1819–1827 (2015).
239. Zimmermann, G. *et al.* Small molecule inhibition of the KRAS–PDEδ interaction impairs oncogenic KRAS signalling. *Nature 2013 497:7451* **497**, 638–642 (2013).
240. Papke, B. *et al.* Identification of pyrazolopyridazinones as PDEδ inhibitors. *Nature Communications 2016 7:1* **7**, 1–9 (2016).
241. Papke, B. *et al.* Identification of pyrazolopyridazinones as PDEδ inhibitors. *Nature Communications 2016 7:1* **7**, 1–9 (2016).
242. Hauser, A. D. *et al.* The SmgGDS splice variant SmgGDS-558 is a key promoter of tumor growth and RhoA signaling in breast cancer. doi:10.1158/1541-7786.MCR-13-0362.

243. Tew, G. W. *et al.* SmgGDS regulates cell proliferation, migration, and NF-kappaB transcriptional activity in non-small cell lung carcinoma. *J Biol Chem* **283**, 963–976 (2008).
244. Nolan, A. *et al.* Proteomic Mapping of the Interactome of KRAS Mutants Identifies New Features of RAS Signalling Networks and the Mechanism of Action of Sotorasib. *Cancers (Basel)* **15**, (2023).
245. Brandt, A. C. *et al.* Splice switching an oncogenic ratio of SmgGDS isoforms as a strategy to diminish malignancy. *PNAS* **117**, 3627–3636 (2020).
246. Hauser, A. D. *et al.* The SmgGDS splice variant SmgGDS-558 is a key promoter of tumor growth and RhoA signaling in breast cancer. *Mol Cancer Res* **12**, 130 (2014).
247. Gelb, M. H. *et al.* Therapeutic intervention based on protein prenylation and associated modifications. *Nature Chemical Biology 2006 2:10* **2**, 518–528 (2006).
248. Zimonjic, D. B. *et al.* In vitro and in vivo effects of geranylgeranyltransferase I inhibitor P61A6 on non-small cell lung cancer cells. *BMC Cancer* **13**, 1–10 (2013).
249. Oughtred, R. *et al.* The BioGRID database: A comprehensive biomedical resource of curated protein, genetic, and chemical interactions. *Protein Science* **30**, 187–200 (2021).
250. Mosaddeghzadeh, N. & Ahmadian, M. R. The RHO Family GTPases: Mechanisms of Regulation and Signaling. *Cells* **10**, (2021).
251. Williams, C. L. The polybasic region of Ras and Rho family small GTPases: a regulator of protein interactions and membrane association and a site of nuclear localization signal sequences. *Cell Signal* **15**, 1071–1080 (2003).
252. Mao, Z. *et al.* KRAS(G12D) can be targeted by potent inhibitors via formation of salt bridge. *Cell Discovery 2022 8:1* **8**, 1–14 (2022).
253. Pappireddi, N., Martin, L. & Wühr, M. A Review on Quantitative Multiplexed Proteomics. *Chembiochem* **20**, 1210 (2019).
254. Koshland, D. E. & Hamadani, K. Proteomics and models for enzyme cooperativity. *Journal of Biological Chemistry* **277**, 46841–46844 (2002).
255. Manadas, B., Mendes, V. M., English, J. & Dunn, M. J. Peptide fractionation in proteomics approaches. *Expert Rev Proteomics* **7**, 655–663 (2010).

256. Tyanova, S., Temu, T. & Cox, J. The MaxQuant computational platform for mass spectrometry-based shotgun proteomics. *Nature Protocols 2016 11:12* **11**, 2301–2319 (2016).
257. Suazo, K. F., Schaber, C., Palsuledesai, C. C., Odom John, A. R. & Distefano, M. D. Global proteomic analysis of prenylated proteins in Plasmodium falciparum using an alkyne-modified isoprenoid analogue. *Scientific Reports 2016 6:1* **6**, 1–11 (2016).
258. Zhang, N. & Li, L. Effects of common surfactants on protein digestion and matrix-assisted laser desorption/ionization mass spectrometric analysis of the digested peptides using two-layer sample preparation. *Rapid Communications in Mass Spectrometry* **18**, 889–896 (2004).
259. Bielow, C., Mastrobuoni, G. & Kempa, S. Proteomics Quality Control: Quality Control Software for MaxQuant Results. *J Proteome Res* **15**, 777–787 (2016).
260. Leutert, M., Rodríguez-Mias, R. A., Fukuda, N. K. & Villén, J. R2-P2 rapid-robotic phosphoproteomics enables multidimensional cell signaling studies. *Mol Syst Biol* **15**, (2019).
261. Neset, L., Takayidza, G., Berven, F. S. & Hernandez-Valladares, M. Comparing Efficiency of Lysis Buffer Solutions and Sample Preparation Methods for Liquid Chromatography–Mass Spectrometry Analysis of Human Cells and Plasma. *Molecules* **27**, 3390 (2022).
262. Jiang, L., He, L. & Fountoulakis, M. Comparison of protein precipitation methods for sample preparation prior to proteomic analysis. *J Chromatogr A* **1023**, 317–320 (2004).
263. Varnavides, G. *et al.* In Search of a Universal Method: A Comparative Survey of Bottom-Up Proteomics Sample Preparation Methods. *J Proteome Res* **21**, 2397–2411 (2022).
264. Johnston, H. E. *et al.* Solvent Precipitation SP3 (SP4) Enhances Recovery for Proteomics Sample Preparation without Magnetic Beads. *Anal Chem* **94**, 10320–10328 (2022).

265. Brenes, A., Hukelmann, J., Bensaddek, D. & Lamond, A. I. Multibatch TMT Reveals False Positives, Batch Effects and Missing Values. *Mol Cell Proteomics* **18**, 1967 (2019).
266. Ting, L., Rad, R., Gygi, S. P. & Haas, W. MS3 eliminates ratio distortion in isobaric labeling-based multiplexed quantitative proteomics. *Nat Methods* **8**, 937 (2011).
267. Shen, Y., Wang, J. & Navlakha, S. A Correspondence Between Normalization Strategies in Artificial and Biological Neural Networks. *Neural Comput* **33**, 3179 (2021).
268. Jeong, A. *et al.* In Vivo Prenylomic Profiling in the Brain of a Transgenic Mouse Model of Alzheimer's Disease Reveals Increased Prenylation of a Key Set of Proteins. *ACS Chem Biol* **17**, 2863–2876 (2022).
269. Kwon, H. J. *et al.* Structure of N-terminal Domain of NPC1 Reveals Distinct Subdomains for Binding and Transfer of Cholesterol. *Cell* **137**, 1213 (2009).
270. Hussey, D. J., Moore, S., Nicola, M. & Dobrovic, A. Fusion of the NUP98 gene with the LEDGF/p52 gene defines a recurrent acute myeloid leukemia translocation. *BMC Genet* **2**, (2001).
271. Gallego Hernanz, M. P. *et al.* Long-term molecular remission in a patient with acute myeloid leukemia harboring a new NUP98-LEDGF rearrangement. *Cancer Med* **8**, 1765–1770 (2019).
272. Končitíková, R. *et al.* Kinetic and structural analysis of human ALDH9A1. *Biosci Rep* **39**, (2019).
273. Singh, S. *et al.* Aldehyde Dehydrogenases in Cellular Responses to Oxidative/electrophilic Stress. *Free Radic Biol Med* **56**, 89 (2013).
274. Suazo, K. F. *et al.* Thinking outside the CaaX-box: an unusual reversible prenylation on ALDH9A1. *RSC Chem Biol* (2023) doi:10.1039/D3CB00089C.
275. Zhang, L., Tschantz, W. R. & Casey, P. J. Isolation and Characterization of a Prenylcysteine Lyase from Bovine Brain*. (1997) doi:10.1074/jbc.272.37.23354.
276. Bienvenut, W. V., Giglione, C. & Meinnel, T. Proteome-wide analysis of the amino terminal status of Escherichia coli proteins at the steady-state and upon deformylation inhibition. *Proteomics* (2015) doi:10.1002/pmic.201500027.

277. Medeiros, B. C. *et al.* The farnesyl transferase inhibitor, tipifarnib, is a potent inhibitor of the MDR1 gene product, P-glycoprotein, and demonstrates significant cytotoxic synergism against human leukemia cell lines. *Leukemia* **21**, 739–746 (2007).
278. Ho, A. L. *et al.* Tipifarnib in head and neck squamous cell carcinoma with HRAS mutations. *Journal of Clinical Oncology* **39**, 1856–1864 (2021).
279. Scott Reid, T., Terry, K. L., Casey, P. J. & Beese, L. S. Crystallographic Analysis of CaaX Prenyltransferases Complexed with Substrates Defines Rules of Protein Substrate Selectivity. *J Mol Biol* **343**, 417–433 (2004).
280. Hougland, J. L., Lamphear, C. L., Scott, S. A., Gibbs, R. A. & Fierke, C. A. Context-dependent substrate recognition by protein farnesyltransferase. *Biochemistry* **48**, 1691–1701 (2009).
281. Huang, W. *et al.* ZC3HAV1 promotes the proliferation and metastasis via regulating KRAS in pancreatic cancer. *Aging* **13**, 18482–18497 (2021).
282. Fernández-Costa, C. *et al.* Impact of the Identification Strategy on the Reproducibility of the DDA and DIA Results. *J Proteome Res* **19**, 3153–3161 (2020).
283. Mohanty, A. *et al.* Acquired resistance to KRAS G12C small-molecule inhibitors via genetic/nongenetic mechanisms in lung cancer. *Sci Adv* **9**, eade3816 (2023).
284. Holstein, S. A., Wohlford-Lenane, C. L. & Hohl, R. J. Consequences of Mevalonate Depletion: DIFFERENTIAL TRANSCRIPTIONAL, TRANSLATIONAL, AND POST-TRANSLATIONAL UP-REGULATION OF Ras, Rap1a, RhoA, AND RhoB. *Journal of Biological Chemistry* **277**, 10678–10682 (2002).
285. Palsuledesai, C. C. *et al.* Metabolic Labeling with an Alkyne-modified Isoprenoid Analog Facilitates Imaging and Quantification of the Prenylome in Cells. *ACS Chem Biol* (2016) doi:10.1021/acschembio.6b00421.
286. Charron, G., Tsou, L. K., Maguire, W., Yount, J. S. & Hang, H. C. Alkynyl-farnesol reporters for detection of protein S-prenylation in cells. *Mol Biosyst* (2011) doi:10.1039/c0mb00183j.

287. Lai, X. A reproducible method to enrich membrane proteins with high-purity and high-yield for an LC-MS/MS approach in quantitative membrane proteomics. *Electrophoresis* **34**, 809 (2013).
288. Hu, S. *et al.* Purification and Identification of Membrane Proteins from Urinary Extracellular Vesicles using Triton X-114 Phase Partitioning. *J Proteome Res* **17**, 86–96 (2018).
289. Fagerberg, L., Jonasson, K., Von Heijne, G., Uhlén, M. & Berglund, L. Prediction of the human membrane proteome. *Proteomics* **10**, 1141–1149 (2010).
290. Jones, J. M., Morrell, J. C. & Gould, S. J. PEX19 is a predominantly cytosolic chaperone and import receptor for class 1 peroxisomal membrane proteins. *J Cell Biol* **164**, 57 (2004).
291. Rucktäschel, R. *et al.* Farnesylation of Pex19p is required for its structural integrity and function in peroxisome biogenesis. *Journal of Biological Chemistry* **284**, 20885–20896 (2009).
292. Yang, P. *et al.* The cytosolic nucleic acid sensor LRRFIP1 mediates the production of type I interferon via a beta-catenin-dependent pathway. *Nat Immunol* **11**, 487–494 (2010).
293. Yang, P. *et al.* The cytosolic nucleic acid sensor LRRFIP1 mediates the production of type I interferon via a β-catenin-dependent pathway. *Nature Immunology 2010 11:6* **11**, 487–494 (2010).
294. Ichioka, F., Kobayashi, R., Katoh, K., Shibata, H. & Maki, M. Brox, a novel farnesylated Bro1 domain-containing protein that associates with charged multivesicular body protein 4 (CHMP4). *FEBS J* **275**, 682–692 (2008).
295. Moudgil, D. K. *et al.* A novel role of farnesylation in targeting a mitotic checkpoint protein, human spindly, to kinetochores. *Journal of Cell Biology* **208**, 881–896 (2015).
296. Ciossani, G. *et al.* The kinetochore proteins CENP-E and CENP-F directly and specifically interact with distinct BUB mitotic checkpoint Ser/Thr kinases. *Journal of Biological Chemistry* **293**, 10084–10101 (2018).
297. Vallett, S. M., Sanchez, H. B., Rosenfeld, J. M. & Osborne, T. F. A Direct Role for Sterol Regulatory Element Binding Protein in Activation of 3-Hydroxy-3-

methylglutaryl Coenzyme A Reductase Gene* A fundamental role for SREBP processing in cholesterol reg. *J Biol Chem* **271**, 12247–12253 (1996).

298. Goldstein, J. L. & Brown, M. S. Regulation of the mevalonate pathway. *Nature* **343**, 425–430 (1990).
299. De Giorgi, M. *et al.* Depletion of essential isoprenoids and ER stress induction following acute liver-specific deletion of HMG-CoA reductase. *J Lipid Res* **61**, 1675–1686 (2020).
300. Blouin, C. M. & Lamaze, C. Interferon gamma receptor: The beginning of the journey. *Front Immunol* **4**, 57350 (2013).
301. Sarrabayrouse, G., Pich, C., Teiti, I. & Tilkin-Mariame, A. F. Regulatory properties of statins and rho gtpases prenylation inhibitiors to stimulate melanoma immunogenicity and promote anti-melanoma immune response. *Int J Cancer* **140**, 747–755 (2017).
302. Vadakekolathu, J., Reeder, S., Coveney, C. & Rutella, S. Tipifarnib Modulates Interferon (IFN)-γ-Inducible Genes in Acute Myeloid Leukemia. *Blood* **134**, 2726–2726 (2019).
303. Bai, F. *et al.* Tipifarnib-mediated suppression of T-bet-dependent signaling pathways. *Cancer Immunology, Immunotherapy* **61**, 523–533 (2012).
304. Prior, I. A., Lewis, P. D. & Mattos, C. A comprehensive survey of Ras mutations in cancer. *Cancer Res* **72**, 2457 (2012).
305. Lanfredini, S., Thapa, A. & O'Neill, E. RAS in pancreatic cancer. *Biochem Soc Trans* **47**, 961–972 (2019).
306. Clinical Significance of ras Oncogene Activation in Human Lung Cancer1 | Cancer Research | American Association for Cancer Research. https://aacrjournals.org/cancerres/article/52/9_Supplement/2665s/498740/Clinical-Significance-of-ras-Oncogene-Activation.
307. East, P. *et al.* RAS oncogenic activity predicts response to chemotherapy and outcome in lung adenocarcinoma. *Nature Communications 2022 13:1* **13**, 1–17 (2022).
308. Randic, T., Kozar, I., Margue, C., Utikal, J. & Kreis, S. NRAS mutant melanoma: Towards better therapies. *Cancer Treat Rev* **99**, 102238 (2021).

309. Al Mahi, A. & Ablain, J. RAS pathway regulation in melanoma. *DMM Disease Models and Mechanisms* **15**, (2022).
310. Awada, H. *et al.* Impact and Outcomes of RAS gene Mutations in Core Binding Factor Acute Myeloid Leukemia. *Blood* **134**, 2720 (2019).
311. Liu, X. *et al.* RAS mutations in acute myeloid leukaemia patients: A review and meta-analysis. *Clinica Chimica Acta* **489**, 254–260 (2019).
312. Fell, J. B. *et al.* Identification of the Clinical Development Candidate MRTX849, a Covalent KRASG12CInhibitor for the Treatment of Cancer. *J Med Chem* **63**, 6679–6693 (2020).
313. Rosen, N. Finally, Effective Inhibitors of Mutant KRAS. *New England Journal of Medicine* **384**, 2447–2449 (2021).
314. Ostrem, J. M., Peters, U., Sos, M. L., Wells, J. A. & Shokat, K. M. K-Ras(G12C) inhibitors allosterically control GTP affinity and effector interactions. *Nature* **503**, 548–551 (2013).
315. Bhattacharya, S. *et al.* Group Behavior and Emergence of Cancer Drug Resistance. *Trends Cancer* **7**, 323–334 (2021).
316. Manandhar, S. P., Hildebrandt, E. R. & Schmidt, W. K. Small-Molecule Inhibitors of the Rce1p CaaX Protease. *J Biomol Screen* **12**, 983 (2007).
317. Winter-Vann, A. M. *et al.* A small-molecule inhibitor of isoprenylcysteine carboxyl methyltransferase with antitumor activity in cancer cells. *Proc Natl Acad Sci U S A* **102**, 4336 (2005).
318. Baum, C. & Kirschmeier, P. Preclinical and clinical evaluation of farnesyltransferase inhibitors. *Curr Oncol Rep* **5**, 99–107 (2003).
319. Campbell, S. L. & Philips, M. R. Post-translational modification of RAS proteins. *Curr Opin Struct Biol* **71**, 180–192 (2021).
320. Sebti, S. M. & Adjei, A. A. Farnesyltransferase inhibitors. *Semin Oncol* **31**, 28–39 (2004).
321. Chen, X., Makarewicz, J. M., Knauf, J. A., Johnson, L. K. & Fagin, J. A. Transformation by Hras G12V is consistently associated with mutant allele copy gains and is reversed by farnesyl transferase inhibition. *Oncogene* **33**, 5442–5449 (2014).

322. Delahaye, C. *et al.* Early Steps of Resistance to Targeted Therapies in Non-Small-Cell Lung Cancer. *Cancers 2022, Vol. 14, Page 2613* **14**, 2613 (2022).
323. Lane, K. T. & Beese, L. S. Thematic review series: Lipid Posttranslational Modifications. Structural biology of protein farnesyltransferase and geranylgeranyltransferase type I. *J Lipid Res* **47**, 681–699 (2006).
324. Reigard, S. A. *et al.* Interplay of isoprenoid and peptide substrate specificity in protein farnesyltransferase. *Biochemistry* **44**, 11214–11223 (2005).
325. Neggers, J. E. *et al.* Target identification of small molecules using large-scale CRISPR-Cas mutagenesis scanning of essential genes. *Nature Communications 2018 9:1* **9**, 1–14 (2018).
326. Findlay, G. M. *et al.* Accurate classification of BRCA1 variants with saturation genome editing. *Nature 2018 562:7726* **562**, 217–222 (2018).
327. Xue, C. & Greene, E. C. DNA Repair Pathway Choices in CRISPR-Cas9-Mediated Genome Editing. *Trends in Genetics* **37**, 639–656 (2021).
328. Lundberg, D. S., Yourstone, S., Mieczkowski, P., Jones, C. D. & Dangl, J. L. Practical innovations for high-throughput amplicon sequencing. *Nature Methods 2013 10:10* **10**, 999–1002 (2013).
329. Kleinstiver, B. P. *et al.* Engineered CRISPR-Cas9 nucleases with altered PAM specificities. *Nature 2015 523:7561* **523**, 481–485 (2015).
330. Andreou, L. V. Isolation of Plasmid DNA from Bacteria. *Methods Enzymol* **529**, 135–142 (2013).
331. Wong, K. H., Jin, Y. & Moqtaderi, Z. Multiplex Illumina Sequencing Using DNA Barcoding. *Curr Protoc Mol Biol* **101**, 7.11.1-7.11.11 (2013).
332. Anzalone, A. V. *et al.* Search-and-replace genome editing without double-strand breaks or donor DNA. *Nature 2019 576:7785* **576**, 149–157 (2019).
333. Chou, Q., Russell, M., Birch, D. E., Raymond, J. & Bloch, W. Prevention of pre-PCR mis-priming and primer dimerization improves low-copy-number amplifications. *Nucleic Acids Res* **20**, 1717–1723 (1992).
334. Qiu, P. *et al.* Mutation detection using Surveyor™ nuclease. *Biotechniques* **36**, 702–707 (2004).

335. Conant, D. *et al.* Inference of CRISPR Edits from Sanger Trace Data. *CRISPR Journal* **5**, 123–130 (2022).
336. Yenerall, P. *et al.* Lentiviral-Driven Discovery of Cancer Drug Resistance Mutations. *Cancer Res* **81**, 4685–4695 (2021).
337. Kolch, W., Berta, D. & Rosta, E. Dynamic regulation of RAS and RAS signaling. *Biochemical Journal* **480**, 1–23 (2023).
338. Healy, F. M., Prior, I. A. & MacEwan, D. J. The importance of Ras in drug resistance in cancer. *Br J Pharmacol* **179**, 2844–2867 (2022).
339. DepMap: The Cancer Dependency Map Project at Broad Institute. https://depmap.org/portal/.
340. Meyers, R. M. *et al.* Computational correction of copy number effect improves specificity of CRISPR-Cas9 essentiality screens in cancer cells. *Nat Genet* **49**, 1779–1784 (2017).
341. Hayes, T. K. *et al.* A functional landscape of resistance to MEK1/2 and CDK4/6 inhibition in NRAS-mutant melanoma. *Cancer Res* **79**, 2352–2366 (2019).
342. Kiessling, M. K. *et al.* Mutant HRAS as novel target for MEK and mTOR inhibitors. *Oncotarget* **6**, 42183 (2015).
343. Johnson, D. B. & Puzanov, I. Treatment of NRAS-Mutant Melanoma. *Curr Treat Options Oncol* **16**, 15 (2015).
344. Han, K. *et al.* CRISPR screens in cancer spheroids identify 3D growth-specific vulnerabilities. *Nature 2020 580:7801* **580**, 136–141 (2020).
345. Costa, E. C. *et al.* 3D tumor spheroids: an overview on the tools and techniques used for their analysis. *Biotechnol Adv* **34**, 1427–1441 (2016).
346. Melissaridou, S. *et al.* The effect of 2D and 3D cell cultures on treatment response, EMT profile and stem cell features in head and neck cancer. *Cancer Cell Int* **19**, (2019).
347. Wang, M. *et al.* Role of tumor microenvironment in tumorigenesis. *J Cancer* **8**, 761–773 (2017).
348. Huang, M. *et al.* Evaluation of AMG510 Therapy on KRAS-Mutant Non–Small Cell Lung Cancer and Colorectal Cancer Cell Using a 3D Invasive Tumor Spheroid System under Normoxia and Hypoxia. *Bioengineering* **9**, (2022).

349. Baker, T. L., Zheng, H., Walker, J., Coloff, J. L. & Buss, J. E. Distinct rates of palmitate turnover on membrane-bound cellular and oncogenic H-Ras. *Journal of Biological Chemistry* **278**, 19292–19300 (2003).
350. Goodwin, J. S. *et al.* Depalmitoylated Ras traffics to and from the Golgi complex via a nonvesicular pathway. *Journal of Cell Biology* **170**, 261–272 (2005).
351. Main, A. & Fuller, W. Protein S-Palmitoylation: advances and challenges in studying a therapeutically important lipid modification. *FEBS J* **289**, 861–882 (2022).
352. Percher, A., Thinon, E. & Hang, H. Mass-Tag Labeling Using Acyl-PEG Exchange for the Determination of Endogenous Protein S-Fatty Acylation. *Curr Protoc Protein Sci* **89**, 14.17.1-14.17.11 (2017).
353. Rocks, O. *et al.* An acylation cycle regulates localization and activity of palmitoylated ras isoforms. *Science (1979)* **307**, 1746–1752 (2005).
354. Agudo-Ibáñez, L., Herrero, A., Barbacid, M. & Crespo, P. H-Ras Distribution and Signaling in Plasma Membrane Microdomains Are Regulated by Acylation and Deacylation Events. *Mol Cell Biol* **35**, 1898 (2015).
355. Busquets-Hernández, C. & Triola, G. Palmitoylation as a Key Regulator of Ras Localization and Function. *Front Mol Biosci* **8**, 659861 (2021).
356. Peng, T., Thinon, E. & Hang, H. C. Proteomic analysis of fatty-acylated proteins. *Curr Opin Chem Biol* **30**, 77–86 (2016).
357. Blanc, M., David, F. P. A. & van der Goot, F. G. SwissPalm 2: Protein S-palmitoylation database. *Methods in Molecular Biology* **2009**, 203–214 (2019).
358. Wang, J. *et al.* Annexin A11 in disease. *Clinica Chimica Acta* **431**, 164–168 (2014).
359. Sang, G. P. *et al.* Human lysyl-tRNA synthetase is secreted to trigger proinflammatory response. *Proc Natl Acad Sci U S A* **102**, 6356–6361 (2005).
360. Luu, W., Hart-Smith, G., Sharpe, L. J. & Brown, A. J. The terminal enzymes of cholesterol synthesis, DHCR24 and DHCR7, interact physically and functionally. *J Lipid Res* **56**, 888–897 (2015).

361. Kennedy, P. R., Barthen, C., Williamson, D. J. & Davis, D. M. HLA-B and HLA-C differ in their nanoscale organization at cell surfaces. *Front Immunol* **10**, 434756 (2019).
362. Braunger, K. *et al.* Structural basis for coupling protein transport and N-glycosylation at the mammalian endoplasmic reticulum. *Science (1979)* **360**, 215–219 (2018).
363. Ahmad Mokhtar, A. M. *et al.* RhoG's Role in T Cell Activation and Function. *Front Immunol* **13**, 845064 (2022).
364. Sterner, R. C. & Sterner, R. M. CAR-T cell therapy: current limitations and potential strategies. *Blood Cancer Journal 2021 11:4* **11**, 1–11 (2021).
365. Kong, E. *et al.* Dynamic Palmitoylation Links Cytosol-Membrane Shuttling of Acyl-protein Thioesterase-1 and Acyl-protein Thioesterase-2 with That of Proto-oncogene H-Ras Product and Growth-associated Protein-43 *. *Journal of Biological Chemistry* **288**, 9112–9125 (2013).
366. Spitzer, J., Landthaler, M. & Tuschl, T. Rapid Creation of Stable Mammalian Cell Lines for Regulated Expression of Proteins Using the Gateway® Recombination Cloning Technology and Flp-In T-REx® Lines. *Methods Enzymol* **529**, 99–124 (2013).
367. Niihori, T. *et al.* HRAS mutants identified in Costello syndrome patients can induce cellular senescence: possible implications for the pathogenesis of Costello syndrome. *Journal of Human Genetics 2011 56:10* **56**, 707–715 (2011).
368. Labenski, M. T. *et al.* SMaSh: A Streptavidin Mass Shift Assay for Rapidly Quantifying Target Occupancy by Irreversible Inhibitors. *Biochemistry* **60**, 2915–2924 (2021).
369. Dye, B. T. Flow cytometric analysis of CFP–YFP FRET as a marker for in vivo protein–protein interaction. *Clin Appl Immunol Rev* **5**, 307–324 (2005).
370. Liu, Z. *et al.* Systematic comparison of 2A peptides for cloning multi-genes in a polycistronic vector. *Scientific Reports 2017 7:1* **7**, 1–9 (2017).
371. Stark, C. *et al.* BioGRID: a general repository for interaction datasets. *Nucleic Acids Res* **34**, D535 (2006).

372. Natwick, D. E. & Collins, S. R. Optimized iLID membrane anchors for local optogenetic protein recruitment. *ACS Synth Biol* **10**, 1009 (2021).
373. Tebo, A. G. & Gautier, A. A split fluorescent reporter with rapid and reversible complementation. *Nature Communications 2019 10:1* **10**, 1–8 (2019).
374. Jafari, R. *et al.* The cellular thermal shift assay for evaluating drug target interactions in cells. *Nature Protocols 2014 9:9* **9**, 2100–2122 (2014).
375. Casar, B. *et al.* RAS at the Golgi antagonizes malignant transformation through PTPRκ-mediated inhibition of ERK activation. *Nature Communications 2018 9:1* **9**, 1–17 (2018).
376. Plowman, S. J. & Hancock, J. F. Ras signaling from plasma membrane and endomembrane microdomains. *Biochimica et Biophysica Acta (BBA) - Molecular Cell Research* **1746**, 274–283 (2005).
377. Sharifi Tabar, M. *et al.* Illuminating the dark protein-protein interactome. *Cell Reports Methods* **2**, 100275 (2022).
378. Nolan, A. *et al.* Proteomic Mapping of the Interactome of KRAS Mutants Identifies New Features of RAS Signalling Networks and the Mechanism of Action of Sotorasib. *Cancers (Basel)* **15**, (2023).
379. Bishop, W. R., Doll, R. & Kirschmeier, P. Farnesyl Transferase Inhibitors: From Targeted Cancer Therapeutic to a Potential Treatment for Progeria. *Enzymes (Essen)* **29**, 275–303 (2011).
380. Guo, J. *et al.* The development of proximity labeling technology and its applications in mammals, plants, and microorganisms. *Cell Communication and Signaling 2023 21:1* **21**, 1–22 (2023).
381. Dunham, W. H., Mullin, M. & Gingras, A. C. Affinity-purification coupled to mass spectrometry: Basic principles and strategies. *Proteomics* **12**, 1576–1590 (2012).
382. Qin, W., Cho, K. F., Cavanagh, P. E. & Ting, A. Y. Deciphering molecular interactions by proximity labeling. *Nature Methods 2021 18:2* **18**, 133–143 (2021).
383. Béganton, B. *et al.* Proximal Protein Interaction Landscape of RAS Paralogs. *Cancers 2020, Vol. 12, Page 3326* **12**, 3326 (2020).

384. Zhang, X., Cao, J., Miller, S. P., Jing, H. & Lin, H. Comparative nucleotide-dependent interactome analysis reveals shared and differential properties of KRas4a and KRas4b. *ACS Cent Sci* **4**, 71–80 (2018).
385. Kovalski, J. R. *et al.* The Functional Proximal Proteome of Oncogenic Ras Includes mTORC2. *Mol Cell* **73**, 830-844.e12 (2019).
386. Adhikari, H. & Counter, C. M. Interrogating the protein interactomes of RAS isoforms identifies PIP5K1A as a KRAS-specific vulnerability. *Nature Communications 2018 9:1* **9**, 1–17 (2018).
387. Adhikari, H. & Counter, C. M. Using BioID to Characterize the RAS Interactome. *Methods Mol Biol* **2262**, 271–280 (2021).
388. Hung, V. *et al.* Spatially resolved proteomic mapping in living cells with the engineered peroxidase APEX2. *Nature Protocols 2016 11:3* **11**, 456–475 (2016).
389. Artan, M., Hartl, M., Chen, W. & de Bono, M. Depletion of endogenously biotinylated carboxylases enhances the sensitivity of TurboID-mediated proximity labeling in Caenorhabditis elegans. *J Biol Chem* **298**, (2022).
390. Bateman, A. *et al.* UniProt: the Universal Protein Knowledgebase in 2023. *Nucleic Acids Res* **51**, D523–D531 (2023).
391. Soriano, O., Alcón-Pérez, M., Vicente-Manzanares, M. & Castellano, E. The Crossroads between RAS and RHO Signaling Pathways in Cellular Transformation, Motility and Contraction. *Genes (Basel)* **12**, (2021).
392. Kiel, C., Matallanas, D. & Kolch, W. The Ins and Outs of RAS Effector Complexes. *Biomolecules* **11**, 1–29 (2021).
393. Guin, S. & Theodorescu, D. The RAS-RAL axis in cancer: evidence for mutation-specific selectivity in non-small cell lung cancer. *Acta Pharmacologica Sinica 2015 36:3* **36**, 291–297 (2015).
394. Adachi, Y. *et al.* Scribble mis-localization induces adaptive resistance to KRAS G12C inhibitors through feedback activation of MAPK signaling mediated by YAP-induced MRAS. *Nature Cancer 2023 4:6* **4**, 829–843 (2023).
395. Yogodzinski, C., Arab, A., Pritchard, J. R., Goodarzi, H. & Gilbert, L. A. A global cancer data integrator reveals principles of synthetic lethality, sex disparity and immunotherapy. *Genome Med* **13**, 1–12 (2021).

396. Nagamura, Y. *et al.* PLEKHA5 regulates the survival and peritoneal dissemination of diffuse-type gastric carcinoma cells with Met gene amplification. *Oncogenesis 2021 10:3* **10**, 1–14 (2021).
397. Lim, K. H. *et al.* Activation of RalA is critical for Ras-induced tumorigenesis of human cells. *Cancer Cell* **7**, 533–545 (2005).
398. Bonello, T. T. & Peifer, M. Scribble: A master scaffold in polarity, adhesion, synaptogenesis, and proliferation. *Journal of Cell Biology* **218**, 742–756 (2019).
399. Simanshu, D. K., Nissley, D. V. & McCormick, F. RAS Proteins and Their Regulators in Human Disease. *Cell* **170**, 17–33 (2017).
400. Fernández-Pisonero, I. *et al.* A hotspot mutation targeting the R-RAS2 GTPase acts as a potent oncogenic driver in a wide spectrum of tumors. *Cell Rep* **38**, (2022).
401. Martini, G. *et al.* EphA2 is a predictive biomarker of resistance and a potential therapeutic target for improving antiepidermal growth factor receptor therapy in colorectal cancer. *Mol Cancer Ther* **18**, 845–855 (2019).
402. Kim, J., Chang, I. Y. & You, H. J. Interactions between EGFR and EphA2 promote tumorigenesis through the action of Ephexin1. *Cell Death Dis* **13**, (2022).
403. Raja, E. *et al.* Tyrosine kinase Eph receptor A6 sensitizes glioma-initiating cells towards bone morphogenetic protein-induced apoptosis. *Cancer Sci* **110**, 3486 (2019).
404. Masuda, M. *et al.* TNIK inhibition abrogates colorectal cancer stemness. *Nature Communications 2016 7:1* **7**, 1–14 (2016).
405. Nathaniel Diehl, J. *et al.* The KRAS-regulated kinome identifies WEE1 and ERK coinhibition as a potential therapeutic strategy in KRAS-mutant pancreatic cancer. *Journal of Biological Chemistry* **297**, (2021).
406. Tiedt, R. *et al.* Integrated CRISPR screening and drug profiling identifies combination opportunities for EGFR, ALK, and BRAF/MEK inhibitors. *Cell Rep* **42**, (2023).
407. Yu, S. H. *et al.* Expanding the Perseus Software for Omics Data Analysis With Custom Plugins. *Curr Protoc Bioinformatics* **71**, e105 (2020).

408. Cmarko, L. *et al.* Secretory carrier-associated membrane protein 2 (SCAMP2) regulates cell surface expression of T-type calcium channels. *Mol Brain* **15**, 1–5 (2022).
409. Liu, L., Guo, Z., Tieu, Q., Castle, A. & Castle, D. Role of secretory carrier membrane protein SCAMP2 in granule exocytosis. *Mol Biol Cell* **13**, 4266–4278 (2002).
410. Luu, T. H., Chaillou, C., Huvelin, J. M., Bard, J. M. & Nazih, H. LXR Activation Down-regulates Lipid Raft Markers FLOT2 and DHHC5 in MCF-7 Breast Cancer Cells. *Anticancer Res* **37**, 4067–4073 (2017).
411. Jin, H. *et al.* Lipid raft protein flotillin-1 is important for the interaction between SOS1 and H-Ras/K-Ras, leading to Ras activation. *Int J Cancer* **152**, 1933–1946 (2023).
412. Solis, G. P. *et al.* Local and substrate-specific S-palmitoylation determines subcellular localization of Gαo. *Nature Communications 2022 13:1* **13**, 1–21 (2022).
413. Goldfinger, L. E. *et al.* An experimentally derived database of candidate ras-interacting proteins. *J Proteome Res* **6**, 1806–1811 (2007).
414. Branon, T. C. *et al.* Efficient proximity labeling in living cells and organisms with TurboID. *Nat Biotechnol* **36**, 880 (2018).
415. Van Puyvelde, B. *et al.* A comprehensive LFQ benchmark dataset on modern day acquisition strategies in proteomics. *Sci Data* **9**, (2022).
416. Demichev, V. *et al.* dia-PASEF data analysis using FragPipe and DIA-NN for deep proteomics of low sample amounts. *Nature Communications 2022 13:1* **13**, 1–8 (2022).
417. Nuevo-Tapioles, C. & Philips, M. R. The role of KRAS splice variants in cancer biology. *Front Cell Dev Biol* **10**, 1033348 (2022).
418. Tsai, F. D. *et al.* K-Ras4A splice variant is widely expressed in cancer and uses a hybrid membrane-targeting motif. *Proc Natl Acad Sci U S A* **112**, 779–784 (2015).
419. Woodley, K. T. & Collins, M. O. Regulation and function of the palmitoyl-acyltransferase ZDHHC5. *FEBS Journal* **288**, 6623–6634 (2021).

420. Stix, R., Lee, C. J., Faraldo-Gómez, J. D. & Banerjee, A. Structure and Mechanism of DHHC Protein Acyltransferases. *J Mol Biol* **432**, 4983–4998 (2020).
421. Swarthout, J. T. *et al.* DHHC9 and GCP16 constitute a human protein fatty acyltransferase with specificity for H- and N-Ras. *Journal of Biological Chemistry* **280**, 31141–31148 (2005).
422. Ko, P. J. *et al.* A ZDHHC5-GOLGA7 Protein Acyltransferase Complex Promotes Nonapoptotic Cell Death. *Cell Chem Biol* **26**, 1716-1724.e9 (2019).
423. Martin, B. R., Wang, C., Adibekian, A., Tully, S. E. & Cravatt, B. F. Global profiling of dynamic protein palmitoylation. *Articles* **84**, (2012).
424. Kong, E. *et al.* Dynamic palmitoylation links cytosol-membrane shuttling of acyl-protein thioesterase-1 and acyl-protein thioesterase-2 with that of proto-oncogene H-Ras product and growth-associated protein-43. *Journal of Biological Chemistry* **288**, 9112–9125 (2013).
425. Toyoda, T., Sugimoto, H. & Yamashita, S. Sequence, expression in Escherichia coli, and characterization of lysophospholipase II. *Biochim Biophys Acta* **1437**, 182–193 (1999).
426. Paul, I. *et al.* Parallelized multidimensional analytic framework applied to mammary epithelial cells uncovers regulatory principles in EMT. *Nature Communications 2023 14:1* **14**, 1–23 (2023).
427. Govindan, R. *et al.* Genomic landscape of non-small cell lung cancer in smokers and never-smokers. *Cell* **150**, 1121–1134 (2012).
428. Chen, Y. I. *et al.* Homophilic ATP1A1 binding induces activin A secretion to promote EMT of tumor cells and myofibroblast activation. *Nat Commun* **13**, (2022).
429. Kota, S. *et al.* A novel three-dimensional high-throughput screening approach identifies inducers of a mutant KRAS selective lethal phenotype. *Oncogene 2018 37:32* **37**, 4372–4384 (2018).
430. Dittmer, T. A. *et al.* Systematic identification of pathological lamin A interactors. *Mol Biol Cell* **25**, 1493–1510 (2014).

431. Zhang, K., Chan, V., Botelho, R. J. & Antonescu, C. N. A tail of their own: regulation of cardiolipin and phosphatidylinositol fatty acyl profile by the acyltransferase LCLAT1. *Biochem Soc Trans* **51**, 1765–1776 (2023).
432. Chan, V. *et al.* The LCLAT1/LYCAT acyltransferase is required for EGF-mediated phosphatidylinositol-3,4,5-trisphosphate and Akt signalling. *bioRxiv* 2023.01.26.524308 (2023) doi:10.1101/2023.01.26.524308.
433. Wei, W. *et al.* Cell type-selective secretome profiling in vivo. *Nature Chemical Biology 2020 17:3* **17**, 326–334 (2020).

Chapter 7
Appendix

Table 7.1. List of cell lines used throughout the study

Cell type	Media	Supplementation
PANC-1	RPMI-1640	Standard
AsPC-1	RPMI-1640	Standard
EA.hy926	DMEM	Standard
HEK293T	DMEM	GlutaMAX
NCI-H23 Cas9 WT	RPMI-1640	Standard
NCI-H23 Cas9 (SmgGDS-607 -/-)	RPMI-1640	Standard
MelJuSo	RPMI-1640	Standard
T24	McCoy's 5A	Standard
RL952	DMEM/F12	Standard
MelJuSo-Cas9	RPMI-1640	0.2 µg/mL Neomycin
RL952-Cas9	DMEM/F12	0.2 µg/mL Neomycin
Trex Flp-In HEK293T	DMEM	GlutaMAX + Blasticidin
APEX2-KRASG12D	DMEM	GlutaMAX + Blasticidin + Hygromycin B
APEX2-KRAS4B	DMEM	GlutaMAX + Blasticidin + Hygromycin B
APEX2-NRAS	DMEM	GlutaMAX + Blasticidin + Hygromycin B
APEX2-HRAS	DMEM	GlutaMAX + Blasticidin + Hygromycin B
MiniTurboID-KRAS4A	DMEM	GlutaMAX + Blasticidin + Hygromycin B
MiniTurboID-KRAS4B	DMEM	GlutaMAX + Blasticidin + Hygromycin B
MiniTurboID-NRAS	DMEM	GlutaMAX + Blasticidin + Hygromycin B

Table 7.2. List of antibodies used throughout the study

Target	Species	Clonality	Dilution	Supplier	Reference
HRAS	Mouse	Monoclonal	1:750	Millipore	MAB3291
KRAS-G12D	Rabbit	Monoclonal	1:1000	Cell Signalling	14429
SmgGDS (RAP1GDS1)	Mouse	Monoclonal	1:500	Santa-Cruz	sc-390003
HSP90	Mouse	Monoclonal	1:1000	Abcam	ab13492
GAPDH	Rabbit	Monoclonal	1:1000	Abcam	ab9485
Vincullin	Rabbit	Monoclonal	1:1000	Abcam	ab91459
Anti-FLAG M2-Peroxidase HR	Mouse	Monoclonal	1:5000	Merck	F1804
Neutravidin-HRP	N/A	N/A	1:1000	Invitrogen	A2664
Mouse IgG, HRP	Mouse	N/A	1:5000	Advansta	R-05071-500
Rabbit IgG, HRP	Mouse	N/A	1:5001	Advansta	R-05072-500

Table 7.3. List of plasmids generated or used throughout the study

Plasmid name	Promoter	TAG	Expression	Use
pU6_sgRNA_H1	U6	N/A	Transient	sgRNA production
pU6_sgRNA_H2	U6	N/A	Transient	sgRNA production
pU6_sgRNA_H3	U6	N/A	Transient	sgRNA production
pU6_sgRNA_H4	U6	N/A	Transient	sgRNA production
pU6_sgRNA_H5	U6	N/A	Transient	sgRNA production
pU6_sgRNA_H6	U6	N/A	Transient	sgRNA production
pU6_sgRNA_K1.2	U6	N/A	Transient	sgRNA production
pU6_sgRNA_K3	U6	N/A	Transient	sgRNA production
pU6_sgRNA_K4	U6	N/A	Transient	sgRNA production
pU6_sgRNA_K5	U6	N/A	Transient	sgRNA production
pCMV-VSV-G	CMV	N/A	Lentivirus	Lentivirus production
psPAX2	CMV	N/A	Lentivirus	Lentivirus production
pLVX-Cas9-Neo	CMV	FLAG	Lentivirus	Cas9 lentivirus production
pOG44	CMV	N/A	TRex Flp-In	FlpIn recombinase
pcDNA™5/FRT/TO	TRE3GS	N/A	TRex Flp-In	FlpIn expression backbone
pcMiniTurbo-KRAS-4a	TRE3GS	FLAG	TRex Flp-In	MiniTurbo proximity labelling
pcMiniTurbo-KRAS-4b	TRE3GS	FLAG	TRex Flp-In	MiniTurbo proximity labelling
pcMiniTurbo-NRAS	TRE3GS	FLAG	TRex Flp-In	MiniTurbo proximity labelling
pc-KRAS4b-CVIM	TRE3GS	FLAG	TRex Flp-In	FLAG S-prenylation screen
pc-KRAS4b-CVIL	TRE3GS	FLAG	TRex Flp-In	FLAG S-prenylation screen
pc-KRAS4b-CVIS	TRE3GS	FLAG	TRex Flp-In	FLAG S-prenylation screen
pc-KRAS4b-SVIM	TRE3GS	FLAG	TRex Flp-In	FLAG S-prenylation screen
pc-KRAS4a-CIIM	TRE3GS	FLAG	TRex Flp-In	FLAG S-prenylation screen
pc-KRAS4a-CIIL	TRE3GS	FLAG	TRex Flp-In	FLAG S-prenylation screen
pc-KRAS4a-SIIL	TRE3GS	FLAG	TRex Flp-In	FLAG S-prenylation screen
pc-KRAS4a-C180S	TRE3GS	FLAG	TRex Flp-In	FLAG S-prenylation screen
pc-NRAS-CVVM	TRE3GS	FLAG	TRex Flp-In	FLAG S-prenylation screen
pc-NRAS-CVVL	TRE3GS	FLAG	TRex Flp-In	FLAG S-prenylation screen
pc-NRAS-CVVS	TRE3GS	FLAG	TRex Flp-In	FLAG S-prenylation screen
pc-NRAS-SVVM	TRE3GS	FLAG	TRex Flp-In	FLAG S-prenylation screen
pc-NRAS-C181S	TRE3GS	FLAG	TRex Flp-In	FLAG S-prenylation screen
pc-HRAS-CVLS	TRE3GS	FLAG	TRex Flp-In	FLAG S-prenylation screen
pc-HRAS-CVLL	TRE3GS	FLAG	TRex Flp-In	FLAG S-prenylation screen
pc-HRAS-CVLM	TRE3GS	FLAG	TRex Flp-In	FLAG S-prenylation screen
pc-HRAS-SVLM	TRE3GS	FLAG	TRex Flp-In	FLAG S-prenylation screen
pc-HRAS-C181S	TRE3GS	FLAG	TRex Flp-In	FLAG S-prenylation screen
pc-HRAS-C184S	TRE3GS	FLAG	TRex Flp-In	FLAG S-prenylation screen
pc-KRAS_HHVR	TRE3GS	FLAG	TRex Flp-In	FLAG S-prenylation screen
pc-HRAS_KHVR	TRE3GS	FLAG	TRex Flp-In	FLAG S-prenylation screen
pc-KRAS_HCXXX	TRE3GS	FLAG	TRex Flp-In	FLAG S-prenylation screen
pc-HRAS_KCXXX	TRE3GS	FLAG	TRex Flp-In	FLAG S-prenylation screen
pc-Lyn11 CFP_KRAS-YFP	TRE3GS	Fluorescent reporter	TRex Flp-In	FRET membrane localization assay
pc-Lyn11 CFP_HRAS-YFP	TRE3GS	Fluorescent reporter	TRex Flp-In	FRET membrane localization assay

Table 7.4. List of siRNAs used throughout the study

Name	Sequence (5'-3')	Supplier
Both splice variants (I1)	GCAAAGATGTTATCAGCTG	Sigma
SmgGDS-607 (C2)	GAACTATAGCAATGAGAAT	Sigma
SmgGDS-558 (BD)	ACGATAGCCATTCGCTTCA	Sigma

Table 7.5. List of KRAS oligonucleotides used for sgRNA vector design

Name	Sequence (5'-3')	Supplier
K1_02_gRNA_top	CACCGTAGTTGGAGCTtGTGGCGT	Sigma
K1_02_gRNA_bot	AAACACGCCACaAGCTCCAACTAC	Sigma
K3_gRNA_top	CACCAATGACTGAATATAAACTTG	Sigma
K3_gRNA_bot	AAACCAAGTTTATATTCAGTCATT	Sigma
K4_gRNA_top	CACCGAATATAAACTTGTGGTAGT	Sigma
K4_gRNA_bot	AAACACTACCACAAGTTTATATTC	Sigma
K5_gRNA_top	CACCCTTGTGGTAGTTGGAGCTtG	Sigma
K5_gRNA_bot	AAACCaAGCTCCAACTACCACAAG	Sigma
NTC_gRNA_top	CACCACCTATAATCGACCACATTT	Sigma
NTC_gRNA_bot	AAACAAATGTGGTCGATTATAGGT	Sigma

Table 7.6. List of genomic amplicon PCR primers used throughout the study

Name	Sequence (5'-3')	Supplier
HRAS_EXON5_1_FW	ACACTCTTTCCCTACACGACGCTCTTCCGATCTGCCGGTCCCTCCTGATCCCA	Sigma
HRAS_EXON5_1_RV	GACTGGAGTTCAGACGTGTGCTCTTCCGATCTCCCTGGGAGTCCCCCTCACC	Sigma
HRAS_EXON5_2_FW	ACACTCTTTCCCTACACGACGCTCTTCCGATCTTGATCCCACAGCAGGGAGCC	Sigma
HRAS_EXON5_2_RV	GACTGGAGTTCAGACGTGTGCTCTTCCGATCTCAGGCCAGGAGACCGGCAG	Sigma
KRAS_EXON2_1_FW	ACACTCTTTCCCTACACGACGCTCTTCCGATCTTTAACCTTATGTGTGACATGTTCT	Sigma
KRAS_EXON2_1_RV	GACTGGAGTTCAGACGTGTGCTCTTCCGATCTTGTTGGATCATATTCGTCCACAAAA	Sigma

Table 7.7. List of HRAS oligonucleotides used for sgRNA vector design

Name	Sequence (5'-3')	Cut-site (DNA)	Cut-site (AA)
H1_gRNA_top	CACCAGTGTGTGCTCTCCTGACGC	532636 (+)	QHKLRKLNPPDESGPGCMSCKCVLSX*(INTRON)
H1_gRNA_bot	AAACGCGTCAGGAGAGCACACACT		
H2_gRNA_top	CACCACACTTGCAGCTCATGCAGC	532665 (-)	QHKLRKLNPPDESGPG*CMSCKCVLSX
H2_gRNA_bot	AAACGCTGCATGAGCTGCAAGTGT		
H3_gRNA_top	CACCCCTCCTGATGAGAGTGGCCC	532673 (+)	QHKLRKLNPPDESG*PGCMSCKCVLSX
H3_gRNA_bot	AAACGGGCCACTCTCATCAGGAGG		
H4_gRNA_top	CACCCTGAACCCTCCTGATGAGAG	532679 (+)	QHKLRKLNPPD*ESGPGCMSCKCVLSX
H4_gRNA_bot	AAACCTCTCATCAGGAGGGTTCAG		
H5_gRNA_top	CACCAGATCCGGCAGCACAAGCTG	532705 (+)	QHKLRK*LNPPDESGPGCMSCKCVLSX
H5_gRNA_bot	AAACCAGCTTGTGCTGCCGGATCT		
H6_gRNA_top	CACCGCTTCCGCAGCTTGTGCTGC	532712 (-)	Q*HKLRKLNPPDESGPGCMSCKCVLSX
H6_gRNA_bot	AAACGCAGCACAAGCTGCGGAAGC		

Table 7.8a. List of primers used for SDM generation of FLAG-RAS mutants

KRAS 4b				Ta
CVIM				
CVIL	**A**	KRAS4b.CVIL_Q5SDM_F	GTGTGTAATTtTGTAAAGAGCTC	57
		KRAS4b.CVIL_Q5SDM_R	TTTGTCTTTGACTTCTTTTTC	
CVIS	**B**	KRAS4b_CVIS_Q5SDM_F	GTGTGTAATTtcGTAACTGTGCC	63
		KRAS4b_CVIS_Q5SDM_R	TTTGTCTTTGACTTCTTTTTC	
SVIM	**C**	KRAS4b.C186S_Q5SDM_F	AAGACAAAGTcTGTAATTATGTAACTG	57
		KRAS4b.C186S_Q5SDM_R	TGACTTCTTTTTCTTCTTTTTAC	
KRAS 4a				
CIIM				
CIIL	**D**	KRAS4a.CIIL_Q5SDM_F	ATGCATTATAtTGTAAAGAGCTCG	57
		KRAS4a.CIIL_Q5SDM_R	TTTTTAATTTTCACACAGCC	
CIIS	**E**	KRAS.4A.CIIS_Q5SDM_F	ATGCATTATAtctTAAAGAGCTCGGATCCAC	57
		KRAS.4A.CIIS_Q5SDM_R	TTTTTAATTTTCACACAGCC	
SIIM	**F**	KRAS.4A.C186S_Q5SDM_F	ATTAAAAAATcCATTATAATGTAACTGTGCC	63
		KRAS.4A.C186S_Q5SDM_R	TTTCACACAGCCAGGAGT	
C180S	**G**	KRAS.4A.C180S_Q5SDM_F	ACTCCTGGCTcTGTGAAAATTAAAAAATG	60
		KRAS.4A.C180SQ5SDM_R	CTTTTCTTCTTTGCTGATTTTTTTC	
NRAS				
CVVM				
CVVL	**H**	NRAS_CVVL_Q5SDM_F	ATGTGTGGTGtcGTAACTGTGCCTTC	64
		NRAS_CVVL_Q5SDM_R	GGCAATCCCATACAACCC	
CVVS	**I**	NRAS_CVVS_Q5SDM_F	ATGTGTGGTGtcGTAAAGAGCTCGG	64
		NRAS_CVVS_Q5SDM_R	GGCAATCCCATACAACCC	
SVVM	**J**	NRAS_C186S_Q5SDM_F	GGATTGCCATcTGTGGTGATG	63
		NRAS_C186S_Q5SDM_R	CATACAACCCTGAGTCCC	
C181S	**K**	NRAS_C181S_Q5SDM_F	ACTCAGGGTTcTATGGGATTGC	65
		NRAS_C181S_Q5SDM_R	CCCATCATCACTGCTGTTG	
HRAS				
CVLS				
CVLL	**L**	HRAS_CVLL_Q5SDM_F	TGTGTGCTCTtaTAACTGTGCCTTCTAG	69
		HRAS_CVLL_Q5SDM_R	CTTGCAGCTCATGCAGCC	
CVLM	**M**	HRAS_CVLM_Q5SDM_F	GTGTGTGCTCatgTAACTGTGCCTTCTAGTTGCC	71
		HRAS_CVLM_Q5SDM_R	TTGCAGCTCATGCAGCCG	
SVLS	**N**	HRAS_SVLS_Q5SDM_F	AGCTGCAAGTcTGTGCTCTCCTAACTGTG	72
		HRAS_SVLS_Q5SDM_R	CATGCAGCCGGGGCCACT	
C181S	**O**	HRAS_C181S_Q5SDM_F	GGCCCCGGCTcCATGAGCTGC	72
		HRAS_C181S_Q5SDM_R	ACTCTCATCAGGAGGGTTCAGCTTCC	
C184S	**P**	HRAS_C184S_Q5SDM_F	TGCATGAGCTcCAAGTGTGTGCTC	72
		HRAS_C184S_Q5SDM_R	GCCGGGGCCACTCTCATC	
Chimera				
KRAS_HHVR	**Q**	KRAS_HRAS_HVR_Q5SDM_F	tgagagtggccccggctgcatgagctgcaagTGTGTAATTATGTAACTGTG	56
		KRAS_HRAS_HVR_Q5SDM_R	tcaggagggttcagcttccgcagcttgtgctgTTTTCGAATTTCTCGAACTAATG	
HRAS_KHVR	**R**	HRAS_KRAS_HVR_Q5SDM_F	aaagaagaaaaagaagtcaaagacaaagTGTGTGCTCTCCTAACTGTG	65
		HRAS_KRAS_HVR_Q5SDM_R	ttaccatctttgctcatcttttctttatgCCGGATCTCACGCACCAA	

Table 7.8b. High-throughput PCR set up for SDM of FLAG-RAS mutants

57	60	63	64	65	69	71	72
A	G	B	H	K	L	M	N
C		F	I	R			O
D		J					P
E							
Q							

Table 7.9. STRING KEGG of RAP1GDS1 Interactors (without prenylated proteins)

GO: KEGG	FDR
Protein processing in endoplasmic reticulum	0.0013
Adherens junction	0.0081
Regulation of actin cytoskeleton	0.0182
Antigen processing and presentation	0.0408

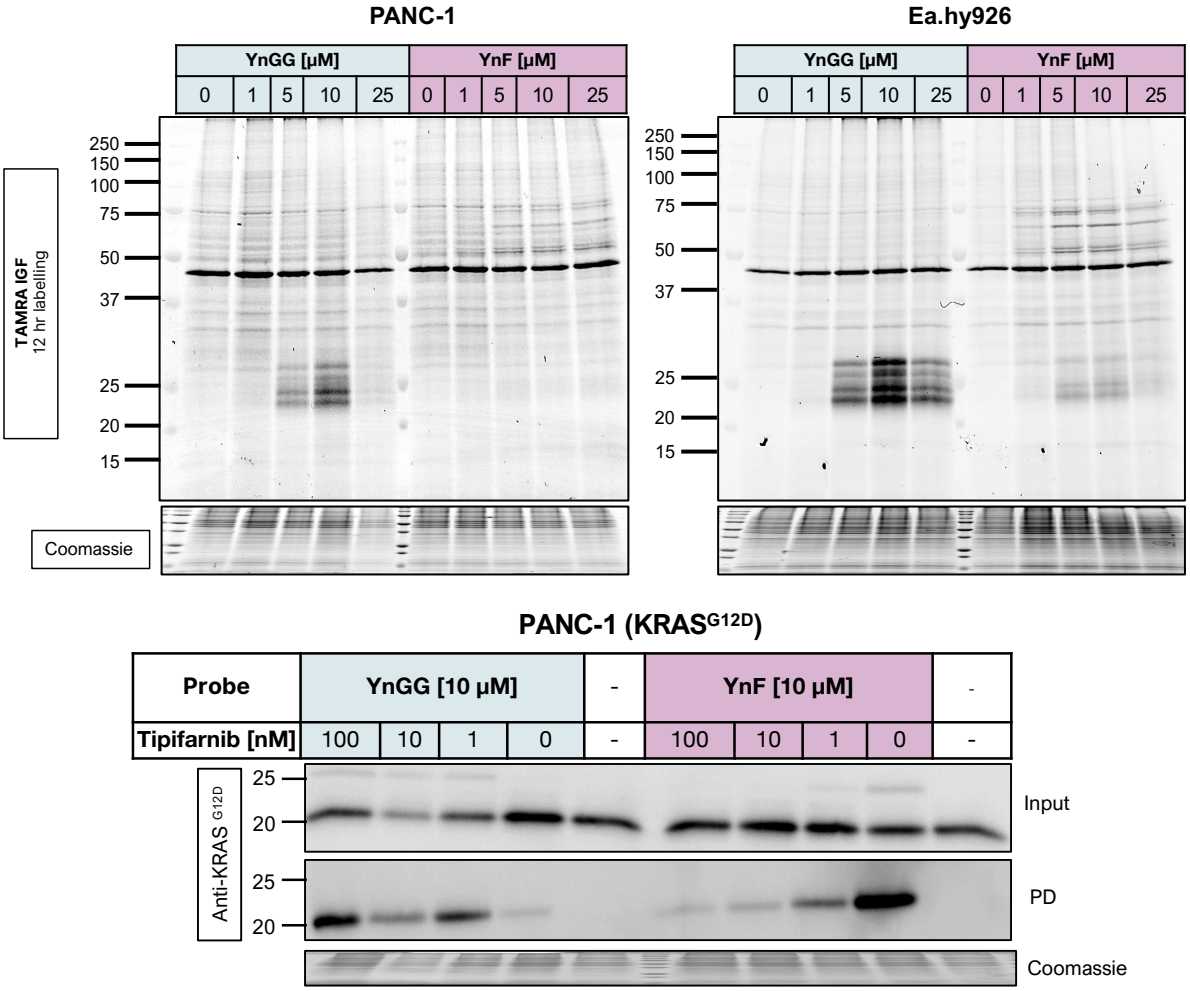

Figure 7.1. Validation of endogenous model system for KRAS prenylation switching. a) PANC-1 YnF and YnGG incorporation profiles with a standard metabolic labelling approach. Cells were incubated with either YnF or YnGG (0, 1, 5, 10, 25 µM) for 12 h before harvesting and click reaction (AzTB) and loading (10 µg) for gel analysis and IGF. The same approach was applied to Ea.hy926 cells, a previously validated cell line for probe incorporation. b) PANC-1 cells were taken forward to YnF/GG pulldown experiments to visualize prenylation switching in response to tipifarnib treatment (0, 1, 10, 100 µM).

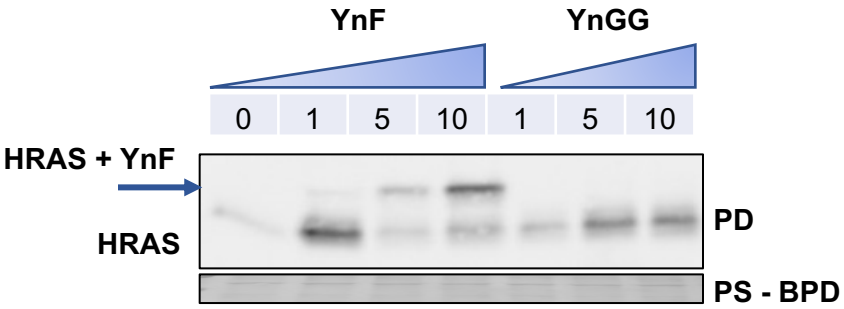

Figure 7.2. Validation of endogenous model system for HRAS pull-down. H23 cells were treated with increasing amounts of YnF and YnGG and subject to click ligation (AzTB) and enrichment (described in Methods). PD – pulldown; BPD – before pulldown; PS – Ponceau S staining.

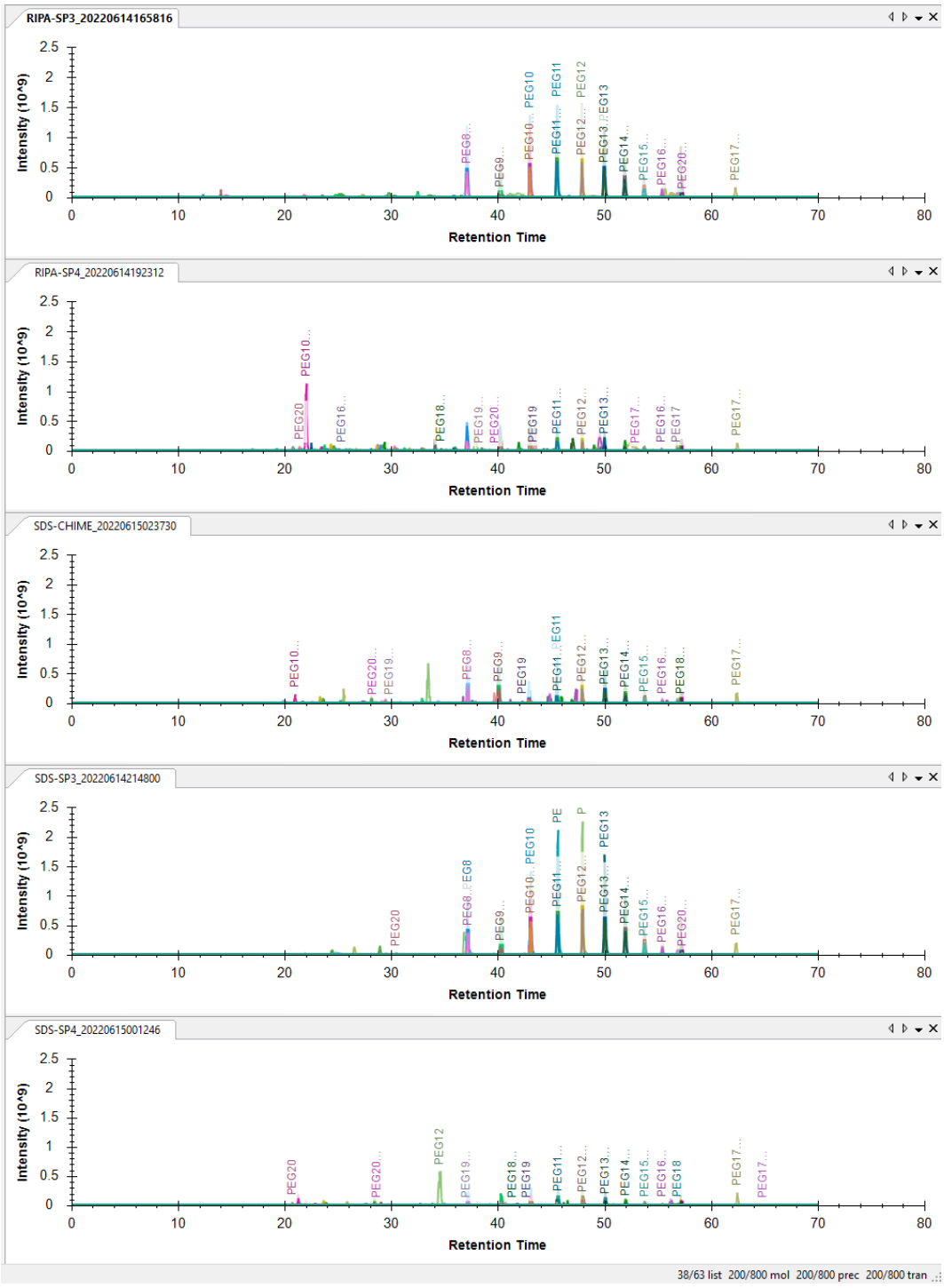

Figure 7.3. Skyline analysis of PEG contamination across purified protein samples

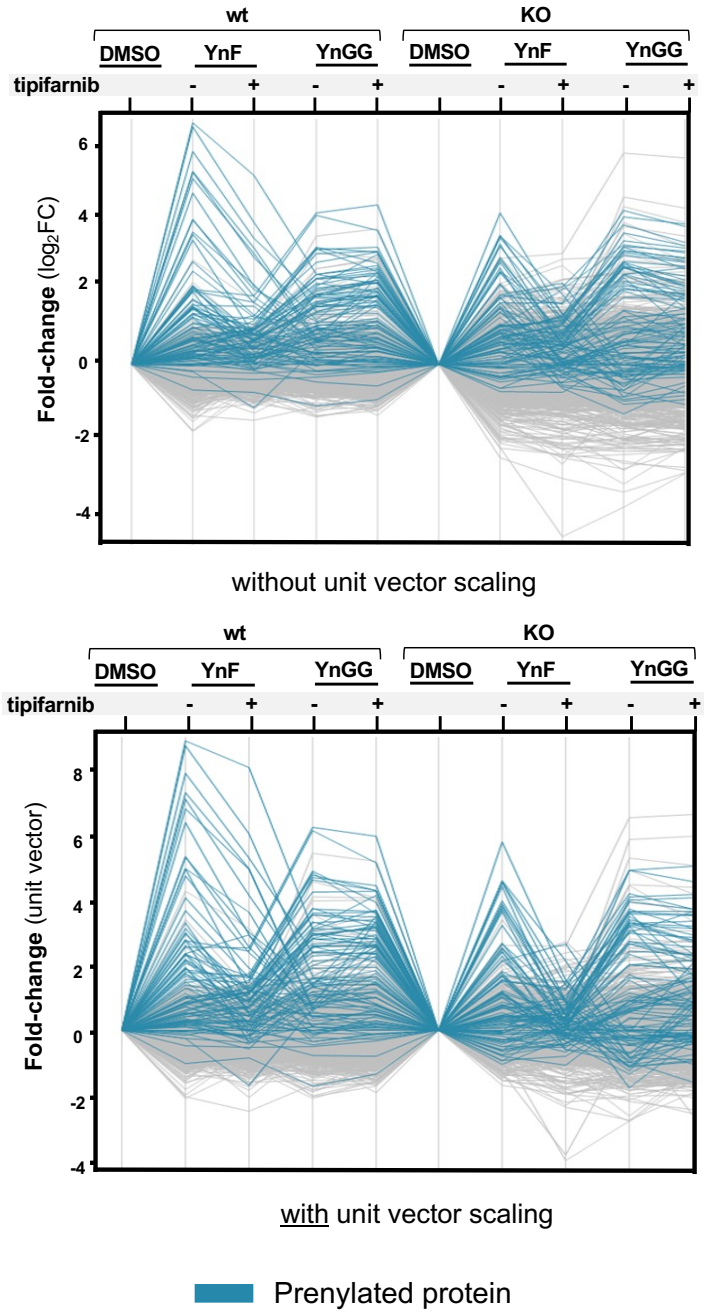

Figure 7.4. Unit vector scaling of H23 *S*-prenylation profiling experiment

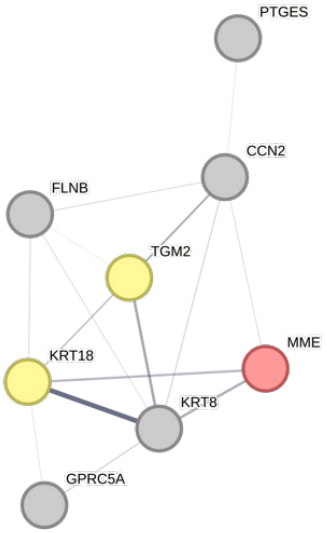

KO DMSO *vs.* WT DMSO		KO + tipifarnib *vs.* WT + tipifarnib		WT tipifanrib *vs.* WT DMSO		KO tipifanrib vs. KO DMSO	
DDA							
UP	**DOWN**	**UP**	**DOWN**	**UP**	**DOWN**	**UP**	**DOWN**
FLNB	NME1	H2AFV	UBE2D3/2	COPS3	ERH		FHL1
TGM2		HSP90AB2P		RPL29	HSP90AB2P		
ARPC5L		ERH					
FHL1							
VPS25							
LMNA							
U2AF1							
DIA							
UP	**DOWN**	**UP**	**DOWN**	**UP**	**DOWN**	**UP**	**DOWN**
CCN2		CCN2	HNRNPCL1	HBB;HBD		DDRGK1	
TGM2		TGM2					
PTGES		PTGES					
MME		MME					
DDT		GNAI3					
GPRC5A		GPRC5A					
ISYNA1		AMPD2					
		FLNB					

Figure 7.5. STRING analysis of substrates in DDA and DIA whole proteome studies of H23 tipifarnib treatment

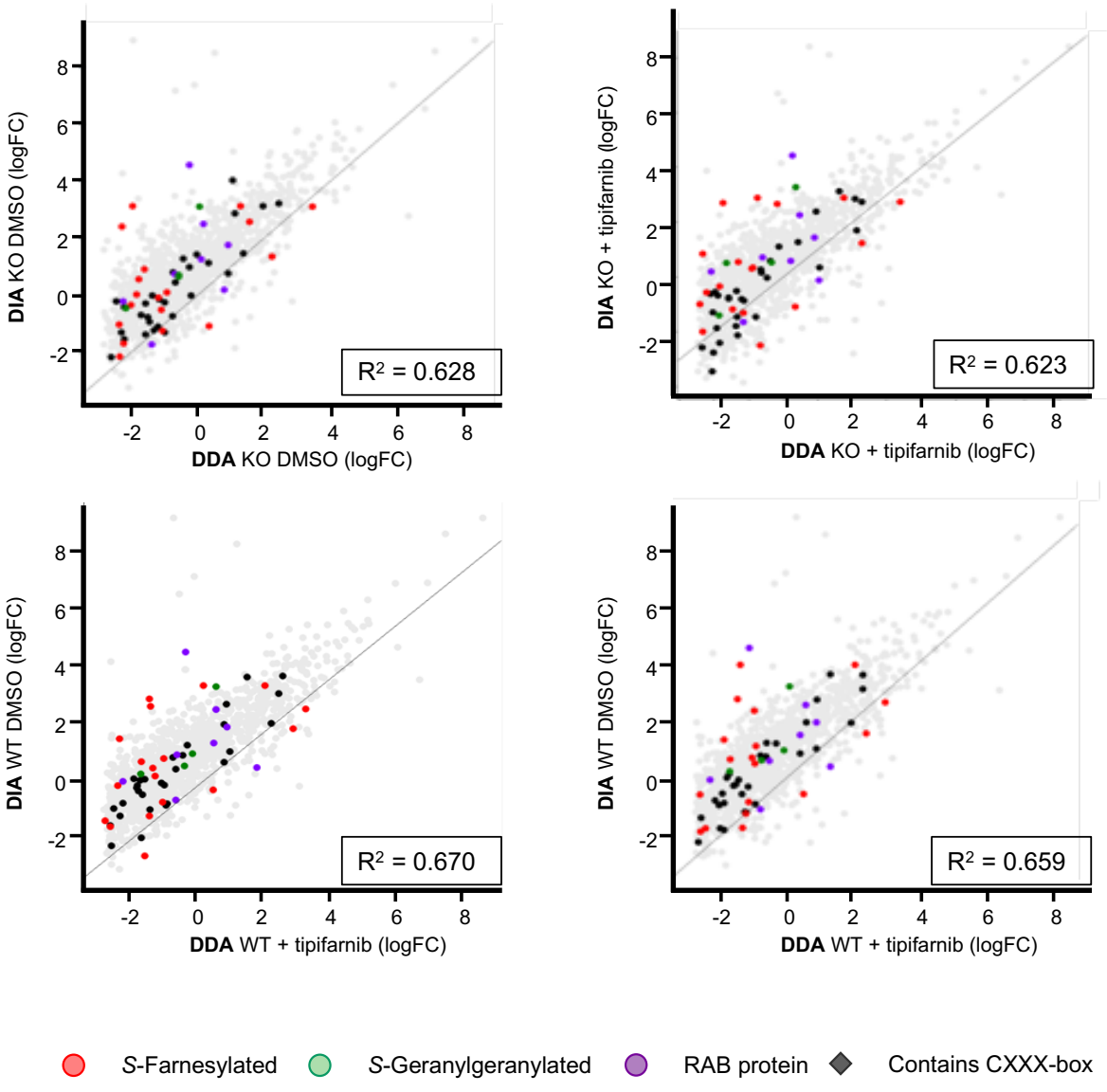

Figure 7.6. Correlation analysis of DIA and DDA whole proteome data of H23 cells

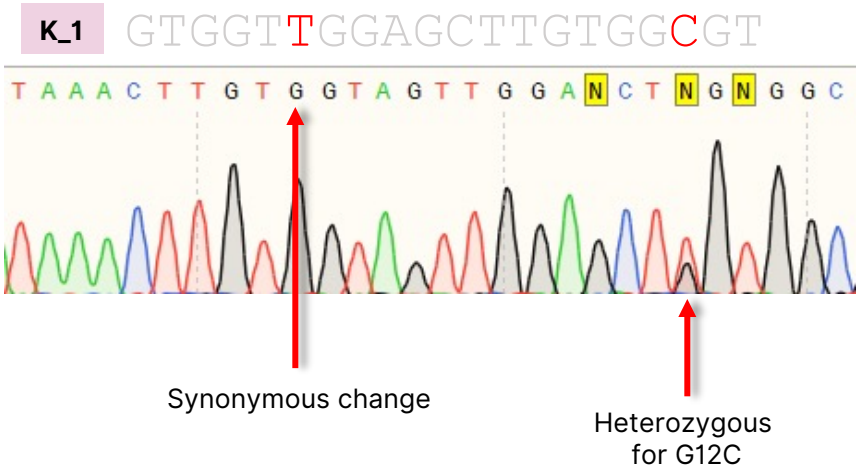

Figure 7.7. Sanger sequencing of KRAS exon in H23 cells reveals heterozygous G12C mutation

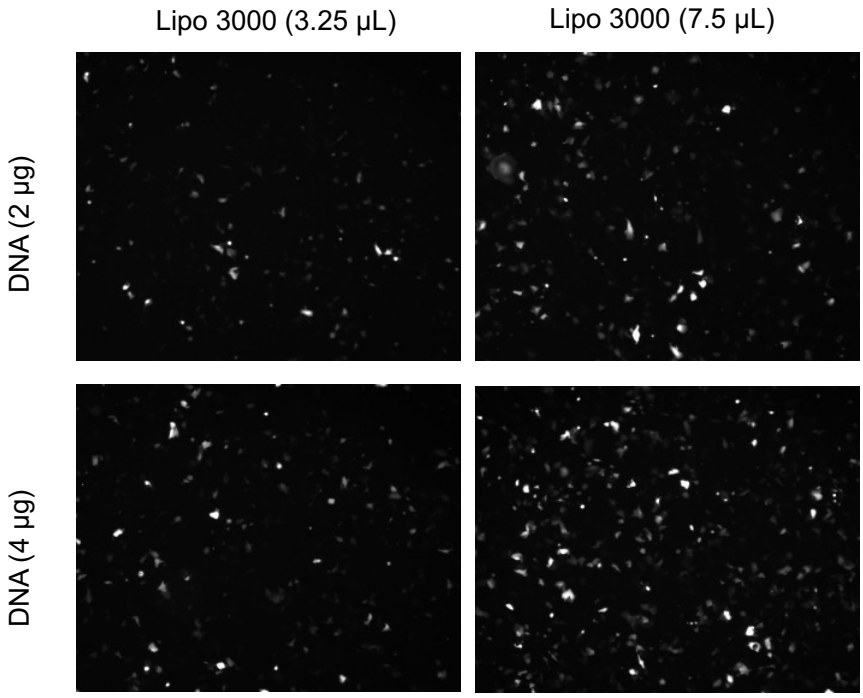

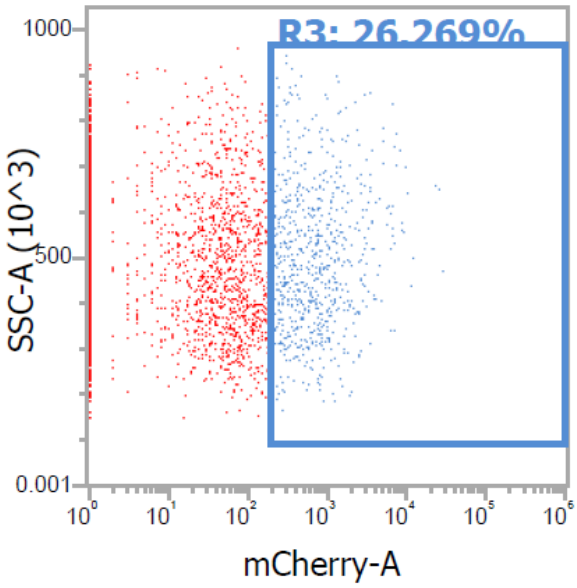

Figure 7.8. Confocal imaging (top) and flow cytometry analysis of mCherry transfected T24 cells to evaluate transfection efficiency. Bottom panel showing maximal transfection efficiency achieved by flow cytometry.

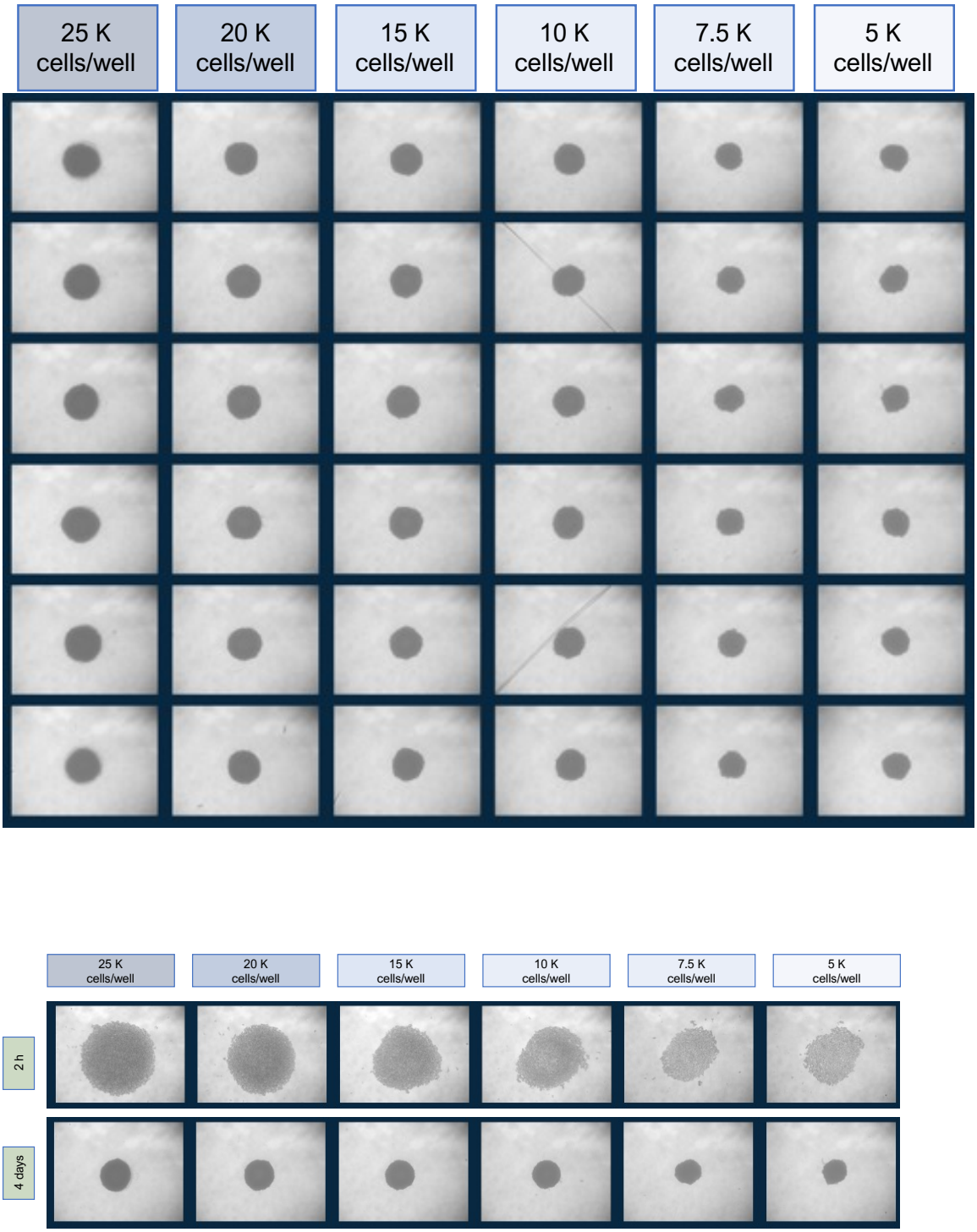

Figure 7.9. IncuCyte images of H23 spheroid formation using increasing seeding densities (top). Spheroids form within 4 days (bottom)

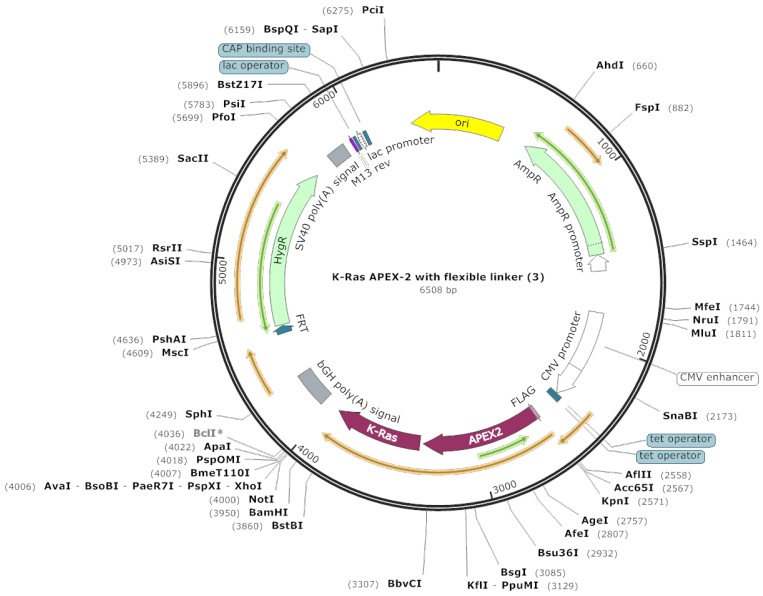

Figure 7.10. Example vector map of plasmid used to generate APEX2-RAS cell lines (shown here for $KRAS^{G12D}$)

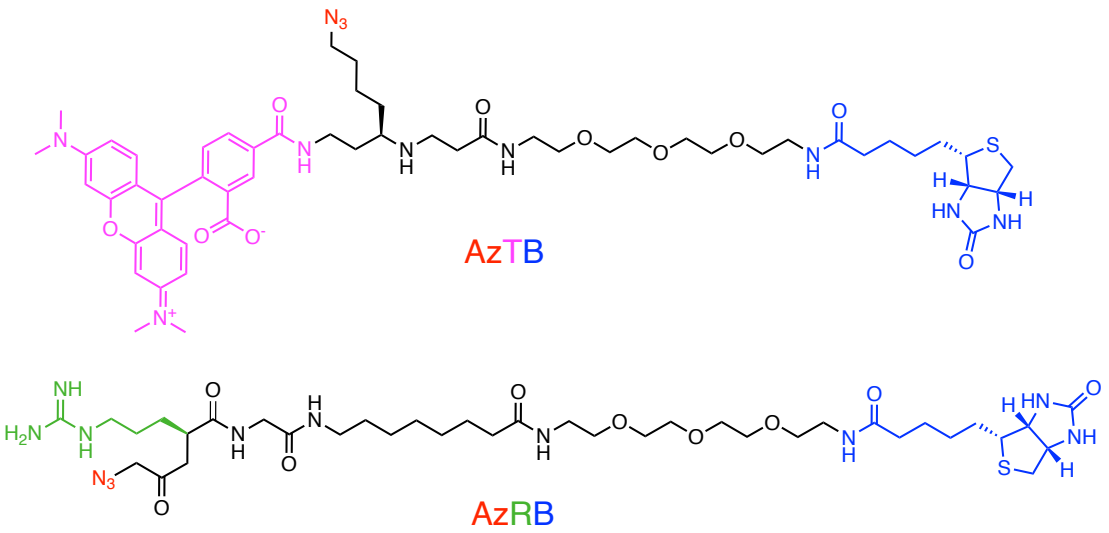

Figure 7.11. Structures of AzTB and AzB capture reagents used in this study[216]. Molecules were synthesized by Dr. Christelle Soudy.